UNIVERSITÀ DEGLI STUDI DELL'INSUBRIA

Dipartimento di Scienza ed Alta Tecnologia

PhD Course in Chemical Sciences, XXVII Cycle

SYNTHESIS, CHARACTERISATION AND PHOTOPHYSICAL PROPERTIES OF d^{10}-METALS LUMINESCENT COMPOUNDS

Supervisor: **Dr. Stefano BRENNA**

PhD Thesis of:

SARA DURINI

Thesis Defence: **January 27th, 2015 (Como, Italy)**

Committee Members: **Prof. Fabrizia GREPIONI**
Prof. Gianmario MARTRA
Dr. Alessandro CASELLI
Dr. Vladimiro DAL SANTO

To my Family, my Friends and my Love.

CONTENTS

ABBREVIATIONS

Bphen	4,7-diphenyl-1,10-phenanthroline
CT	Charge transfer
CTTS	Charge transfer to solvent
dbp	2,9-di-n-butyl-1,10-phenanthroline
dmp	2,9-dimethyl-1,10-phenanthroline
dpep	2,9-diphenetyl-1,10-phenanthroline
dpp	2,9-diphenyl-1,10-phenanthroline
dppb	1,2-bis(diphenylphosphino)benzene
dppe	1,2-bis(diphenylphosphino)ethane
dppFe	1,1^{I}-bis(diphenylphosphino)ferrocene
dppm	1,1-bis(diphenylphosphino)methane
dppp	1,3-bis(diphenylphosphino)propane
FET	Field effect transistor
hfac	hexafluoroacetylacetonate
HOMO	Highest occupated molecular orbitals
lact	L-(+)-lactate
lactH	L-(+)-lactic acid
LC	Ligand centred
LEC	Light-emitting electrochemical cell
LGOs	Ligand group orbitals
LLCT	Ligand to ligand charge transfer
LMCT	Ligand to metal charge transfer
$L^{F,F}$	1-(pyridin-2-yl)-3-(2,6-difluorophenyl)imidazo[1,5-*a*]pyridine
L^{I}	4-((4-(diphenylamino)phenyl)ethynyl)benzoic acid
L^{Me}	1-(pyridin-2-yl)-3-*o*-tolylimidazo[1,5-*a*]pyridine
L^{O}	2-(1-(pyridin-2-yl)imidazo[1,5-*a*]pyridin-3-yl)phenolate
L^{OH}	2-(1-(pyridin-2-yl)imidazo[1,5-*a*]pyridin-3-yl)phenol
LUMO	Lowest unoccupated molecular orbitals
MC	Metal centred
MLCT	Metal to ligand charge transfer
OLED	Organic light emitting diodes
PGMs	Platinum group metals
phen	1,10-phenathroline
POP	bis(2-(diphenylphospino)-phenyl)ether

Chapter 1

Introduction

During the last decades there has been a remarkable growth in the study of luminescent molecules and the technology of fluorescence has advanced at an accelerating pace in many different fields of sciences. One of the reason why research concerning luminescent compounds is very popular, is because of their application in genetic engineering,[1] nanotechnologies,[2] near-field optics[3] and photovoltaic technology,[4] to name a few; furthermore luminescent techniques evolved into a primarily research tool in the life and material sciences due to their sensitivity, ease of use and versatility.

1.1 PHOTOLUMINESCENCE

1.1.1 FLUORESCENCE AND PHOSPHORESCENCE PROCESSES

Luminescence is a phenomenon that occurs when a substance emits light from an electronically excited state to return to its ground state. Molecule's electrons can have different energies which are correlated to how much they are bounded to the molecule's nuclei. Electrons can only take on certain discrete values of energy, so it is better to speak about energy levels: to each energy level correspond an electronic state.

When the radiation hits a molecule, an electron can take energy from the incident photon because of the interaction between the electric field of the radiation and the field generated from the electrons. If the photon's energy is the same as the energy gap between two electronic states, there is a high probability for a molecule to absorb the light and an electron could be promoted from the ground state to an excited level. The absorption process has hence occurred.

When the molecule returns to the ground electronic state from its excited electronic state with a radiative decay process, it discards its excitation energy as a photon. A more common fate is nonradiative decay, in which the excess energy is transferred into the vibration, rotation and translation modes of the surrounding molecules. Photoluminescence is then defined as an emission of light that occurs from electronically excited states and it can be formally divided into two categories, fluorescence and phosphorescence, depending on the nature of the excited state, the emission pathway and consequently the lifetime.

It is tempting to think that all possible transitions are permissible and that an electron can afford a change of state from an initial orbital to any other orbital, but quantum mechanical principles state it is not so. It follows that the probability of a molecule to absorb and emit the light is regulated by the selection rules, that means that not all the electronic transitions between states with different energies are allowed. A full description of selections rules is complicated and goes beyond the scopes of this thesis. Broadly speaking selection rules arise from the conservation of angular momentum during a transition and from the fact that a photon's spin is 1. A general rule is that transitions with no change of overall spin angular momentum are allowed ($\Delta S = 0$), i.e. transitions between states with the same multiplicity (singlet – singlet, triplet – triplet). The spin multiplicity is $2S+1$, that is the number of possible orientation of spin angular momenta, where S is the angular spin moment. When the electrons are paired there is no net spin and $S = 0$: this arrangement gives a singlet configuration. If a molecule has a single electron then $S = ½$, this configuration is classified as a doublet. When there are two unpaired electrons $S = 1$, so $2S+1 = 3$, this case is called triplet. An electron in an excited orbital can have the same or the opposite spin orientation as the ground-state electron. Consequently, in theory, each promotion to a higher level could give different excited states. Since parallel arrangement of spins in an electronic configuration lies lower in energy than the antiparallel arrangement, for states arising from the same configuration, the triplet state generally lies lower in energy than the singlet state.

The phenomenon of fluorescence is a radiative transition between two energy levels with the same multiplicity. Upon absorption of light after radiation the molecule is taken to an excited singlet electronic state, that is the electron in the excited orbital is paired to the second electron in the ground state. After that the excited molecule undergoes radiationless decay: the electron steps down to the lowest excited state between the different vibrational levels, losing energy in a non radiative way. If the system cannot dissipate the larger energy difference needed to lower the molecule to the ground electronic state, the excited molecule might survive long enough to undergo spontaneous emission and release the remaining excess energy as radiation. Since return to the ground state is spin allowed, the emission of photon occurs rapidly. Emission rate of fluorescence are typically 10^8 s^{-1}, so that emission of radiation is near 10 ns after the exciting radiation is extinguished. In phosphorescence, the spontaneous emission may persist for longer

periods, typically fractions of seconds or seconds (sometimes even hours); this difference suggests that this process involves the storage of energy in a reservoir from which it slowly leaks.

Phosphorescence is emission of light from triplet excited states, it is therefore defined as a radiative process occurring between electronic states with different spin multiplicity. Since it is formally forbidden it is a significant less favourable process that typically occurs at a slower rate compared to fluorescence emission. The sequence of events leading to the phosphorescence for a molecule with a singlet ground state are showed in Figure 1.1.

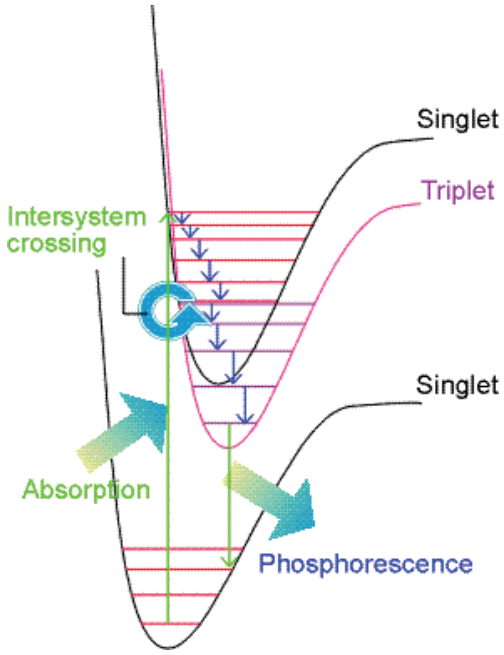

Figure 1.1. Sequence of the events giving phosphorescence process: after absorption of a photon the molecule goes to a vibronic excited singlet state, then it undergoes intersystem crossing leading the system in a triplet state. The radiative transition from the lower triplet excited state to the ground state is Phosphorescence.

The first steps are the same as in fluorescence, but the presence of a triplet excited state plays a decisive role. The singlet and the triplet excited state share a common geometry at the point where their potential energy curves intersect. Hence, if there is a mechanism for unpairing two electron spins, the molecule may undergo intersystem crossing, a nonradiative transition between states of different multiplicity, and become a triplet state. The system is now stepping down the triplet's vibrational ladder, and at the lowest energy level is "trapped" because the triplet state is at a lower energy than the corresponding singlet and the molecule cannot radiate its energy because return to the

ground state is spin-forbidden. The radiative transition, however, is not totally forbidden because the spin orbit coupling, that was responsible for the intersystem crossing, also breaks the selection rule. The molecule are therefore able to emit weakly and the emission may continue long after the initial excited state was formed.

The transitions that occur in a molecule during the absorption and emission processes can be illustrated by the Jablonski diagram (Figure 1.2). Jablonski diagram is a simplified representation of the relative positions of the vibronic energy levels of a molecule. The ground vibrational state of each electronic state are correctly located vertically, but the relative horizontal locations of the column bears no relation to the nuclear separation in the states; in addition some possible processes, such as quenching or solvent interaction, are not considered. Examination of the Jablonski diagram reveals that after the process of absorption of the light a fluorophore is excited to some higher vibrational level of either S_1 or S_2. Afterwards it undergoes an internal conversion process within 10^{-12} seconds or less and relaxes to the lowest vibrational state of S_1. Since fluorescence lifetime are typically near 10^{-8} seconds, internal conversion is generally complete prior to emission. Hence, florescence emission generally results from a thermally equilibrate excited state, that is, the lowest energy vibrational state of S_1.

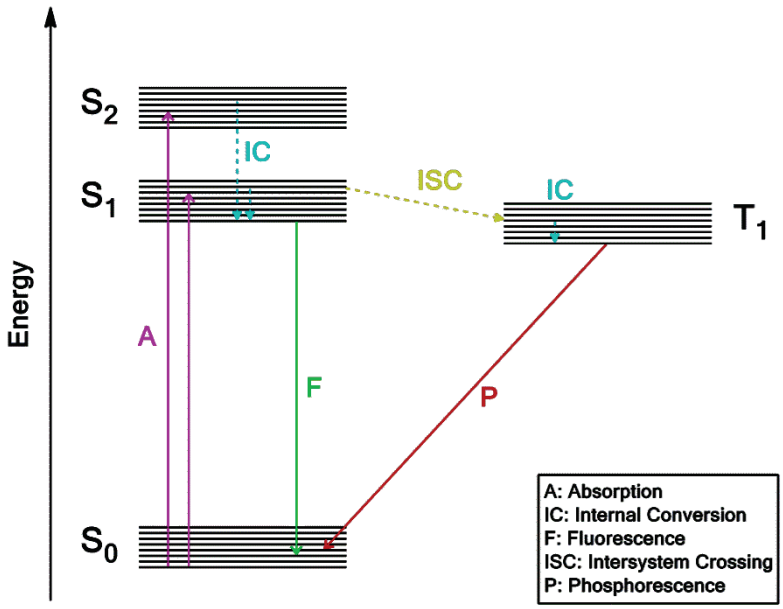

Figure 1.2. Jablonski diagram.

This fact leads to a general property of fluorescence emission, known as Kasha's rule[5]: photon emission is expected in appreciable yield only from the lowest excited state, in other words the same fluorescence emission spectra is generally observed irrespective of the excitation wavelength. In fact, upon excitation into higher electronic and vibrational levels, the excess energy is quickly dissipated leaving the fluorophore in the lowest vibrational levels of the lowest excited electronic state. This relaxation occurs in 10^{-12} seconds and is presumably a result of a strong overlap among numerous states of nearly equal energy. Because of this rapid relaxation, emission spectra are usually independent of the excitation wavelength.

Return to the ground state from the excited state S_1 occurs to a higher excited vibrational ground state level, which then quickly reaches thermal equilibrium. This transitions occur in about 10^{-15} seconds and are illustrated as "vertical transitions" to underline the instantaneous nature of light absorption and emission. it follows that all electronic transitions occur without change in the position of the nuclei (Franck-Condon principle).[5]

Molecules in S_1 can undergo an intersystem crossing, that is a radiationless transition between electronic states of different multiplicity, to the first triplet state T_1. Phosphorescence is the term used for the emission from this state, in which the electron in the excited orbital has the same spin orientation as the electron in the ground state. As a result transition from T_1 to the singlet ground state is forbidden and consequently the rate constants for triplet emission are several orders of magnitude smaller than those for fluorescence. Furthermore, since triplet states have lower energy than the corresponding singlet state, emission is shifted to longer wavelengths relative to the fluorescence. Phosphorescence is not common in solutions at room temperature because there exist many deactivation processes that compete with emission, such as non-radiative decay and quenching processes. It should be noted that the distinction between fluorescence and phosphorescence is not always clear, specifically for transition metal-ligand complexes, which display mixed singlet-triplet excited states.

As a general principle the phenomenon of luminescence displays some typical characteristics. Theoretically emission and absorption spectra should exhibit a vibrational fine structure: following light absorption the molecule is excited to another electronic state and to many possible vibrational states, with the emission instead there is a transition from the lowest excited state (as stated by Kasha's rule) to the electronic

ground state in one of many populated vibrational levels. In addition absorption and emission spectra should have an approximate mirror image relation because the spacings between vibrational levels are roughly equal and the transitions probability are similar since electronic excitation does not greatly alter the nuclear geometry. This is well illustrated by the emission and absorption spectra of anthracene (Figure 1.3):

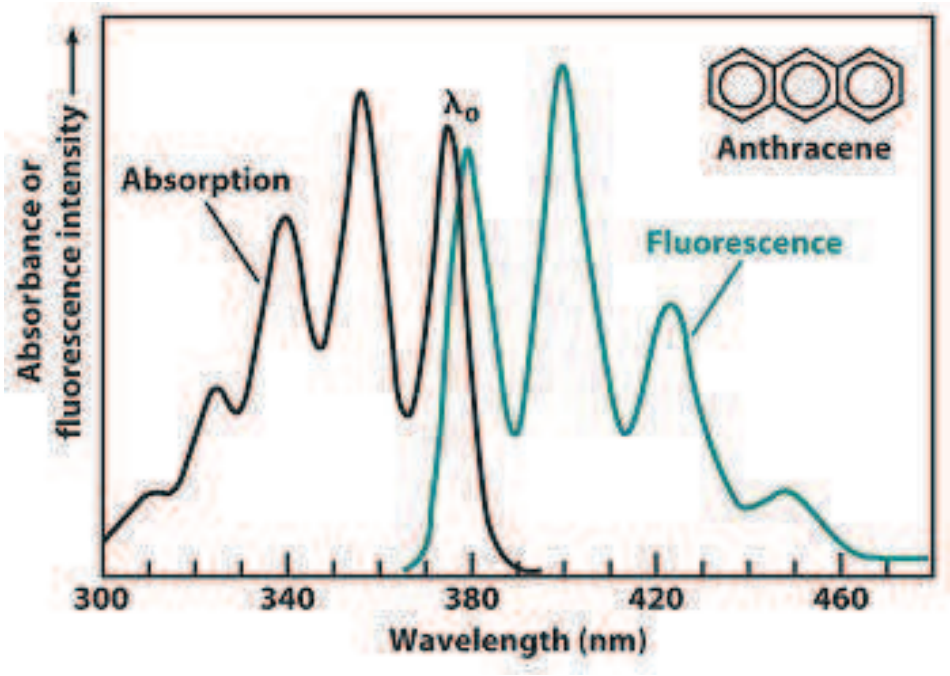

Figure 1.3. Absorption and fluorescence emission spectra of anthracene.

Nevertheless a lot of molecules show absorption and emission spectra without vibrational fine structure (Figure 1.4), what is more, sometimes a substance that displays the vibrational structure in a non polar solvent can lose it in a polar one. This behaviour is influenced by different aspect: broad bands are observed if vibrational levels are close or when there are interactions with the solvent.

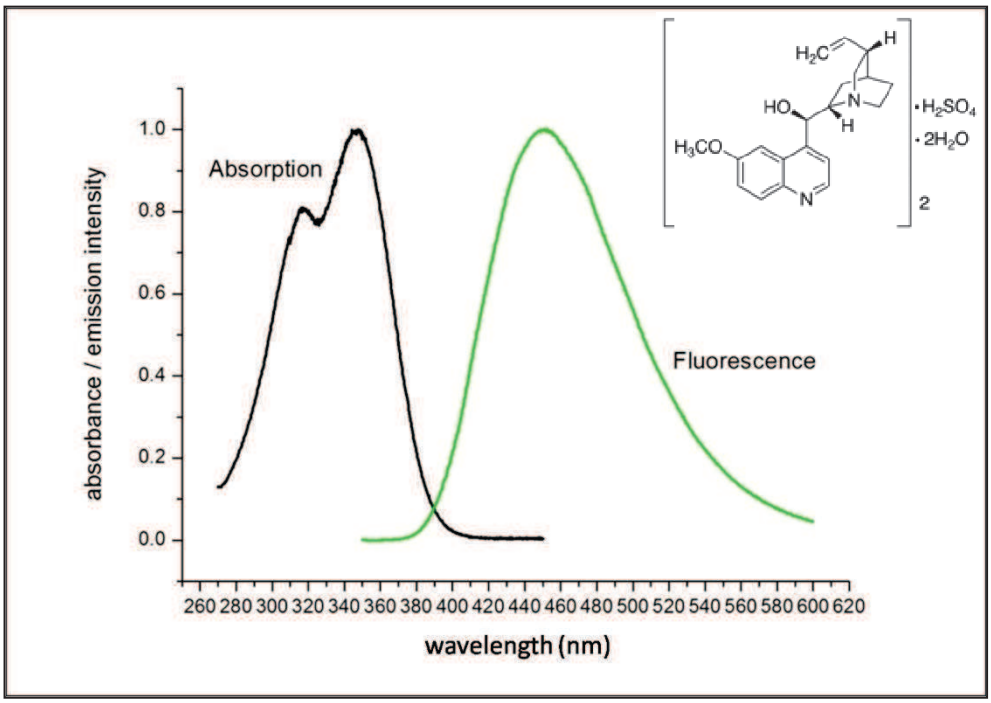

Figure 1.4. Absorption and fluorescence emission spectra of quinine sulphate.

Another typical characteristic of this phenomena is that the energy of the emission is less than that of absorption, in other words fluorescence (and even more so phosphorescence) occurs at lower energies or longer wavelengths (batochromic shift). The difference between the maximum excitation and emission wavelength is called "Stokes Shift" and the examination of the Jablonski diagram reveals that it is correlated with the energy that the molecule dissipates with non-radiative processes. The rapid decay to the lowest vibrational level of S_1 in conjunction with the decay of the electron into higher vibrational levels of S_0, result in loss of excitation energy.

1.1.2 PHOTOLUMINESCENCE LIFETIME AND QUANTUM YIELDS

Photoluminescence quantum yield (PLQY) and lifetime are two important properties of a fluorophore that can be measured. Quantum yield is a value that shows the efficiency of the luminescence process and it is given by the number of emitted photons over the number of absorbed photons. Lifetime is a measure of the time that a fluorophore takes to decay from the excited state to the ground state.

These properties can be best understood with a simplified Jablonski diagram, as the one shown in Figure 1.5:

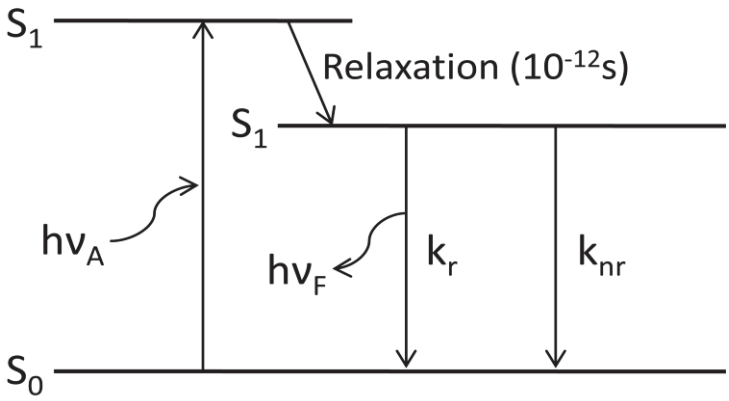

Figure 1.5. A simplified Jablonski diagram to illustrate the meaning of quantum yield and lifetime.

This diagram does not show all relaxation processes involved in the luminescence phenomenon but draws the attention on those responsible to return to the ground state. In particular we are interested in the emissive rate of the fluorophore (k_r) and its rate of non radiative decay (k_{nr}) to S_0. The fluorescence quantum yield is the ratio of the number of photons emitted to the photons absorbed. The rate constants k_r and k_{nr} both depopulate the excited state. The fraction of fluorophore that decays through emission, and hence the quantum yield, is given by:

$$Q = \frac{k_r}{k_r + k_{nr}}$$

PLQY can be close to unity if the radiationless decay rate is much smaller than the rate of radiative decay, that is $k_{nr} << k_r$. We note that the energy yield of fluorescence is always

less than unity because of Stokes losses. For convenience we have grouped all possible non-radiative decay processes with the single rate constant k_{nr}.

The quantum yield can be determined by absolute measurement using an integrating sphere, an optical device which is able to average the emitted light over all directions. Further information about integrating sphere and calculations to obtain the absolute value of PLQY will be given in the experimental section.

Lifetime of the excited state is defined as a measure of the time that takes the excited state of a molecule to decay to the ground state; generally fluorescence lifetimes are in the range of nanoseconds. The excited state (S_1) of a fluorophore undergoes decay following first order kinetics and its general behaviour can be described by the rate equation:

$$-\frac{d[S_1]}{dt} = (k_r + k_{nr})[S_1] = (k_{obs})[S_1]$$

The rate constant of decay (k_{obs}) is defined by the contribution of both radiative (k_r) and non-radiative (k_{nr}) deactivation pathways, therefore, for the fluorophore shown in Figure 1.5, lifetime can be described as follow:

$$\tau = \frac{1}{k_{obs}}$$

and the integrated law shows an exponential decay:

$$[S_1]_t = [S_1]_0 \, e^{-t/\tau}$$

where $[S_1]_0$ is concentration of S_1 at time zero, i.e. when has been flashed by the first light impulse.

We can understand better this concept if we put $t=\tau$:

$$[S_1]_t = [S_1]_0 \, e^{-t/\tau} = [S_1]_0 \, e^{-\tau/\tau} = \frac{[S_1]_0}{e}$$

Lifetime describe the time that the excited population of a fluorophore require to decay to 1/e (36.8%) of his initial value.

Obviously the value "τ" describes all possible decay that the excited singlet state can undergo, not only radiative decay, which can be described instead by the value τ_n (natural lifetime) and is given by:

$$\tau_n = \frac{1}{k_r}$$

Since $k_r < k_{obs}$ it follows that $\tau_n > \tau$, and the value of τ will be closer to τ_n, as lower will be the contribution of non radiative processes.

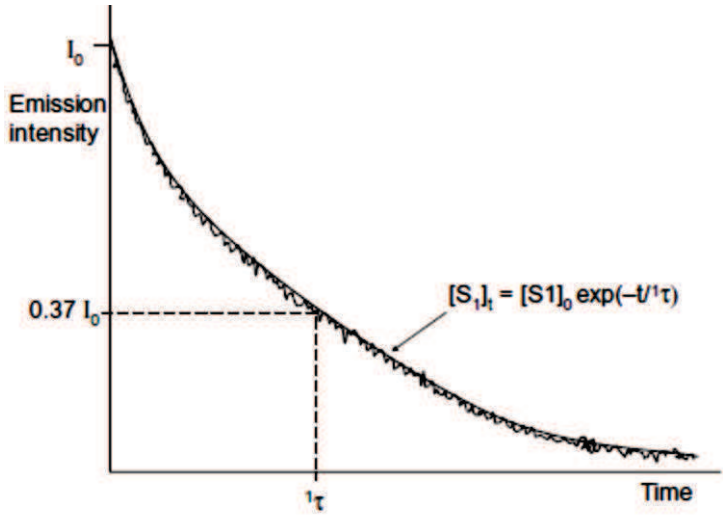

Figure 1.6. Exponential decay of emission intensity for a general fluorophore.

1.1.3 LUMINESCENCE QUENCHING

A problem that could affect intensity of emission is quenching, that is a non radiative deactivation of the excited state by which the molecule returns to the ground state without emission of light; this can be due to a wide variety of processes occurring within the molecule in relation to the environment. Collisional quenching can occur when some other molecules, which are called quenchers, in solution deactivate the fluorophore in the excited state upon contact. A lot of molecules can act as collisional quenchers: oxygen, halogens, amines and electron-deficient molecules like acrylamide to name some examples. The mechanism of quenching varies with the fluorophore-quencher pair. For instance, quenching of indole by acrylamide is probably due to electron transfer from indole to acrylamide, which does not occur in the ground state. Quenching by halogen and heavy atoms occurs due to spin–orbit coupling and intersystem crossing to the triplet state.

Aside from collisional quenching, fluorescence quenching can occur by a variety of other processes. Fluorophores can form non-fluorescent complexes with quenchers. This process is referred to as static quenching since it occurs in the ground state and does not rely on diffusion or molecular collisions. Quenching can also occur by a variety of trivial, i.e., non-molecular mechanisms, such as attenuation of the incident light by the fluorophore itself or other absorbing species.

1.1.4 SPECTROFLUORIMETER

Fluorescence experiments require attention to experimental details because there are many potential artefacts that can distort the data. Both emission and excitation spectra can be recorded with a spectrofluorimeter: an emission spectrum is the wavelength distribution of an emission measured at a single constant excitation wavelength; conversely an excitation spectrum is the dependence of emission intensity, measured at a single emission wavelength, upon scanning the excitation wavelength. Such spectra can be presented on either a wavelength scale or a wavenumber scale. Light of a given energy can be described in terms of its wavelength λ, frequency ν, or wavenumber. The usual units for wavelength are nanometres, and wavenumbers are given in units of cm^{-1}. Wavelengths and wavenumbers are easily interconverted by taking the reciprocal of each value. For example, 400 nm corresponds to $(400 \cdot 10^{-7}\ cm)^{-1} = 25000\ cm^{-1}$. The presentation of fluorescence spectra on the wavelength or wavenumber scale has been a subject of debate. Admittedly, the wavenumber scale is linear in energy.

In Figure 1.7 is represented a schematic diagram of a spectrofluorimeter:

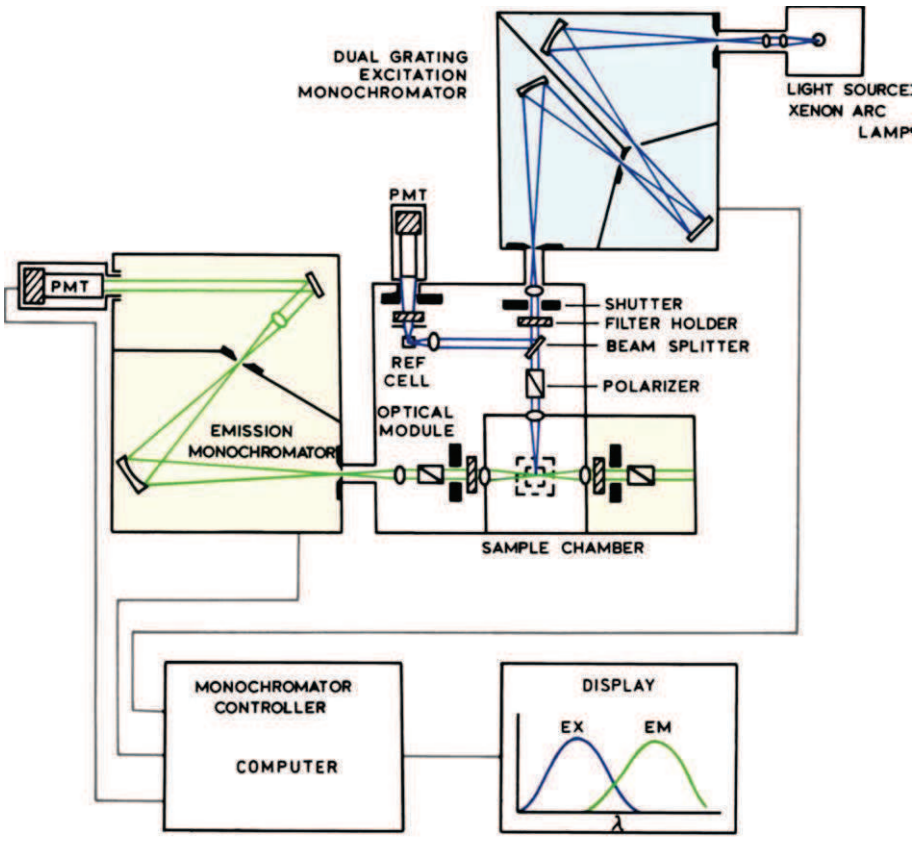

Figure 1.7. Schematic diagram of a spectrofluorimeter.

The source of exciting light is a xenon lamp, which can achieve high intensities at all wavelengths ranging upward 250 nm. The generated light is focused on a monochromator to select the excitation wavelength. In this schematic it contains two gratings, which decreases stray light, that is, light with wavelengths different from the chosen one; in addition, this monochromator uses concave gratings, produced by holographic means to further decrease stray light. The monochromatic beam hits the sample and the chromatic composition of emitted light is analysed by another monochromator, which requires an angular positioning of 90° respect to the incident beam in order to avoid recording light transmitted from the lamp. Furthermore the intensity of emission is detected with photomultiplier tubes and quantified with an appropriate electronic devices. The output is usually presented in graphical form and stored digitally.

The optical module in Figure 1.7 also shows some useful components that surrounds the sample holder. There are shutters to eliminate the exciting light or to close off the emission channel, a beam splitter in the excitation light path to reflect part of the excitation light to a reference cell, which contains a stable reference fluorophore. In this schematic there are also polarisers, that generally are removable so that can be used only for measurements of fluorescence anisotropy, or when it's necessary to select particular polarised components of the emission and/or excitation. Another useful feature is the ability to place optical filters into the excitation or the emission light path. Filters are often needed, in addition to monochromators, to remove unwanted wavelength in the excitation beam, or to remove scattered light from the emission channel.

An ideal spectrofluorimeter should have the following characteristics:

- the light source must yield a constant photon output at all wavelengths;
- the monochromator must pass photons of all wavelengths with equal efficiency;
- the monochromator efficiency must be independent of polarization;
- the detector (photomultiplier tube) must detect photons of all wavelengths with equal efficiency.

Unfortunately, light sources, monochromators, and photomultiplier tubes with such ideal characteristics are not available. In contrast to absorption measurement, in which the nonindeal behaviour of the components is “corrected” thank to comparative measurement with a blank, emission intensity measurements are absolute. As a result, one have to compromise on the selection of components and to correct for the non - ideal response of the instrument; most programs used to elaborate signals acquired from the instrument, in fact, are provided with correction files which allow the achievement of “correct” spectra.

1.2 TRANSITION METALS BASED LUMINESCENT COMPLEXES

One of the most fascinating field of research dealing with luminescence is the one that focuses the attention on planning and synthesising transition metal based luminescent complexes; in the last few decades the development of this complexes has received a considerable attention because they play a very important role not only in chemical or biochemical applications but also in many different fields of science.

A deep investigation of this class of complexes is due to some their interesting features, such as relatively long lifetime of the excited state (10 ns - 10 μs), wide Stokes' Shift, a general good stability: this and other more specific characteristics can open this branch to various experiment in clinical chemistry or biophysics.[6]

1.2.1 ELECTRONIC TRANSITIONS IN TRANSITION METALS COMPLEXES

Spectroscopic properties of transition metals complexes are used to gain an understanding about the electronic energy changes in complexes. Prior to discussing the spectral properties of this complexes it is useful to have an understanding of their electronic states: Molecular Orbital Theory can describe with a good approximation both ground and excited states.

As a general approach we can start from the construction of molecular orbitals for an octahedral complex. For a complex $[ML_6]$ with L σ-donor ligand, the valence orbitals available on the central metal will be the (n – 1)*d*, n*s* and n*p*; the ligand orbitals involved in σ bonds will be six lone pair orbital (in case of π-bonding ligands, additional orbital should be considered). Using symmetry properties of the orbitals it is possible to find proper combination of nine metal orbitals and six ligand orbitals: molecular orbitals are obtained from linear combinations of metal and ligands atomic orbitals having the same symmetry. The first step is to construct linear combination of the ligands orbitals, or ligand group orbitals (LGOs), that will overlap with metal orbitals along the octahedral bond axes. These LGOs must match the symmetries of the metal orbitals available for bonding. Symmetry properties of metal valence orbitals in an octahedral complex can be determined by referring to an O_h character table, which reveals that *s* orbital transforms

as a a_{1g}, the set of *p* orbitals as t_{1u} and the five *d* orbitals lose their degeneracy to form e_g and t_{2g} sets. In order to actually participate in a σ bond within the complex, a metal orbital must be capable of positive overlap with a ligand group orbital directed along the bonding axes. For the moment, let us merely consider the directional requirement and ignore the fact that, for positive overlap, the metal and ligand orbitals must also have the same sign. The a_{1g} metal orbital will be spherical, therefore being capable of overlap with LGOs on all axes. The t_{1u} and e_g sets all have lobes concentrated along the bond directions and thus are also capable of bond participation, as it is shown in Figure 1.8a for the d_{x2-y2} orbital; the t_{2g} sets, instead, have lobes directed between the bonding axes and thus do not yield net overlap with ligand orbitals, as it is shown in Figure 1.8b.

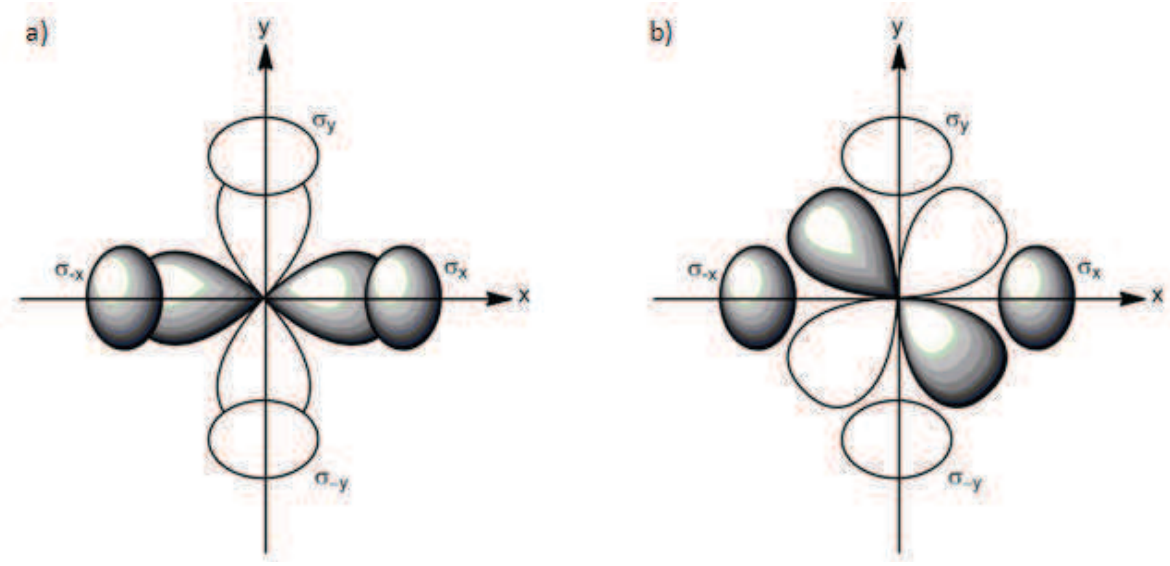

Figure 1.8. Overlap of ligands orbitals in the xy plane with metal d_{x2-y2} (a) and d_{xy} (b) orbitals.

The foregoing analysis has shown that LGOs to be constructed for the σ bonds of an octahedral complex must be of a a_{1g}, t_{1u} and e_g symmetries. It is worth noting that determining the symmetries of the orbital that will participate in the bonding do not tell us what specific combinations of the ligand lone-pair orbital should be used in constructing the six LGOs. We can have an idea about this process considering, as a simple example, the overlap with a_{1g} metal orbital. The sign of the wave function for the metal a_{1g} orbital is everywhere positive. The six ligand can interact equally with this orbital, and each contributing orbital must also have a positive sign.

Thus the a_{1g} LGO can be constructed from an additive combination of the six ligand orbital:

$$\sum_{a_{1g}} = \frac{1}{\sqrt{6}}(\sigma_x + \sigma_{-x} + \sigma_y + \sigma_{-y} + \sigma_z + \sigma_{-z})$$

Where Σ and σ represent the wave functions for the ligand group orbital and the contributing ligand orbitals, respectively, and $\frac{1}{\sqrt{6}}$ is a normalisation constant. A similar approach can be followed to obtain the wave functions for the LGOs with different symmetries that will overlap with the metal *p* and *d* orbitals. Since the metal t_{2g} orbitals cannot participate in *σ* overlap, they are considered nonbonding molecular orbitals in complexes where there is no possibility for π bonding; if there are ligand orbitals of appropriate symmetry available, the t_{2g} orbitals will be involved in π bonds. In Figure 1.9 is shown a typical molecular orbital energy diagram for the bonds in an octahedral complex:

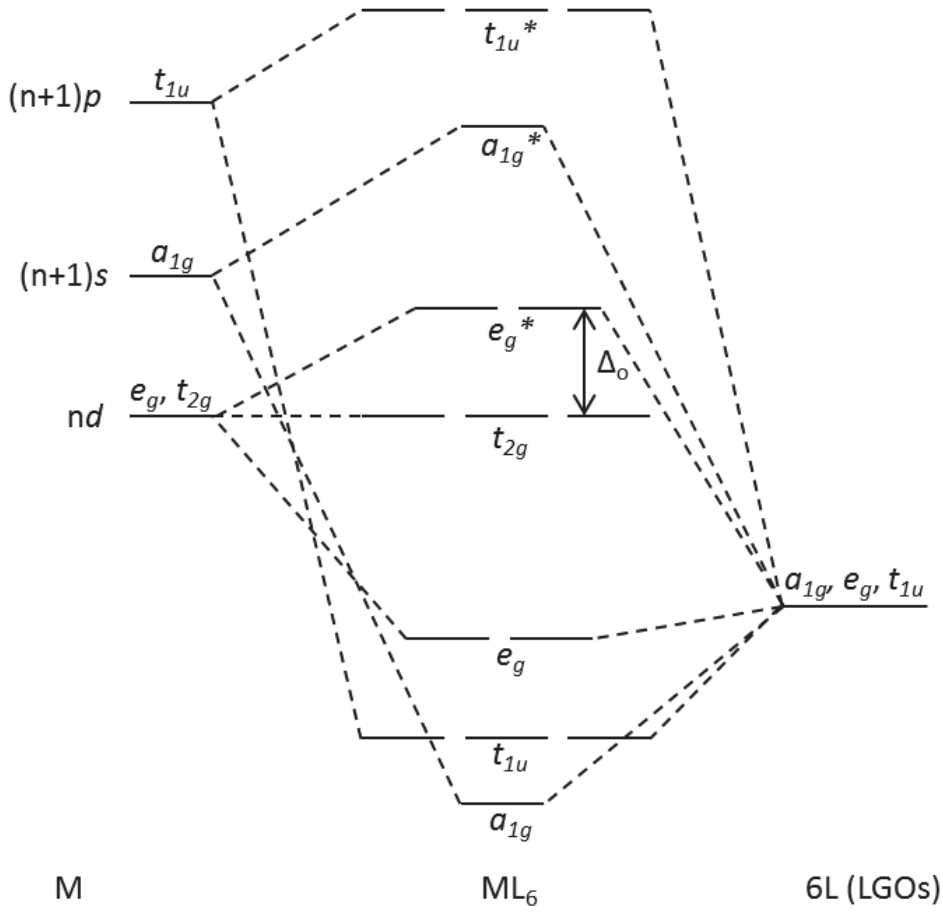

Figure 1.9. A *σ*-bond molecular orbital diagram for a complex of octahedral geometry.

There are several approximations involved and the diagram shown is only qualitatively accurate; however this does not detract from the usefulness of the diagram. It is certain that the overlap of the metals 4*s* and 4*p* orbitals with ligand group orbitals is considerably better than that of 3*d* orbitals. Consequently, the a_{1g} and the t_{1u} molecular orbitals are the lowest in energy and the corresponding a^*_{1g} and t^*_{1u} antibonding orbitals the highest in energy. The e_g and e^*_g are displaced less from their barycentre because of poorer overlap. The t_{2g} orbitals, being nonbonding in a σ-only system, are not displaced at all from their original energy.

This procedure may also be applied to the generation of MO diagram for complexes of other geometries. The metal atom or ion in each case will have the same nine valence orbitals available for bonding, but their symmetry properties will vary from one geometry to another. A σ molecular orbital diagram for a tetrahedral and square planar complex is shown in Figure 1.10a. For a tetrahedral ML_4 complex the metal *s* and *p* orbitals have a_1 and t_2 symmetries, while the five *d* orbitals are split into two sets: *e* and t_2; the four LGOs will consist of a t_2 set and one orbital with a_1 symmetry. The t_2 LGOs can interact with both sets of metal t_2 orbitals to give three sets of σ MOs: one bonding, one slightly antibonding and one clearly antibonding. In the diagram for the tetrahedral complex we can also note that, in contrast to the octahedral case, the metal *e* orbitals are now nonbonding and the separation between them and the next highest t_2 orbital is labelled Δ_t.

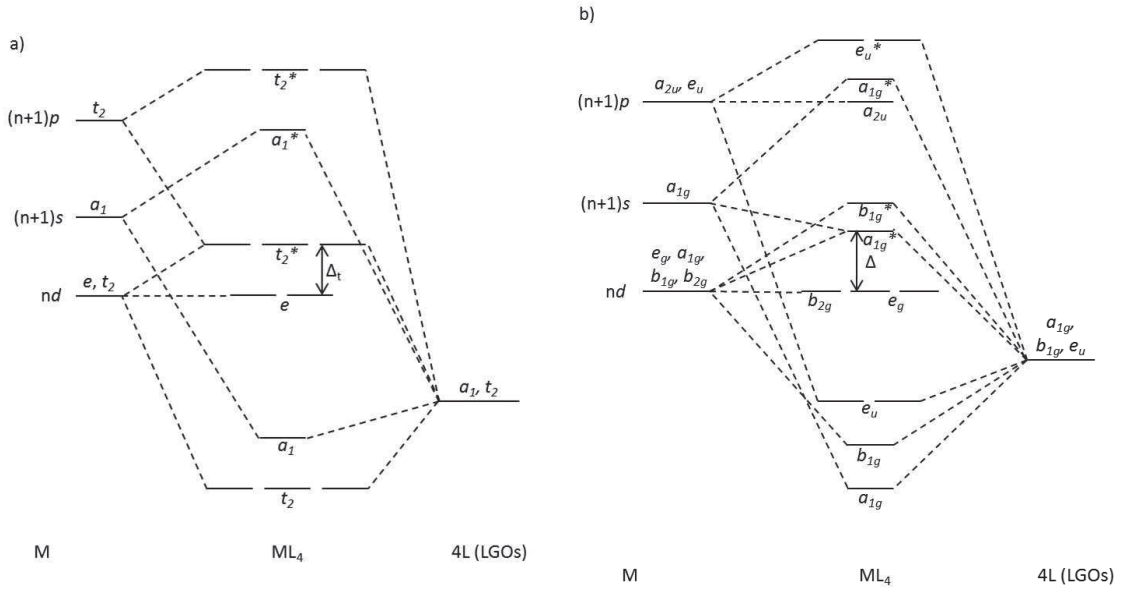

Figure 1.10. σ-bond MO diagrams for a complex of tetrahedral (a) and square planar (b) geometry.

For complexes adopting a square planar geometry, the metal *d* orbitals are split into a_{1g}, e_g, b_{2g} and b_{1g}; *p* orbitals also lose their degeneracy, giving a_{2u} and e_u. The four ligands, which will be oriented along the x and y axes will appear as a_{1g}, b_{1g} and e_u. From the diagram we can note that a_{1g} LGO overlaps with both a_{1g} metal orbitals, producing three MOs of this symmetry, as already seen in the case of tetrahedral complex; in addition in Figure 1.10b is shown that several metal orbitals (a_{2u}, e_g and b_{2g}) remain nonbonding because they are not engaged in net overlap with the ligand orbitals.

In addition to forming σ bonds, many ligands are capable of a π bonding interaction with a metal. As a rule, metal and ligand orbitals participating in π bonds will lie perpendicular to the internuclear axes. The ligand group orbitals capable of interactions in an octahedral complex fall into four symmetry categories: t_{2g}, t_{1u}, t_{2u} and t_{1g}. A transition metal possess only two types of orbitals that could use for π bonds: t_{2g} (d_{xy}, d_{xz}, d_{yz}) and t_{1u} (p_x, p_y, p_z); however the members of the t_{1u} set are directed towards the ligands and therefore participate in strong σ bond. The t_{2g} orbitals, on the other hand, are directed between the ligands, consequently they can readily π-bond to LGOs of matching symmetry: π-bonding in an octahedral complex is thus limited to the orbitals of t_{2g} symmetry, the other ligand group orbitals remain nonbonding. The result is that the bonding t_{2g} level is lowered and the value of Δ_o increases relative to what it would be in a σ-only system. A molecular orbital diagram including π interactions for an octahedral $M(CO)_6$ complex is shown in Figure 1.11.

These energy level diagrams can be very useful in order to describe the possible transitions occurring in metal complexes, according to the orbital type they arise from; this is observable in Figure 1.12 for a metal complex in an octahedral symmetry.

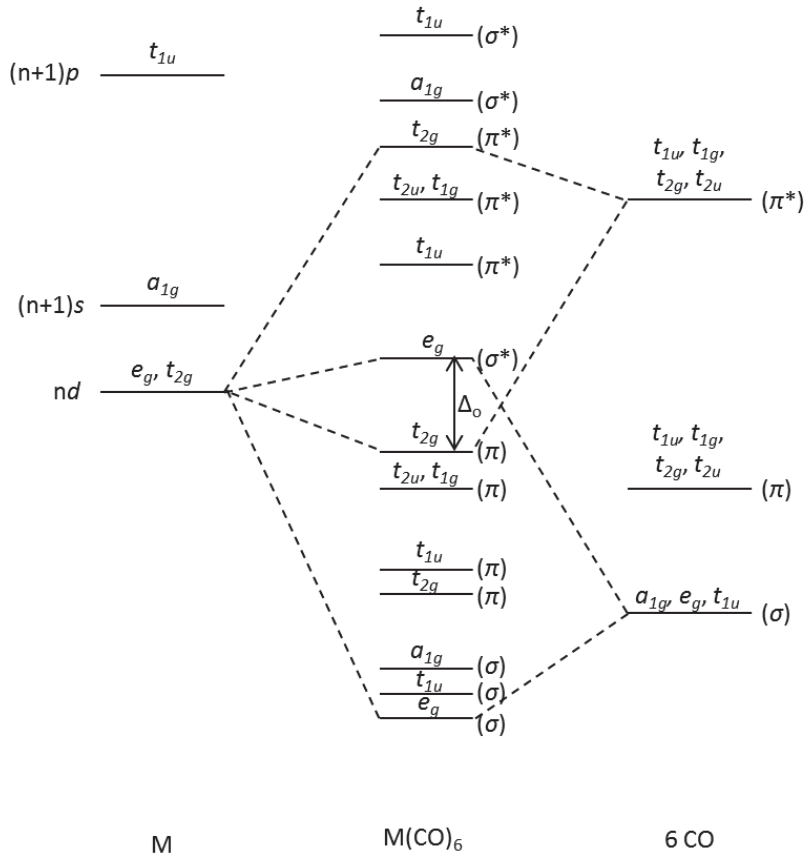

Figure 1.11. MO diagram for an octahedral $M(CO)_6$ complex including both σ and π interactions. Correlations lines are drawn only to those molecular orbitals to which the metal d electrons contribute.

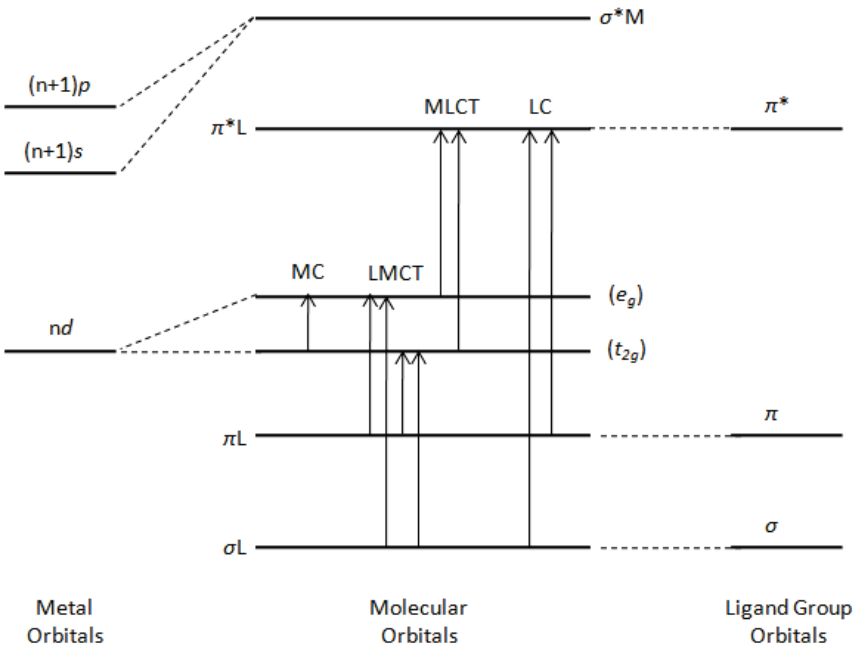

Figure 1.12. Simplified MO diagram showing principal electronic transitions for a transition metal complex with octahedral geometry.

Observing the diagram we can identify three different type of electronic transitions:

- **Metal Centred (MC):** these are transitions between molecular orbital mainly localised on metal centre, for instance d → d transitions. However this process in not favourable since d → d (or t → e) transitions are forbidden due to selection rules, as a consequence the phenomena will occur with weak intensity.
- **Ligand Centred (LC):** in this case electron transitions occur between ground and excited states both localised onto the ligand. Broadly speaking emission in the visible range are observed for transitions involving π-π* orbitals.
- **Charge Transfer (CT):** this class include all transitions between molecular orbitals localised on different elements and, as Figure 1.12 reveal, there are two types depending on whether the electron move from metal orbital to ligand orbital (MLCT) or viceversa (LMCT).

There are also other type of less common transitions which are not shown in Figure 1.12: **Charge Transfer To Solvent (CTTS)**, occurring from a metal centred orbital to a solvent's orbital and **Ligand to Ligand Charge Transfer (LLCT)**, occurring between two different ligands' orbitals.

In general for luminescent phenomena occurring for transition metal complexes the involved mechanism belong to the charge transfer type, particularly is quite common that electrons are promoted from metal centred molecular orbitals to orbitals localised on the ligand.

1.2.2 d^{10}- METALS LUMINESCENT COMPLEXES

The development of transition metals based luminescent compounds has received an increasing attention along with the expansion of their field of applications. They are used as emitters for organic light emitting diodes (OLEDs), which have recently entered the mass market in displays for smartphones and tablet PCs, and lightning applications, furthermore their role in solar conversion devices has became fundamental with the years. Other new promising uses are light-emitting electrochemical cells (LECs), chemical sensors, resonator for organic laser and photocatalyst.

Most of the complexes used so far often contains d^6 or d^8 metal centres from the Platinum Group Metals such as platinum(II),[7] iridium(III),[8] ruthenium(II)[9] or rhenium(I),[10] but these metals do not satisfy all the criteria required recently to be employed in order to obtain potential materials for the applications listed above. Effectively, not only high performances, good processability and a certain chemical robustness are required, in addition materials used for these applications need to be well-accessible and cheap. Unfortunately PGMs are quite rare and expensive, and consequently a crucial aim in this field is the synthesis of luminescent compounds based on less expensive and more abundant transition metals.

Among other metal centres, those with d^{10} configuration proved to satisfy this goal, and complexes based on M(I) (M = Cu, Ag, Au)[11] or M(II) (M = Zn, Cd)[12] have received a particularly attention since the nineties due to their strong luminescence at ambient temperature and especially in the solid state[13]. Unlike Ir(III), Pt(II), Ru(II) or Re(I) complexes, no self quenching occurs even for high concentrations or in bulk samples; besides the d-s transitions on the metal centres, ligand-centred transitions and inter-ligand transitions, the emissive state of the d^{10} transition-metal complexes includes charge-transfer transitions between the metal centre and ligands. MLCT electronic transitions in coordination compounds are normally more intense when compared to the other type. As far as emission is concerned, when MLCT excited state are the lowest-lying, they are generally characterised by long lifetime and potentially intense luminescence, even though exceptions are possible. While luminescent MLCT excited state of d^6 metal complexes, in particular those of Ru(II), can be strongly affected by the presence of upper lying MC orbitals, which can be partially populated through thermal activation from the

MLCT state and prompt non-radiative deactivation pathways and photochemical degradation, d^{10} complexes show closed shell and consequently cannot suffer this kind of problem (nevertheless undesired non-radiative deactivation processes of their MLCT levels can be favoured by other factors) as can be observed in Figure 1.13.

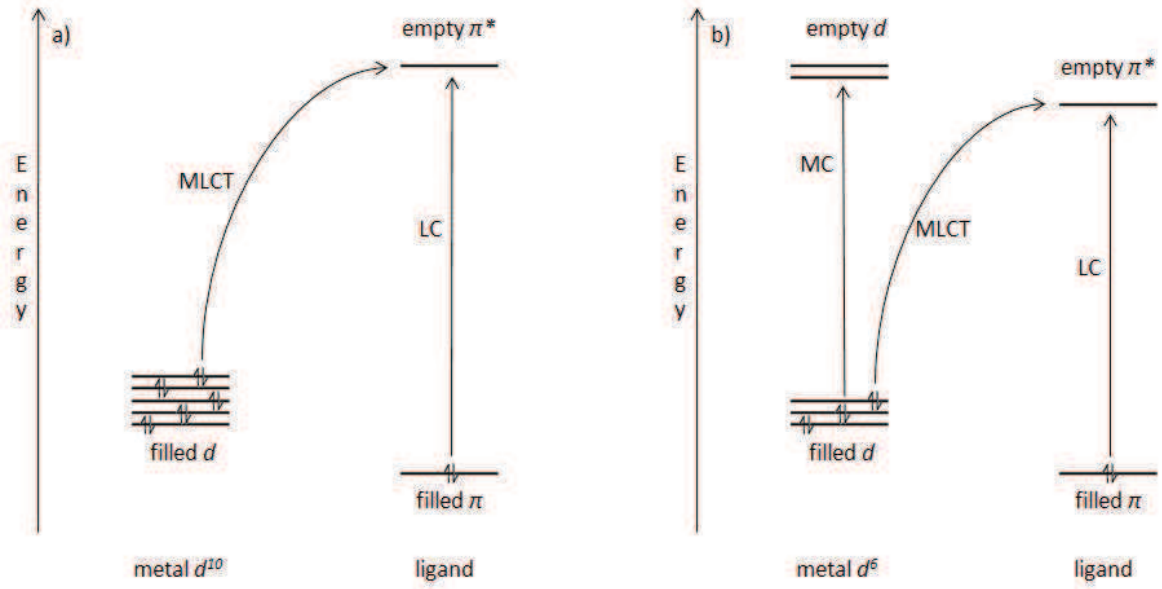

Figure 1.13. Comparison between electronic transition occurring in d^{10} metal complexes (a) and d^6 metal complexes (b).

Furthermore this class of complexes exhibit a high structural diversity and show emission with several class of ligands and, based on the involvement of metal to ligand charge transfer or ligand to ligand charge transfer, the emission colour of these complexes can be tuned by systematically variation of the ligand system. Finally, from an application point of view, they are especially favourable due to the high abundance (Figure 1.14), low price and easy accessibility of these metals.

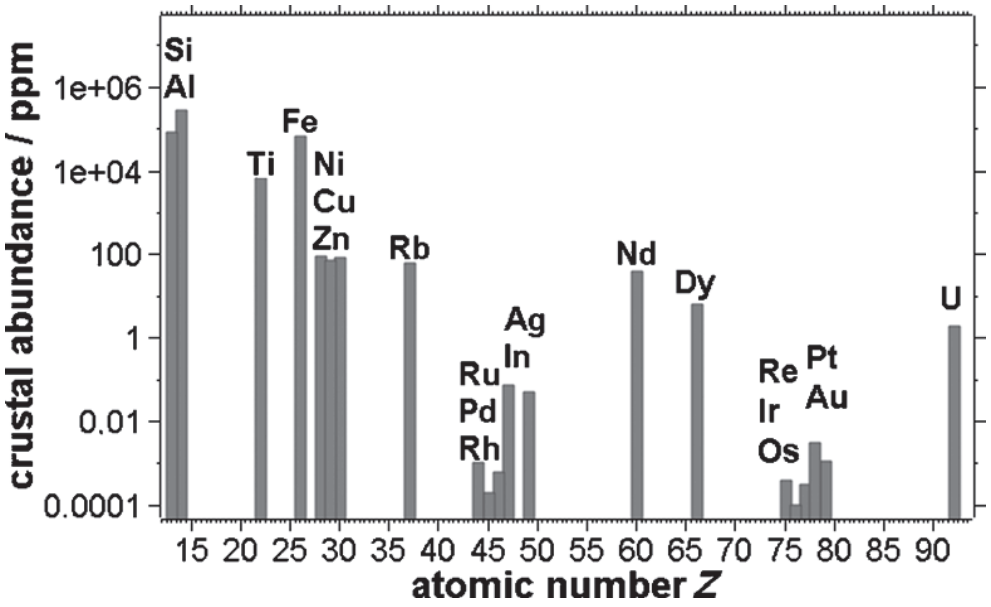

Figure 1.14. Abundance of selected elements in Earth's crust. Copper, zinc and silver are several orders of magnitude more abundant than elements Ru, Re, Ir and Pt.

The synthesis of this complexes is often carried out at room temperature (or in mild conditions) by a simple mixing of the suitable metal precursor and the ligand, achieving high yields. In literature a broad variety of coordinating atoms have been reported, in particular it has been shown that nitrogen and phosphorus containing ligands can be favourable for Zn and Cu. Therefore, the colours of the emission of many complexes can be tuned by changing the electronic structure of the complex introducing electron-donating or –withdrawing groups on the ligand, even the solubility can be modified by introducing other appropriate substituent.[14]

In this regard, there have been great achievements in the development of luminescent compounds containing d^{10} metals including both mononuclear[15] and polynuclear[16] species and especially those containing neutral N based ligands have showed great promise.

Relevant examples of heteroleptic complexes of d^{10} metals M(N∩N) systems (M = Cu, Zn, Ag; N∩N = bidentate nitrogen ligand) bearing phosphines as ancillary ligands or halides with different stoichiometry and geometries with luminescent properties have been published.

As far as Zn(II) complexes concern, Wang have coordinated substituted 2,2'-bipyrimidines (Figure 1.15a) and 2,2'-dipyridylamino derived ligands to $ZnCl_2$ (Figure 1.15b). Other functionalised dipyridylamines have been recently used by Song (Figure 1.15c) and

Schindler (Figure 1.15d). Finally, Ghosh reported on the structure and photoluminescence behavior of Zn(II) and Cd(II) atropoisomers containing unsymmetrical diimines (Figure 1.15e).

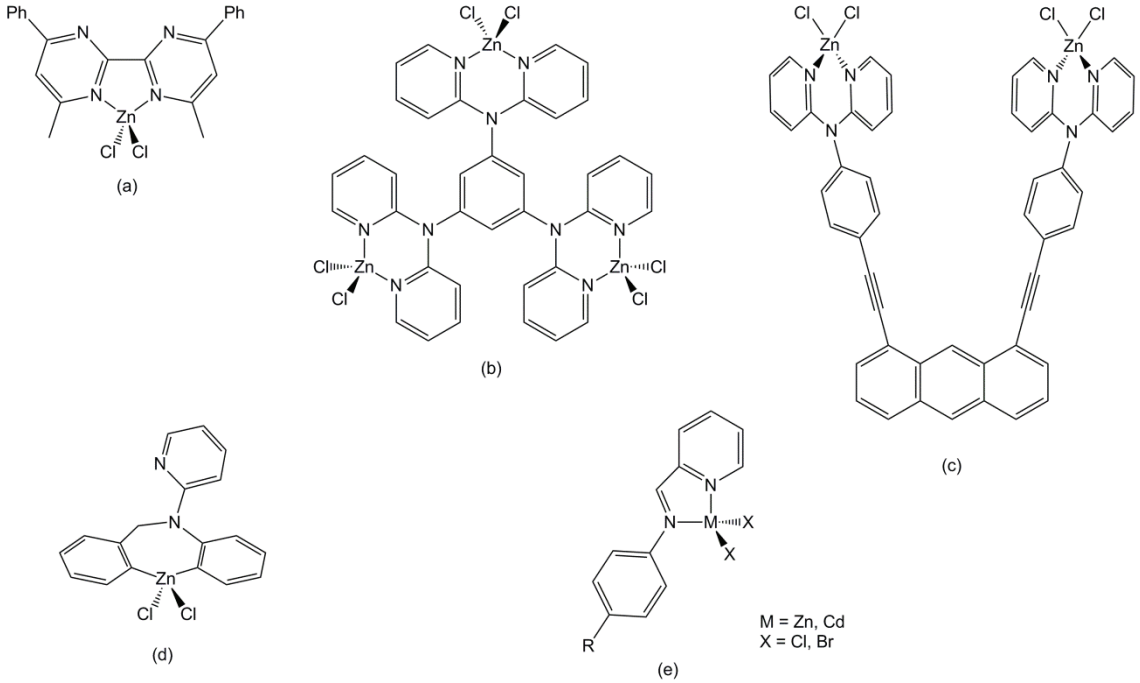

Figure 1.15. Examples of M(N∩N)X_2 systems (M = Zn, Cd; N∩N = bidentate nitrogen ligand; X = halide) showing luminescence.

As far as regard the heteroleptic coordination scenario of Cu(I) and Ag(I) it has been widely investigated. McMillin and co-workers reported mixed-ligand Cu(I) complexes prepared from 1,10-phenantroline and bis[2-(diphenylphosphino)phenyl]ether[17] characterised by remarkably high emission quantum yield from their metal to ligand charge transfer excited state. Other numerous examples have been prepared following this path[18]. Recently Nierengarten *et al.* have deeply investigated heteroleptic Cu(I) complexes combining various phenantroline derivatives with different bis-phosphine ligands, obtaining a wide library of these derivatives that has been systematically investigated (Figure 1.16 and 1.17).

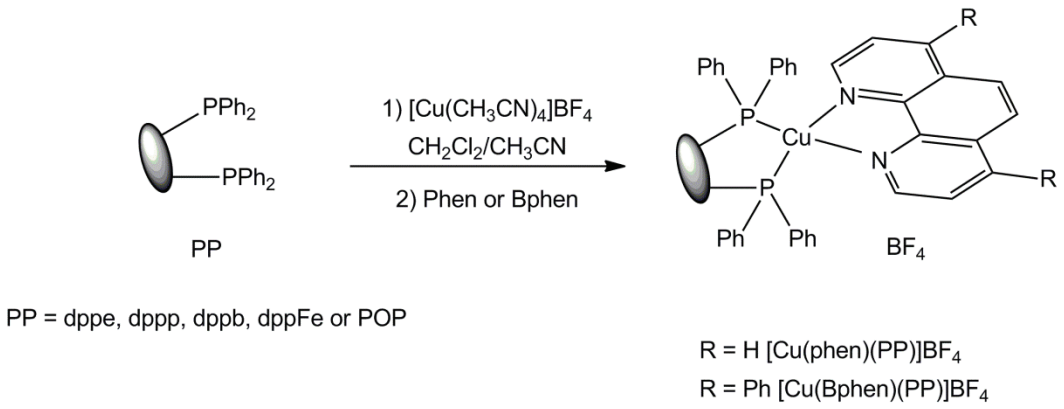

Figure 1.16. Procedure for preparation of heteroleptic $[Cu(NN)(PP)]^+$ derivatives from 1,10-phenantroline and 4,7-diphenyl-1,10-phenantroline.

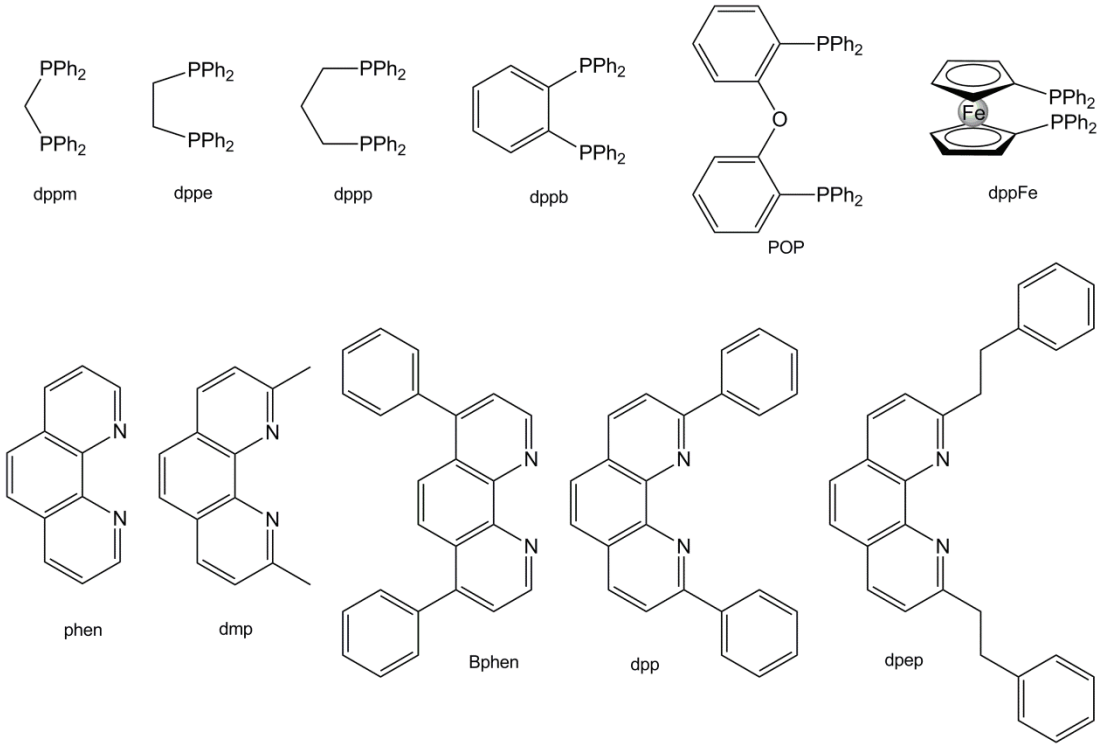

Figure 1.17. List of NN and PP ligands used for preparation of heteroleptic $[Cu(NN)(PP)]^+$ complexes.

Following these systematic studies on $[Cu(PP)(NN)]^+$ compounds, analogous heteroleptic silver complexes have been investigated by Nierengarten and co-workers in 2013.[19] Before them only few examples of analogous derivatives have been effectively investigated.[20] For representative examples H. T. Hor et al. Used PPh_3 ligand to synthesize the $[Ag(PPh_3)(phen)](X)$ compounds, where X = BF_4 or PF_6, and more recently, the bisphosphine derivative $[Ag(phen)(PPh_3)_2^+][X^-]$ was structurally characterized using a functionalized acylpyrazolonate anion by Cingolani and co-workers. It is noteworthy that

C. Pettinari et al., studying some families of silver compounds in depth, have reported interesting structural characterisations of dinuclear silver compounds of general formula $[(AgX)_2(PP)(NN)_2]$, where X = ClO_4 or NO_3.

1.3 CHAPTERS OUTLINE

In the past the coordination chemistry of N-based multidentate ligands,[21] with special attention to pyrazole and its analogues (imidazole, triazole) both in their neutral[22] and anionic azolate forms,[23] has been widely explored in this research group. Based on the contest illustrated above and on previous work developed in the research group where this work has been carried out, in this thesis is reported the synthesis, the characterisation and the description of the photophysical properties of different classes of d^{10} metal luminescent complexes.

Progressing the investigation in these fields, herein in Chapter 2 are reported studies conducted on Cu(I) luminescent complexes bearing lactate anion, to investigate possible correlations between emission and the rigidity imposed by the anion through H-bond catemeric structure. Chapter 3 is focused on Zn(II) complexes containing 3-aryl substituited 1-pyridylimidazo[1,5-*a*]pyridine ligands, which show moderate to good PLQY and an interesting behaviour related to their structural characteristics. Chapter 4 is dedicated to Cu(I) and Ag(I) heteroleptic complexes; in particular the attention has been directed to $[Ag(NN)(P)]^+$ (NN = 2-(1-(pyridin-2-yl)imidazo[1,5-a]pyridin-3-yl)phenol) compounds as they showed nice PLQY and a fine-tuning of the emissive properties depending on the electronic properties of the coordinated phosphines.

Chapter 2

Luminescent Cu(I) Complexes Bearing Lactate as Anion

As reported in the literature, copper (I) complexes often exhibit weak luminescence emission and short-living excited states.[24] In particular, for tetrahedral complexes, it has been demonstrated that the quenching of luminescence could be due to i) a distortion of the excited state which increases non-radiative decay of the emissive excited state, ii) the dissociation of a ligand in the excited state, or iii) an interaction with the solvent which leads to the formation of very short living exciplexes.

According with recent studies,[25] the introduction of sterically demanding ligands lead to enhanced emission reducing non-radiative processes imposing a rigid surrounding around the metal centre.

Typically copper(I) based systems investigated are those formulated as $[Cu(NN)_2]^+$, where NN represents a chelating ligand with a phenanthroline or a bipyridine metal-binding domain.[26] The precursor of this class of complexes is $[Cu(phen)_2]^+$ (phen = 1,10-phenanthroline), which however does not exhibit luminescent properties; the introduction of substituents in position 2 and 9 of the ligand induces an enhancement of steric hindrance around copper, resulting in a more stable excited state.

Figure 2.1 reports two of the most investigated examples of substituted phenanthroline commonly used to achieve luminescent Cu(I) complexes: 2,9-dimethyl-1,10-phenanthroline (dmphen) and 2,9-diphenyl-1,10-phenanthroline (dpphen).[27]

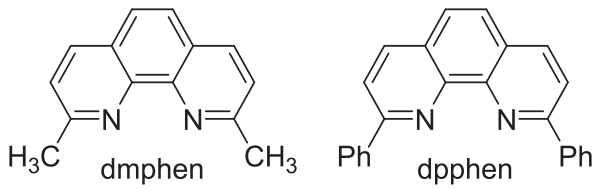

Figure 2.1 Two examples of substituted phenanthrolines employed to prepare luminescent Cu(I) complexes.

Luminescent Cu(I) complexes containing phosphorous ligands have been investigated as well, starting from homoleptic species bearing triphenylphosphine formulated as $[Cu(PPh_3)_3X]$ (X =Cl, Br, I).[28] Then, McMillin[29] reported in his works studies on heteroleptic Cu(I) complexes containing both N- and P-coordinating ligands achieving not only an improvement of the emission properties, but also longer lifetime in the solid state. Nevertheless, deeply investigation on the species $[Cu(dmphen)(PPh_3)_2]^+$ (dmphen = 2,9-dimethyl-1,10-phenanthroline) revealed strong quenching of luminescence due to

formation of exciplex with coordinating solvents, such as methanol. The introduction of a chelating phosphine led to the decrease of ligand dissociation when the molecule is in the excited state and consequently there is no significant solvent-induced formation of exciplex. Among these derivatives, the family of mononuclear $[Cu(phen)(POP)]^+$ complexes, where phen indicates a differently 2,9-substituted 1,10 phenanthroline and POP is bis[2-(diphenylphosphino)phenyl]ether, showed impressive emission efficiency compared to $[Cu(NN)_2]^+$ compounds. Complexes of this class are depicted in Figure 2.2:

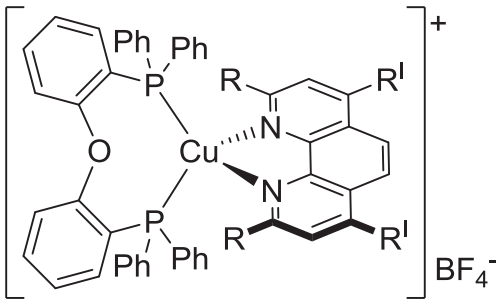

1 R = phenetyl; R^I = H

2 R = Bu; R^I = H

3 R = Me; R^I = H

Figure 2.2 Complexes of the class $[Cu(phen)(POP)]^+$.

One of the most successful Cu(I) based luminophore is $[Cu(dmphen)(POP)]^+$,[30] which outstanding photophysical performances make it attractive for the realisation of highly efficient OLEDs (Organic Light Emitting Diodes),[31] LECs (Light-Emitting Electrochemical Cells)[32] and other electroluminescent devices.[33]

Progressively, in a number of papers numerous studies on similar efficient systems formulated as $[Cu(NN)(PP)]^+$, bearing NN ligands different from phenanthroline and either POP as chelating phosphorous ligand,[34] or other P-coordinating ligands[35] have been reported. Finally also $[Cu(PP)_2]^+$ complexes containing chelating phosphorous ligands have shown interesting feature for application in optoelectronic devices.[36]

Interestingly, in all the systems described so far, the anion functions only as spectator, since the steric hindrance is always imposed by modifying phosphorous ligands or adjusting substituents on phenanthroline.

In the light of the above, in this work we report the investigation on luminescent copper(I) complexes where the steric rigidity imposed on the metal centre is somehow controlled by the counterion, thanks to the possibility to establish hydrogen bonds via OH groups. The influence of the extended catemeric structure on the luminescent properties of the corresponding complexes is highlighted in the Chapter.

2.1 [Cu(PPh$_3$)$_2$(lact)] AS PRECURSOR

2.1.1 SYNTHESIS AND CHARACTERISATION

In a previous thesis work carried out in this research group the complex [Cu(PPh$_3$)$_2$(lact)] (lact = L-(+)-lactate) has been synthesized and deeply investigated.[37]

In the first step of the synthetic strategy has been obtaining the precursor [Cu(lact)$_2$(H$_2$O)]·H$_2$O starting from copper sulphate pentahydrate and concentrated ammonia and following the procedure explained in Figure 2.3.

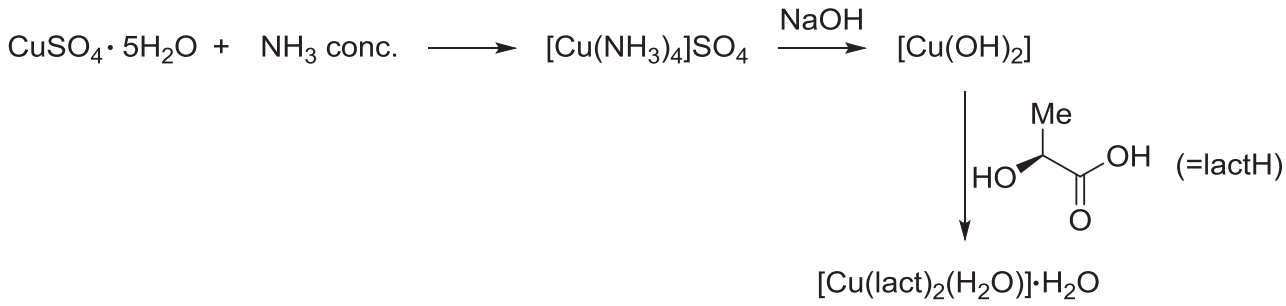

Figure 2.3 Synthetic strategy yielding [Cu(lact)$_2$(H$_2$O)]·H$_2$O.

Then, [Cu(PPh$_3$)$_2$(lact)] has been obtained, as reported in Figure 2.4, by reduction of [Cu(lact)$_2$(H$_2$O)]·H$_2$O with excess of triphenylphosphine in refluxing ethanol.

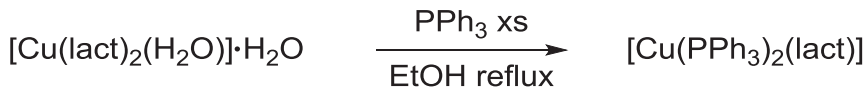

Figure 2.4 Procedure followed to obtain [Cu(PPh$_3$)$_2$(lact)].

The product has been characterised by elemental analysis, infrared and NMR spectroscopy; moreover, single crystals suitable for X-ray analysis were obtained by slow diffusion of hexane in a concentrated dichloromethane solution of [Cu(PPh$_3$)$_2$(lact)] (see text for a detailed comment).

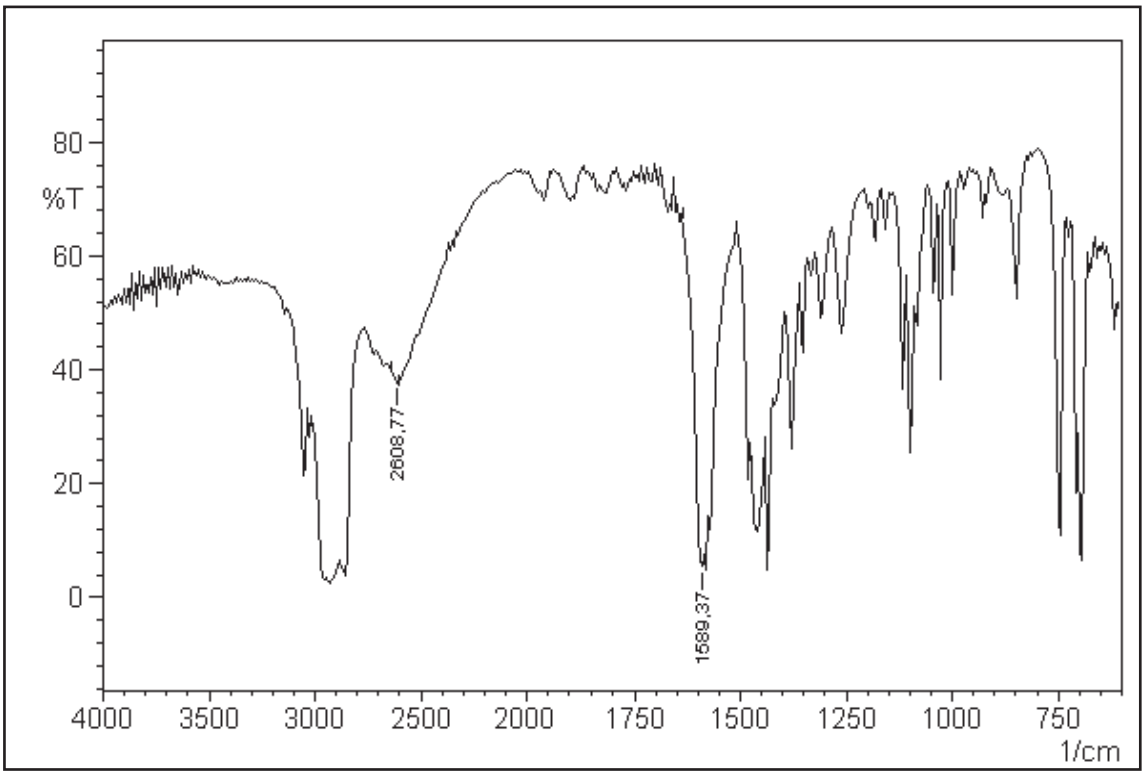

Figure 2.5 Infrared spectrum (nujol mull) of $[Cu(PPh_3)_2(lact)]$.

The infrared spectrum (nujol mull, Figure 2.5) shows an intense band at 1589 cm^{-1} attributed at the carboxylate group of the lactate anion; in addition it is noteworthy the occurrence of a broad band at 2609 cm^{-1} indicative of the presence of strong hydrogen bonds. To prove this, isotopic substitution has been carried out stirring a suspension of $[Cu(PPh_3)_2(lact)]$ in acetone-d_6 in the presence of D_2O, for 24 hours. After filtration, it has been possible to isolate a white solid, formulated as $[Cu(PPh_3)_2(lact\text{-}D)]$ (lact-D = deuterated lactate anion) according to elemental analysis and spectroscopic data (vide infra). As expected, the former broad band attributed to O-H is shifted to lower wavenumber, namely from 2678 ($\nu_{O\text{-}H}$) to 2144 cm^{-1} ($\nu_{O\text{-}D}$).

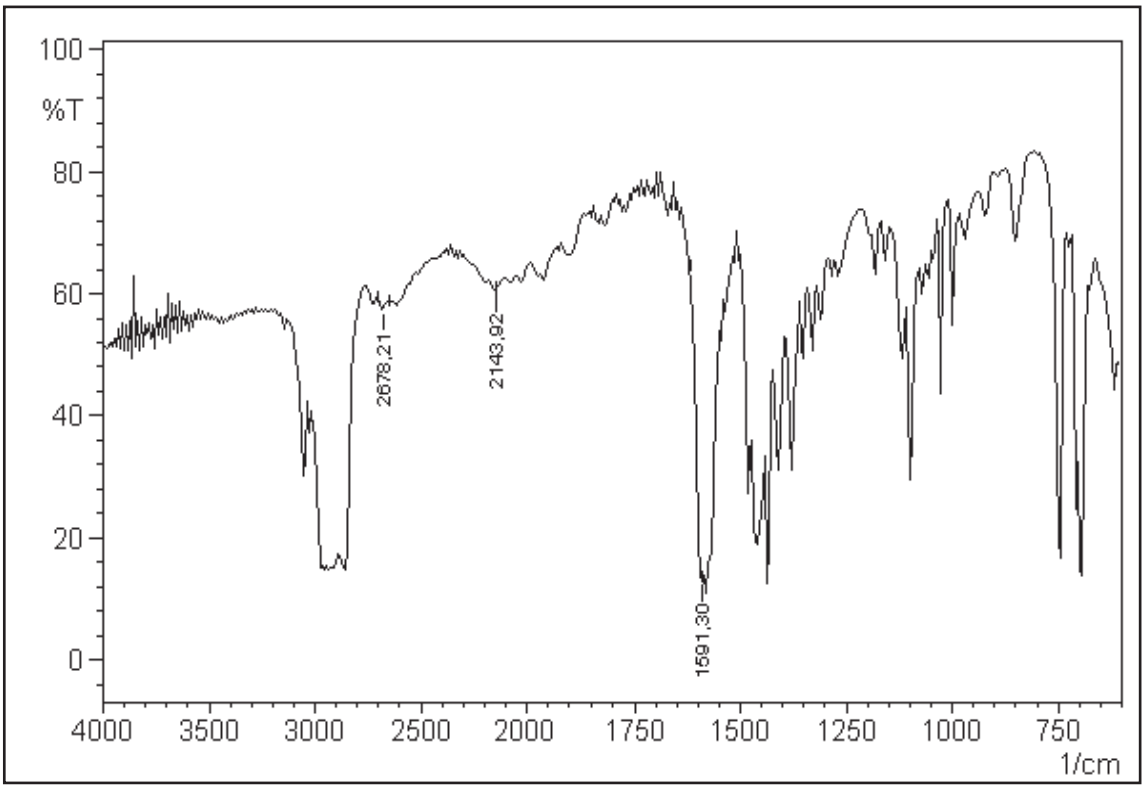

Figure 2.6 Infrared spectrum (nujol mull) of $[Cu(PPh_3)_3(lact\text{-}D)]$.

Additional information about species $[Cu(PPh_3)_2(lact)]$ have been obtained by NMR analysis: the ^1H NMR spectrum registered in dichloromethane-d_2 at room temperature (Figure 2.7) shows signals related to aromatic protons of triphenylphosphine (7.28-7.43 ppm) and the resonances in the aliphatic region due to the lactate anion (CH centred at 4.05 ppm and CH_3 at 1.32 ppm). The analysis of the integration of the signals revealed a 1:2 ratio between the lactate and PPh_3 around the copper(I) centre.

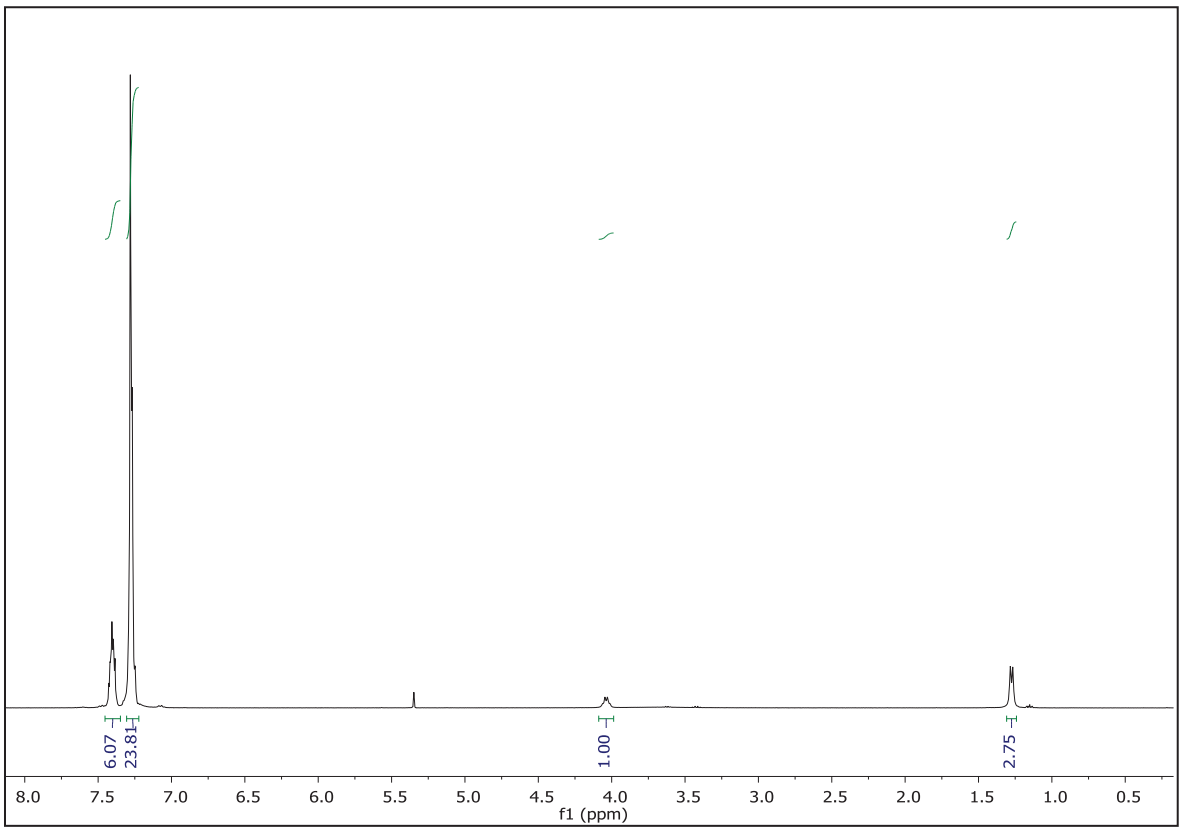

Figure 2.7 ^{1}H NMR spectrum (dichloromethane-d_2, 25°C) of [Cu(PPh_3)$_2$(lact)].

Signals attributed to lactate anion are quite broad and not resolved, most probably because of the presence of a fast dynamic exchange process at room temperature. On lowering the temperature, the signals become sharper and the expected multiplicities appear (doublet (C*H*$_3$, $^{3}J_{HH}$ = 6.8 Hz) and quartet (C*H*, $^{3}J_{HH}$ =6.8 Hz), respectively) (Figure 2.8). Worthy of note, the same resolved pattern can be achieved by adding few drops of D_2O to the initial dichloromethane- d_2 solution, at room temperature (Figure 2.9). Thus, it can be concluded that the fast dynamic exchange process observed for [Cu(PPh_3)$_2$(lact)] is prevented at low temperatures, and mainly associated to the presence of H-bonds (maintained in solution) in the molecular structure of the complex.

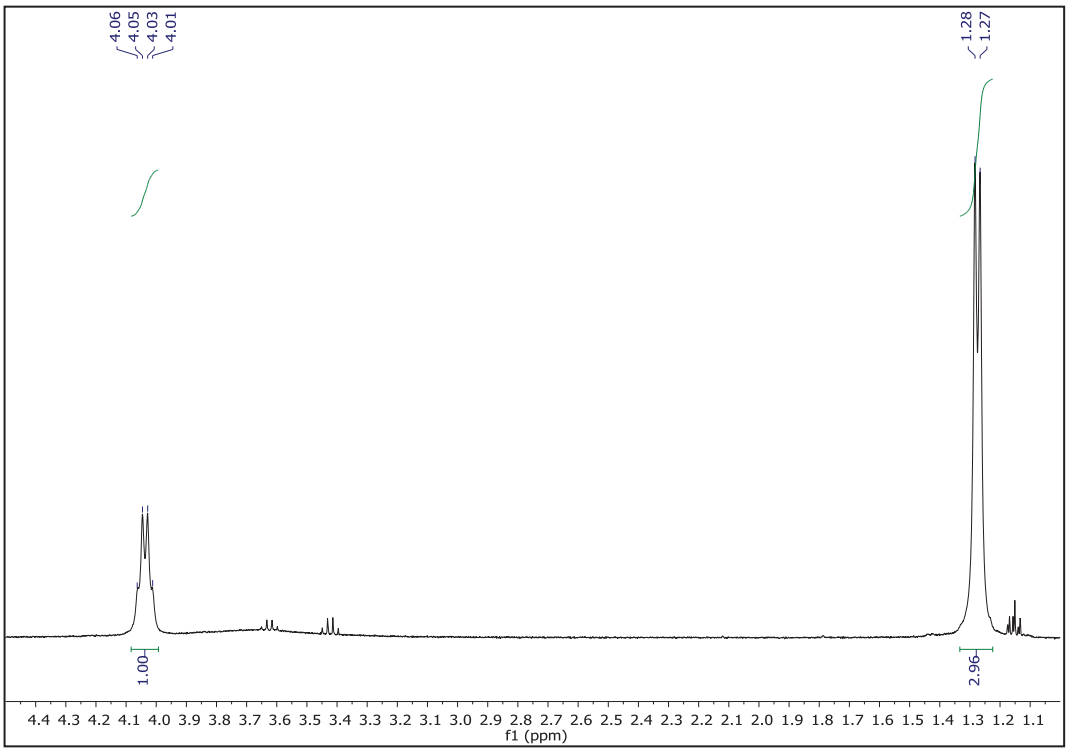

Figure 2.8 ^{1}H NMR spectrum (dichloromethane-d_2, -30°C) of [Cu(PPh_3)$_2$(lact)]; enlargement of the aliphatic region.

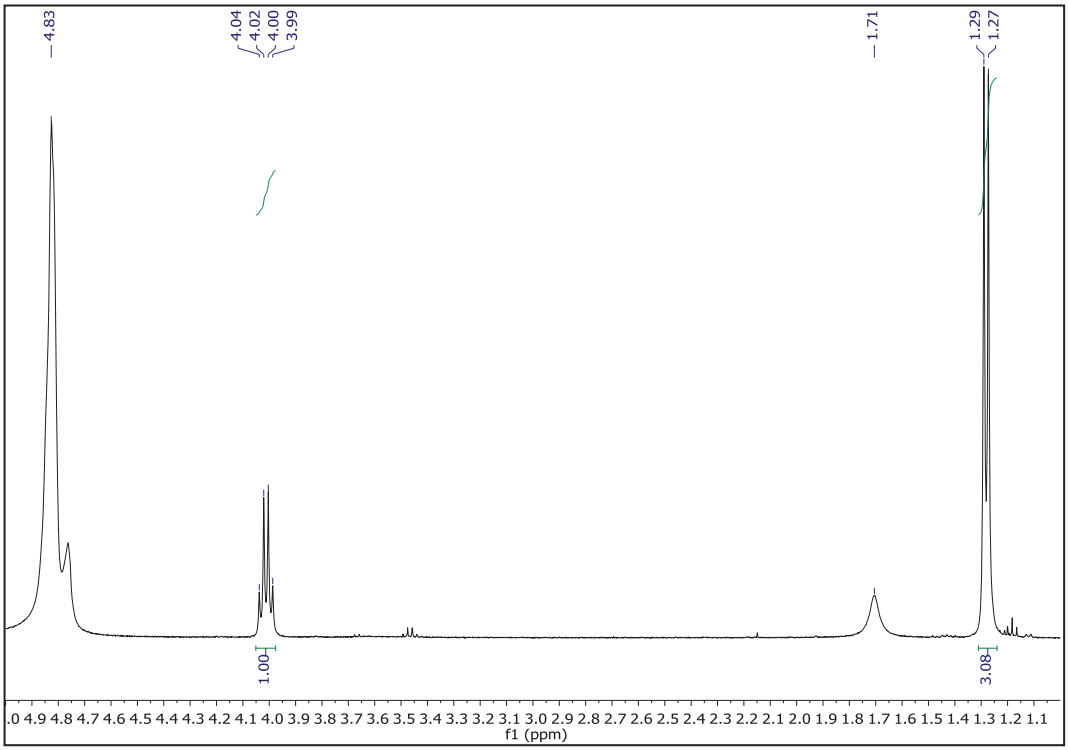

Figure 2.9 ^{1}H NMR spectrum (dichloromethane-d_2/D_2O, 25°C) of [Cu(PPh_3)$_2$(lact)]; enlargement of the aliphatic region.

The $^{31}P\{^{1}H\}$ NMR spectrum recorded at room temperature in dichloromethane-d_2 (Figure 2.10) exhibits a sharp singlet at -2.67 ppm attributable to the presence of two equivalent molecules of triphenylphosphine. Notably, no changes in the spectrum are observed either by lowering the temperature, or by addition of D_2O at room temperature.

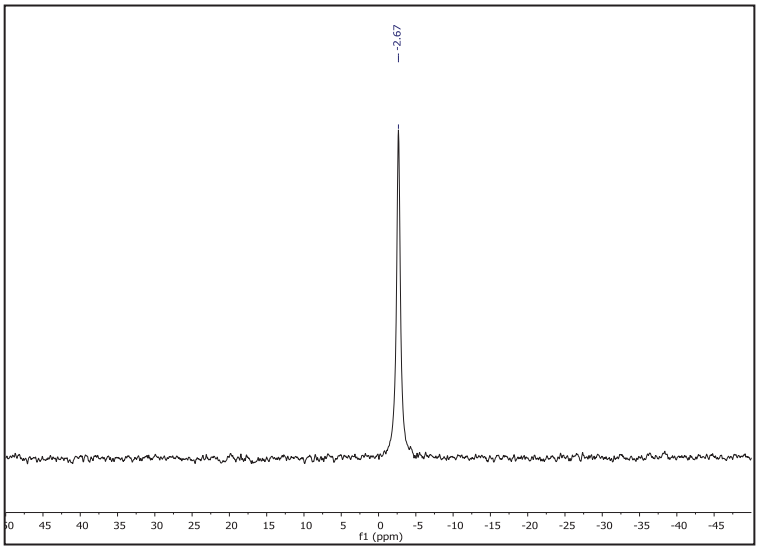

Figure 2.10 $^{31}P\{^{1}H\}$ NMR spectrum (dichloromethane-d_2, 25°C) of $[Cu(PPh_3)_2(lact)]$.

As said, single crystal X-ray diffraction analysis allowed to unequivocally determine the molecular structure of $[Cu(PPh_3)_2(lact)]$.

Interestingly, by applying different techniques and conditions, the compound crystallized in two different habits: according to solvent molecules found in the lattice, these can be respectively formulated as $[Cu(PPh_3)_2(lact)]\cdot$hexane, obtained by layering hexane onto a CH_2Cl_2 solution of the $[Cu(PPh_3)_2(lact)]$, and $[Cu(PPh_3)_2(lact)]\cdot MeOH\cdot H_2O$ crystallised by slow cooling of a hot saturated methanol solution of the compound.

As expected, in both X-ray structures the copper ion shows a tetrahedral geometry, surrounded by two phosphorous of two PPh_3 ligands and one lactate molecule coordinating in a O,O-bidentate mode via the carboxylate and the hydroxyl group. Such a coordination is quite common for this anion when bound to transition metals.[38] Selected bond lengths (Cu-P and Cu-O) and angles are collected in Table 2.1; values for the two structures are in accordance with literature data for similar systems.

As mentioned above, depending on the crystallization process, $[Cu(PPh_3)_2(lact)]$ gave rise to two species, namely $[Cu(PPh_3)_2(lact)]\cdot$hexane and $[Cu(PPh_3)_2(lact)]\cdot MeOH\cdot H_2O$, which

differentiate for the solvent molecules present in the lattice. This has a great impact on the nature of H-bonding interactions found among adjacent molecules in the structure itself.

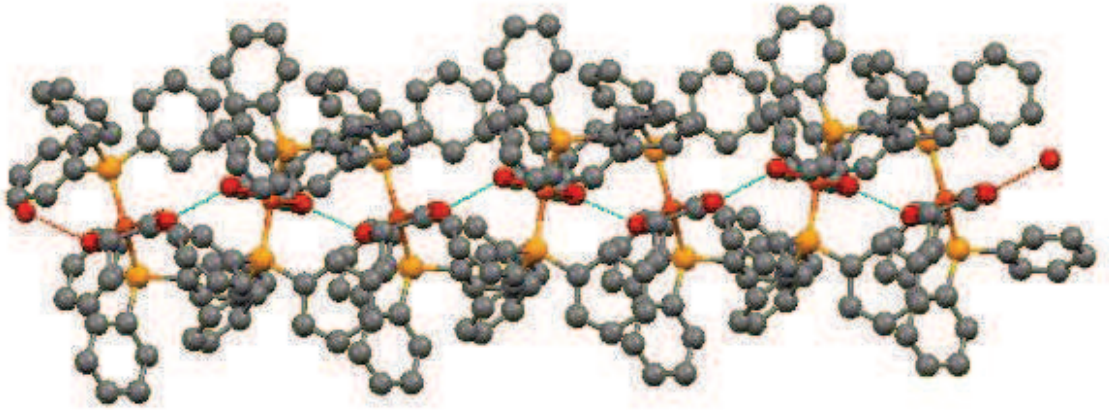

Figure 2.11 Supramolecular structure of $[Cu(PPh_3)_2(lact)]\cdot$hexane; hydrogen bonds are highlighted in light blue.

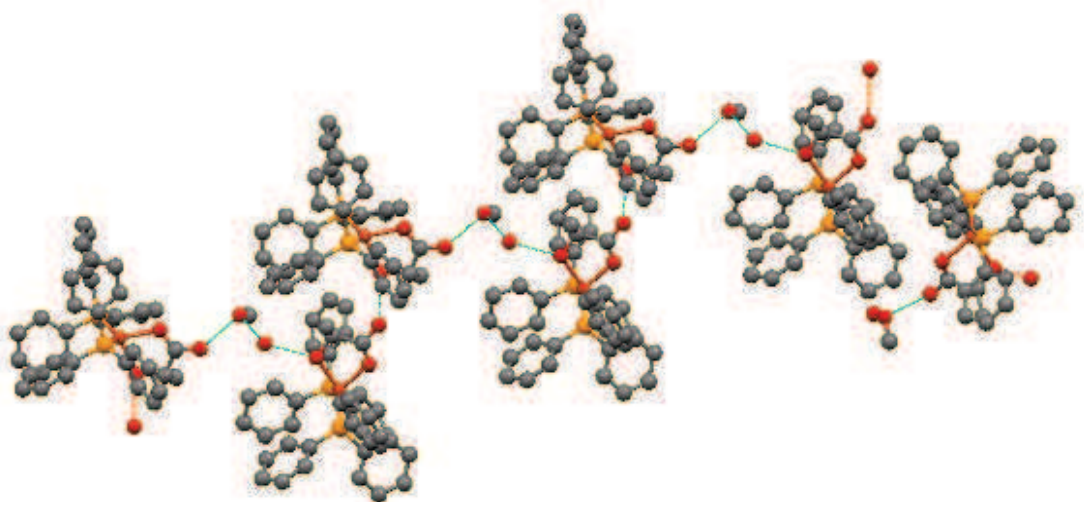

Figure 2.12 Supramolecular structure of $[Cu(PPh_3)_2(lact)]\cdot H_2O\cdot MeOH$; hydrogen bonds are highlighted in light blue.

Actually, as reported in Figure 2.11, $[Cu(PPh_3)_2(lact)]\cdot$hexane shows hydrogen bonds between the OH of one lactate anion and the non-coordinated oxygen of a carboxylate group belonging to an adjacent lactate molecule. This leads to a mono-dimensional network (a catemeric structure) and reflects the infrared evidences (see the $\nu_{O\text{-}H}$ broad band at 2609 cm^{-1} discussed earlier). On the other hand, in $[Cu(PPh_3)_2(lact)]\cdot MeOH\cdot H_2O$ the hydrogen-bonds network is a little more complex, involving the lactate anion, water and methanol (Figure 2.12). In this case, the structure is better described as composed by

dimers of [Cu(PPh_3)$_2$(lact)], where the two units are held together by O-H···O (d = 2.587 Å) bonds between the hydroxyl group of one lactate molecule and the carboxylate mojety of another molecule. Then, these dimers are connected by a more complicated H-bonding network (O_{lact}-H···O_w-H···O_{Me}-H···$O_{carboxylate}$) where two lactate molecules of two different dimers are linked by H_2O/MeOH bridges.

As it will be highlighted in the next section, these structural features tremendously influence the emission properties of these compounds.

[Cu(PPh_3)$_2$(lact)]·hexane			
Bond	Lenght (Å)	Angle	Degrees (°)
Cu-P1	2.224	O1-Cu-O2	79.25
Cu-P2	2.243	O1-Cu-P1	113.37
Cu-O1	2.061	O2-Cu-P2	110.88
Cu-O2	2.106	P1-Cu-P2	124.03
[Cu(PPh_3)$_2$(lact)]·H_2O·MeOH			
Bond	Lenght (Å)	Angle	Degrees (°)
Cu-P1	2.250	O1-Cu-O2	75.93
Cu-P2	2.250	O1-Cu-P1	108.70
Cu-O1	2.087	O2-Cu-P2	106.39
Cu-O2	2.227	P1-Cu-P2	126.97

Table 2.1 Bond lengths and angles of complex [Cu(PPh_3)$_2$(lact)] obtained by X-ray diffraction.

2.1.2 LUMINESCENT PROPERTIES

The luminescent properties of $[Cu(PPh_3)_2(lact)]$ have been investigated in the solid state and normalised excitation and emission spectra are reported in Figure 2.13.

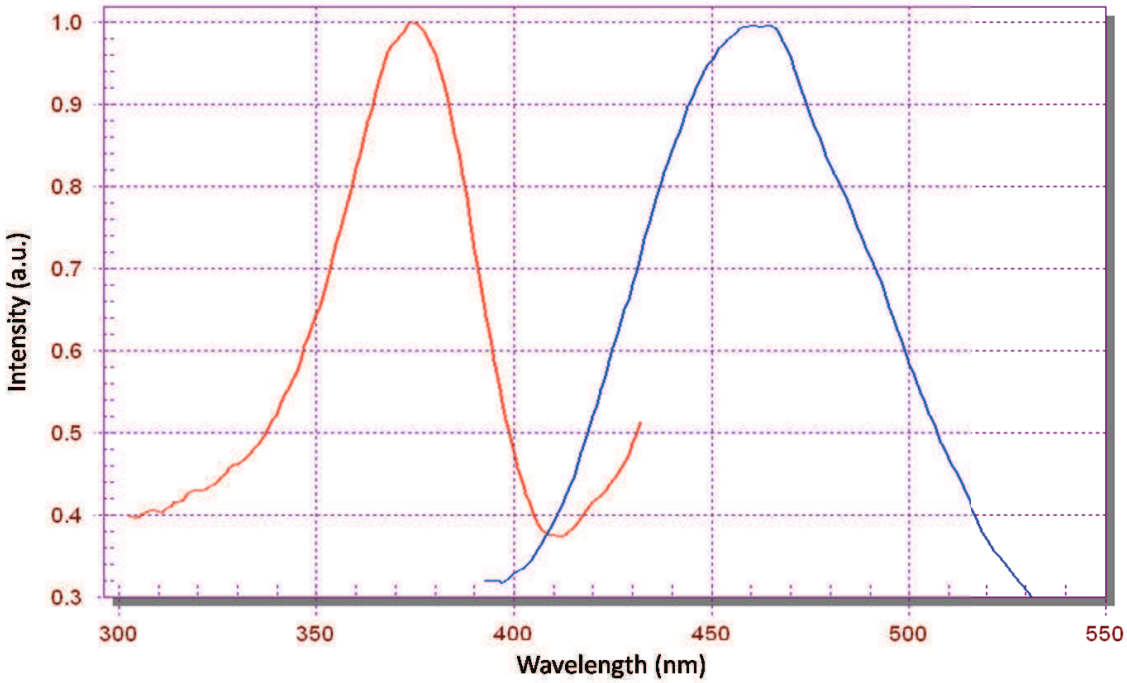

Figure 2.13 Normalised excitation and emission spectra of $[Cu(PPh_3)_2(lact)]$ in the solid state.

The complex exhibits an intense luminescence in the blue region of the visible light, in the solid state (powder as obtained after synthesis): exciting at 374 nm, emission λ_{max} is recorded at 461 nm. Under constant irradiation, the complex undergoes photobleaching,[39] that is the reduction of emission intensity of a fluorophore by exposure to incident light. Regarding $[Cu(PPh_3)_2(lact)]$, its emission intensity decreases over time with an half-life time of about 40 minutes. This is illustrated in Figure 2.14, which reports emission spectra registered at fixed time intervals, and in Figure 2.15, where is reported the decay of emission *vs.* time. One of the main reason leading to photobleaching is the possible reaction of the excited state with molecular oxygen. As regards $[Cu(PPh_3)_2(lact)]$, this can be excluded: indeed, the photobleaching process was observed also when the sample was excited under an argon atmosphere (in a previously deossigenated (Ar) chamber). Further studies are in due course to better clarify this point.

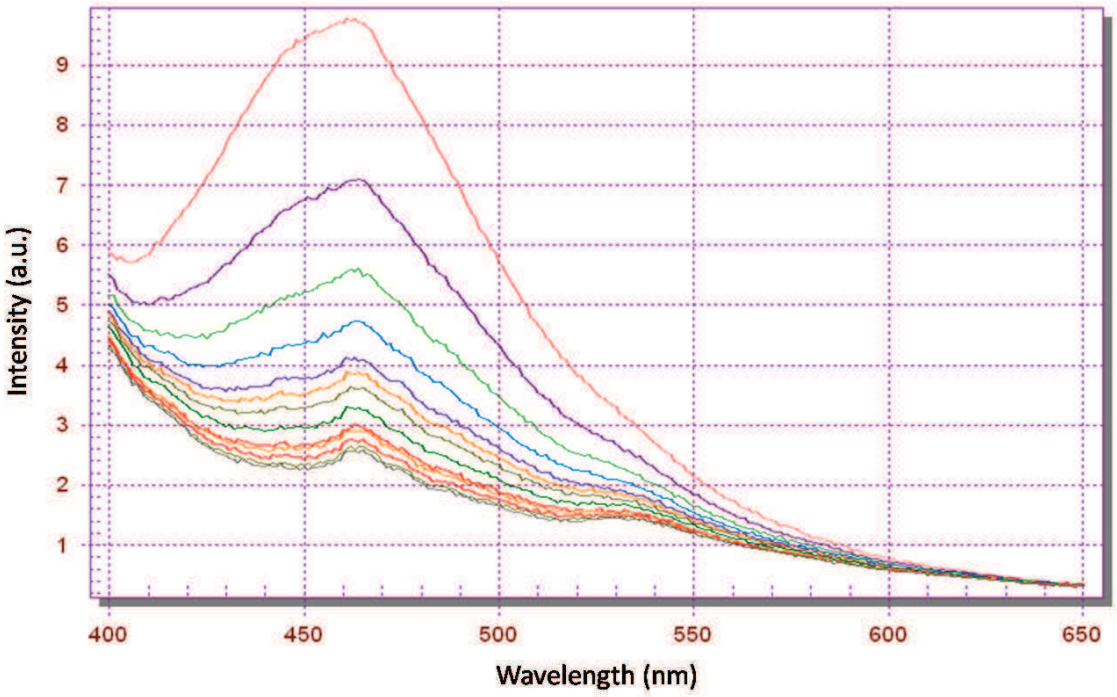

Figure 2.14 Series of emission spectra of $[Cu(PPh_3)_2(lact)]$ registered at fixed intervals.

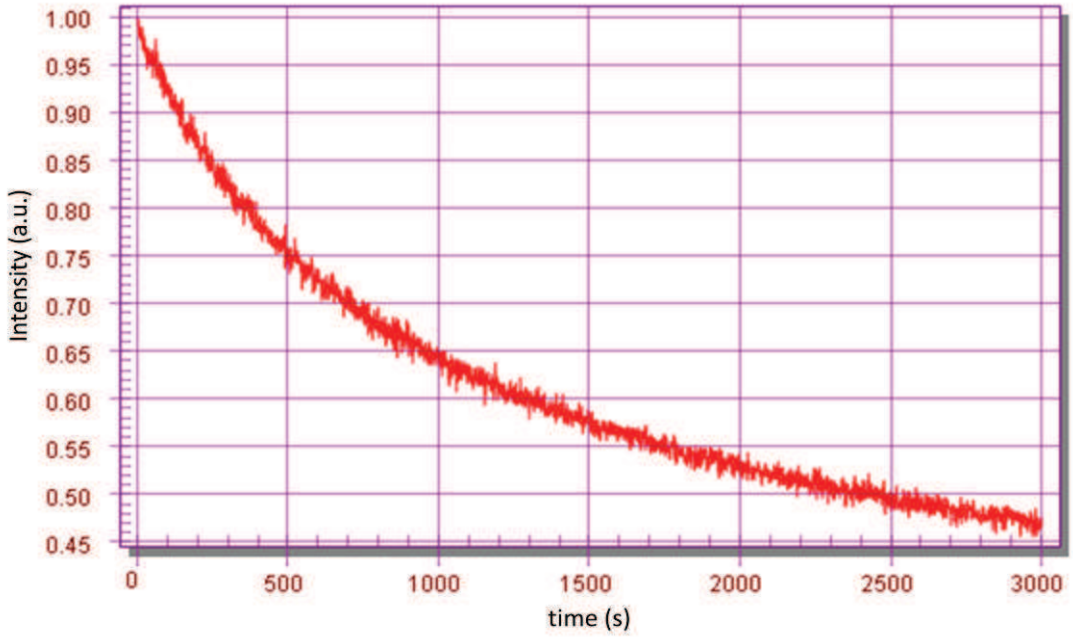

Figure 2.15 Emission intensity of $[Cu(PPh_3)_2(lact)]$ *vs.* time.

Nonetheless, $[Cu(PPh_3)_2(lact)]$ shows a very interesting structure-properties relation: its original blue emission is strictly dependent from structural parameters, especially from the presence of a specific H-bonding network. Actually, this complex does not show luminescence emission in solution, where the already discussed dynamic process takes place and the catemeric structure is probably interrupted. A close association between

these H-bonds and the blue emission of $[Cu(PPh_3)_2(lact)]$ has been confirmed by photoluminescence measurements performed on grinded single crystals of $[Cu(PPh_3)_2(lact)]\cdot$hexane and $[Cu(PPh_3)_2(lact)]\cdot MeOH\cdot H_2O$. As said, as regards geometry and bond lengths and angles around the copper centre (Table 2.1), these two species show similar characteristics, the main difference between them being the H-bonds network generated by lactate and the solvent molecules in the lattice. Worthy of note, only grinded crystals of species $[Cu(PPh_3)_2(lact)]\cdot$hexane show photophysical properties identical to $[Cu(PPh_3)_2(lact)]$ (when measured as powder obtained by synthesis). On the contrary, $[Cu(PPh_3)_2(lact)]\cdot MeOH\cdot H_2O$ does not show any emission in the solid state. Reasonably, the diverse H-bonding network imposed by methanol and water favours non radiative decay, thus dramatically reducing the emission intensity. As a further prove, also the fully deuterated compound $[Cu(PPh_3)_2(lact\text{-}D)]$ (isolated as described in Section 2.1.1), did not show luminescence emission when irradiated with UV light. It is known that isotopic substitution with deuterium usually reduces the rate of non-radiative decay (see Chapter 3 for better explanation), hence increasing the emission intensity. However, in this specific case, changing the H-bonds catemeric structure into a D-bonds network, led to the opposite result, with the D-bonds structure somehow enhancing non radiative decay.

Unlikely, during this work it has not been possible to measure lifetime decays, which would have surely give more accurate information on the photophysical behaviour of these species.

2.2 SUBSTITUTION REACTIONS ON [Cu(PPh$_3$)$_2$(lact)]

2.2.1 SYNTHESIS AND CHARACTERISATION

Starting from the results achieved with [Cu(PPh$_3$)$_2$(lact)], substitution reactions on this complex have been carried out introducing a chelating phosphorous ligand or an aza-bidentate ligand, with the aim of tuning the emission features.

Firstly, attempts to replace the two molecules of triphenylphosphine with 1,1-bis(diphenylphosphino)methane (dppm) were performed. The reaction taking place has been initially considered as reported in Figure 2.16.

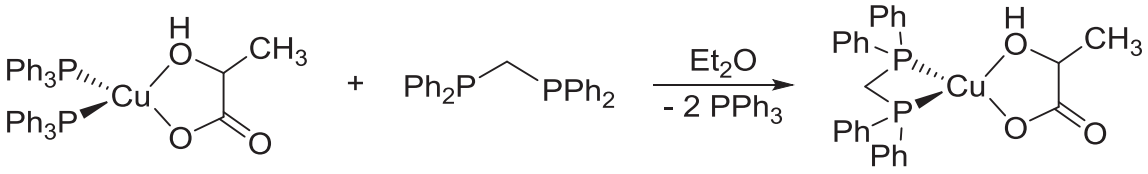

Figure 2.16 Substitution reaction performed with 1,1-bis(diphenylphosphino)methane.

The product has been obtained by adding [Cu(PPh$_3$)$_2$(lact)] to a solution of dppm in diethylether, in a 1:1 molar ratio.

Elemental analysis of the sample reports a Cu:lactate:dppm ratio of 1:1:1, therefore, in the beginning, the species has been formulated as [Cu(dppm)(lact)]$_n$. Nevertheless, further analysis conducted on the solid obtained do not confirm the above mentioned hypothesis.

Indeed, infrared spectroscopy (Figure 2.17) revealed the presence of two different bands in the carbonylic region, respectively at 1610 and 1583 cm^{-1}; the latter is very close to one observed for [Cu(PPh$_3$)$_2$(lact)] (1589 cm^{-1}), and can be easily associated to the C=O stretching of lactate anion coordinated in a bidentate mode; conversely, the vibration at 1610 cm^{-1} can be attributed to C=O stretching of a lactate group coordinated in a monodentate mode. It follows that the complex [Cu(dppm)(lact)]$_n$ exhibits two differently coordinated lactate molecules, so, presumably, the product can be formulated as a

dinuclear species $[Cu(dppm)(lact)]_2$, with the two lactate anions showing a different behaviour toward the metal.

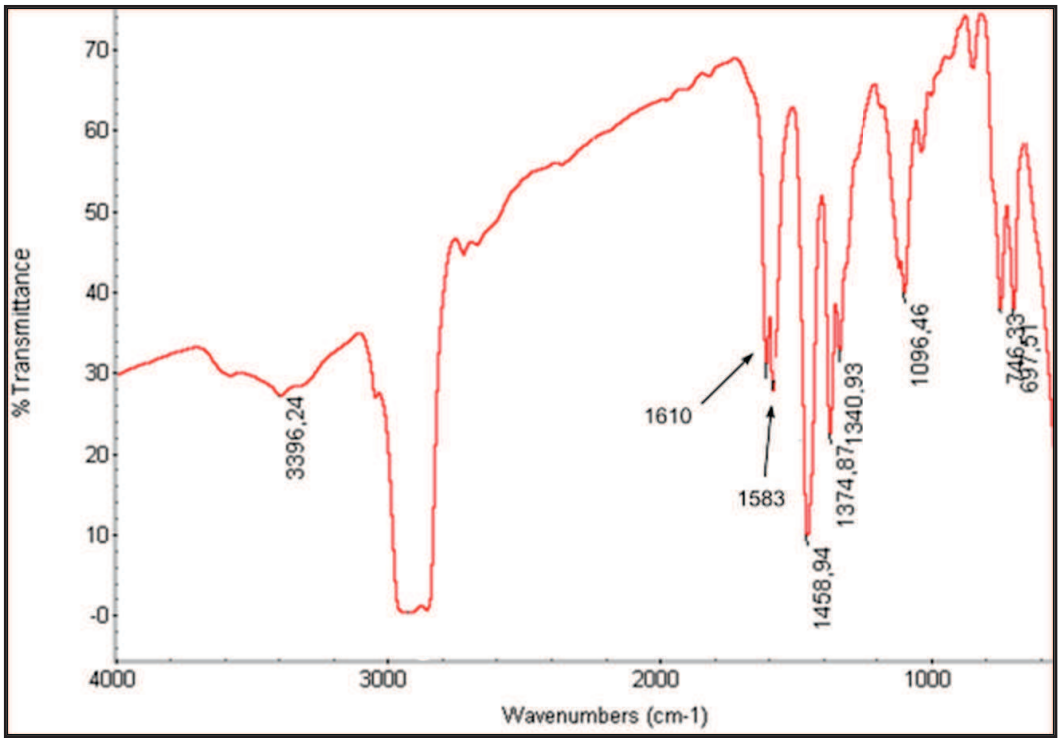

Figure 2.17 Infrared spectrum (nujol mull) of $[Cu(dppm)(lact)]_2$.

This was eventually confirmed by X-ray analysis (Figure 2.18) performed on single crystal obtained by slow diffusion of hexane into a concentrated solution of $[Cu(dppm)(lact)]_2$ in dichloromethane

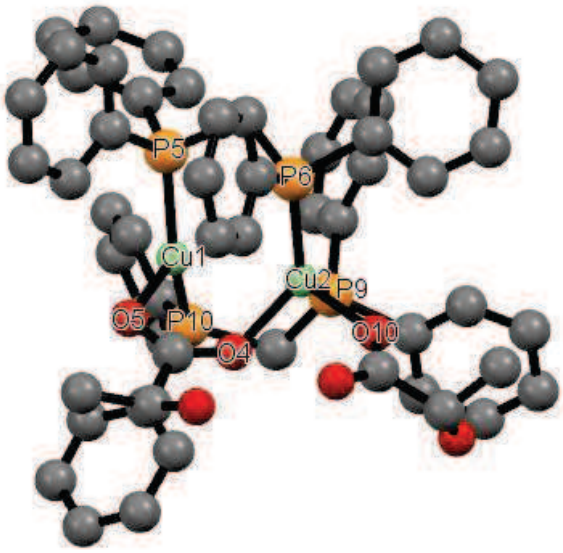

Figure 2.18 X-ray crystal structure of $[Cu_2(\mu\text{-}dppm)_2(\mu\text{-}\eta^2\text{-}lact)(\eta^1\text{-}lact)]$. Hydrogen atoms are omitted for clarity.

The crystal structure confirms the dimeric nature of the complex: Cu1 and Cu2 being bridged by two molecules of 1,1-bis(diphenylphosphino)methane, as well as one lactate anion coordinated via oxygens of its carboxylate moieties (O4 and O5). The second anion is coordinated toward Cu2 via one oxygen atom of the carboxylate in a mono-dentate mode. As a consequence, the geometry around the two copper atoms is different, being respectively trigonal for Cu1 (with P5-Cu1-O5 = 113.27°(2)) and tetrahedral for Cu2. The complex is then better formulated as $[Cu_2(\mu\text{-dppm})_2(\mu\text{-}\eta^2\text{-lact})(\eta^1\text{-lact})]$ (**1**). Selected bond lengths and angles are reported in Table 2.2. It is notheworthy that Cu···Cu is 2.854(2) Å, value close to the radii sum (2.8 Å) and comparable with that reported in literature for dinuclear copper(I) complexes which show strong cuprophilic interactions.[40] As it will be discussed later on, these cuprophilic interactions, which are often invoked as leading to enhanced luminescence properties, could be the reason for better luminescent performances of $[Cu_2(\mu\text{-dppm})_2(\mu\text{-}\eta^2\text{-lact})(\eta^1\text{-lact})]$ when compared to $[Cu(PPh_3)_2(lact)]$.

The solution behaviour of $[Cu_2(\mu\text{-dppm})_2(\mu\text{-}\eta^2\text{-lact})(\eta^1\text{-lact})]$ (**1**) was also investigated. In the ^1H NMR spectrum recorded in acetone-d_6 at room temperature (Figure 2.19) it was not possible to distinguish between the two differently coordinated lactate anions, which are described by only two signals in the spectrum, respectively at 3.99 ppm (CH) and 1.30 ppm (CH_3). The signal at 2.84 ppm is clearly related to the OH on lactate anion (attributed according to isotopic shift with deuterium), whereas in the aliphatic region the resonances of CH_2 on dppm are identifiable at 3.55 ppm; these appear quite broad probably due to a fluxional exchange process which involves phosphorous ligands in solution at room temperature. This could also be the reason why it is not possible to distinguish between the two lactate anions. Finally, signals related to PPh_3 appear in the aromatic region (7.03-7.59 ppm). The integration of the signals allow to confirm the stoichiometry of the complex showing a 1:1 molar ratio between dppm and lactate.

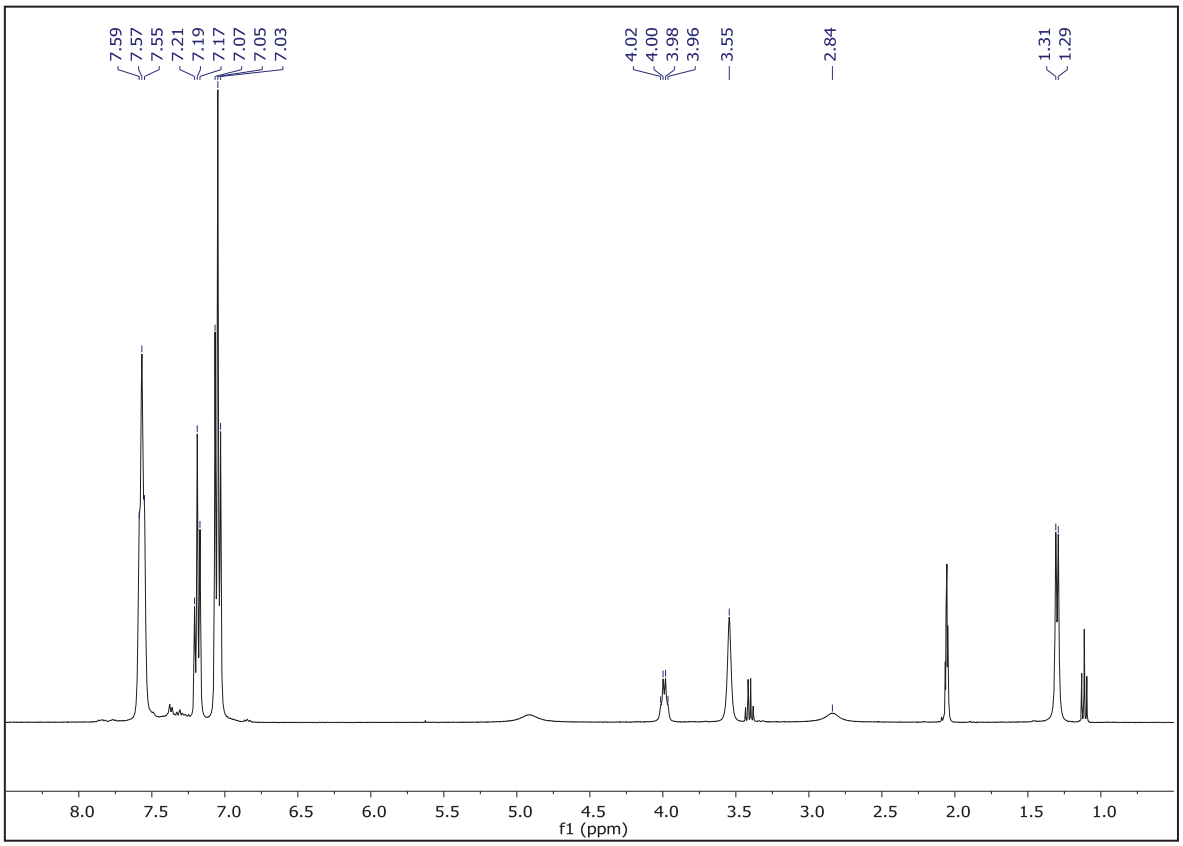

Figure 2.19 ^{1}H NMR spectrum (acetone-d_6, 25°C) of [Cu_2(μ-dppm)$_2$(μ-η^2-lact)(η^1-lact)] (**1**).

In Figure 2.20 is reported the ^{31}P{^{1}H} NMR spectrum of this derivative, characterized by a sharp singlet centred at -13.6 ppm.

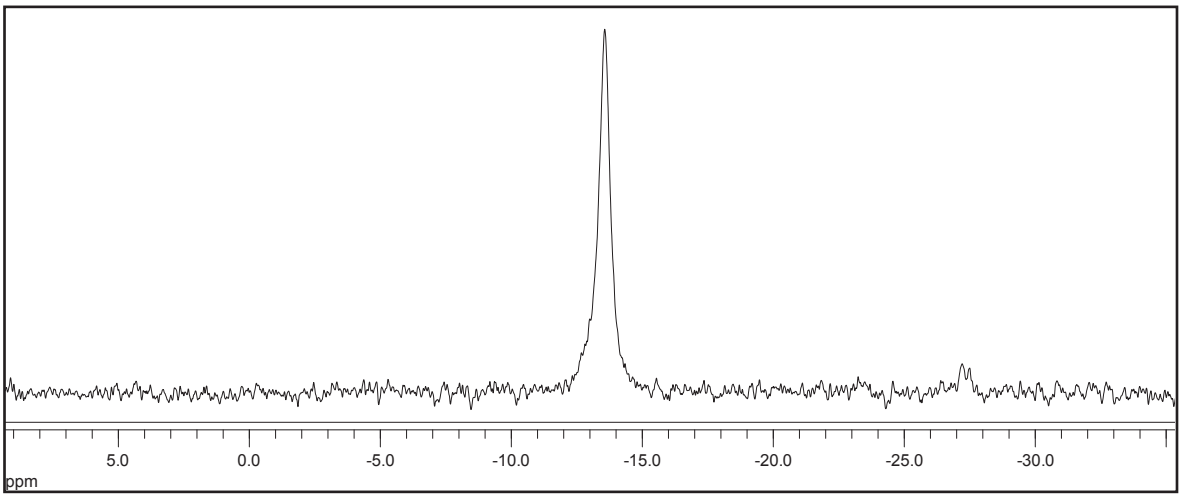

Figure 2.20 ^{31}P{^{1}H} NMR spectrum (acetone-d_6, 25°C) of [Cu_2(μ-dppm)$_2$(μ-η^2-lact)(η^1-lact)] (**1**).

Therefore, it can be concluded that the molecular structure of $[Cu_2(\mu\text{-dppm})_2(\mu\text{-}\eta^2\text{-lact})(\eta^1\text{-lact})]$ (**1**) in the solid state is different from that observed in solution, where dissociation equilibria play a significant role.

Subsequently, the substitution of the two molecules of triphenylphosphine in $[Cu(PPh_3)_2(lact)]$ with aza-bidentate ligands has been tried. Treating $[Cu(PPh_3)_2(lact)]$ with one equivalent of 1,10-phenanthroline, following a similar procedure described for dppm, allowed to isolate an ochre crystalline air-stable solid. The coordination scenario deduced by ^{1}H NMR investigation (Figure 2.21) performed on the derivative in dichloromethane-d_2 at room temperature, reveals the presence of lactate and 1,10-phenanthroline together with the signals of aromatic protons of triphenylphosphine.

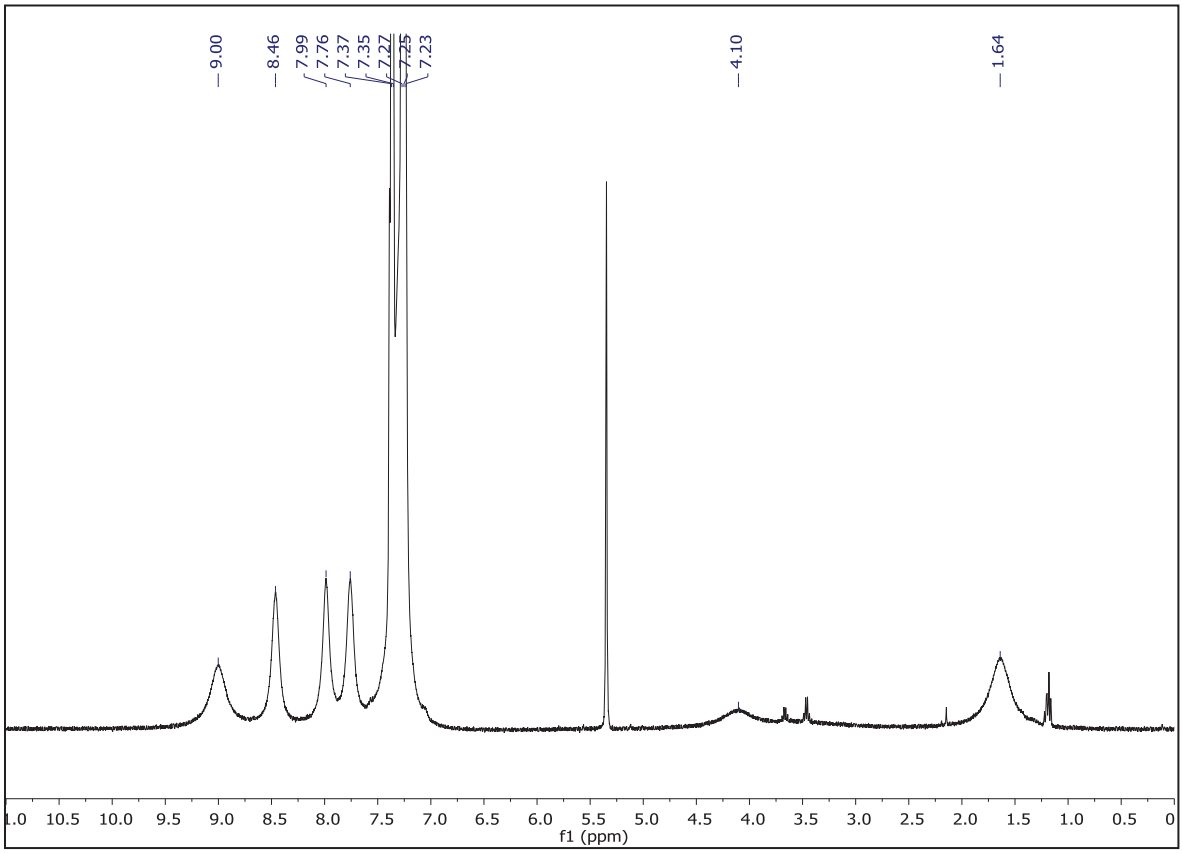

Figure 2.21 ^{1}H NMR spectrum (dichloromethane-d_2, 25°C) of $[Cu(phen)(PPh_3)_2(lact)]$ (**2**).

It stands to reason that the complete substitution of the two PPh_3 molecules by means of 1,10-phenanthroline has not occurred; moreover, integrals reveal a nearly 1:2:1 ratio among phenathroline:triphenylphosphine:lactate, later corroborated by elemental analysis. The complex obtained can thus be formulated as $[Cu(phen)(PPh_3)_2(lact)]$ (**2**).

In the ^{31}P {H} NMR spectrum (Figure 2.22) the phosphorous atom of triphenylphosphine is described by a singlet at 2.2 ppm, quite broad due to the coordination to the copper centre.

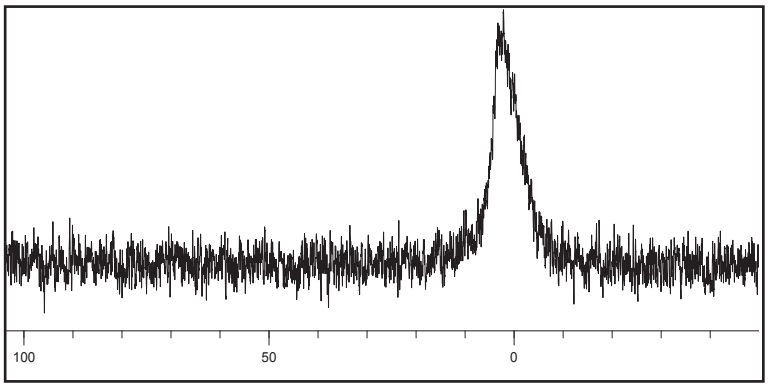

Figure 2.22 ^{31}P {H} NMR spectrum (dichloromethane-d_2, 25°C) of $[Cu(phen)(PPh_3)_2(lact)]$ (**2**).

The coordination mode of the lactate anion in the complex has been clarified by infrared spectroscopy (Figure 2.23), where the vibration due to C=O groups is found at 1614 cm^{-1}, very close to the one observed for the monodentate lactate in $[Cu_2(\mu\text{-dppm})_2(\mu\text{-}\eta^2\text{-lact})(\eta^1\text{-lact})]$ (1610 cm^{-1}). Then, in compound $[Cu(phen)(PPh_3)_2(lact)]$ the anion is singly bound to copper, as well.

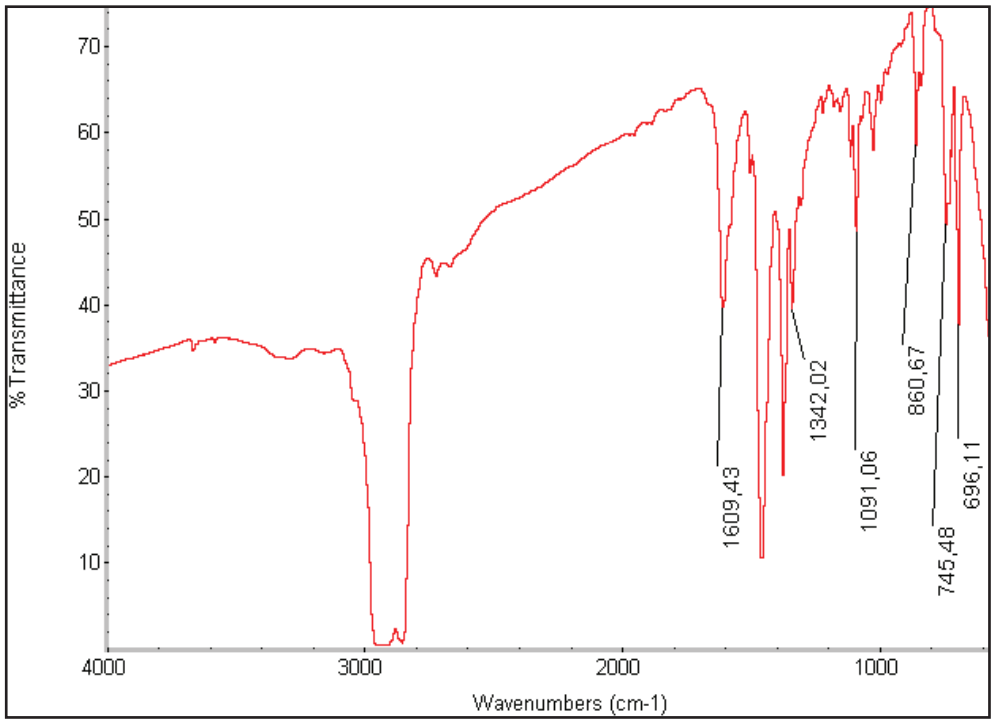

Figure 2.23 Infrared spectrum (nujol mull) of $[Cu(phen)(PPh_3)_2(lact)]$ (**2**).

In addition to spectroscopic characterisation, an X-ray structural analysis has been performed in order to confirm the coordination environment around the metal centre (Figure 2.24 and 2.25). X-ray quality crystals have been obtained by slow diffusion of diethylether in a concentrated solution of the complex in dichloromethane.

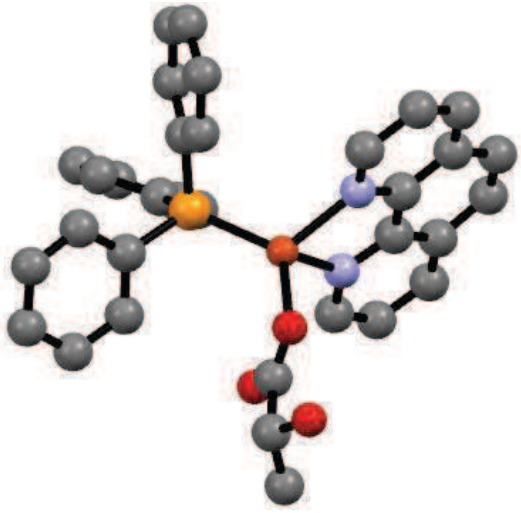

Figure 2.24 Crystal structure of [Cu(phen)(PPh_3)(lact)] (**2**). Hydrogen atoms are omitted for clarity.

Surprisingly, the structure obtained revealed unexpected results: the copper centre results in a distorted tetrahedral N_2PO-environment (bond lengths and angles are reported in Table 2.2), where, together with the chelating 1,10-phenathroline and the monodentate lactate anion, only one molecule of triphenylphosphine participate to the coordination. Probably this discrepancy with respect to spectroscopic data obtained for the species isolated after synthesis can be attributed to dissociation equilibria established during the slow process of crystallisation, where PPh_3 could dissociate from the metal centre. Unfortunately, all other attempts to grow single crystals representative of the powder failed.

Nevertheless, the X-ray analysis confirmed the monodentate coordination of the lactate anion, as proved by Cu-O distances (Table 2.2): the coordination to copper lengthen C59-O3 bond (1.259(2) Å), while C59-O4 exhibits a length closer to the typical C=O double bond (1.220(1) Å).

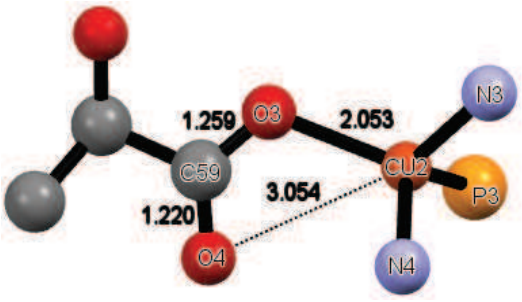

Figure 2.25 Core of crystal structure of [Cu(phen)(PPh_3)(lact)] (**2**).

Finally, a further complex belonging to this class has been obtained introducing the aza-bidentate ligand 2-(1-(pyridin-2-yl)imidazo[1,5-a]pyridin-3-yl)phenol (L^{OH}), which structure is reported in Figure 2.26. This ligand and its corresponding Zn(II) and Ag(I) complexes will be deeply illustrated in Chapters 3 and 4.

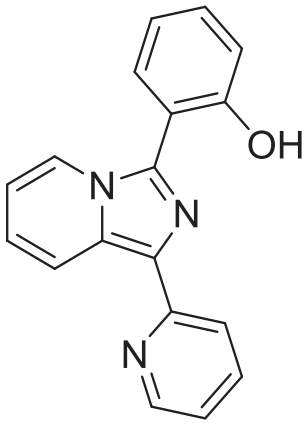

Figure 2.26 Structure of 2-(1-(pyridin-2-yl)imidazo[1,5-a]pyridin-3-yl)phenol (L^{OH}).

A modified procedure, in respect with the one followed for the other substitution reactions described in this chapter, has allowed the preparation of the final complex. Initially a mixture of [Cu(PPh_3)$_2$(lact)] treated with one equivalent of L^{OH} in diethylether was allowed to stir at room temperature for 24 hours, then the solvent volume was reduced to half and methanol was added. The obtained yellow solution was allowed to stir for one hour at 50°C, subsequently the solvent was removed under reduced pressure yielding a yellow solid. The crude product was suspended in diethylether and a yellow crystalline solid was isolated after filtration.

Again, data obtained by spectroscopic characterisation of the derivative reveal a coordination scenario including, together with lactate anion, triphenylphosphine and L^{OH}, thus the complete substitution of PPh_3 by means of the *N*,*N*-bidentate ligand has not occurred. Infrared spectroscopy (Figure 2.27) shows a weak vibrational band for lactate which is not similar, neither for the shape nor for the wavenumber (1600 cm^{-1}) to the stretchings observed for lactate anion in the other complexes described in this chapter.

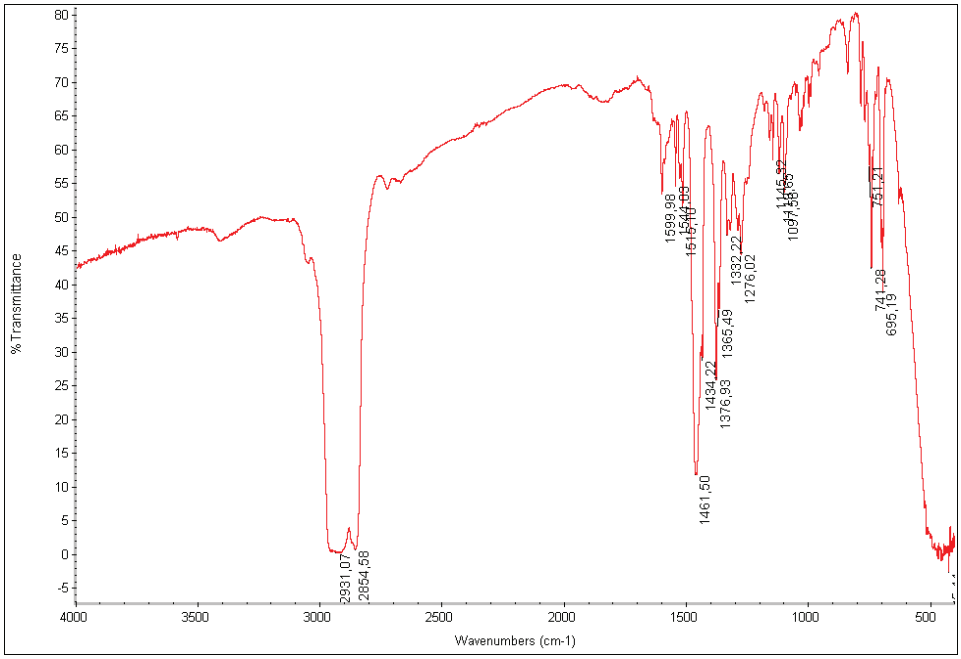

Figure 2.27 Infrared spectrum (nujol mull) of $[Cu(PPh_3)_2(L^{OH})](lact)$ (**3**).

Though the ^1H NMR spectrum (Figure 2.28) does not show a high resolution, probably because of dissociation equilibria which are established in solution, at room temperature it is sufficient to distinguish between triphenylphosphine signals (7.36–7.03 ppm) and broad signals attributed to L^{OH} (8.01–6.86 ppm) in the aromatic region and to suppose a 1:2:1 ratio between L^{OH}:PPh_3:lact. This stoichiometry is consistent with elemental analysis. In the $^{31}P\{^1H\}$ NMR spectrum, the presence of a sharp singlet let us presume that the two triphenylphosphine molecules are chemically equivalent.

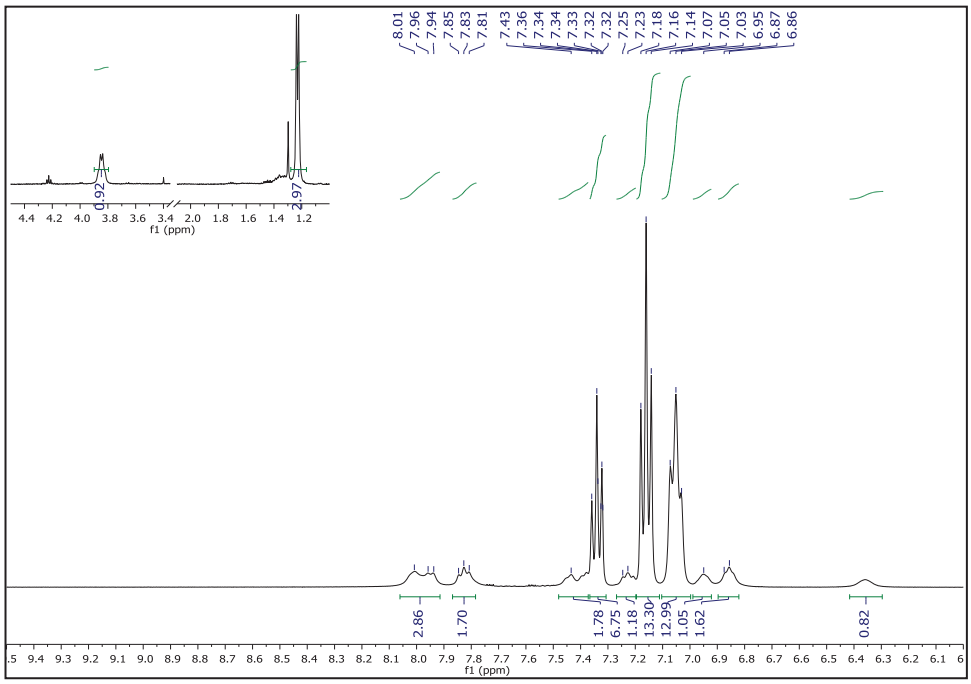

Figure 2.28 ^{1}H NMR spectrum (dichloromethane-d_2, 25°C) of [Cu(PPh_3)$_2$(L^{OH})](lact) (**3**). Inset: alkyl signal from lactate group.

X-ray analysis performed on single crystal of the complex (obtained by slow diffusion of hexane into a solution of the compound in dichloromethane) allowed to characterise this species in the solid state (Figure 2.29).

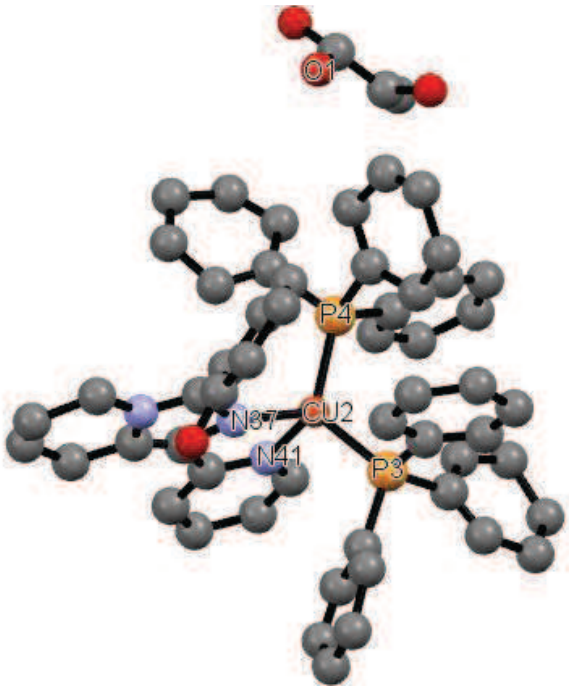

Figure 2.29 Crystal structure of [Cu(PPh_3)$_2$(L^{OH})](lact) (**3**). Hydrogen atoms are omitted for clarity.

The copper(I) centre is in a N_2P_2 tetra-coordinated environment, composed by two triphenylphosphine ligands and the two nitrogen atoms of L^{OH} and can be defined as being in a distorted tetrahedral geometry. Selected bond lengths and angles are reported in Table 2.2.

Differently from what observed before, in compound $[Cu(PPh_3)_2(L^{OH})](lact)$ (**3**) the anion is out of the first coordination sphere of copper, Cu-O measuring ca. 7.6 Å.

$[Cu_2(\mu\text{-dppm})_2(\mu\text{-}\eta^2\text{-lact})(\eta^1\text{-lact})]$ (1)			
Atoms	Lenght (Å)	Atoms	Angle (°)
Cu1-Cu2	2.854	P6-Cu2-O10	111.16
Cu1-P5	2.221	P6-Cu2-O4	117.95
Cu1-P10	2.246	O4-Cu2-O10	90.40
Cu2-P6	2.254	P9-Cu2-O4	110.05
Cu2-P9	2.277	P9-Cu2-O10	97.96
Cu1-O5	2.054	P9-Cu2-P6	122.36
Cu2-O4	2.073	P5-Cu1-O5	113.27
Cu2-O10	2.033	P5-Cu1-P10	93140
		P10-Cu1-O5	103.05
		(P-Cu-P)plane - (Cu-O5)bond	157.93
$[Cu(phen)(PPh_3)_2(lact)]$ (2)			
Bond	Lenght (Å)	Angle	Degrees (°)
Cu2-O3	2.053	N3-Cu-N4	79.04
Cu2-O4	3.054	N3-Cu-O3	109.68
Cu2-N3	2.132	N4-Cu-O3	103.02
Cu2-N4	2.068	N3-Cu-P3	116.32
Cu2-P3	2.185	N4-Cu-P3	126.26
C59-O3	1.259	O3-Cu-P3	116.42
C59-O4	1.220	O3-C59-O4	126.00
$[Cu(PPh_3)_2(L^{OH})](lact)$ (3)			
Bond	Length (Å)	Angle	Degrees (°)
Cu2-N37	1.979	N37-Cu-N41	78.54
Cu2-N41	2.056	N37-Cu-P3	114.38
Cu2-P3	2.271	N41-Cu-P3	110.41
Cu2-P4	2.276	N37-Cu-P4	113.66
Cu2-O1	7.571	N41-Cu-P4	111.03
		P3-Cu-P4	120.90

Table 2.2 Bond lengths and angles of complex obtained by X-ray diffraction.

2.2.2 LUMINESCENT PROPERTIES OF DERIVATIVES

Due to the abovementioned equilibria often detected for these species in solution, their photophysical properties have been investigated only in the solid state. The synthesised derivatives showed significant differences when compared to their precursor $[Cu(PPh_3)_2(lact)]$.

Regarding species $[Cu_2(\mu\text{-dppm})_2(\mu\text{-}\eta^2\text{-lact})(\eta^1\text{-lact})]$, a 35-nm batochromic shift to the green region of the visible spectrum is observed (Figure 2.30), λ_{max} being 496 nm when excited at 353 nm (λ_{max} = 461 for $[Cu(PPh_3)_2(lact)]$).

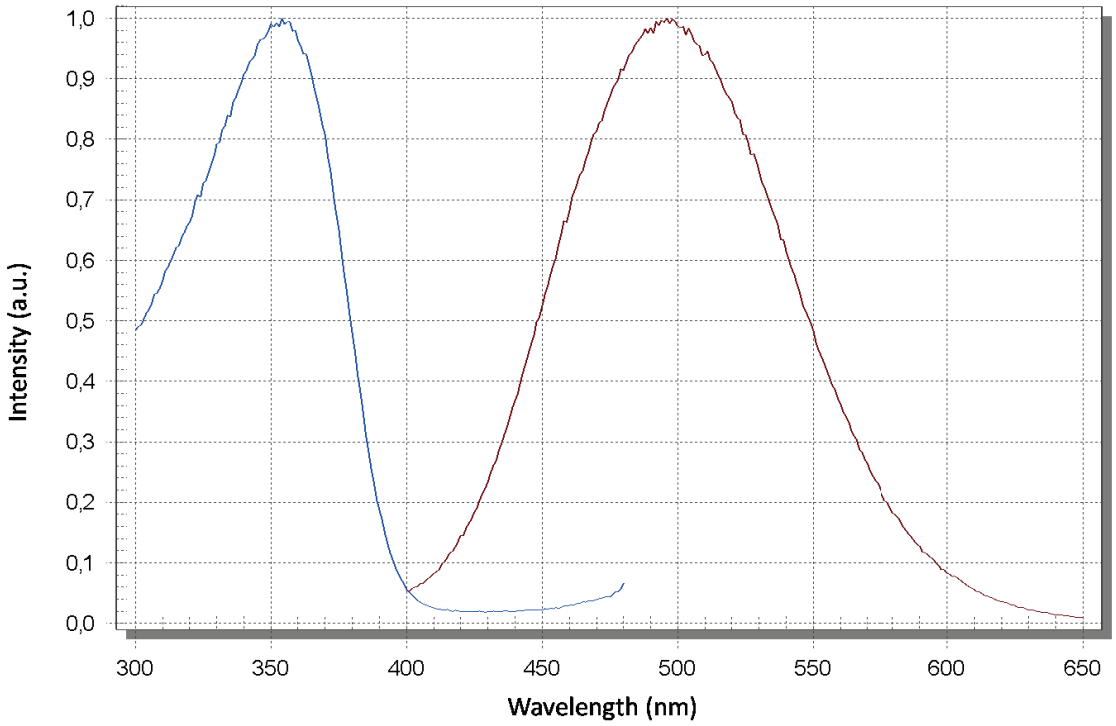

Figure 2.30 Normalised excitation and emission spectra of $[Cu_2(\mu\text{-dppm})_2(\mu\text{-}\eta^2\text{-lact})(\eta^1\text{-lact})]$.

Additionally, this complex showed a remarkable emission which does not undergo photobleaching over time: in fact, as shown in Figure 2.31, emission spectra recorded at 15-minute intervals over 2 hours, exhibit a weak decrease of intensity, moving from an initial value of 5 V to 4.5 V over more than two hours time (remember that $[Cu(PPh_3)_2(lact)]$ showed an half-life time of 40 minutes).

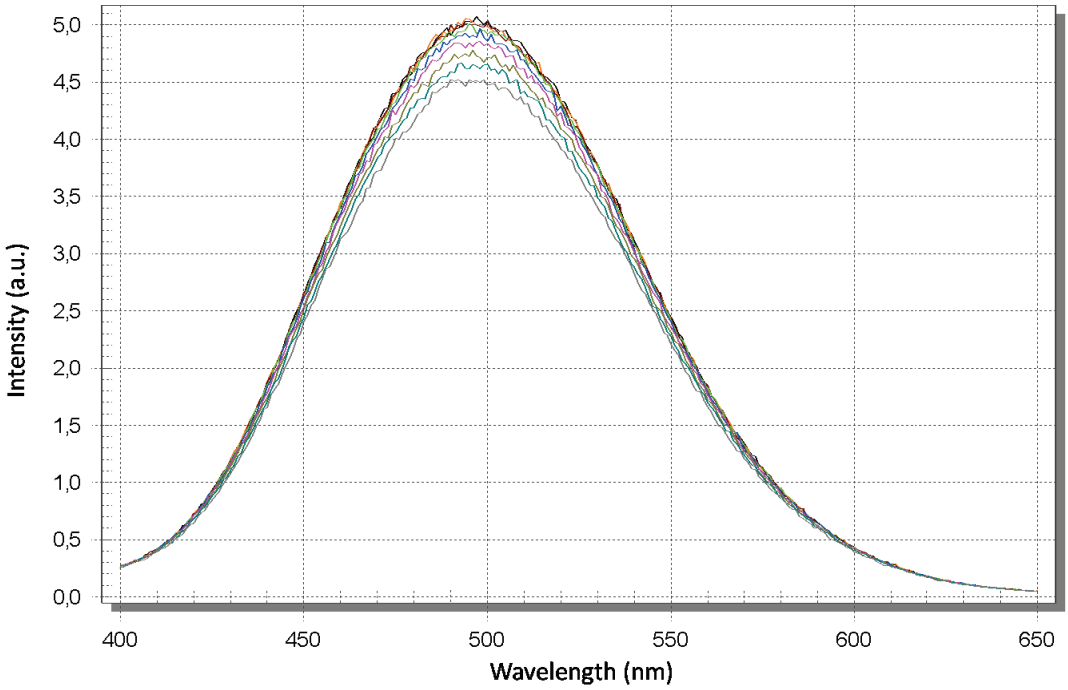

Figure 2.31 Series of emission spectra registered at 15-minute intervals over 2 hours.

Compound [Cu(phen)(PPh_3)$_2$(lact)] displayed good luminescence emission in the solid state, as well (Figure 2.32); the maximum wavelength of emission is centred at 529 nm (upon excitation at 395 nm), further batochromically shifted with respect to the dppm-derivative.

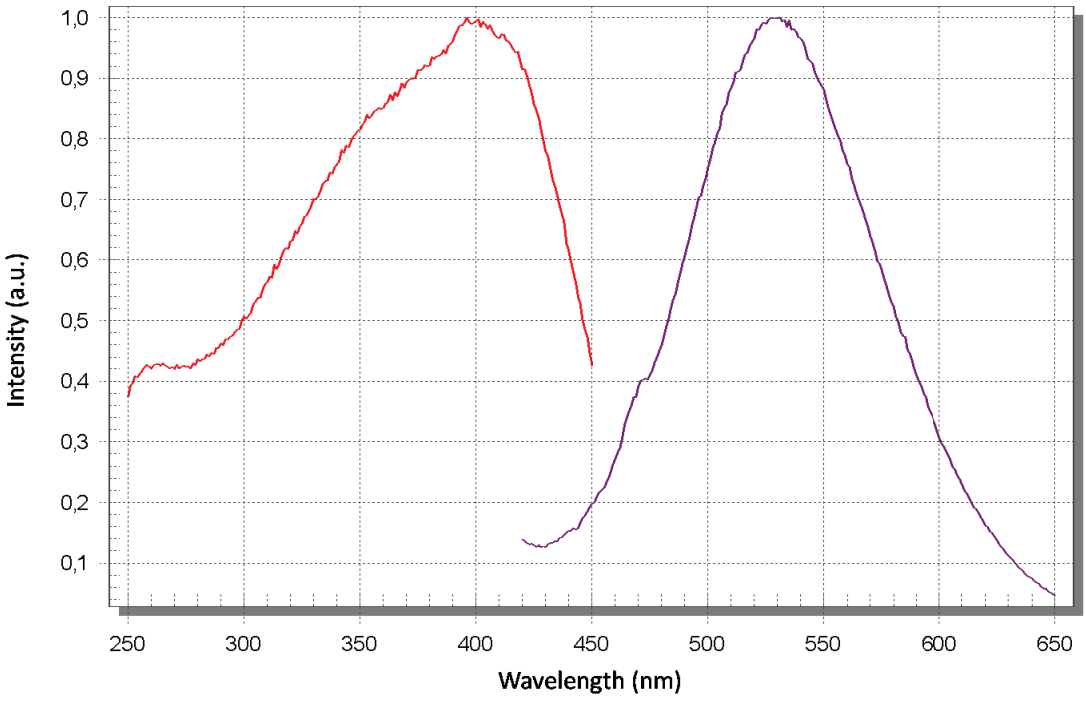

Figure 2.32 Normalised excitation and emission spectra of [Cu(phen)(PPh_3)$_2$(lact)].

Finally, derivative [Cu(PPh_3)$_2$(L^{OH})](lact), has shown a small variation of luminescence emission when compared to the precursor [Cu(PPh_3)$_2$(lact)] (λ_{max} of emission being 469 nm with an excitation λ_{max} of 420 nm).

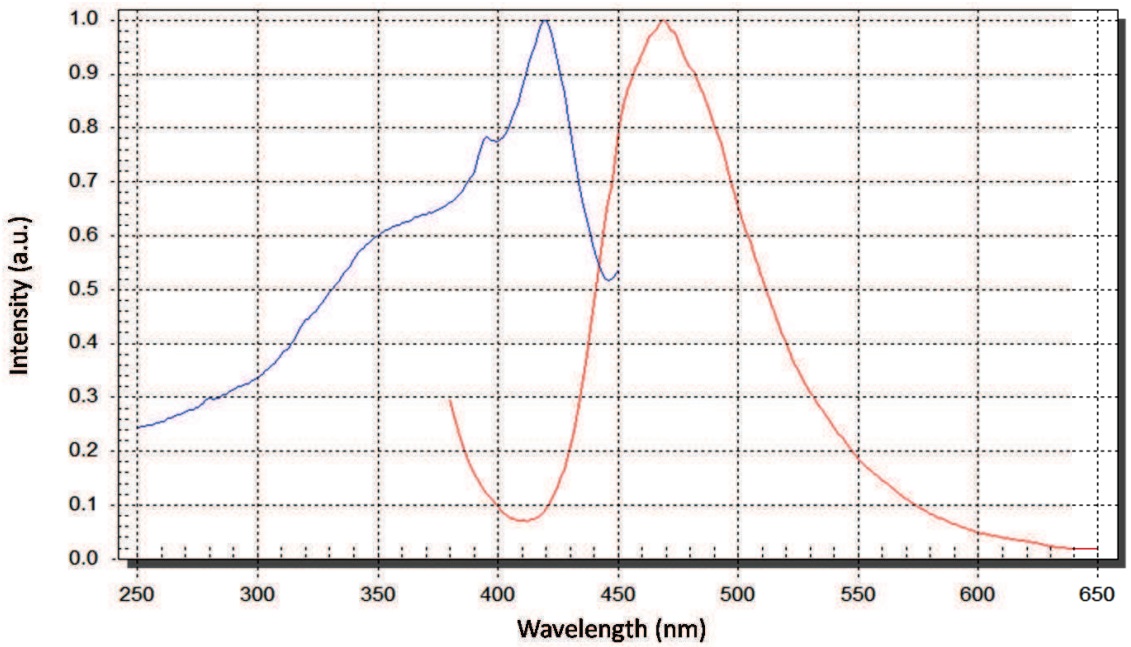

Figure 2.33 Normalised excitation and emission spectra of [Cu(PPh_3)$_2$(L^{OH})](lact).

Concluding, compound [Cu(PPh_3)$_2$(lact)] can be considered as a valid precursor for the synthesis of luminescent copper(I) complexes. As demonstrated, substitution reactions with different P- and N-donor ligands allowed to easily tune the emission properties of the corresponding derivatives. Unfortunately, these class of complexes showed poor absolute photoluminescence quantum yields (i. e. Φ_{PL} = 8% for [Cu(PPh_3)$_2$(lact)]; 17% for [Cu_2(μ-dppm)$_2$(μ-η^2-lact)(η^1-lact)]; 4% for [Cu(phen)(PPh_3)$_2$(lact)]; 3% for [Cu(PPh_3)$_2$(L^{OH})](lact)). Further studies and measurements (lifetime decay) will hopefully give better insights.

Chapter 3

Blue Emitting Zn(II) Complexes with 3-Aryl-Substituted 1-Pyridylimidazo[1,5-*a*]pyridine Ligands

Numerous zinc(II) complexes are known to exhibit intense fluorescence at room-temperature[41] and there has been substantial research into the potential application of zinc(II) complexes for fluorescence-based OLED devices. Zinc containing compounds appeared in the literature revealing high luminescent performances and especially compounds with neutral N-based ligands have shown great promises. Relevant examples of $Zn(N\cap N)X_2$ systems (N∩N = bidentate nitrogen ligand; X = halide) with luminescent properties have been published. Recently Chaudhury reported efficient dinuclear zinc(II) and cadmium(II) blue emitters whose emission was due to ligand centred π←π* transitions[42] (Figure 3.1a); Wang reported two blue phosphorescent zinc complexes of 4,4^{I}-diphenyl-6,6^{I}-dimethyl-2,2^{I}-bipyrimidine (pmbp) emitting at room temperature in the solid state[43] (Figure 3.1b); Larionov synthesized luminescent Zn(II) and Cd(II) complexes containing pyridophenazine derivatives[44] (Figure 3.1c); furthermore, Housecroft et *al.* first reported the use of zinc(II) complexes as photosensitiser in dye sensitised solar cells.[45]

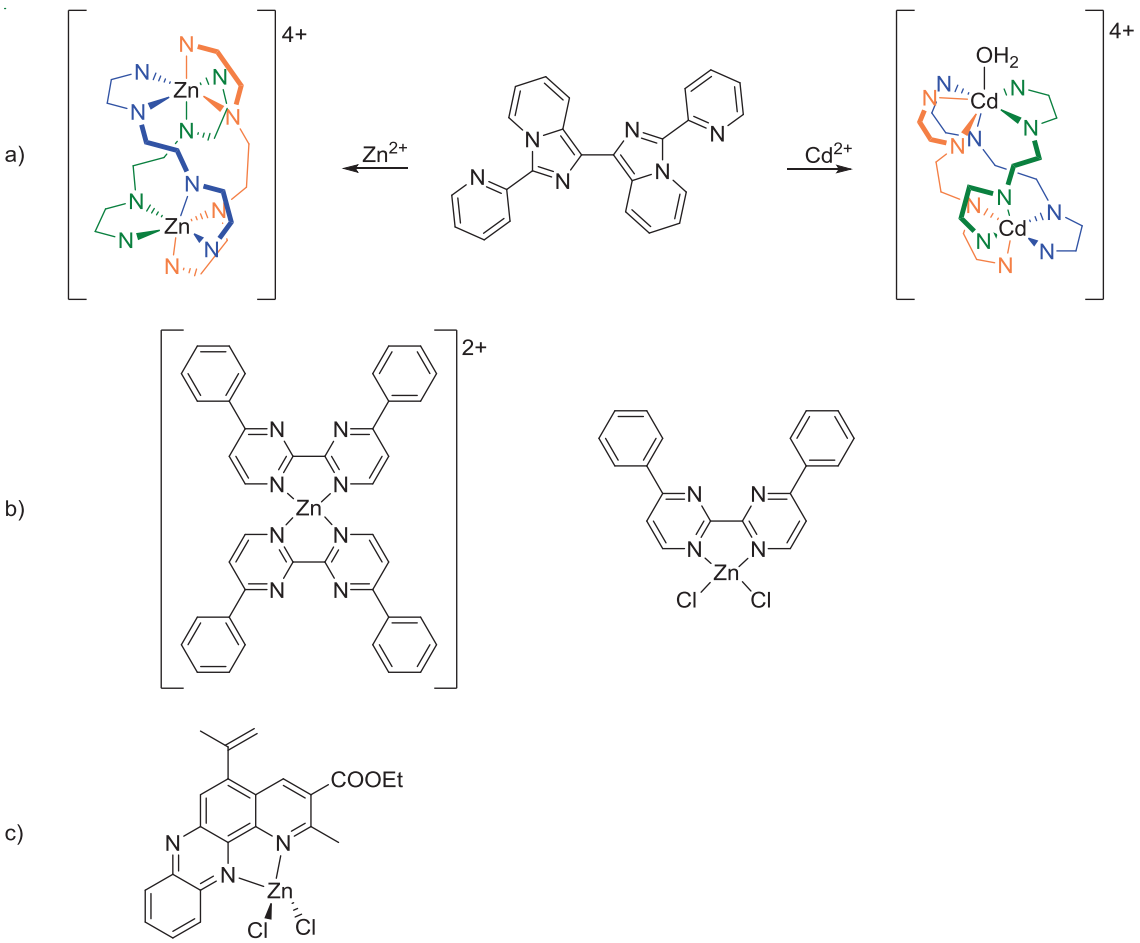

Figure 3.1 Examples of luminescent Zn(II) and Cd(II) systems containing N∩N bidentate nitrogen ligands.

As already said, this research group has deeply investigated the coordination chemistry of N-based multidentate ligands.[21-23] Progressing in this field, herein it has been conducted a study on the photophysical properties of zinc(II) compounds with 3-aryl-substituted 1-pyridylimidazo[1,5-*a*]pyridine ligands. Heterocycles having the imidazo[1,5-*a*]pyridine skeleton (Figure 3.2) are known to possess unique photophysical properties,[46] with potential applications in the field of OLEDs,[47] and organic thin-layer field effect transistors (FET).[48] Moreover, different 1-pyridylimidazo[1,5-*a*]pyridines have been coordinated to transition metals giving rise to highly luminescent coordination compounds based on Re(I),[49] Zn(II) or Cd(II)[41] and Ru(II) or Os(II)[50] metal centres.

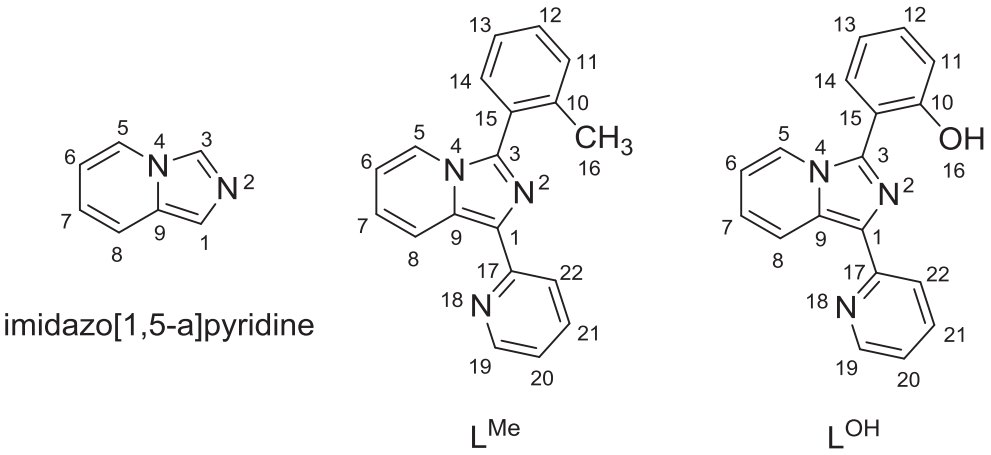

Figure 3.2 1-(Pyridin-2-yl)imidazo[1,5-*a*]pyridinyl ligands employed in this work.

As it will be highlighted in the Chapter, the N∩N-bidentate ligands 1-(pyridin-2-yl)-3-*o*-tolylimidazo[1,5-*a*]pyridine (L^{Me}) and 2-(1-(pyridin-2-yl)imidazo[1,5-*a*]pyridin-3-yl)phenol (L^{OH}) (Figure 3.2) have been coordinated to ZnX_2 fragments (X = Cl, Br, I), thus obtaining six novel zinc(II) mononuclear compounds formulated as $[Zn(L^{R})X_2]$ (R = Me, OH). Then, the attention was focused on ligand 2-(1-(pyridin-2-yl)imidazo[1,5-*a*]pyridin-3-yl)phenol to synthesize a series of zinc(II) compounds of the general formula $[Zn(L^{OH})_2](Y)_2 \cdot nH_2O$, where Y represents a polyatomic anion (Y = ClO_4^-, NO_3^-, BF_4^-, PF_6^-). The synthesis, full spectroscopic characterisation of these complexes and an exploration of their photoluminescent properties in the solid state are reported.

3.1 SYNTHESIS AND CHARACTERISATION OF Zn(II) COMPLEXES

3.1.1 [Zn(L^R)X_2] DERIVATIVES

Ligands L^{Me} and L^{OH} were prepared following a published procedure.[51] Their purity was assessed by ^1H, $^{13}C\{^1H\}$ NMR and elemental analysis. Zinc(II) complexes **4-9** were prepared by reaction of the corresponding anhydrous ZnX_2 salt (X = Cl, Br, I) with one equivalent of L^{Me} (**4-6**) or L^{OH} (**7-9**), in methanol, at room temperature (Figure 3.3).[52] All complexes are yellow crystalline powders and they have been characterised by elemental analysis and infrared spectroscopy.

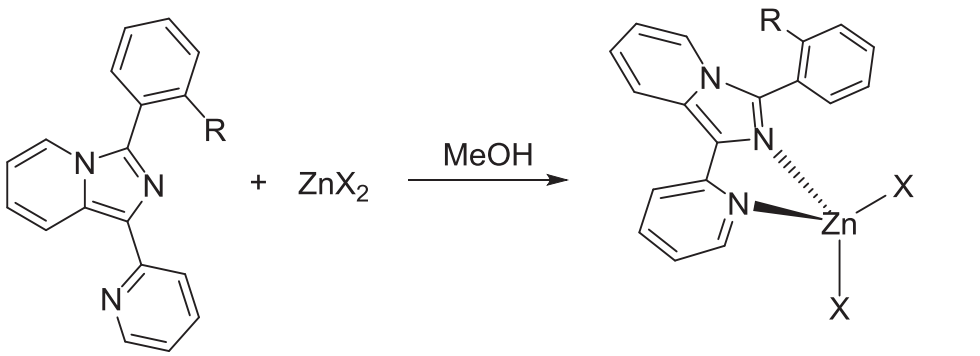

R = CH_3, X = Cl (**4**), Br (**5**), I (**6**)

R = OH, X = Cl (**7**), Br (**8**), I (**9**)

Figure 3.3 Synthesis of complexes **4-9**.

In their infrared spectrum (nujol mull) the [Zn(L^R)X_2] species show the typical pattern of the ligands, with sharp and intense stretching bands in the region 1516-1614 cm^{-1} and an additional band of medium intensity around 1640 cm^{-1} ($\nu_{C=N}$). Furthermore, the infrared spectra of compounds **7-9** registered in hexachlorobutadiene show a sharp stretching band at about 3280 cm^{-1} due to the OH vibration. The shape of this band allows to conclude that, in the complex, the hydroxo group is not involved in any H-bonding; in addition, the infrared spectrum of free L^{OH} in hexachlorobutadiene shows a very broad vibration in the region 3100-2450 cm^{-1}, suggesting the presence of strong intermolecular H-bonds in its structure. This feature was eventually confirmed by the X-ray single crystal analysis performed on L^{OH}.[53] The ^1H and $^{13}C\{^1H\}$ NMR spectra (dichloromethane-d_2, 25°C) of complexes **4-6** are reported in Figures 3.4 – 3.9.

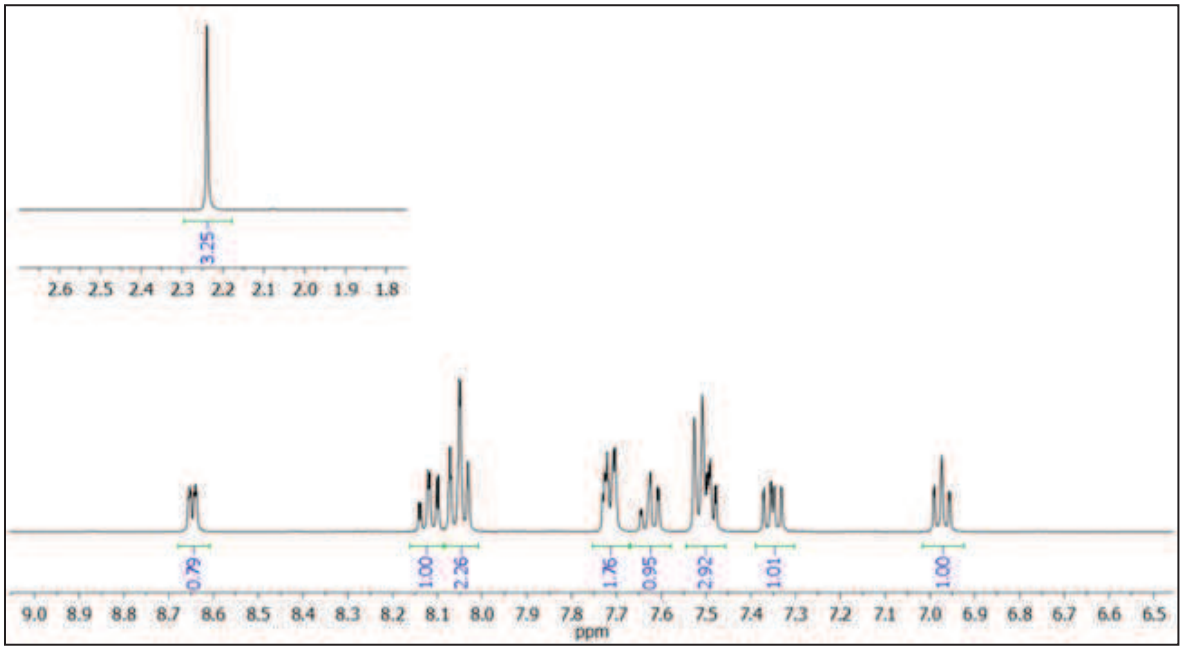

Figure 3.4 ^{1}H NMR (dichloromethane-d_2, 25°C) of compound [Zn(L^{Me})Cl_2].

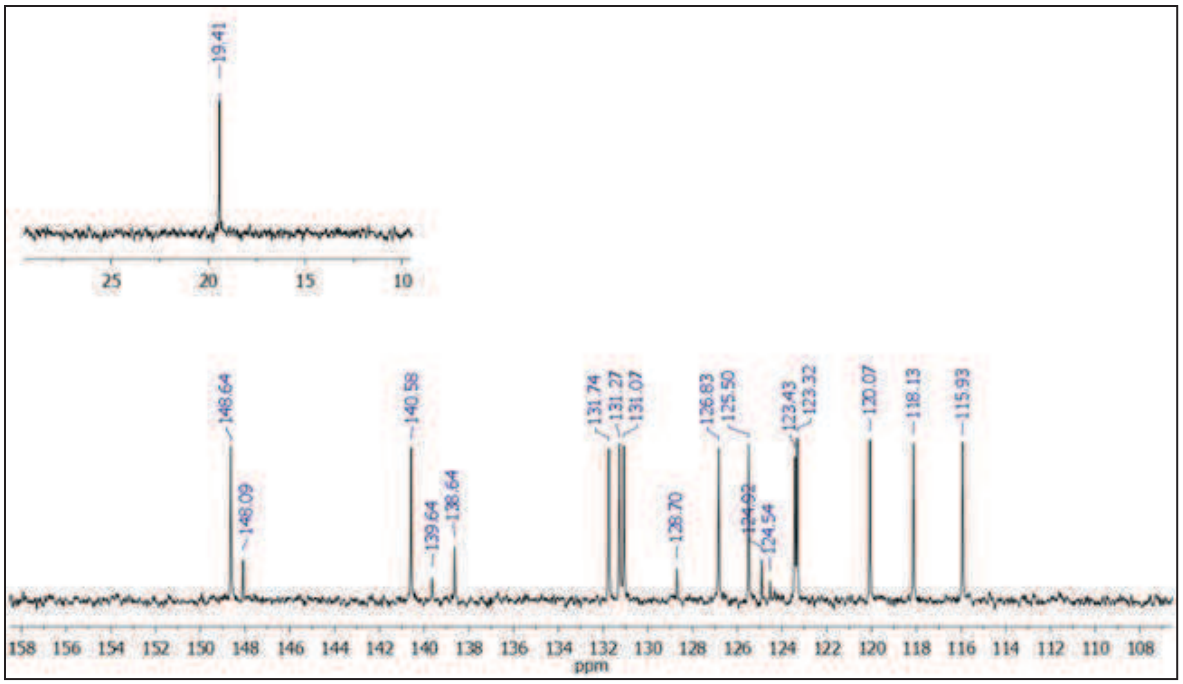

Figure 3.5 $^{13}C\{^{1}H\}$ NMR (dichloromethane-d_2, 25°C) of compound [Zn(L^{Me})Cl_2].

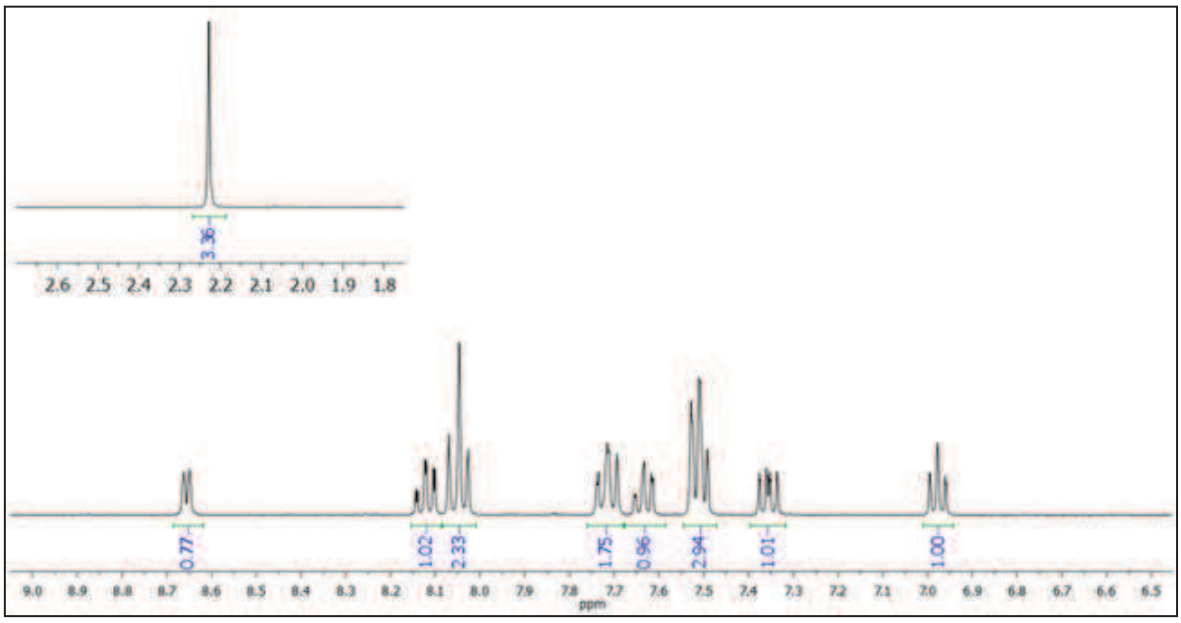

Figure 3.6 ^{1}H NMR (dichloromethane-d_2, 25°C) of compound [Zn(L^{Me})Br_2].

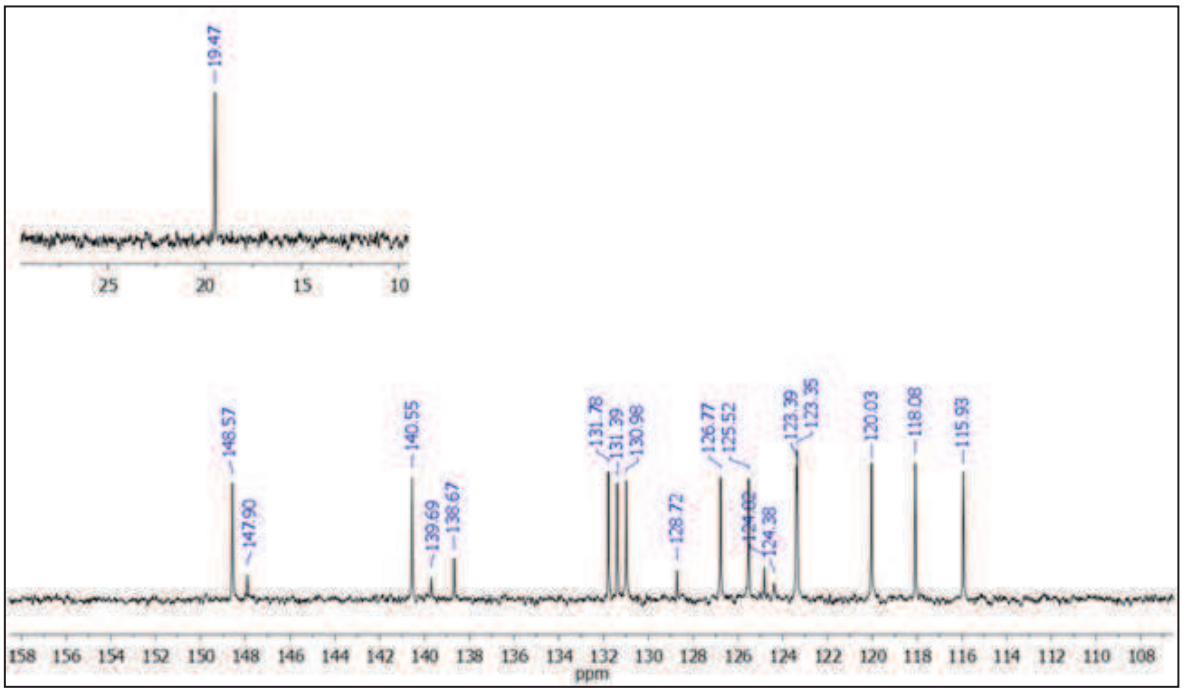

Figure 3.7 $^{13}C\{^{1}H\}$ NMR (dichloromethane-d_2, 25°C) of compound [Zn(L^{Me})Br_2].

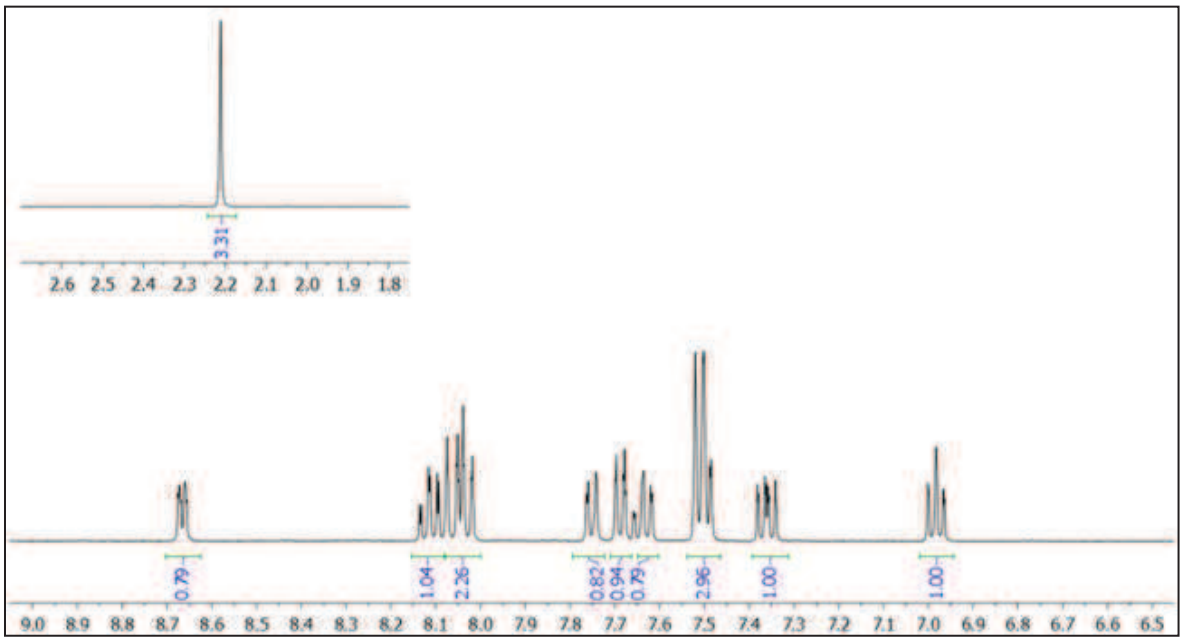

Figure 3.8 ^{1}H NMR (dichloromethane-d_2, 25°C) of compound [Zn(L^{Me})I_2].

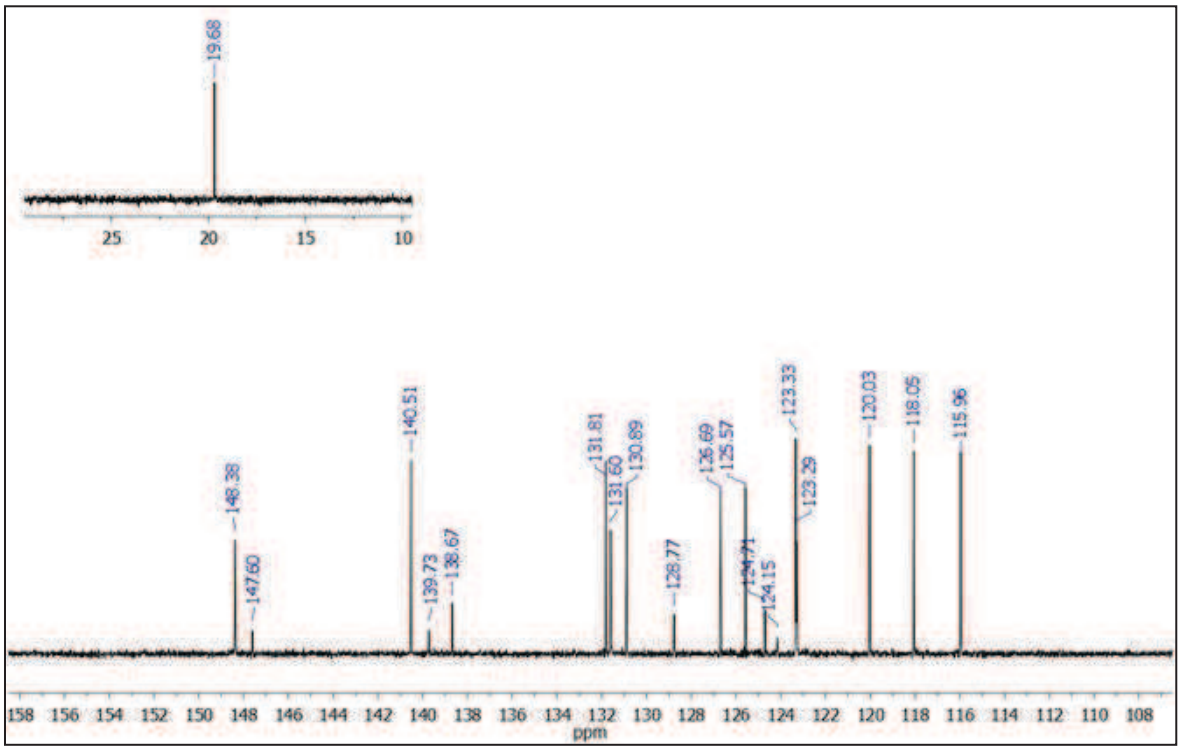

Figure 3.9 ^{13}C{^{1}H} NMR (dichloromethane-d_2, 25°C) of compound [Zn(L^{Me})I_2].

They show the expected pattern of ligand L^{Me}, with some slight shifts due to the *N*,*N*-coordination to the metal centre. On the contrary, compounds **7-9** did not show an adequate solubility in chlorinated solvents; the ^{1}H NMR spectrum recorded in DMSO-d_6 at 25°C showed quite broad signals in the 6 to 8 ppm range and a peak at about 9-10 ppm

due to the OH substituent (as an example, see ^{1}H NMR of complex **7** in Figure 3.10). The presence of such an unresolved pattern suggests a possible lability for these complexes, with ligand L^{OH} partially dissociated in solution, in the presence of strongly coordinating solvents such as DMSO.

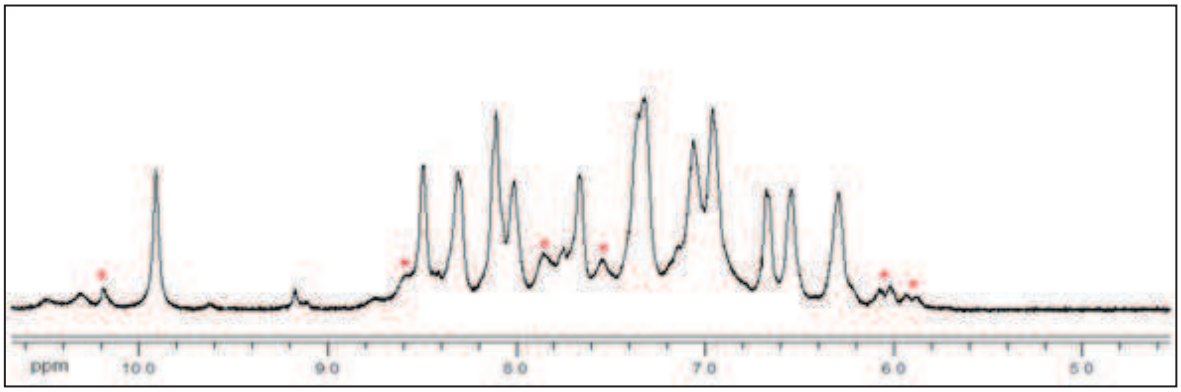

Figure 3.10 ^{1}H NMR (DMSO-*d*6, 20°C) of compound $[Zn(L^{OH})Cl_2]$. The peaks marked with red asterisks are attributed to partially dissociated L^{OH}.

Three of the complexes, namely $[Zn(L^{Me})Cl_2]$ (**4**), $[Zn(L^{Me})I_2]$ (**6**) and $[Zn(L^{OH})Cl_2]$ (**7**), were characterised via single-crystal X-ray diffraction analysis (Figures 3.11, 3.12 and 3.13).

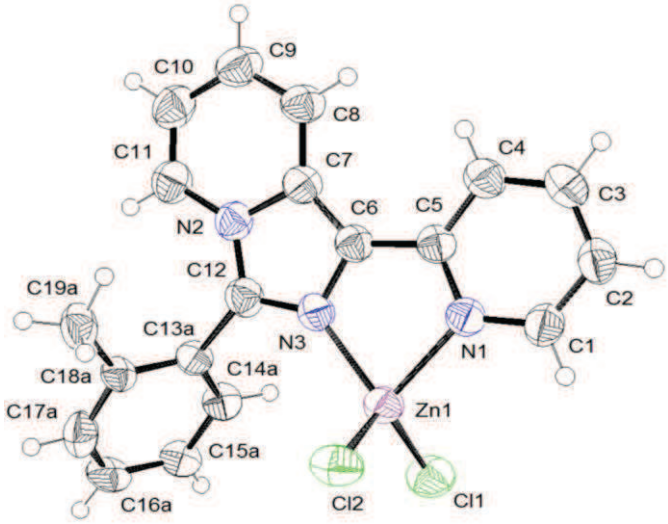

Figure 3.11 ORTEP representation of $[Zn(L^{Me})Cl_2]$ (**4**) at 35% probability level. Selected bond lengths (Å) and angles (º): Zn(1)-N(1) 2.083(4), Zn(1)-N(3) 2.044(3), Zn(1)-Cl(1) 2.206(1), Zn(1)-Cl(2) 2.223(2); N(1)-Zn(1)-Cl(1) 110.7(1), N(1)-Zn(1)-Cl(2) 109.9(1), N(3)-Zn(1)-Cl(1) 120.0(1), N(3)-Zn(1)-Cl(2) 111.1(1), Cl(1)-Zn(1)-Cl(2) 117.94(5), N(1)-Zn(1)-N(3) 81.0(1), N(1)-C(5)-C(6)-N(3) -4.6(5), N(1)-C(5)-C(6)-C(7) 174.2(4), N(2)-C(12)-C(13)-C(18) -69.0(1).

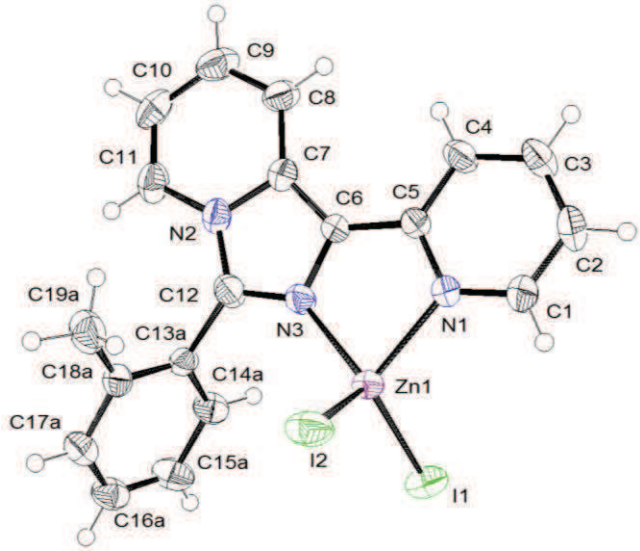

Figure 3.12 ORTEP representation of [Zn(L^{Me})I_2] (**6**) at 35% probability level. Selected bond lengths (Å) and angles (º): Zn(1)-N(1) 2.078(3), Zn(1)-N(3) 2.038(3), Zn(1)-I(1) 2.5316(5), Zn(1)-I(2) 2.5382(5); N(1)-Zn(1)-I(1) 107.88(9), N(1)-Zn(1)-I(2) 112.52(9), N(3)-Zn(1)-I(1) 121.06(9), N(3)-Zn(1)-I(2) 108.09(9), I(1)-Zn(1)-I(2) 119.81(2), N(1)-Zn(1)-N(3) 80.8(1), N(1)-C(5)-C(6)-N(3) -5.4(4), N(1)-C(5)-C(6)-C(7) 171.0(4), N(2)-C(12)-C(13)-C(18) -78.0(9).

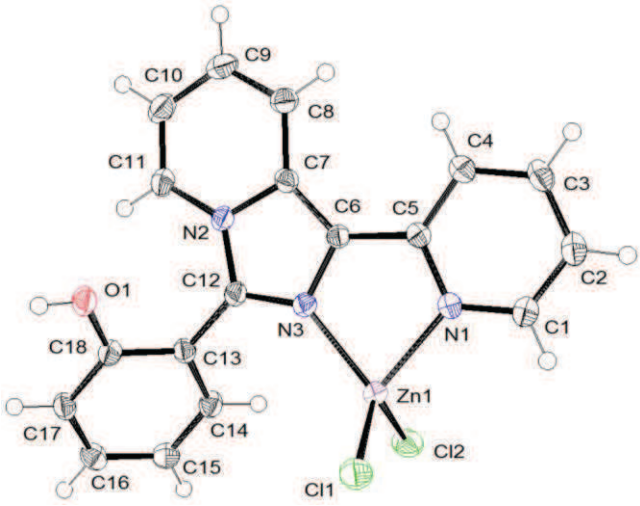

Figure 3.13 ORTEP representation of [Zn(L^{OH})Cl_2] (**7**) at 50% probability level (DMF molecule omitted for clarity). Selected bond lengths (Å) and angles (º): Zn(1)-N(1) 2.070(2), Zn(1)-N(3) 2.039(2), Zn(1)-Cl(1) 2.217(1), Zn(1)-Cl(2) 2.2147(9); N(1)-Zn(1)-Cl(1) 112.7, N(1)-Zn(1)-Cl(1) 112.75(7), N(1)-Zn(1)-Cl(2) 108.71(7), N(3)-Zn(1)-Cl(1) 117.89(7), N(3)-Zn(1)-Cl(2) 113.46(7), Cl(1)-Zn(1)-Cl(2) 117.15(3), N(1)-Zn(1)-N(3) 80.94(9), N(1)-C(5)-C(6)-N(3) -1.5(4), N(1)-C(5)-C(6)-C(7) 179.7(3), N(2)-C(12)-C(13)-C(18) 129.7(4).

The zinc atoms of all complexes are in a four coordinated environment composed by the two halido ligands and two nitrogen atoms of the 1-pyridylimidazo[1,5-*a*]pyridine ligand. In complexes **4**, **6** and **7** ligand L^R is bound in a bidentate mode via the pyridine moiety

(N_{py}) and the pyridine-like nitrogen of the imidazo part (N_{im}) of the molecule. Thus, the hydroxy group of L^{OH} in **7** does not interact with the metal center, despite the high affinity between zinc and oxygen. As expected, the geometry around each metal center is tetrahedral, and bond distances and angles for each zinc atom are comparable to those found in previously described complexes having an analogous $Zn(N\cap N)Cl_2$[21c] and $Zn(N\cap N)I_2$[54] environment. Dihedral angles show a nearly planar configuration for the pyridyl-imidazo[1,5*a*]pyridine moiety of the ligand: N(1)-C(5)-C(6)-N(3) and C(4)-C(5)-C(6)-C(7) angles measuring -4.6(5)° and -5.7(7)° (in $[Zn(L^{Me})Cl_2]$), -5.4(4)° and -9.2(6)° (in $[Zn(L^{Me})I_2]$) and -1.5(4)° and -0.8(5)° (in $[Zn(L^{OH})Cl_2]$). The aryl substituent in position 3 of the imidazo[1,5*a*]pyridine (see Figure 3.2 for atom numbering) rotates along the C(12)-C(13) bond, the two planes containing the 3-aryl and the imidazo-pyridine skeleton being twisted respectively by 59.70° (**4**), 65.35° (**6**) and 47.27° (**7**). Compound **7** crystallized with two molecules of DMF per unit cell, and the hydroxyl group in L^{OH} is involved in a H-bonding interaction (O-H···O = 2.624(3) Å) with the oxygen of a neighbouring solvent molecule.

For complexes **4**, **6** and **7** detailed X-ray structural parameters are reported in Section 6.18.

3.1.2 COMPUTED GEOMETRIES

Geometries of complexes **4**, **6** and **7** were optimized starting from the corresponding X-ray structures. Due to the close similarities of IR and UV-Vis spectra for complexes **4**-**6** and **7**-**9** it is reasonable to assume for these species similar geometries. Accordingly, geometries of compounds **5**, **8** and **9** were calculated starting respectively from the atomic coordinates obtained by X-ray diffraction of **4** (for **5**) and **7** (for **8** and **9**) by substituting the appropriate halogen atoms. As easily predictable, all species present very similar features, with a tetrahedral coordination around the zinc atom and a planar disposition of the pyridyl and imidazo-pyridine rings. The substituted phenyl groups are twisted with respect to the imidazo-pyridine plane, with a corresponding dihedral angle ψ ranging from 120° to 130° (see Figure 3.14). Table 3.1 reports significant distances and angles relative to the zinc coordination sphere of complexes **4**-**9**. The calculated bond

lengths and angles within the coordination sphere of the metal for **4**, **6** and **7** are in good agreement with the X-ray structural data. As shown in Table 3.1, the major discrepancy between the calculated structure and the X-ray data is the value of the dihedral angle ψ. A relaxed potential energy scan (adopting the semi-empirical PM7 level of theory)[55] performed on complex **4** shows two large plateau of the minimum energy in the ranges ψ = 80° - 110° and ψ = 250° - 280° (Figure 3.14). The conformation found in the X-ray crystal structural determination is thus clearly due to crystal lattice extra-stabilization present in the solid state.

	4	**4**[a]	**5**	**6**	**6**[a]	**7**	**7**[a]	**8**	**9**
Zn-$N_{(py)}$	2.089	2.083	2.082	2.081	2.078	2.088	2.070	2.084	2.081
Zn-$N_{(im)}$	2.067	2.044	2.057	2.052	2.038	2.069	2.039	2.060	2.065
Zn-X(1)	2.234	2.206	2.374	2.551	2.532	2.234	2.215	2.373	2.574
Zn-X(2)	2.239	2.223	2.378	2.559	2.538	2.241	2.217	2.380	2.580
X-Zn-X	117.4	117.9	117.5	118.9	119.8	117.3	117.1	117.6	117.5
N-Zn-N	79.7	81.0	79.8	79.8	80.7	78.5	80.9	89.9	79.9
$N_{(im)}$-Zn-C-C(R)	120.7	122.1	119.3	123.5	116.5	122.5	129.7	122.9	123.7

Table 3.1 Computed bond lengths (Å) and angles (deg) for complexes **4**-**9** (DFT, PBE0\TZ2P\QZ4P(Zn)). [a]Data obtained by X-ray diffraction.

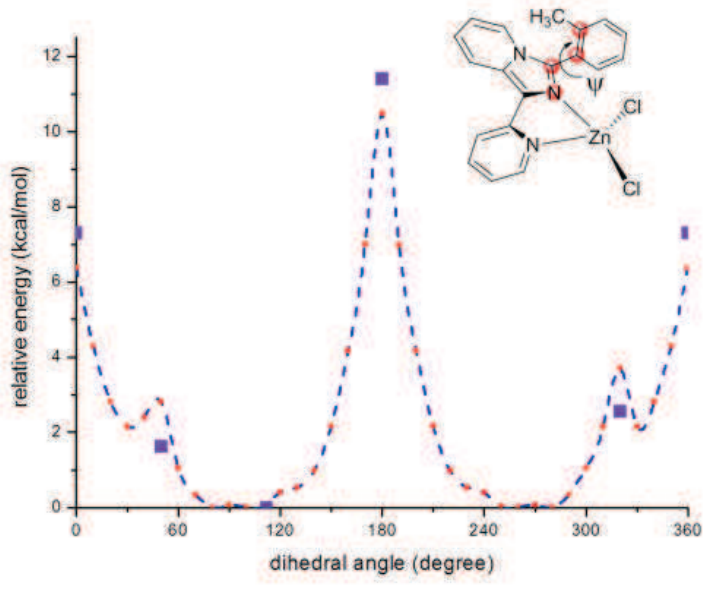

Figure 3.14 Relaxed potential energy scan performed on complex **4**. Squares represent values obtained with DFT, PBE0\TZ2P\QZ4P(Zn) level of theory, circles those obtained with the semi-empirical PM7 method.

3.1.3 $[Zn(L^{OH})_2](Y)_2 \cdot nH_2O$ DERIVATIVES

Complexes **10**, **11** and **12** have been prepared following similar procedures, by reacting ligand L^{OH} with the corresponding zinc(II) salt, namely $Zn(ClO_4)_2 \cdot 6H_2O$, $Zn(NO_3)_2 \cdot 6H_2O$ and $Zn(BF_4)_2 \cdot nH_2O$, in a 2:1 ligand:metal ratio, in methanol, at room temperature. They all are yellow crystalline powders and have been characterised by elemental analysis, infrared spectroscopy and thermogravimetric analysis. Accordingly, they are formulated respectively as $[Zn(L^{OH})_2](ClO_4)_2 \cdot H_2O$ (**10**), $[Zn(L^{OH})_2](NO_3)_2 \cdot H_2O$ (**11**), $[Zn(L^{OH})_2](BF_4)_2 \cdot 4H_2O$ (**12**).[56]

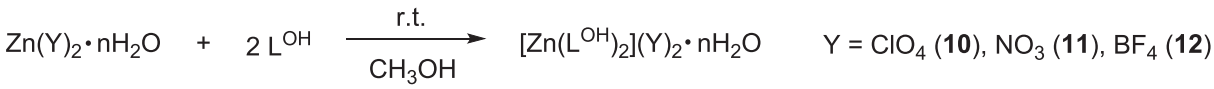

Figure 3.15 Syntheses of $[Zn(L^{OH})_2](Y)_2 \cdot nH_2O$ complexes.

On the contrary, the direct reaction of $Zn(PF_6)_2 \cdot nH_2O$ with two equivalents of L^{OH}, following the aforementioned procedure, did not generate the desired $[Zn(L^{OH})_2](PF_6)_2 \cdot H_2O$ (**13**) complex. Actually, the product isolated after workup was later formulated as $[Zn(L^{OH})_2(PO_2F_2)](PF_6)$ (**14**) in accordance with the elemental analysis and ^{31}P NMR evidences (see below). The water molecules in the starting zinc(II) hexafluorophosphate salt caused partial hydrolysis of the PF_6^- to $PO_2F_2^-$.[57] Consequently, a different approach was followed to prepare pure $[Zn(L^{OH})_2](PF_6)_2 \cdot H_2O$ (**13**): first, a methatetic exchange reaction was performed (Scheme 2, **A**) by treating a suspension of complex $[Zn(L^{OH})_2](NO_3)_2 \cdot H_2O$ in acetonitrile with two equivalents of KPF_6. Unfortunately, incomplete NO_3^-/PF_6^- substitution occurred, and compound **13** was recovered in very low yield (<10%). Thus, despite silver hexafluorophosphate being known to undergo partial hydrolysis[57b], a reaction involving $AgPF_6$ was attempted (Scheme 2, **B**). This salt was added to a dichloromethane solution of compound $[Zn(L^{OH})Cl_2]$ (**7**) (prepared as previously described in this Chapter, Section 3.1.1), resulting in the formation of insoluble AgCl and a solution of **13**, which was isolated as a yellow powder after removal of the solvent and recovery with diethylether.

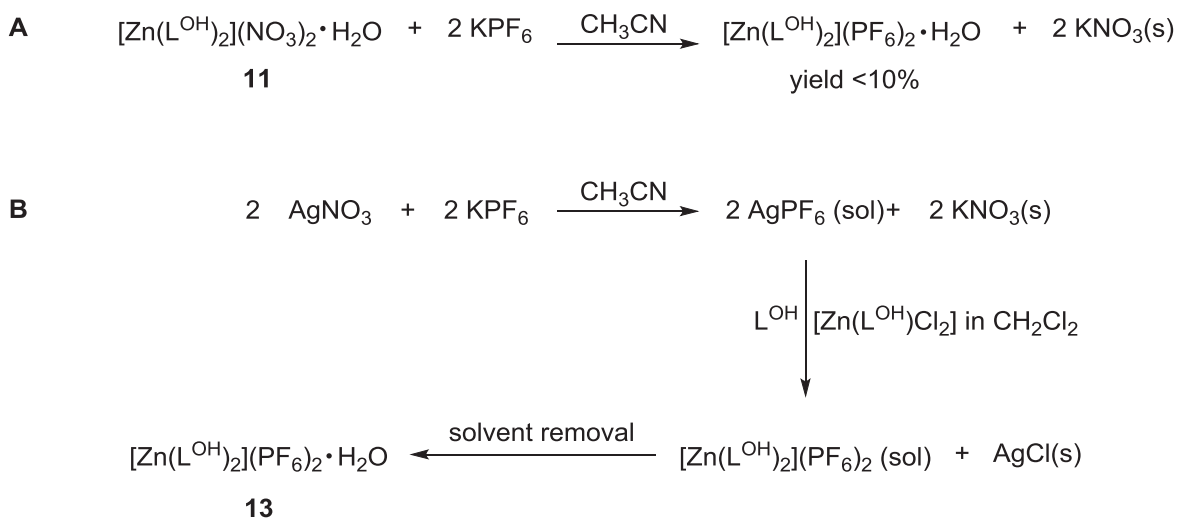

Figure 3.16 Synthetic procedures to prepare pure $[Zn(L^{OH})_2](PF_6)_2 \cdot H_2O$ (**13**): methatetic substitution starting from $[Zn(L^{OH})_2](NO_3)_2 \cdot H_2O$ (**11**) (**A**) and synthesis via $AgPF_6$ (**B**).

As expected, in their infrared spectrum (nujol mull) all $[Zn(L^{OH})_2](Y)_2 \cdot nH_2O$ species show the typical pattern of the ligand, with sharp and intense stretching bands in the region 1614-1516 cm^{-1} and an additional band of medium intensity around 1640 cm^{-1} ($\nu_{C=N}$). Furthermore, the infrared spectra of compounds **10-13** show a very broad band at about 3300 cm^{-1} due to the OH vibration, and a broad stretching in the region 1300-1000 cm^{-1} attributable to the counter anions (see experimental for attributions).

The ^1H NMR spectra (acetone-d_6 25°C) of complexes **10-13** show the expected pattern of ligand L^{OH}, with some slight shifts due to the *N*,*N*-coordination to the metal centre. Low-intensity additional peaks associated to free ligand are also detected, thus suggesting a possible lability for these complexes, with ligand L^{OH} partially dissociated in solution.

The $^{31}P\{^1H\}$ NMR spectrum of compound $[Zn(L^{OH})_2](PF_6)_2 \cdot H_2O$ (Figure 3.17, top) shows the expected septet ($^1J_{PF}$ = 708 Hz) due to uncoordinated hexafluorophosphate. As previously mentioned, treatment of $Zn(PF_6)_2$ hydrate with two equivalents of ligand L^{OH} afforded the complex $[Zn(L^{OH})_2(PO_2F_2)](PF_6)_2 \cdot H_2O$, which showed a different ^{31}P NMR pattern. Actually, in accordance with other PF_6^- / $PO_2F_2^-$ containing transition metals compounds,[57] the spectrum recorded for **14** consists of two sets of distinct sharp signals, respectively centred at -17.9 ppm and -144.4 ppm (Figure 3.17, bottom). The upper field signal appears as a septet ($^1J_{PF}$ = 706 Hz) and is associated to uncoordinated PF_6^-, whereas the lower field signal is a triplet ($^1J_{PF}$ = 950 Hz) and attributed to μ-$PO_2F_2^-$.

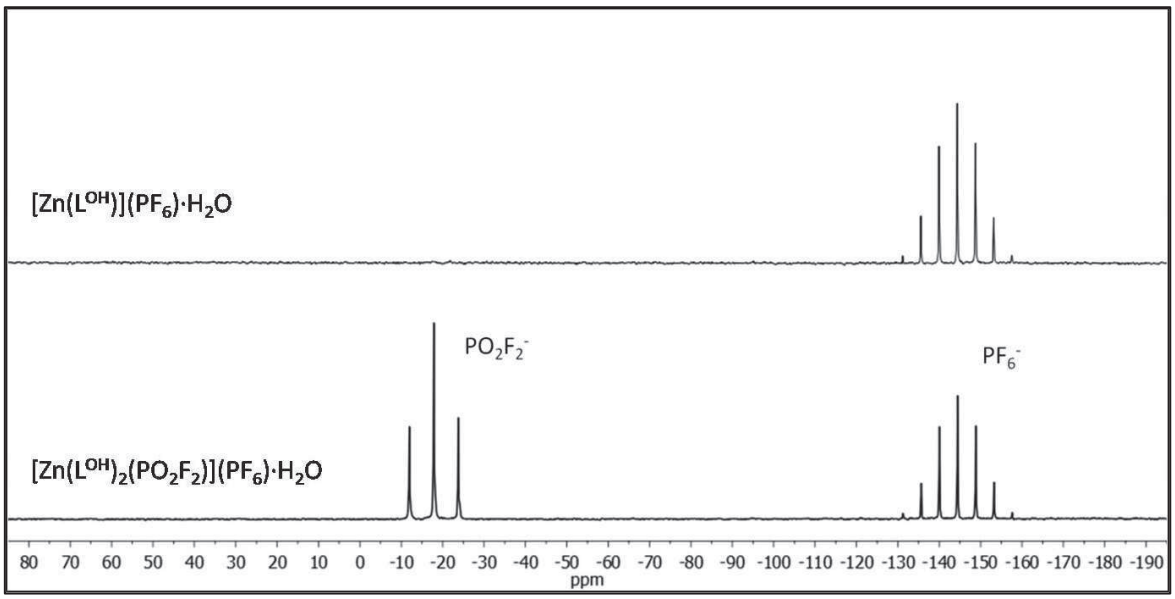

Figure 3.17 $^{31}P\{^{1}H\}$ NMR spectra (acetone-d_6, 25°C) of hexafluorophosphate containing complexes: top, $[Zn(L^{OH})_2](PF_6)_2\cdot H_2O$ (**13**); bottom, $[Zn(L^{OH})_2(PO_2F_2)](PF_6)\cdot H_2O$ (**14**).

The presence of water molecules in the complexes have been confirmed by thermogravimetric analysis (TGA). As an example, Figure 3.18 reports the TGA plot recorded for $[Zn(L^{OH})_2](ClO_4)_2\cdot H_2O$ (**10**), where a weight loss of 1.95% is detected at about 60°C and associated to the presence of one water molecule (calculated m/m loss = 2.10%) in the crystal packing of **10**. This feature was eventually confirmed by single crystal X-ray analysis performed on **10**. For compound $[Zn(L^{OH})_2](BF_4)_2\cdot 4H_2O$ (**12**), the TGA trace (Figure 3.19) shows two consecutive and distinct losses (4.12%), respectively at about 100°C and 260°C, associated to the presence of four water molecules (in accordance to elemental analysis). Most probably, two different kind of water molecules interact with the complex: the first two molecules, lost at 100°C (calculated m/m loss = 4.06%) likely belong to the outer coordination sphere of $[Zn(L^{OH})_2](BF_4)_2\cdot 4H_2O$. It is then necessary to heat the sample up to 260°C to lose the two remaining water molecules in the first, inner coordination sphere around the metal center (calculated m/m loss = 4.23%). Also for compounds $[Zn(L^{OH})_2](NO_3)_2\cdot H_2O$ (**11**) (Figure 3.20; drop: -2.47% (experimental) *vs*. -2.30% (calculated)) and $[Zn(L^{OH})_2](PF_6)_2\cdot H_2O$ (**13**) (Figure 3:21 drop: -1.99% (experimental) *vs*. -1.90% (calculated)) the experimental data are in good agreement with the expected values.

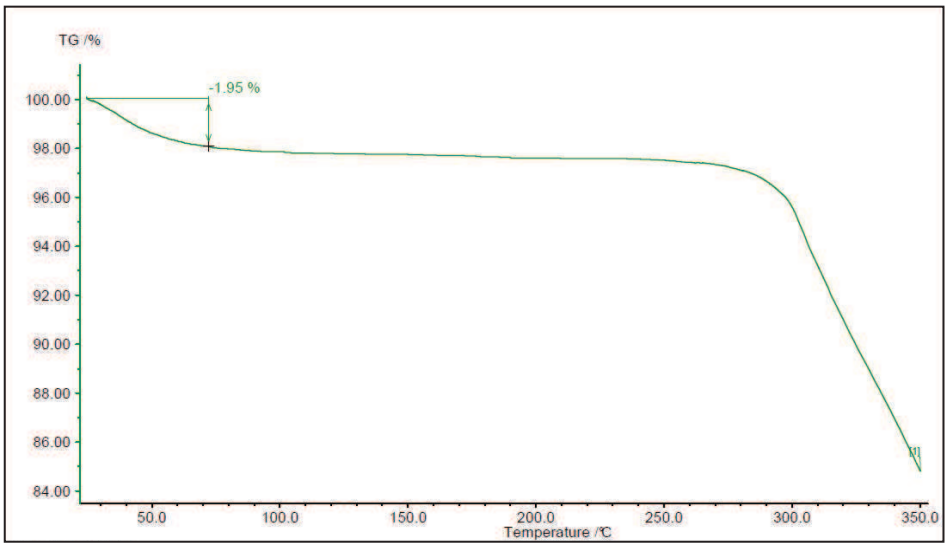

Figure 3.18 TGA trace (heating rate = 10°C/min) for $[Zn(L^{OH})_2](ClO_4)_2 \cdot H_2O$ (**10**).

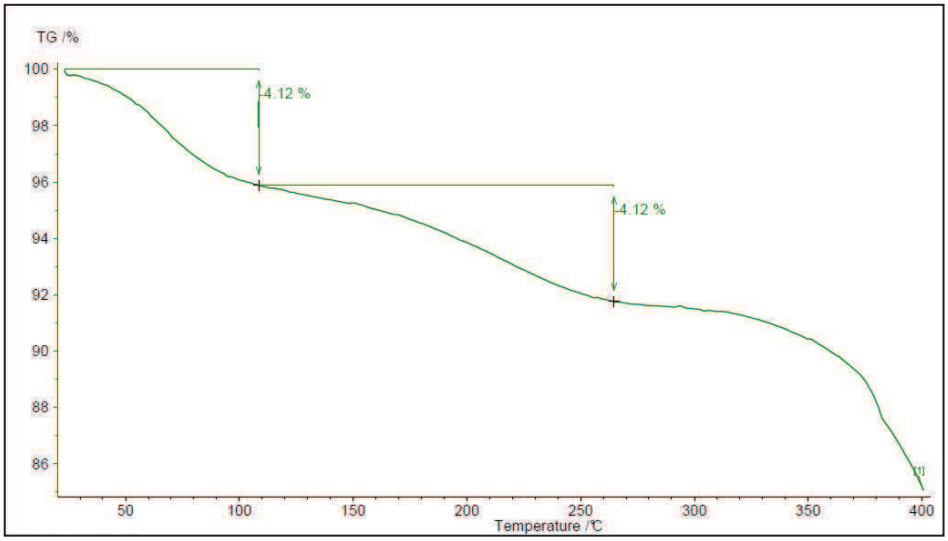

Figure 3.19 TGA trace (heating rate = 10°C/min) for $[Zn(L^{OH})_2](BF_4)_2 \cdot 4H_2O$ (**12**).

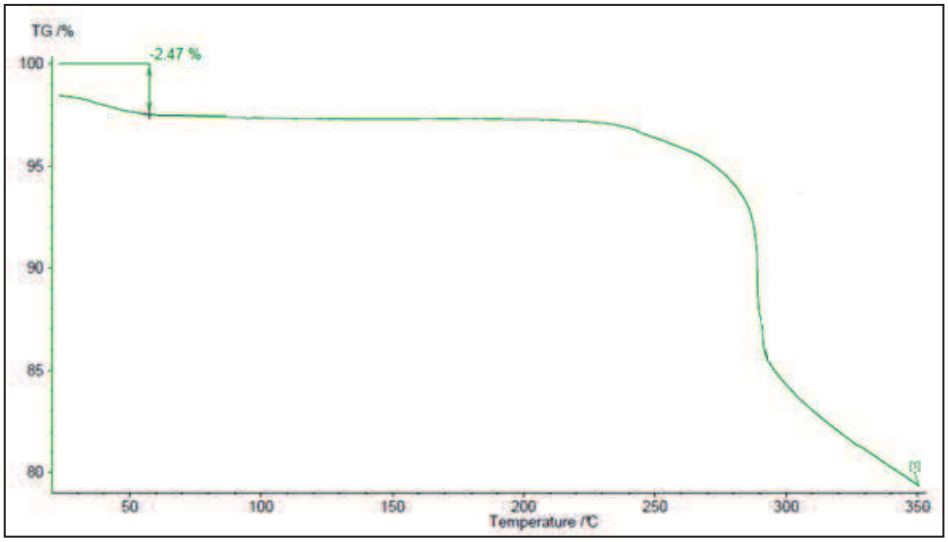

Figure 3.20 TGA trace (heating rate = 10°C/min) for $[Zn(L^{OH})_2](NO_3)_2 \cdot H_2O$ (**13**).

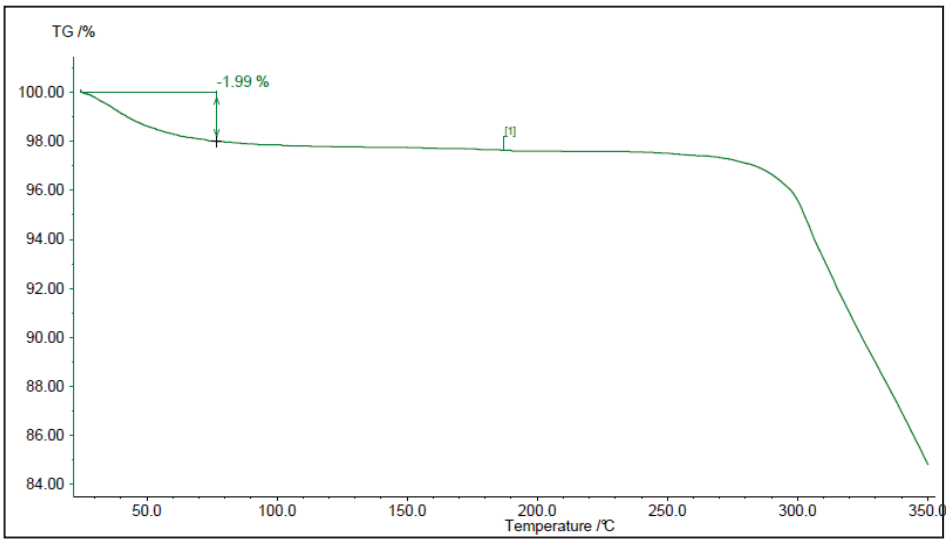

Figure 3.21 TGA trace (heating rate = 10°C/min) for $[Zn(L^{OH})_2](PF_6)_2 \cdot H_2O$ (**13**).

Complex $[Zn(L^{OH})_2](ClO_4)_2 \cdot H_2O$ (**10**) was characterised via single-crystal X-ray diffraction analysis (Figure 3.22). In **10**, the zinc centre shows a penta-coordination, with a N_4O environment deriving from two molecules of ligand L^{OH}, each binding in a *N*,*N*-bidentate mode via the pyridine moiety (N_{py}) and the pyridine-like nitrogen of the imidazo part (N_{im}) of the molecule. The fifth coordination site is occupied by one oxygen atom of a perchlorato ligand, the other ClO_4^- anion lying in the outer coordination sphere of the metal.

The zinc atom shows a trigonality index τ = 0.73,[58] thereby suggesting that the geometry around the metal is mainly described as trigonal bipyramidal. The two Zn-N_{im} distances (Zn(1)-N(2) = 2.024(5) Å; Zn(1)-N(5) = 2.049(4) Å) are slightly shorter than the Zn-N_{py} distances (Zn(1)-N(1) = 2.097(5) Å; Zn(1)-N(4) = 2.070(5) Å), while the Zn(1)-O(3) (ClO_4^-) bond distance is 2.229(4) Å. All parametrical data agree with those found in the literature for zinc(II) complexes having an analogous N_4O environment.[59] Dihedral angles within each pyridyl-imidazo[1,5-*a*]pyridine molecule confirm the nearly planar configuration expected for this skeleton, N(1)-C(5)-C(6)-N(2) and N(4)-C(23)-C(24)-N(5) measuring 2.4(7)° and 11.1(7)°, respectively. Finally, the plane of the phenol substituent is twisted with respect to the plane of the imidazo[1,5-*a*]pyridine moiety by 55.8(2)° and 57.3(2)° in the two molecules of ligand. In Figure 3.22, a hydrogen bond (dashed line) between the

hydroxyl group of ligand L^{OH} and a water molecule is highlighted, the O-H···O distance being 2.658(7) Å with an O-H···O angle of 177.5°.

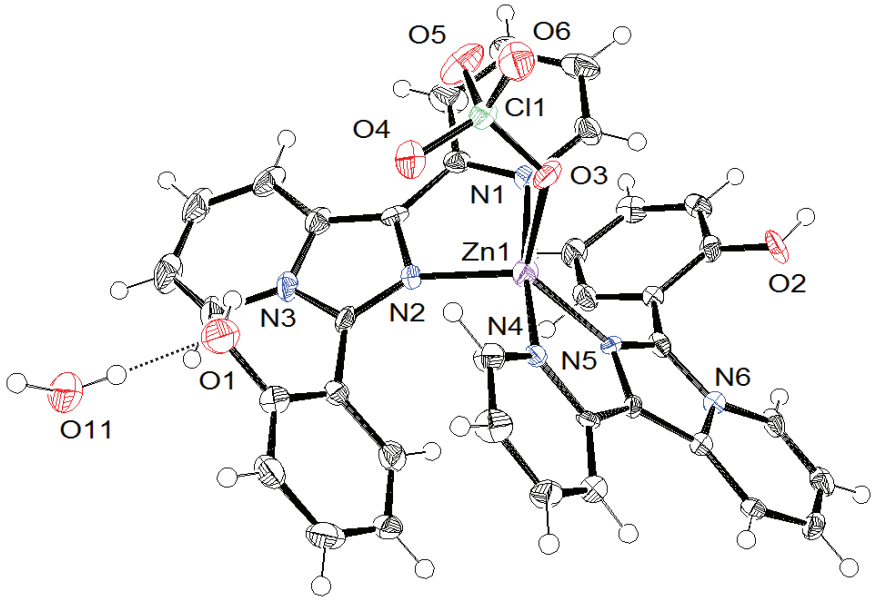

Figure 3.22 ORTEP representation of $[Zn(L^{OH})_2](ClO_4)_2 \cdot H_2O$ (**10**) at 50% probability level (uncoordinated ClO_4^- anion omitted for clarity). Selected bond lengths (Å) and angles (º): Zn(1)-N(1) 2.097(5), Zn(1)-N(2) 2.024(5), Zn(1)-N(4) 2.070(5), Zn(1)-N(5) 2.049(4); Zn(1)-O(3) 2.229(4), N(1)-Zn(1)-N(4) 168.3(2), N(5)-Zn(1)-O(3) 124.7(2), N(2)-Zn(1)-N(5) 122.0(2), N(2)-Zn(1)-O(3) 113.2(2), N(5)-Zn(1)-N(1) 102.2(2), N(4)-Zn(1)-O(3) 85.4(2), N(1)-Zn(1)-O(3) 83.5(2), N(4)-Zn(1)-N(5) 80.9(2), N(1)-C(5)-C(6)-N(2) 2.4(7), N(4)-C(23)-C(24)-N(5) 11.1(7).

Also in the case of the tetrafluoborate derivative $[Zn(L^{OH})_2](BF_4)_2 \cdot 4H_2O$ (**12**) it was possible to perform an X-ray structural investigation. Unfortunately, all attempts to grow single crystals of **12** in non coordinating solvents failed, and single crystals suitable for X-ray analysis were only obtained by the slow diffusion of diethylether into an acetonitrile solution of $[Zn(L^{OH})_2](BF_4)_2 \cdot 4H_2O$. Therefore solvent molecules replaced the coordinated water molecules from compound $[Zn(L^{OH})_2](BF_4)_2 \cdot 4H_2O$ (**12**) (Figure 3.23), thus the species structurally characterised can be formulated as $[Zn(L^{OH})_2(CH_3CN)_2](BF_4)_2$ (**12b**).

As expected, in this complex the two molecules of ligand L^{OH} are *N*,*N*-coordinated to the metal center (Figure 3.24), with Zn-N distances measuring respectively 2.128(3) Å (Zn(1)-N(1)) and 2.169(3) Å (Zn(1)-N(2)). The octahedral environment around the metal ion is then filled by the abovementioned acetonitrile molecules (d_{Zn-N} = 2.185(3) Å). The structure is stabilised by the presence of H-bonding interactions between one fluorine atom of a BF_4^- and the hydroxo substituent on ligand L^{OH} ($d_{F\cdots O}$ = 2.687(5) Å).

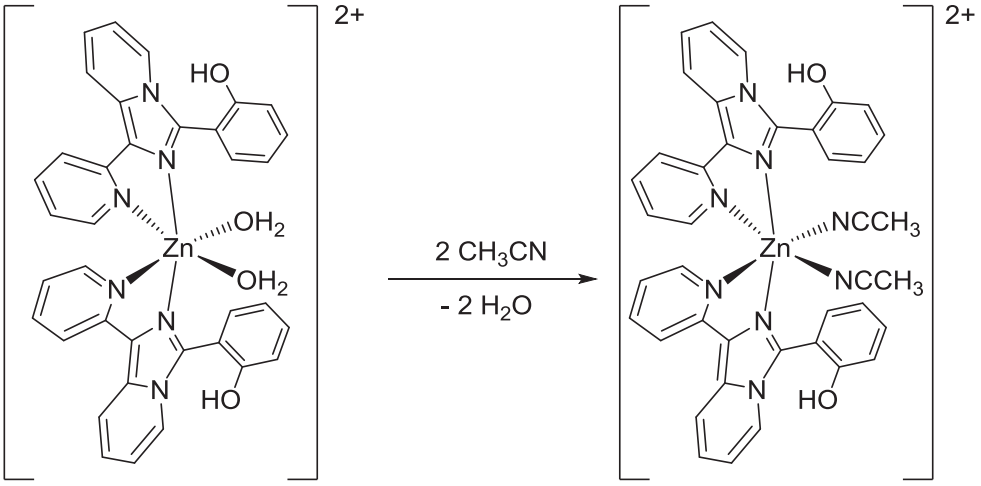

12 **12b**

Figure 3.23 Replacement of water molecules in **12** to give **12b**.

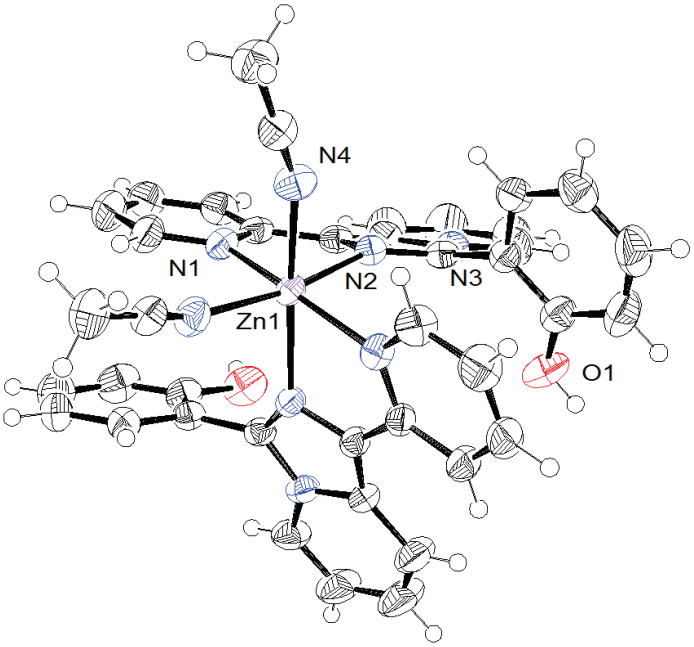

Figure 3.24 ORTEP representation of complex $[Zn(L^{OH})_2(CH_3CN)_2](BF_4)_2$ (**12b**) at 50% probability level (BF_4^- anions omitted for clarity). Selected bond lengths (Å) and angles (º): Zn(1)-N(1) 2.128(3), Zn(1)-N(2) 2.169(3), Zn(1)-N(4) 2.185(3), N(1)-Zn(1)-N(2) 76.8(1), N(1)-Zn(1)-N(1)' 166.1(2), N(1)-Zn(1)-N(4) 95.1(1), N(2)-Zn(1)-N(4) 94.2(1), N(1)-C(5)-C(11)-N(4) 8.7(5).

For complexes **10** and **12b** detailed X-ray structural parameters are reported in Section 6.18

3.2 PHOTOPHYSICAL PROPERTIES OF $[Zn(L^R)X_2]$ COMPLEXES

In Figure 3.25 are reported the UV-vis spectra of L^{Me}, $[Zn(L^{Me})Cl_2]$ (**4**), and ligand L^{OH}, $[Zn(L^{OH})Cl_2]$ (**7**) recorded as $1 \cdot 10^{-5}$ M solution in CH_2Cl_2. A shoulder appears at about 310-330 nm in the spectra of the complexes, clearly related to the presence of ligands L^{Me} and L^{OH}, respectively. In order to have a better insight about the transitions attributable to the complexes, the UV spectra of the corresponding ligands were subtracted[60] from the experimental UV spectra of species **4** and **7**, hence giving a clear visualization of the spectra of the complexes (solid lines in Figure 3.25).

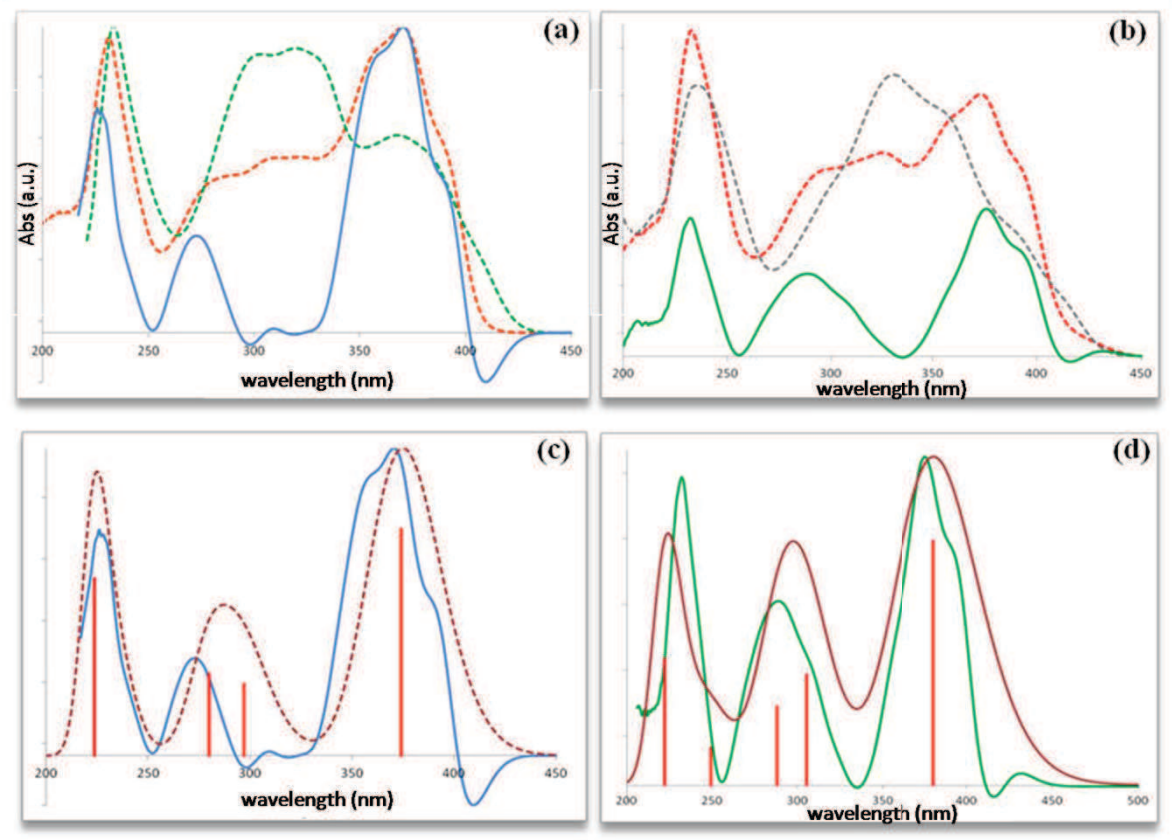

Figure 3.25 Top left: UV-vis spectra for L^{Me} (dashed green), $[Zn(L^{Me})Cl_2]$ (dashed orange) and their difference (solid blue line); top right: UV-vis spectra for L^{OH} (dashed grey), $[Zn(L^{OH})Cl_2]$ (dashed red) and their difference (solid green line); bottom left: Subtracted (solid blue) and calculated (dashed brown) UV-vis spectra for $[Zn(L^{Me})Cl_2]$ (oscillator strength > 0.1 are shown as straight red lines); bottom right: Subtracted (solid green) and calculated (dashed brown) UV-vis spectra for $[Zn(L^{OH})Cl_2]$ (oscillator strength > 0.1 are shown as straight red lines). All samples were measured as $1 \cdot 10^{-5}$ M solution in CH_2Cl_2.

For complexes **4-7** three bands were found around 370, 270 and 230 nm respectively, the band at lower energy (defining the absorption maximum) shows a marked vibrational

pattern with an energy separation of about 1260 cm^{-1} between the main subpeaks. Similar absorption (but without vibronic transitions) were found in the free ligand L^{Me}, where the intensity of the first two bands was reversed with respect to those of the complexes.

Taking complex **4** as a prototypal of the **4-6** species, TD-DFT calculations were performed (CH_2Cl_2 solvent) revealing four principal transitions (Osc. Strength > 0.10) (Table 3.2). The singlet at lower energy derives from a quite 'pure' HOMO / LUMO transition for both complex **4** and free ligand L^{Me}. Also states S3, S4 for complex **4** and states S2, S3, S4 for ligand L^{Me} are derived by pure transition starting from the HOMO orbital and ending in the LUMO, LUMO +1, +2 or +3, respectively. On the contrary the S17 transition (related to the intense higher energy band in the UV spectrum) is mixed, having various components the most significant of which is the HOMO-8 → LUMO in complex **4** (Table 3.2).

#	Energy (cm^{-1})	Wavelength (nm)	f	Composition (%)
		Ligand L^{Me}		
1	25426.3	393 (ε = 46255 $dm^3mol^{-1}cm^{-1}$)	0.577	H → L (98%)
2	29387.5	340	0.410	H → L+1 (99%)
3	30391.6	329	0.193	H → L+2 (96%)
4	33227.0	301	0.242	H → L+3 (96%)
5	43049.3	232	0.267	H-2 → L+1 (34%); H-5 → L (26%); H-1 → L+1 (14%); H-2 → L (8%)
		Ligand L^{OH}		
1	26555.2	377 (ε = 64835 $dm^3mol^{-1}cm^{-1}$)	0.616	H → L (98%)
2	20869.5	324	0.195	H → L+1 (91)
3	31779.3	315	0.319	H → L+2 (89%)
4	34011.8	294	0.235	H → L+3 (95%)
5	44435.0	225	0.166	H-3 → L (47%); H → L+9 (16%); H → L+10 (18%)
6	45557.7	220	0.166	H-2 → L+1 (19%); H-4 → L (35%); H-6 → L (14%)
		Complex **4**		
1	26711.7	374 (ε = 75000 $dm^3mol^{-1}cm^{-1}$)	0.738	H → L (99%)
3	33660.2	297	0.232	H → L+2 (93%)
4	35727.4	280	0.266	H → L+3 (98%)
5	44690.7	224	0.577	H-8 → L (64%); H-2 → L+2 (9%); H-2 → L+3 (6%)
		Complex **7**		
1	26267.2	381 (ε = 69620 $dm^3mol^{-1}cm^{-1}$)	0.744	H → L (99%)
3	32768.9	305	0.337	H → L+2 (90%); H-1 → L (4 %)
4	34739.3	288	0.241	H → L+3 (54%); H-1 → L (38 %); H → L+2 (6 %)
5	45023.8	222	0.387	H-8 → L (34 %); H → L+7 (26 %); H → L+6 (11 %)

Table 3.2 Relevant electronic transitions for L^{Me}, L^{OH} and complexes **4** and **7** (H: HOMO orbital, L: LUMO orbital; only electronic transitions with an oscillator strength value higher than 0.10 are reported).

The HOMO orbitals of the ligand and the complex have strictly related features. They consist of π orbitals localized on the pyridyl and imidazo-pyridine rings with only a very slight involvement of the tolyl group. Also, the LUMO orbitals (π symmetry) share identical features for the ligand and complex and are totally localized on the pyridyl and imidazo-pyridine skeletons without any contribution from the tolyl moiety. Figure 3.26 shows frontier molecular orbitals for L^{Me} and complex **4**. Complexes **5-9** show similar patterns, with all principal absorptions imputable to intra-ligand (π-π*) transitions. HOMO/LUMO energies show also similar values. The coordination to zinc causes a slight decrease in energy of both frontier orbitals but the ΔE separation remains more or less constant (about 4.1 eV).

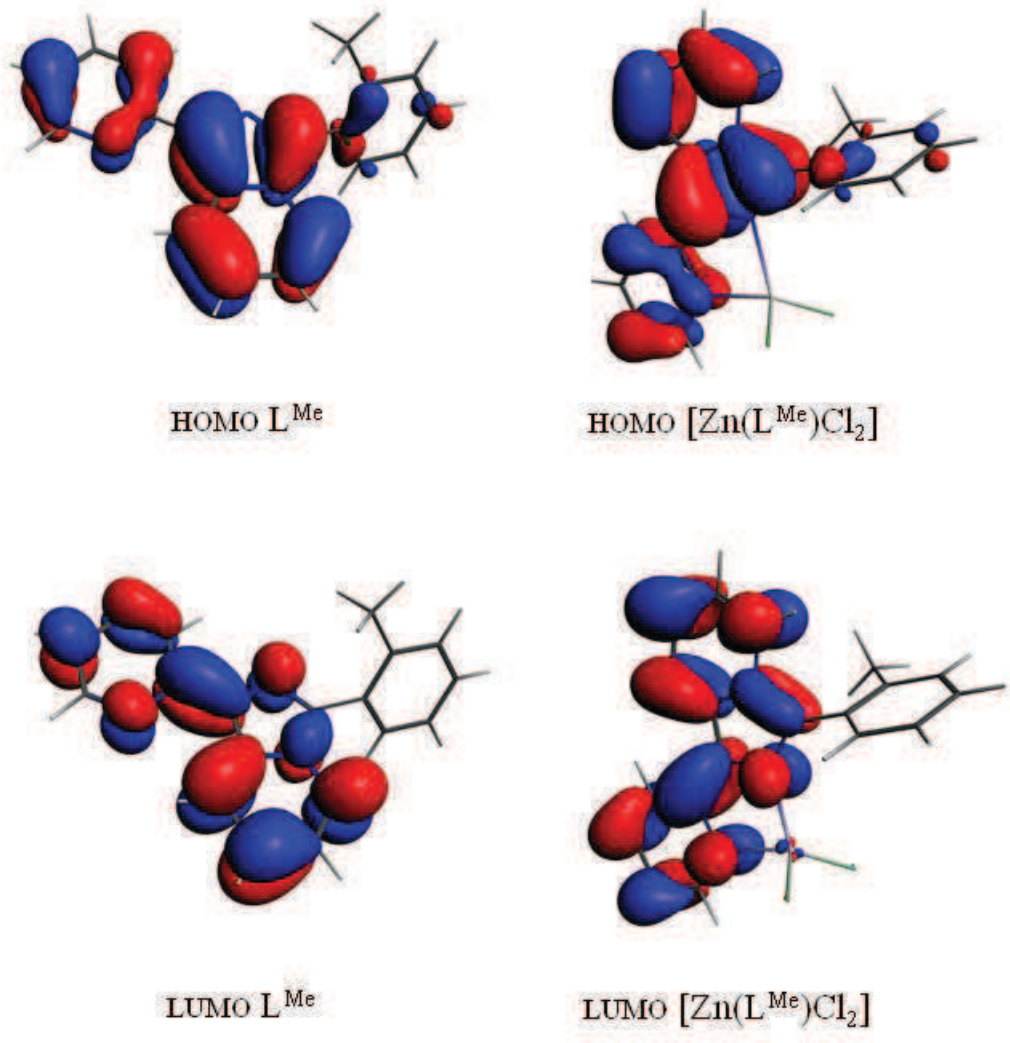

Figure 3.26 Frontier molecular orbitals for ligand L^{Me} and complex $[Zn(L^{Me})Cl_2]$ (**4**): (a) HOMO L^{Me}; (b) HOMO $[Zn(L^{Me})Cl_2]$; (c) LUMO L^{Me}; (d) LUMO $[Zn(L^{Me})Cl_2]$.

3.3 LUMINESCENT BEHAVIOUR OF Zn(II) COMPLEXES IN THE SOLID STATE

3.3.1 [Zn(L^R)X_2] DERIVATIVES

Due to partial dissociation of ligands L^R observed in solution, the luminescent properties of compounds **4-9** were only investigated in the solid state. The excitation and emission spectra of complexes **4-6** and **7-9**, and of the corresponding ligands measured on powder samples at ambient temperature show similar patterns. In particular, the ligands show a marked vibrational structure in their emission spectra, with subpeaks separation of about 1300 cm^{-1} (Figure 3.27). The vibrational structure is also evident in the emission spectra of complexes **4-6**, but it appears less pronounced in species **8-9**, and totally disappears with **7**.

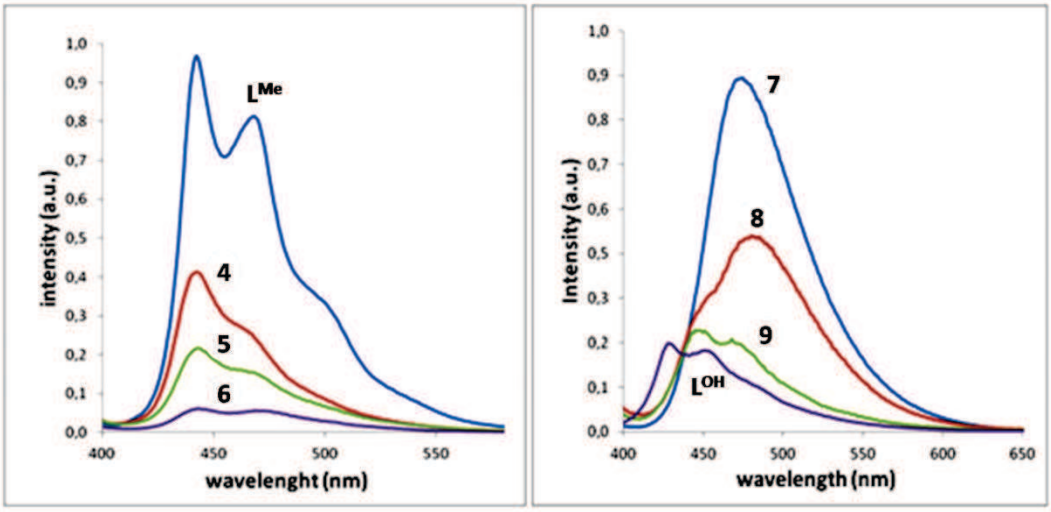

Figure 3.27 Emission spectra in the solid state of ligand L^{Me} and complexes **4-6** (left) and ligand L^{Me} and complexes **7-9** (right).

	λ_{exc} (nm)	λ_{max} (nm)	Φ_{PL}	
L^{Me}	418	442	0.66	(0.65)[a]
L^{OH}	400	452	0.15	(0.37)[a]
L^{OD}	400	430	0.38	
4	398	442	0.40	
5	413	443	0.21	
6	397	443	0.07	
7	419	482	0.29	
8	418	480	0.18	
9	423	444	0.10	

Table 3.3 Luminescent properties of the compounds [Zn(L^R)X_2], in the solid state.
[a]Absolute Φ_{PL} measured in solution (CH_2Cl_2, $1 \cdot 10^{-5}$ M).

The decrease of emission quantum yield moving from chloride to iodide in the two series of complexes **4-6** and **7-9** is likely a consequence of the increase in the atomic number of the halogen bound to the zinc center which causes a spin-orbit enhancement, which in turn favors intersystem-crossing. The effect of halide on fluorescence emission is nicely showed by plotting the quantum yields of complexes *vs*. the atomic mass of the halide ligands (Figure 3.28). A straight line with a high correlation coefficient is obtained for both series **4-6** and **7-9**.

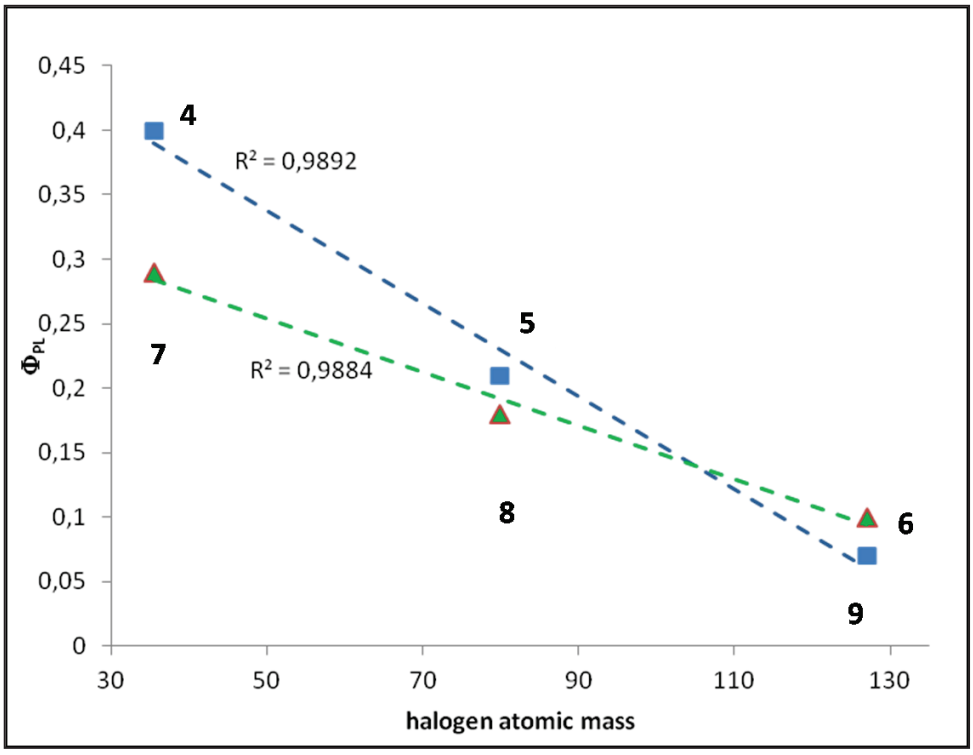

Figure 3.28 Absolute photoluminescent quantum yield (Φ_{PL}) of complexes **4-9** *vs*. atomic mass of the halides.

A similar correlation is evidenced by plotting the quantum yields *vs* the molecular mass of the complexes (Figure 3.29). In the last plot, it is also possible to introduce the free ligands, showing the clear discordance in behaviour of L^{OH} when compared to L^{Me}. Indeed, only the quantum yield of the free L^{Me} (blue square) aligns well with those of the corresponding complexes, while the Φ_{PL} value of the free L^{OH} (green triangle) does not follow this trend.

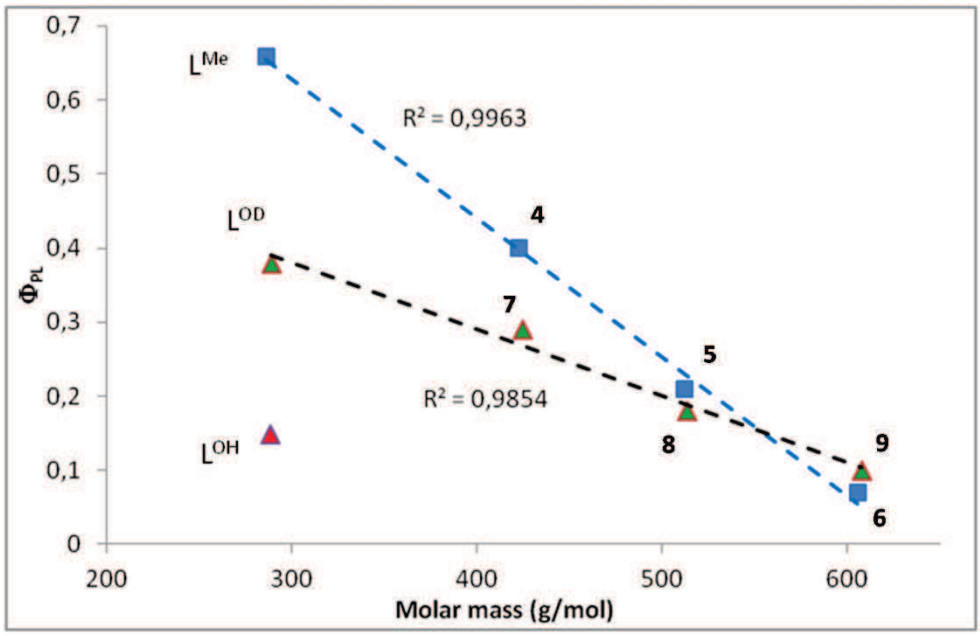

Figure 3.29 Absolute photoluminescent quantum yields (Φ_{PL}) *vs*. molar mass of ligands L^{Me}, L^{OH} and L^{OD} and complexes $[Zn(L^{Me})X_2]$ (**4-6**, blue squares) and $[Zn(L^{OH})X_2]$ (**7-9**, green triangles).

A possible interpretation of the different behavior of L^{Me} and L^{OH} can be found in the crystal structure of the two ligands. Actually, in a previous work[53], the X-ray crystal structure of both ligands L^{Me} and L^{OH} was investigated. In the solid state, L^{OH} can be described as a catemeric 1D network (Figure 3.30), whereas on the contrary L^{Me} shows discrete molecular assembly (Figure 3.31).

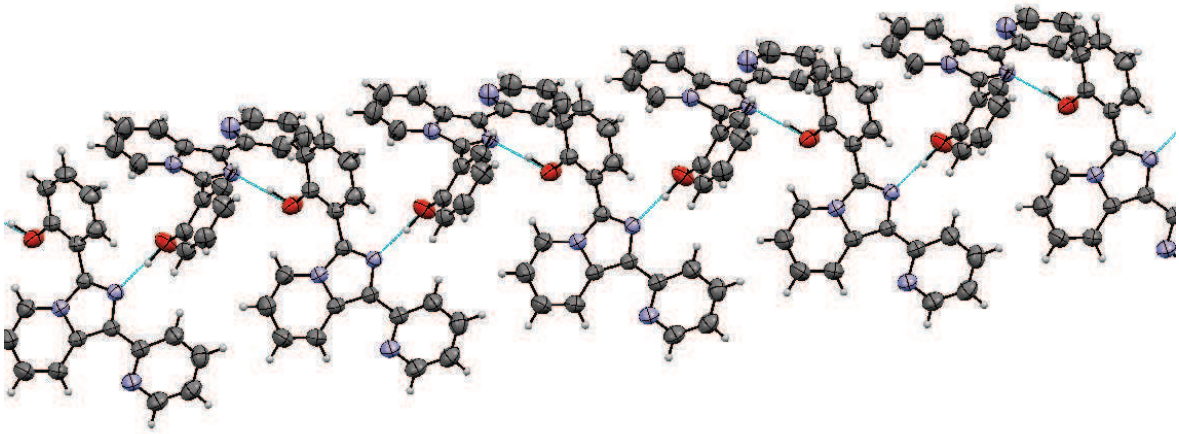

Figure 3.30 X-ray crystal structure of L^{OH} with O-H···N intermolecular H-bonds.

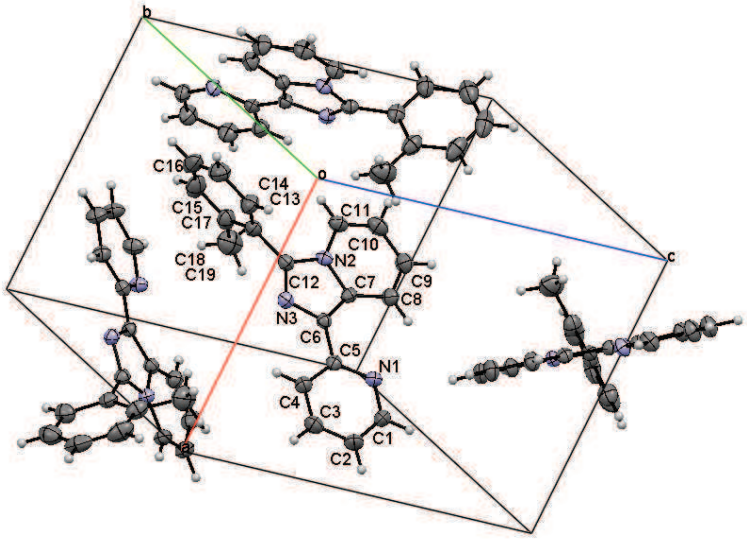

Figure 3.31 Unit cell in the X-ray crystal structure of L^{Me}.

It is possible that the large extent of H-bonds connectivity found in L^{OH} favours thermal relaxation causing a dramatic decrease of fluorescence emission of L^{OH} with respect to L^{Me}. In addition, when in solution (CH_2Cl_2, $1 \cdot 10^{-5}$ M), L^{OH} shows a remarkable increase in emission intensity, with a value of Φ_{PL} double with respect to the solid state (0.37 and 0.15 respectively, Table 3.3).

In a following experiment, the hydroxyl group of L^{OH} was deuterated by treating the ligand with D_2O, in acetone-d_6. Actually, it is known that high-frequency C-H stretching vibrations ($\nu \approx 3000$ cm^{-1}) contribute to non-radiative $S_1 \rightarrow S_0$ transition, and isotopic substitution leading to C-D bonds (having lower vibrational energy, $\nu \approx 2200$ cm^{-1}) often reduce the rate of non-radiative decay, hence increasing the quantum yield.[61] Also in this case, the deuterated (L^{OD}) species showed in the solid state a Φ_{PL} value definitely higher than L^{OH}. Moreover, when the Φ_{PL} value of L^{OD} is correlated to the molar mass (see green triangle in Figure 3.29), a good alignment with $[Zn(L^{OH})X_2]$ (**7-9**) complexes is noticed. The odd collocation of L^{OH} quantum yields with respect to its zinc(II) halide adducts has to be ascribed to the abovementioned intermolecular O-H···N interactions in the crystal structure, which result in a non radiative relaxation process. When L^{OH} is coordinated to zinc, the capability to give rise to H-bonds is hindered (see the absence of H-bonds in the infrared spectrum of **7**, Figure 3.32, which, on the contrary, are clearly visible in the

infrared spectrum of L^{OH}, Figure 3.31) and the spin-orbit coupling due to the heavy atom predominantly controls the relaxation processes.

A similar influence of H-bonds in tuning fluorescence emission was already reported for other zinc(II) compounds.[62]

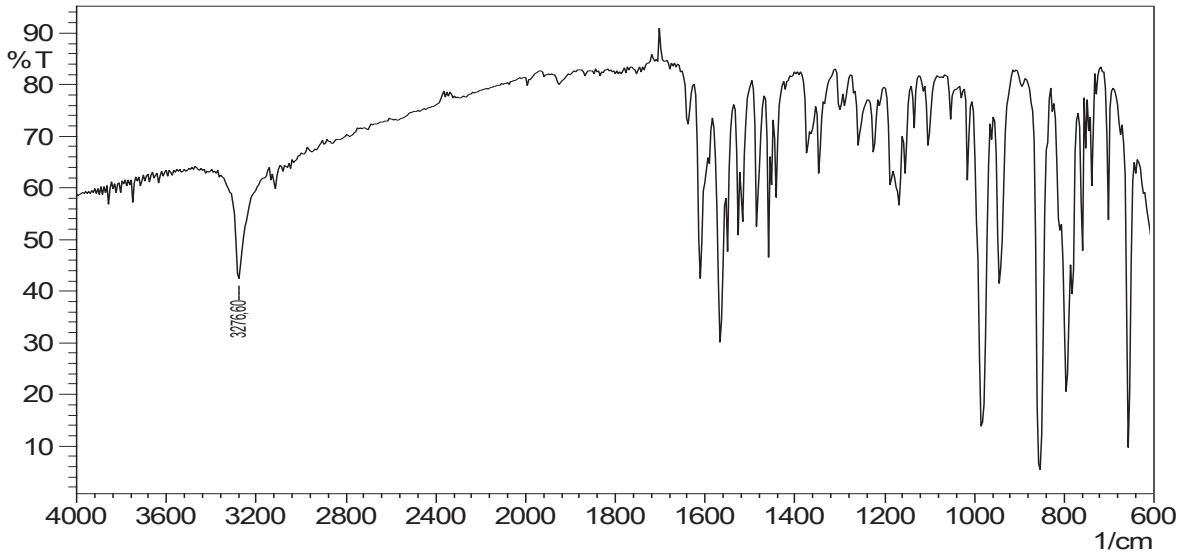

Figure 3.32 Infrared spectrum (hexachlorobutadiene) of $[Zn(L^{OH})Cl_2]$.

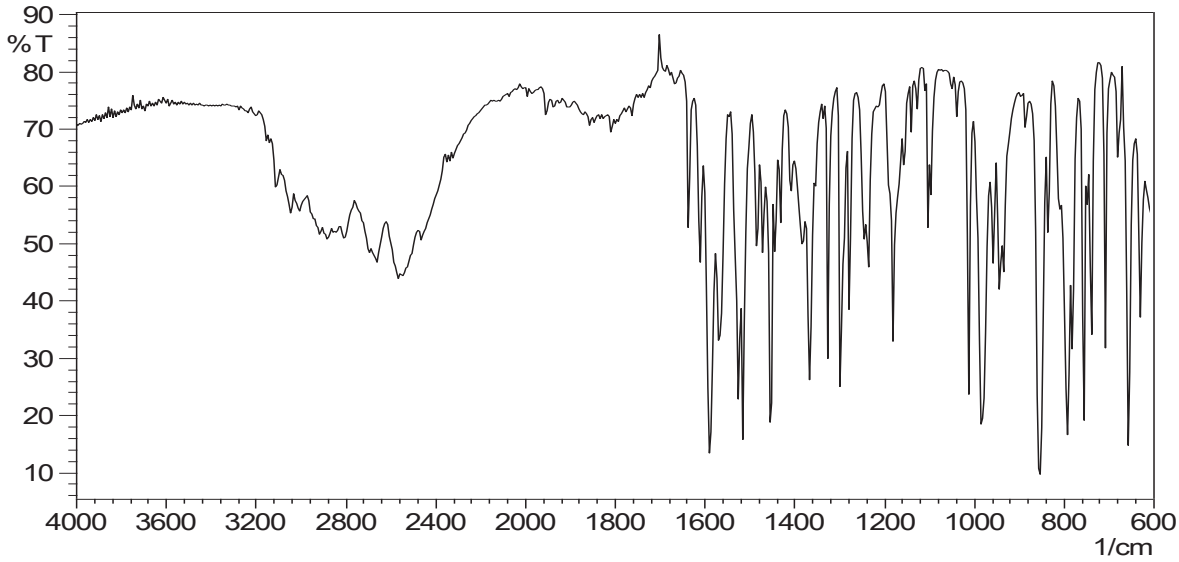

Figure 3.33 Infrared spectrum (hexachlorobutadiene) of L^{OH}.

3.3.2 $[Zn(L^{OH})_2](Y)_2 \cdot nH_2O$ DERIVATIVES

Again, due to the partial dissociation of ligand L^{OH} in solution as observed in the ^1H NMR spectra of $[Zn(L^{OH})_2](Y)_2$ derivatives, their luminescent properties were only investigated in the solid state. Preliminary data obtained for the complexes and for the free ligand L^{OH} are collected in Table 3.3, while their emission spectra are presented in Figure 3.34.

	Y	λ_{exc} (nm)	λ_{max} (nm)	Φ_{PL}
L^{OH}	-	402	452	0.15
7	ClO_4	452	493	0.14
8	NO_3	421	468	0.16
9	BF_4	451	491	0.09
10	PF_6	452	494	0.12
11	PO_2F_2	469	500	0.17

Table 3.4 Photoluminescent properties of compounds $[Zn(L^{OH})_2]Y_2 \cdot nH_2O$, in the solid state.

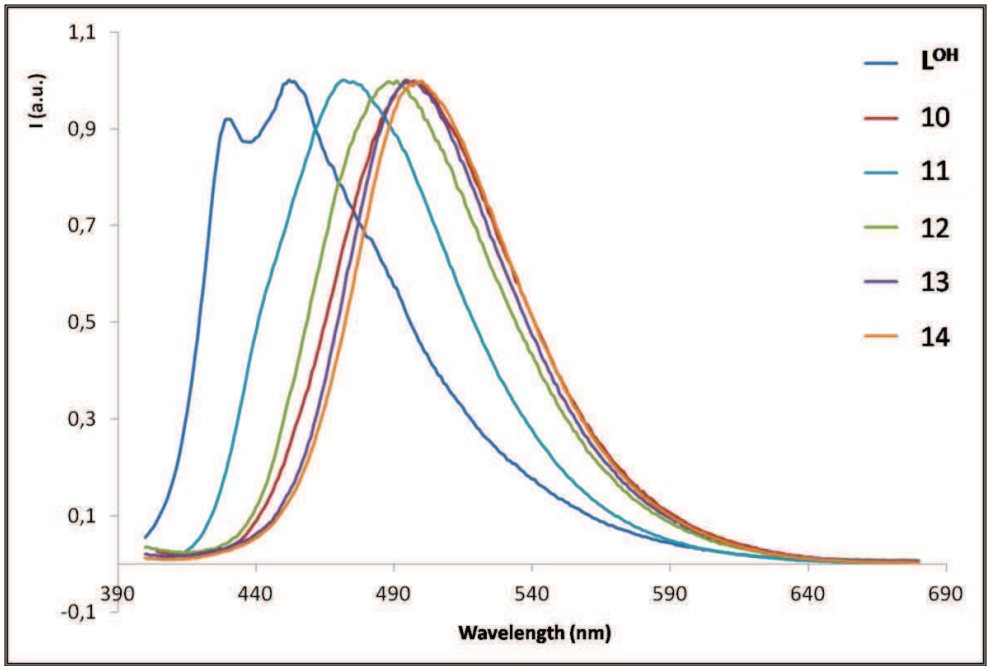

Figure 3.34 Normalized emission spectra of ligand L^{OH} and of complexes **10-14**, recorded in the solid state.

In the solid state, all complexes show similar emission profiles, positioned in the blue-green region (468-500 nm). The emission maxima of compounds **10**, **12**, **13** and **14** are red shifted of about 40-48 nm with respect to free L^{OH}, while a different behaviour is noticed for compound $[Zn(L^{OH})_2](NO_3)_2 \cdot H_2O$ (**11**), displaying a remarkably minor bathochromic

shift (16 nm). This is somehow also reflected by the excitation spectra of the complexes (Figure 3.35), where the trace associated to the nitrato-derivative is clearly characterised by a diverse shape and maximum peak (λ_{exc} = 421 nm) compared to derivatives **10**, **12**, **13** and **14** (all showing a λ_{exc} in the region 451-469 nm).

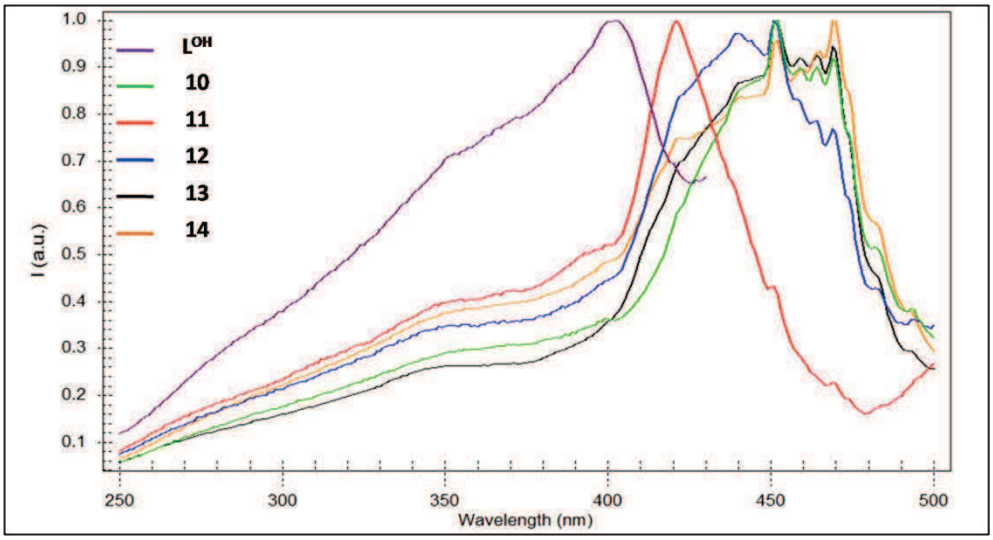

Figure 3.35 Normalized excitation spectra of ligand L^{OH} and of complexes **10-14**, recorded in the solid state.

When measured as powder samples, complexes **10**-**14** exhibited moderate absolute photoluminescence quantum yields (Φ_{PL}), with experimental values comprised between 0.09 and 0.16 (Table 3.4), slightly lower than those found for the previously described $[Zn(L^{OH})X_2]$ species. At first, this was associated to the presence of water molecules in the molecular structure of the complexes (as detected by TGA and X-ray analysis), which could in principle increase thermal non-radiative decays, leading to a reduced emission intensity. Thus, an additional experiment was conducted: complex $[Zn(L^{OH})_2](ClO_4)_2 \cdot H_2O$ (**10**) was cautiously oven-dried overnight at 120°C to remove water from the lattice. A yellow crystalline compound was obtained, later formulated as $[Zn(L^{OH})_2](ClO_4)_2$ (**10b**) according to elemental analysis and spectroscopic evidences. The absolute quantum yield of this de-hydrated species **10b** was measured, giving an experimental value of 0.11, very close to that found for its hydrated counterpart $[Zn(L^{OH})_2](ClO_4)_2 \cdot H_2O$ (**10**) (0.14, entry 2 in Table 3.4). Then, a direct relation between the presence of water molecules in complexes **10**-**14** and their moderate Φ_{PL} was excluded. Further detailed studies on these compounds are ongoing with the aim of clarifying this point.

Chapter 4

Heteroleptic Complexes of Cu(I) and Ag(I)

Extensive efforts have been focused on N-heterocyclic-containing Cu(I) and Ag(I) complexes for replacing luminescent transition metals compounds based on ruthenium or other noble metals in chemical sensors,[63] probes of biological systems,[64] and energy-conversion devices[65] due to their advantages such as having abundant resources, low cost and non toxic properties.

It is reported that a rigid metal-chelating ligand bond, a high ligand field strength, and low oxidation states of the central metal ion, all play crucial roles in facilitating MLCT contributions in the emissive states.[66]

As already mentioned in Chapter 2, over the past decade, increasing attention has been paid to luminescent Cu(I) complexes based on both (N,N) and (P,P) ligands. Compared to "classical" $[Cu(NN)_2]^+$ systems, mixed ligand compounds involving bulky phosphines exhibit improved emission properties, because the steric and the π-acidic characteristic inhibit the excited-state distortion as well as enhance the energy level of the excited states by stabilising the Cu(I) species.[67] In 2002 McMillin and co-workers reported the first example of a highly emissive mononuclear cuprous complex, $[Cu(dbp)(POP)]^+$ (dbp = 2,9-di-n-butyl-1,10-phenanthroline and POP = bis(2-diphenylphosphino)phenyl)ether), with a good quantum efficiency of 0.16 in dichloromethane solution and 0.69 in a polymethyl metacrylate film.[68] This key finding has inspired significant research activities, in fact in recent years numerous examples of heteroleptic Cu(I) complexes have been reported and their emission properties deeply investigated.[69]

The interesting properties above illustrated, stimulated a parallel study aimed at the investigation of another class of emissive d^{10} metal complexes based on another metal of group 11: Ag(I). To the best of our knowledge only few examples of analogous silver(I) mixed ligands derivatives have been effectively investigated so far.[20] Ag(I) has revealed to be a favourable and fashionable ion for this aim because of its coordination diversity and flexibility as well as its positive coordination tendency with various donor atoms.[70] In 1977 silver containing systems have been the subject of studies from a structural point of view: Stein and Knobler reported the synthesis and a deep structural investigation of a 1:1 complex of silver nitrate and triphenylphosphine, formulated as $[Ag(PPh_3)(NO_3)]_n$.[71] In this compound silver is coordinated to three nitrate oxygen atoms, two from one nitrate group and one from another nitrate group, and to phosphorous. Furthermore, in solution it undergoes anion exchange with halides and sodium azide.

Progressively, the chemistry of Ag(I) phosphines compounds revealed to be complex and multifaceted because of variable geometries for the d^{10} Ag(I) ion, its kinetic lability and the ease for disproportionation, polimerisation and ligand scrambling reactions; in fact most of the isolated Ag(I) phosphines complexes revealed to be susceptible to decomposition, particularly the trigonal ones.[72] Hor reported the isolation of some stable mixed ligand Ag(I) species passing through the substitution reaction of $[Ag(PPh)_3(NO_3)]_n$ with diimine ligands.[73] In his work he illustrated that the displacement of the nitrate group with chelating diimines occur easily because of the lability of the coordinating anion (Figure 4.1); the obtained trigonal complexes (Figure 4.2) showed good stability when isolated and stocked away from light.

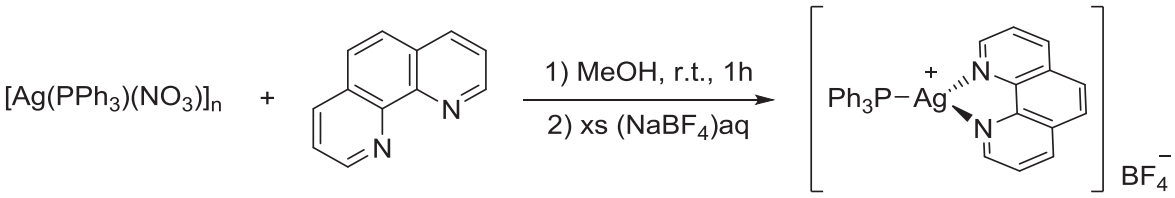

Figure 4.1 Procedure of substitution reaction of $[Ag(PPh_3)(NO_3)]_n$ with 1,10-phenantroline for the preparation of trigonal complex $[Ag(PPh_3)(phen)]BF_4$. Preparation of the other analogous derivatives follows a similar procedure.

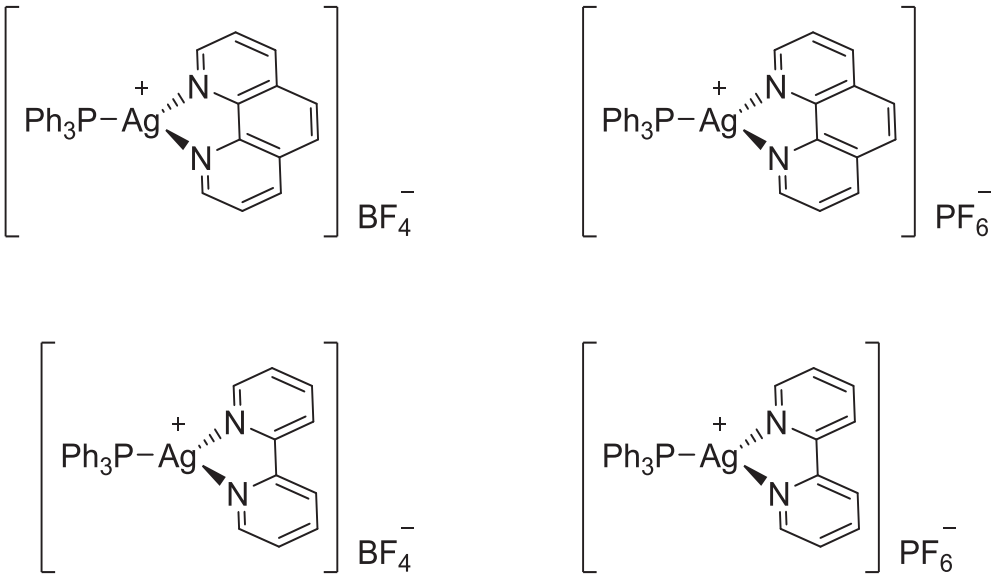

Figure 4.2 List of the trigonal $[Ag(PPh_3)(NN)]^+$ derivatives obtained starting from $[Ag(PPh_3)(NO_3)]_n$ and chelating diimines as precursors.

Subsequently it has been reported the synthesis and the structural characterisation of the bisphosphine derivative $[Ag(phen)(PPh_3)_2]^+[X]^-$ using a functionalized acylpyrazolonate anion;[74] in addition, more recently, Nierengarten *et al.* described the synthesis of new silver heteroleptic complexes incorporating both phenanthroline and PP ligands.[75] Varying the length of the spacer in the PP derivatives and the degree of steric hindrance of the phenanthroline ligand allowed to understand their structural effects on the resulting compounds; furthermore NMR studies has been useful to clarify the behaviour of the different complexes in solution.

Although the above mentioned complexes have been fully characterised from a structural point of view and their behaviour in solution has been deeply clarified, we noted that the optical properties of this derivatives has been moved to the background so far. We thus became interested in a deeper understanding of the photophysical performances of copper(I) and silver(I) compounds and possibly in tuning the colour of the emission by systematical variation of the ligand system. The work presented in this chapter concerns the preparation and the characterisation of different heteroleptic Cu(I) and Ag(I) complexes coordinated with different phosphorous ligands and 2-(1-(pyridin-2-yl)imidazo[1,5-a]pyridin-3-yl)phenol (L^{OH}) as chelating aza-bidentate ligand. Furthermore, photophysical properties of this compounds has been systematically investigated in order to rationalise the emission properties depending on the different electronical features and steric demanding of the phosphorous ligands. As far as concern complexes, three different classes have been achieved: synthesis of $[Cu(L^{OH})_2(BF_4)]$ and derivatives and synthesis of $[Ag(L^{OH})(L^{O})]$ (L^{O} = 2-(1-(pyridin-2-yl)imidazo[1,5-a]pyridin-3-yl)phenolate) and derivatives have been carried out in parallel; subsequently the attention has been focused on another series having the general formula $[Ag(L^{OH})(P)](NO_3)$, where P represents a monodentate phosphorous ligand.

4.1 SYNTHESIS AND CHARACTERISATION OF $[Ag(L^{OH})(L^{O})]$ AND $[Cu(L^{OH})_2(BF_4)]$

Ligand L^{OH} was prepared as shown in Chapter 3 and its purity was assessed by ^{1}H, ^{13}C NMR (chloroform-*d*, 25°C) and elemental analysis.

The reaction scheme in Figure 4.3 shows that the silver precursor has been obtained by reaction of the ligand with $Ag(NO_3)$ in 2:1 molar ratio to the metal in acetonitrile, in the presence of an excess of triethylamine.

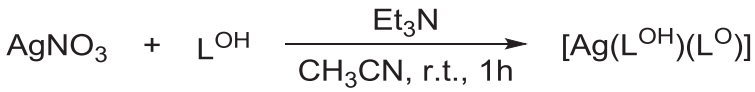

Figure 4.3 Reaction scheme for the synthesis of the precursor $[Ag(L^{OH})(L^{O})]$ (**15**).

The resulting complex is a lemon-green crystalline powder and it has been characterised by elemental analysis, infrared spectroscopy and ^{1}H NMR.

Evidence of the displacement of the nitrate anion with the ligand anion can be confirmed by the infrared spectrum (nujol mull) shown in Figure 4.4; in fact the strong broad band in the region 1410 - 1350 cm^{-1} due to the asymmetric NO_3^- stretching cannot be observed. In addition the species shows the typical pattern of the ligand, with sharp and intense stretching bands in the region 1510 - 1600 cm^{-1} and an additional band of medium intensity around 1630 cm^{-1} attributable to C=N stretching.

Complexation of silver with the ligand can be confirmed by ^{1}H NMR analysis; as can be seen in Figure 4.5, the spectrum obtained in dichloromethane-d_2 exhibits signals that can be attributed to the ligand slightly shifted if compared to the free ligand.

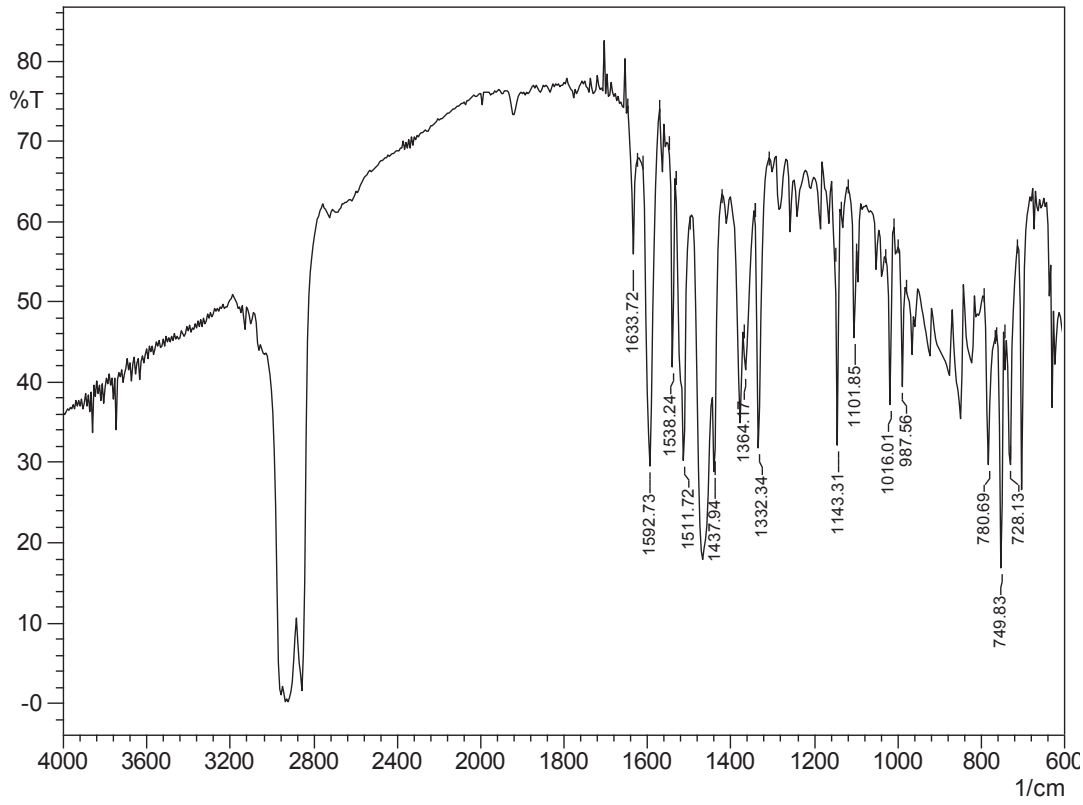

Figure 4.4 IR spectrum (nujol mull) of [Ag(L^{OH})(L^{O})] (**15**).

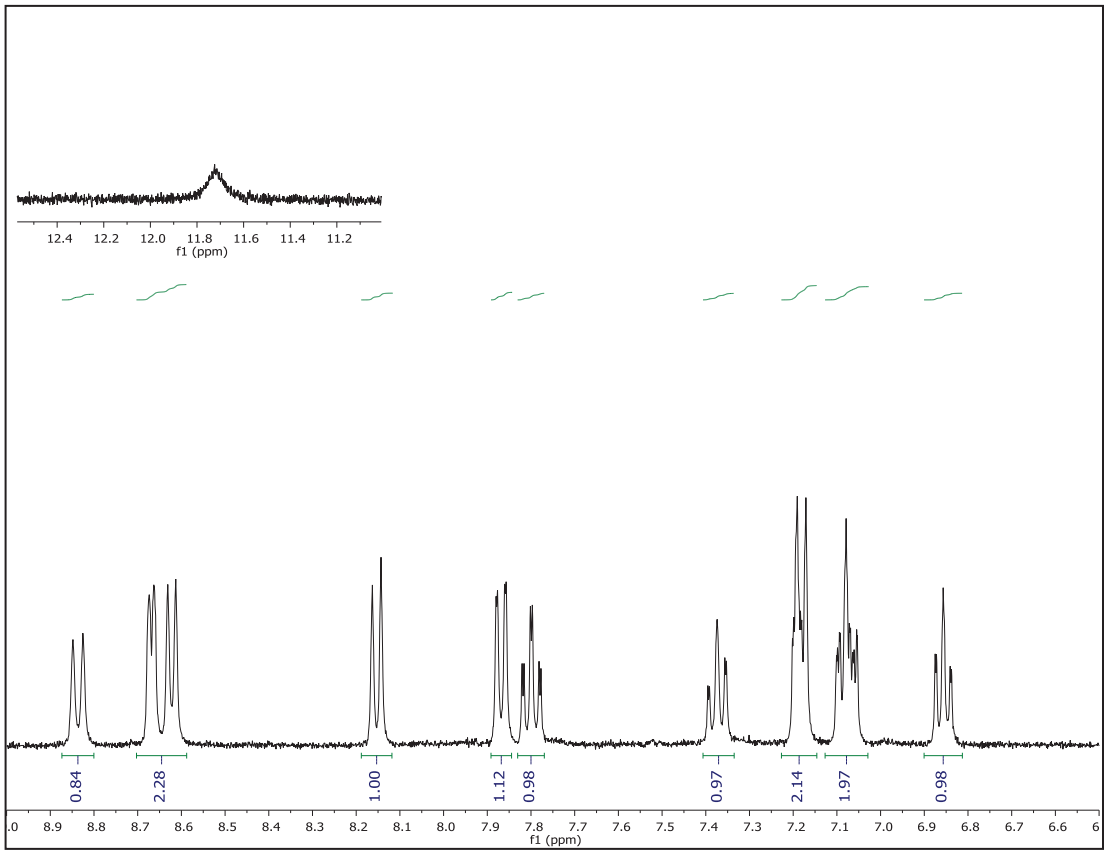

Figure 4.5 ^{1}H NMR spectrum (dichloromethane-d_2, 25°C) of [Ag(L^{OH})(L^{O})] (**15**).

As regards the copper species, $[Cu(CH_3CN)_4]BF_4$ was used ad starting material, which was reacted with L^{OH} in the presence of a base. In this case displacement of the anion has revealed to be a complex aspect. After various attempts, neither changing reaction conditions nor using stronger bases, allowed us to afford the expected complex and the isolated species was then formulated $[Cu(L^{OH})_2(BF_4)]$ (**16**), easily obtained with the methodology illustrated in Figure 4.6.

$$[Cu(CH_3CN)_4]BF_4 \quad + \quad 2\,L^{OH} \xrightarrow[CH_3CN,\ r.t.,\ 1h]{} [Cu(L^{OH})_2]BF_4$$

Figure 4.6 Reaction scheme for the synthesis of precursor $[Cu(L^{OH})_2]BF_4$ (**16**).

The product is an orange-rust crystalline powder and has been characterised via elemental analysis and infrared spectroscopy; ^1H NMR characterisation, instead, has not been possible because of solubility difficulties.

In Figure 4.7 is reported the infrared spectrum of compound **16** which, as expected, reveals the presence of tetrafluoborate anion broad bands around 979, 1049 and 1116 cm^{-1}, as well as the typical ligand pattern at 1513, 1545, 1595 and 1636 cm^{-1}.

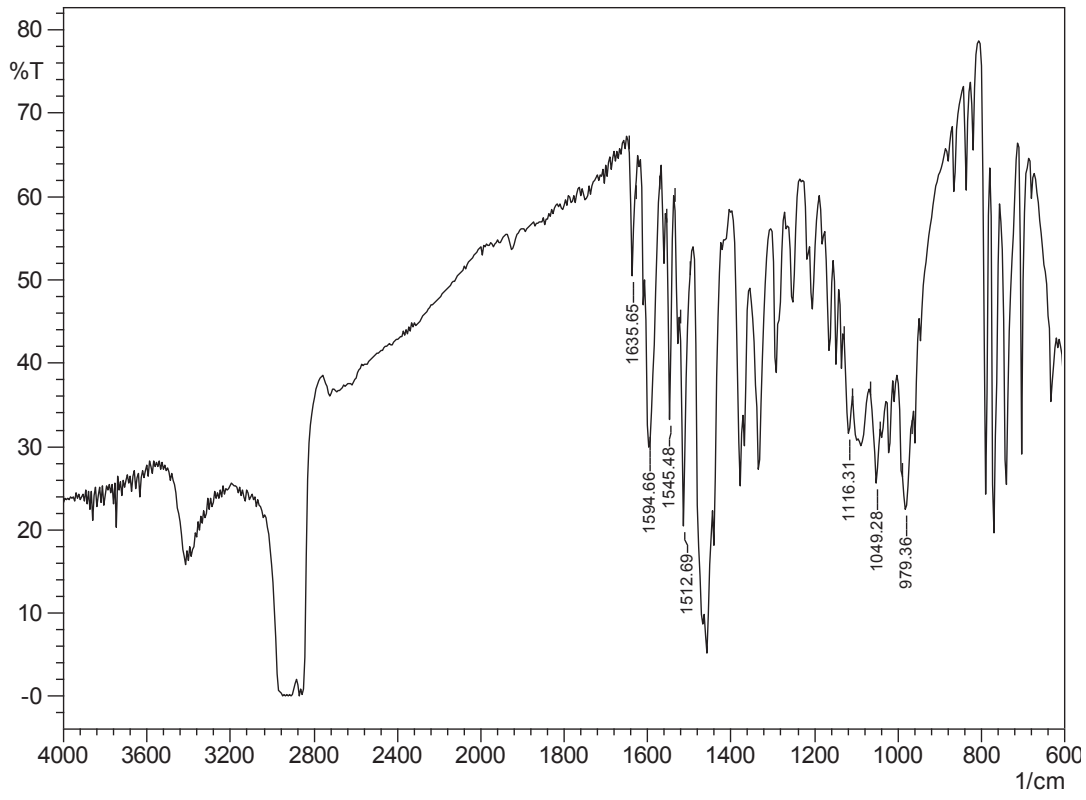

Figure 4.7 IR spectrum (nujol mull) of $[Cu(L^{OH})_2(BF_4)]$ (**16**).

It is noteworthy that this copper precursor does not exhibit luminescence, nevertheless we kept on with the course of this parallel research with copper and silver. The following step was trying to introduce phosphorous ligands on the metal centres in order to achieve complexes with good and tunable emission of both classes of derivatives.

The followed procedure is the same both for copper and for silver compounds and is illustrated in Figure 4.8 and 4.9:

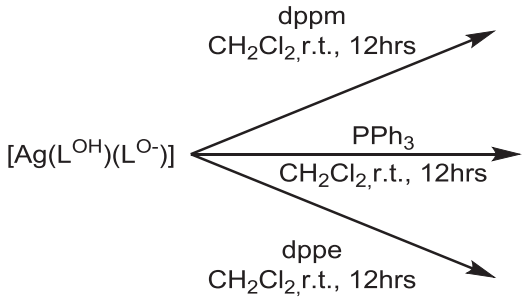

Figure 4.8 Substitution reactions with phosphines on Ag(I) precursor.

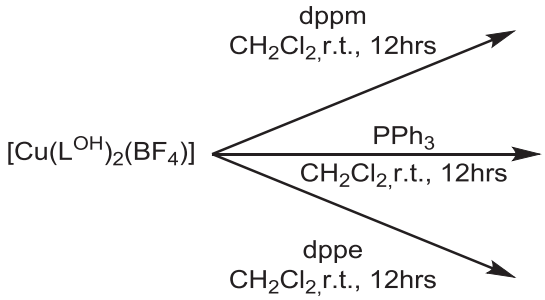

Figure 4.9 Substitution reactions with phosphines on Cu(I) precursor.

The reaction has been carried out in dichloromethane where, to a suspension of the precursor, an excess of phosphine (2.5:1) was added and the mixture was allowed to stir until it became a yellowish solution (it generally took about 12 hours). Final products were all isolated as yellow powders, but, even after different attempts of purification processes, it has not been possible to repeatedly confirm their purity by elemental analysis. Furthermore, the stoichiometry deduced from integrals in the ^{1}H NMR spectrum did not match with the one figured out from elemental analysis. This fact leads to the conclusion that probably there is no strict correspondence between species in the solid state and in solution. In addition to these complex aspects, Ag(I) complexes showed really weak emission, while Cu(I) derivatives did not emit at all. For that reason we decided to conduct the research work focusing the attention to another class of heteroleptic complexes.

4.2 [Ag(P)(L^{OH})](NO_3) DERIVATIVES

4.2.1 SYNTHESIS AND CHARACTERISATION

Since the aim of this part of the work was to deepen the study of heteroleptic complexes with the possibility of tuning luminescence emission, the attention has been focused on "simplified" systems based on Ag(I). We wondered whether the procedure illustrated in 1988 by Hor and developed by Nierengarten *et al.* could lead to emitting and tunable silver(I) derivatives so, instead of isolating a precursor coordinating two L^{OH} ligands, using one of them as anion and then introducing mono- and bidentate phosphines, we directed our interest toward "simpler" trigonal heteroleptic $[Ag(NN)(P)]^+$ complexes, achievable from direct reaction without isolation of intermediate and bearing only monodentate phosphorous ligands.

The first complex of this class has been prepared using PPh_3 as P-donor, following the procedure reported in Figure 4.10:

$$AgNO_3 + PPh_3 \xrightarrow[\text{r.t., 1h}]{CH_2Cl_2/MeOH} \{[Ag(PPh_3)NO_3]_n\} \xrightarrow[\text{r.t., 1h}]{L^{OH}} [Ag(PPh_3)(L^{OH})](NO_3)$$

Figure 4.10 Reaction scheme for the synthesis of compound $[Ag(PPh_3)(L^{OH})](NO_3)$.

This is a slightly modified procedure compared to the one reported by Nierengarten *et al.*:[75] in the paper they synthesise new silver heteroleptic complexes starting from an equimolar mixture of $AgBF_4$, PP ligand, and 1,10-phenanthroline (phen), and the mononuclear tetrahedral complex $[Ag(PP)(phen)]^+$ has been obtained as tetrafluoroborate salt in our case. To achieve the trigonal silver(I) compound, an equimolar solution of triphenylphosphine and $AgNO_3$ was allowed to stir for one hour in CH_2Cl_2/MeOH (5:1), then L^{OH} was added and the complex $[Ag(PPh_3)(L^{OH})](NO_3)$ (**17**) has been obtained as nitrate salt. The presence of a polymeric intermediate by reaction with PPh_3 is supposed according to the structural studies reported by Stein and Kobler.[71]
The final compound has been characterised by elemental analysis, infrared spectroscopy, ^1H NMR and $^{31}P\{^1H\}$ NMR spectroscopy.

In its infrared spectrum registered by ATR-IR technique (Figure 4.11), together with the expected broad band at about 1319 cm^{-1} due to the asymmetric stretching of NO_3^- anion, we can observe signals due to the presence of triphenylphosphine: a broad medium-weak absorption at 3054 cm^{-1}, which overlaps with signal of the hydroxide on the aromatic ring of L^{OH}, is attributable to C-H stretching of aromatic ring in phosphines while the sharp vibration at 1096 cm^{-1} is due to typical P-C stretching for P-Ph bonds. Furthermore additional bands at 1436, 1456, 1514 and 1595 cm^{-1} can be assigned to ligand adsorptions.

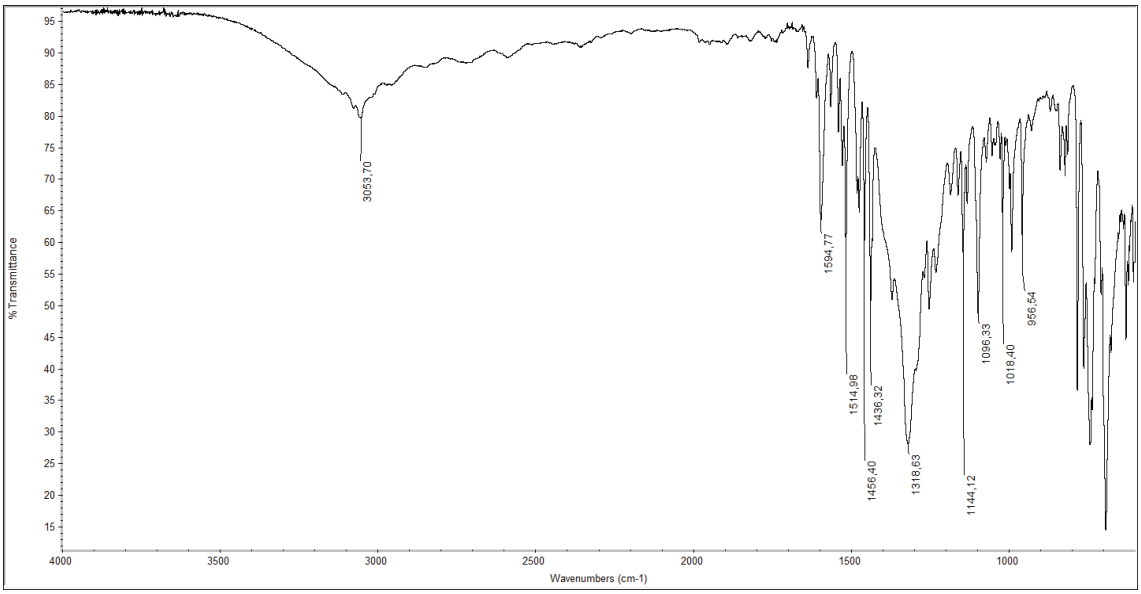

Figure 4.11 Infrared spectrum (ATR-IR technique) of $[Ag(PPh_3)(L^{OH})](NO_3)$ (**17**).

The presence of triphenylphosphine and L^{OH} is also proven by ^1H NMR data, as reported in Figure 4.12: as a consequence of coordination to the metal centre, both molecules shows different chemical shifts compared to those observable for free ligands. Moreover, integration of signals allow to establish the 1:1 ratio between the L^{OH} and PPh_3.

$^{31}P\{^1H\}$ NMR spectroscopy can be very useful to establish the structural assignment of the complex. The $^{31}P\{^1H\}$ NMR spectrum of $[Ag(PPh_3)(L^{OH})](NO_3)$ (**17**) at room temperature shows a single "doublet" centred at 17.68 ppm (Figure 4.13).

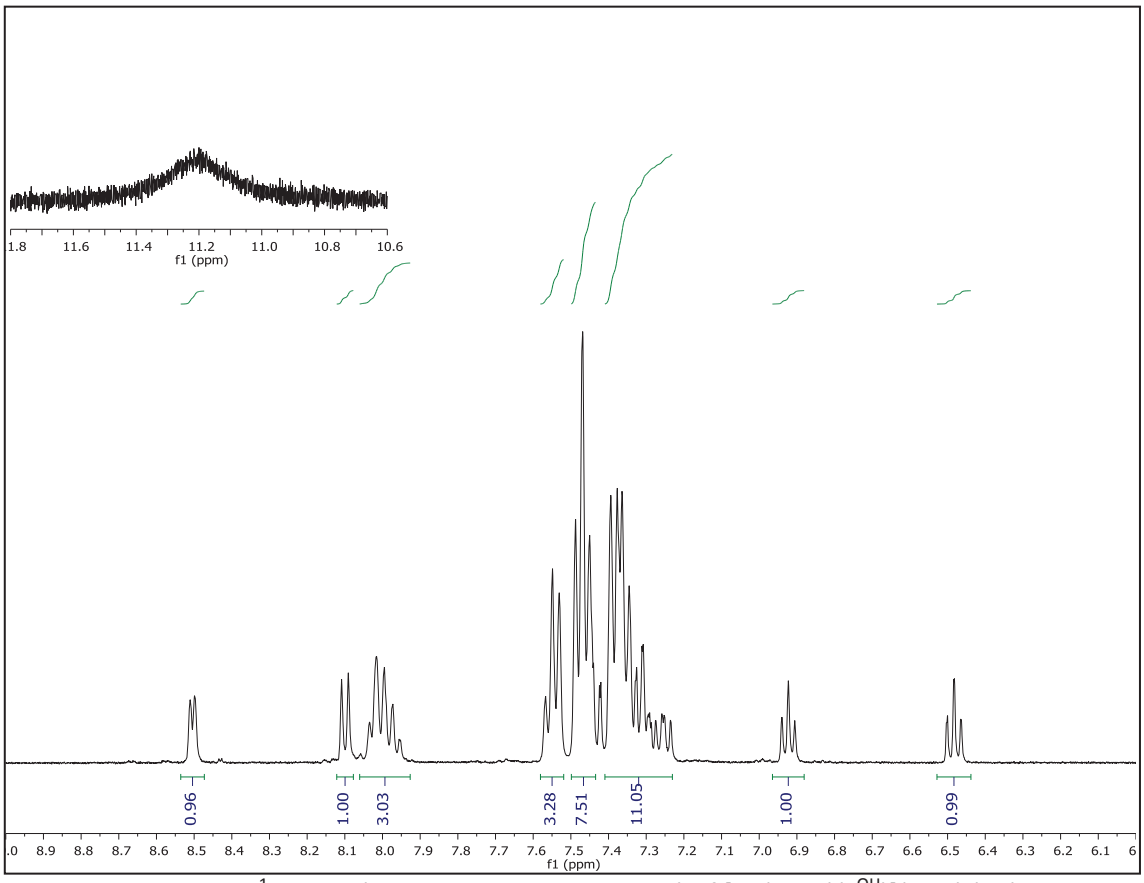

Figure 4.12 ^{1}H NMR (dichloromethane-d_2, 25°C) of [Ag(PPh$_3$)(L^{OH})](NO$_3$) (**17**).

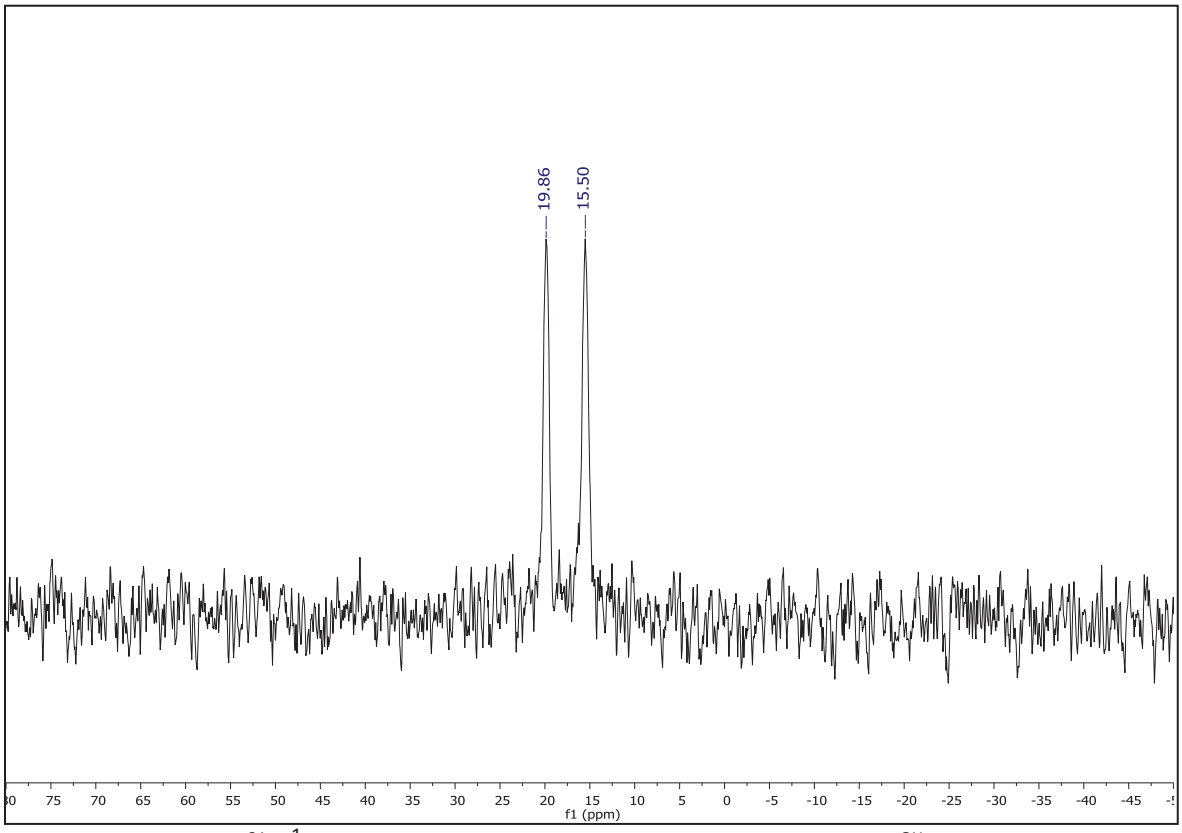

Figure 4.13 ^{31}P{^{1}H} NMR (dichloromethane-d_2, 25°C) of [Ag(PPh$_3$)(L^{OH})](NO$_3$) (**17**).

Due to (^{107}Ag, ^{109}Ag)-^{31}P coupling, ^{31}P{^{1}H} NMR spectra for silver(I) phosphines complexes are typically characterised by a diagnostic pair of doublets for each phosphorous environment. The high kinetic lability of monodentate phosphines leads to a rapid ligand exchange on the NMR time scale and low temperatures for resolution of the silver-phosphorous coupling is necessary.[76] In order to observe a perfect match between the expected signals and the experiment and to confirm the nature of the complex, a low temperature ^{31}P{^{1}H} NMR experiment has been carried out (Figure 4.14). In fact by lowering the temperature the signals broadens and, as expected, they split into two doublets at 243 K. Signals can be resolved with further lowering the temperature and the splitting due to the coupling to the silver centre can be accurately resolved, giving the doublet of doublets highlighted in figure 4.15. The values for the coupling constants are ^{1}J(^{107}Ag-^{31}P) = 641 Hz and ^{1}J(^{109}Ag-^{31}P) = 738 Hz, values that match with those reported in literature.*

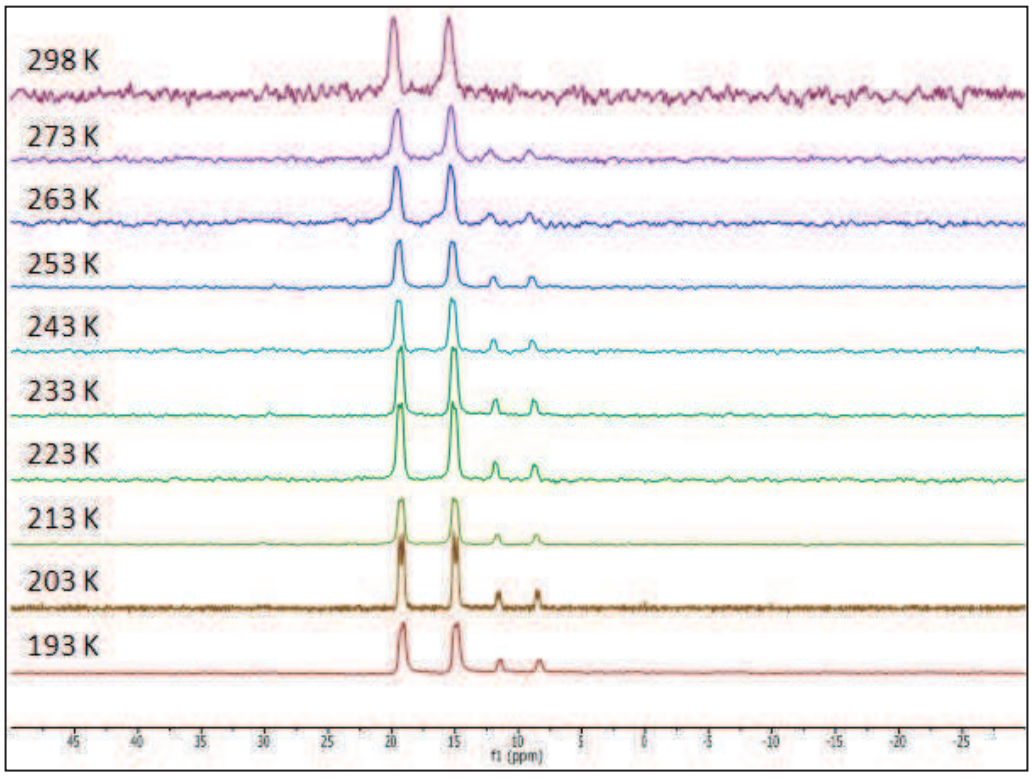

Figure 4.14 Variable temperature ^{31}P{^{1}H} NMR spectra (dichloromethane-d_2) of [Ag(PPh$_3$)(L^{OH})](NO$_3$) (**17**).

* The assignment of each coupling to the correct isotope is based on their relative intensities and on the calculation of the ^{1}J(^{107}Ag-^{31}P)/^{1}J(^{109}Ag-^{31}P) ratio, which should approach the theoretical value of γ(^{107}Ag-^{31}P)/ γ (^{109}Ag-^{31}P) = 1.15

Additionally, when the temperature is lowered, another doublet appears centred at 10.13 ppm, which can also be resolved at 203 K. In this case value of ^{1}J couplings are $^{1}J(^{107}Ag\text{-}^{31}P)$ = 468 Hz and $^{1}J(^{109}Ag\text{-}^{31}P)$ = 538 Hz, suggesting the presence of a species with a different geometry. Comparing this values with those found in literature we can suppose that this signals are due to the resonance of the phosphorous coupling with the two isotopes of silver in a tetrahedral environment,[76] so we can assume that in this case there is one oxygen from nitrate anion that complete the coordination sphere to give the tetrahedral complex.

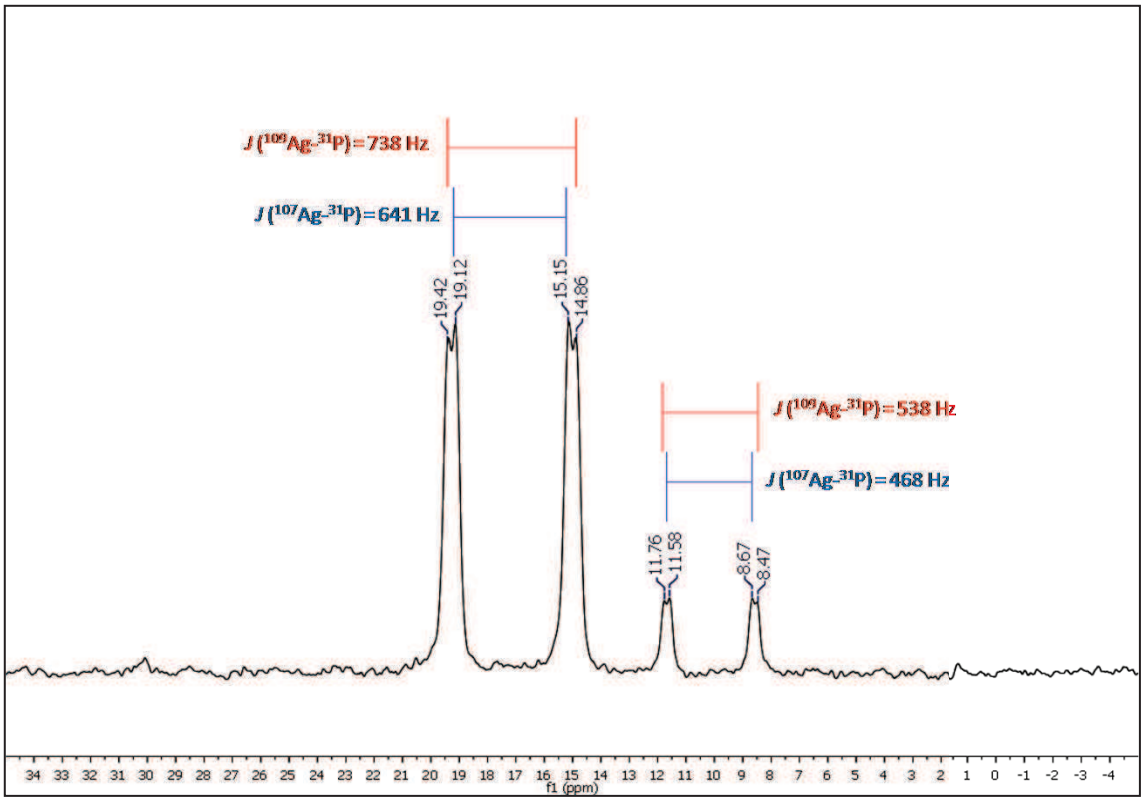

Figure 4.15 $^{31}P\{^{1}H\}$ NMR (dichloromethane-d_2, -60°C) of $[Ag(PPh_3)(L^{OH})](NO_3)$ (**17**).

Since signal related to the tetrahedral complex emerge only when the temperature is lowered below 0°C, and in any case it does not appear in a significant amount, we can clearly affirm that at room temperature the only species present shows the Ag centre in a trigonal coordination.

This was eventually confirmed by the X-ray structural analysis performed on single crystal of the complex, which is shown in Figure 4.16. X-ray quality crystals were grown by vapour diffusion of Et_2O into a CH_2Cl_2 solution of $[Ag(PPh_3)(L^{OH})](NO_3)$ (**17**).

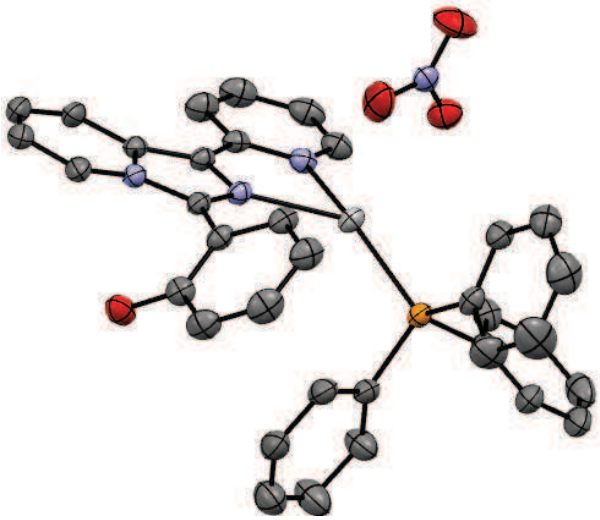

Figure 4.16 ORTEP representation of $[Ag(PPh_3)(L^{OH})](NO_3)$ at 50% probability level. Hydrogen atoms are omitted for clarity.

The crystal structure revealed the formation of a mononuclear heteroleptic complex where the silver(I) cation is in a slightly distorted N,N,P-trigonal environment surrounded by PPh_3 and L^{OH} coordinating in a chelating mode. Reported values definitely agree with a trigonal geometry since Ag-P and Ag-N bond lengths are comparable between them (Ag-P4 = 2.3 Å; Ag-N3 = 2.4 Å and Ag-N3 = 2.3 Å), while the longer distance Ag-O(NO_3) (2.7 Å) reveal the presence of a ionic interaction between the metal centre and the anion.

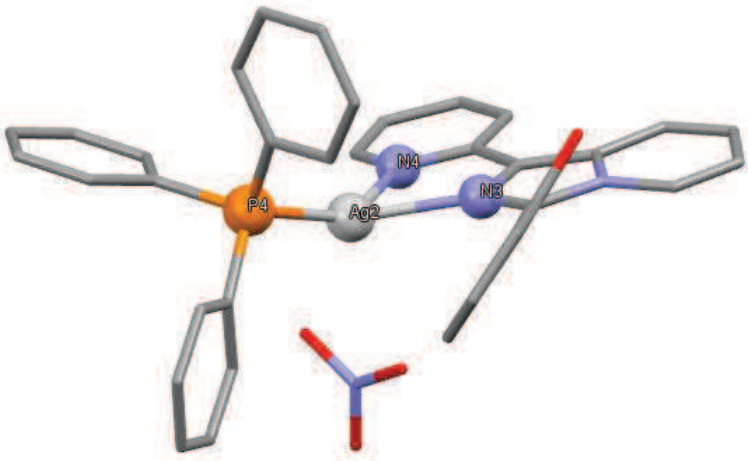

Figure 4.17 Crystal structure of $[Ag(PPh_3)(L^{OH})](NO_3)$ (**17**). Ag2, N3, N4 and P4 atoms are labelled to highlight the trigonal geometry around the metal centre.

The trigonal geometry around the metal centre is better shown in Figure 4.17 and confirmed by the N-Ag-P angles, N3-Ag-P4 = 130.4° and N3-Ag-P4 = 144.2°, respectively; as far as concern N3-Ag-N4 angle, it deviates from the other because of the constriction imposed by chelating coordination of the aza-bidentate ligand. Another prove that verified the "trigonality" of the coordination is pointed out by the small inclination angle (α = 25.1°) of the Ag-P bond from the plane containing N3-Ag-N4 atoms, so distortion from planarity is minimal (Figure 4.18).

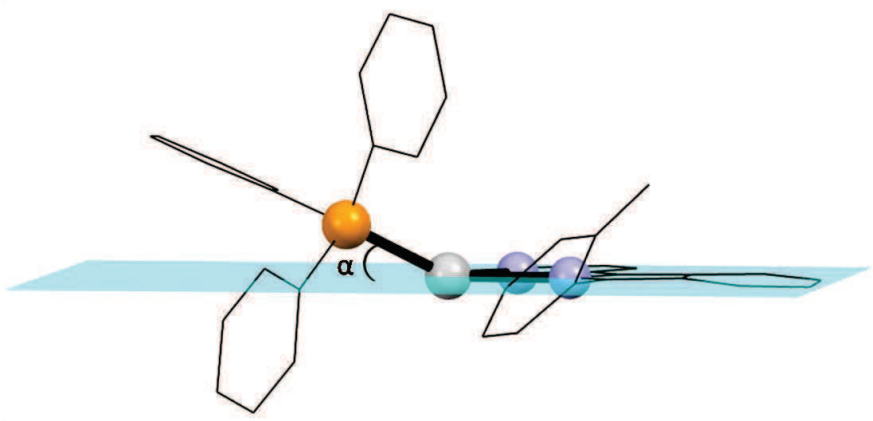

Figure 4.18 Crystal structure of [Ag(PPh_3)(L^{OH})](NO_3). Plane containing Ag, N3 and N4 atoms and the angle between the plane and Ag-P4 bond are highlighted.

Selected bond lengths and angles are listed Table 4.1.

The characterisation of complex [Ag(PPh_3)(L^{OH})](NO_3) (**17**) and the understanding of its behaviour in solution, encouraged us to proceed with the natural progression of this work, that is synthesising and characterising analogous heteroleptic complexes introducing different phosphorous ligands on the metal centre.

In Figure 4.19 is illustrated the generalised procedure followed to obtain all silver(I) derivatives, and in Figure 4.20 are depicted the phosphorous ligands used.

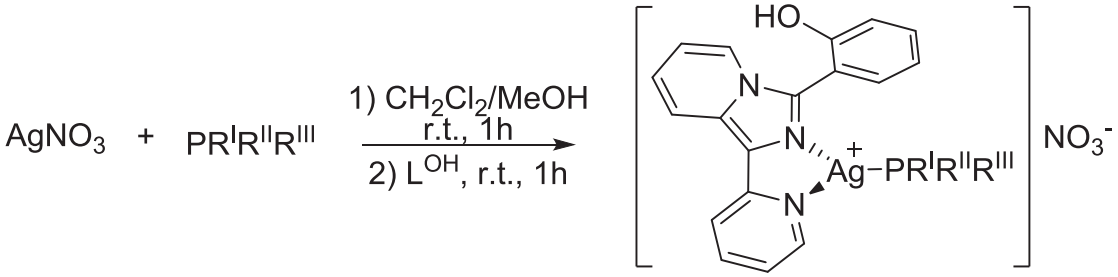

Figure 4.19 Preparation of [Ag(P)(L^{OH})](NO_3) complexes.

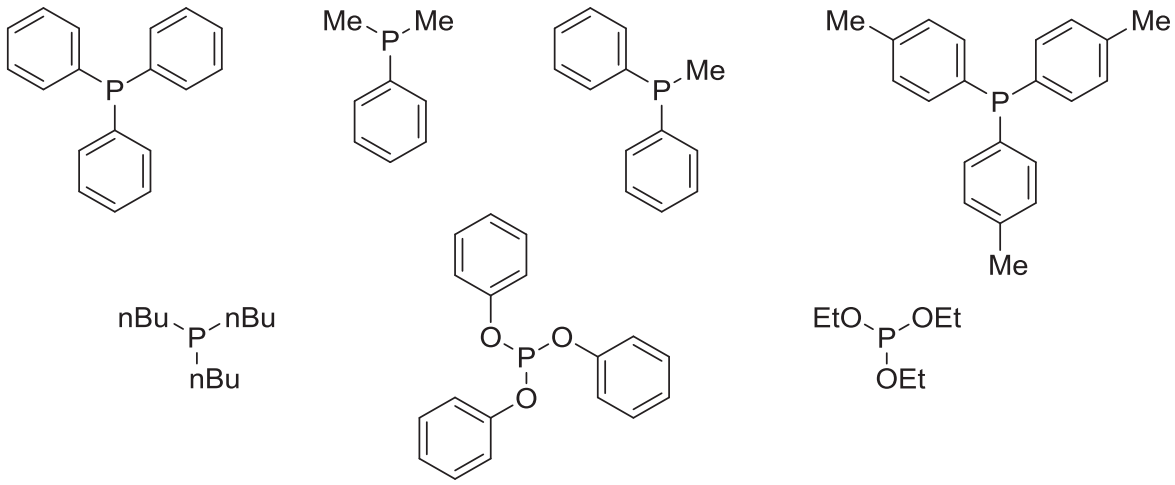

Figure 4.20 Phosphorous ligands used in the present work.

All the complexes belonging to this class have been easily characterised using the same techniques, *i.e.* elemental analysis, infrared spectroscopy, ^{1}H NMR and $^{31}P\{^{1}H\}$ NMR spectroscopy. They exhibit similar features compared to $[Ag(PPh_3)(L^{OH})](NO_3)$ (**17**) and analogies with its behaviour in solution. Hereunder are reported results obtained for each complex.

To modify steric hindrance and electronic features on metal centre, dimethylphenylphosphine has been introduced as phosphorous ligand and the resulting yellow crystalline powder can be formulated as $[Ag(PMe_2Ph)(L^{OH})](NO_3)$ (**18**).

The infrared spectrum (Figure 4.21) shows the broad band due to the presence of nitrate anion at 1308 cm^{-1}, C-H stretching due to aromatic ring and to P-Ph bonds appear respectively at 3077 and 1103 cm^{-1}, in addition a medium-strong band at 1371 cm^{-1} is attributable to P-CH_3 vibration. Cleary the typical pattern of the ligand is observed with adsorptions at 1515 and 1597 cm^{-1}.

Coordination of the L^{OH} ligand and dimethylphenylphosphine has been proven by ^{1}H NMR spectroscopy (Figure 4.22), where integrating signals allowed to determinate the 1:1 ratio between the two ligands.

Behaviour in solution monitored through $^{31}P\{^{1}H\}$ NMR spectroscopy (Figure 4.23) revealed only slightly different from that of the complex with tryphenyphosphine: at room temperature it displays only one broad signal at -20.9 ppm, which can be resolved

in two doublets by lowering the temperature to 243 K and gives $^{1}J(^{107}Ag\text{-}^{31}P)$ = 663 Hz and $^{1}J(^{109}Ag\text{-}^{31}P)$ = 767 Hz. Over the range of temperature it is possible to observe the resonance of ^{31}P coupling with the two isotopes of silver attributable to the appearance of the tetrahedral complex.

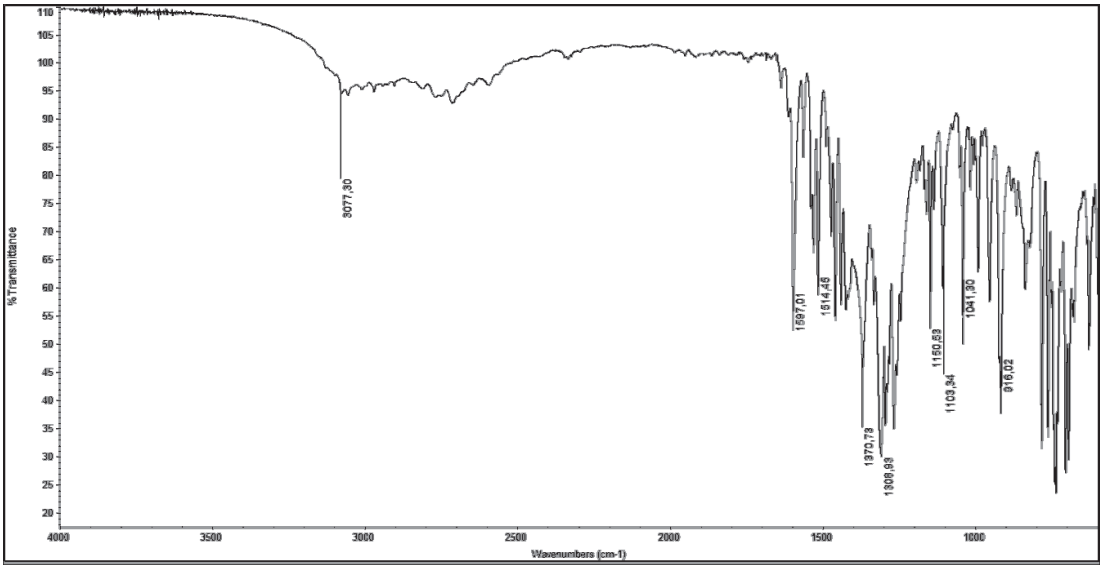

Figure 4.21 Infrared spectrum (ATR-IR technique) of $[Ag(PMe_2Ph)(L^{OH})](NO_3)$ (**18**).

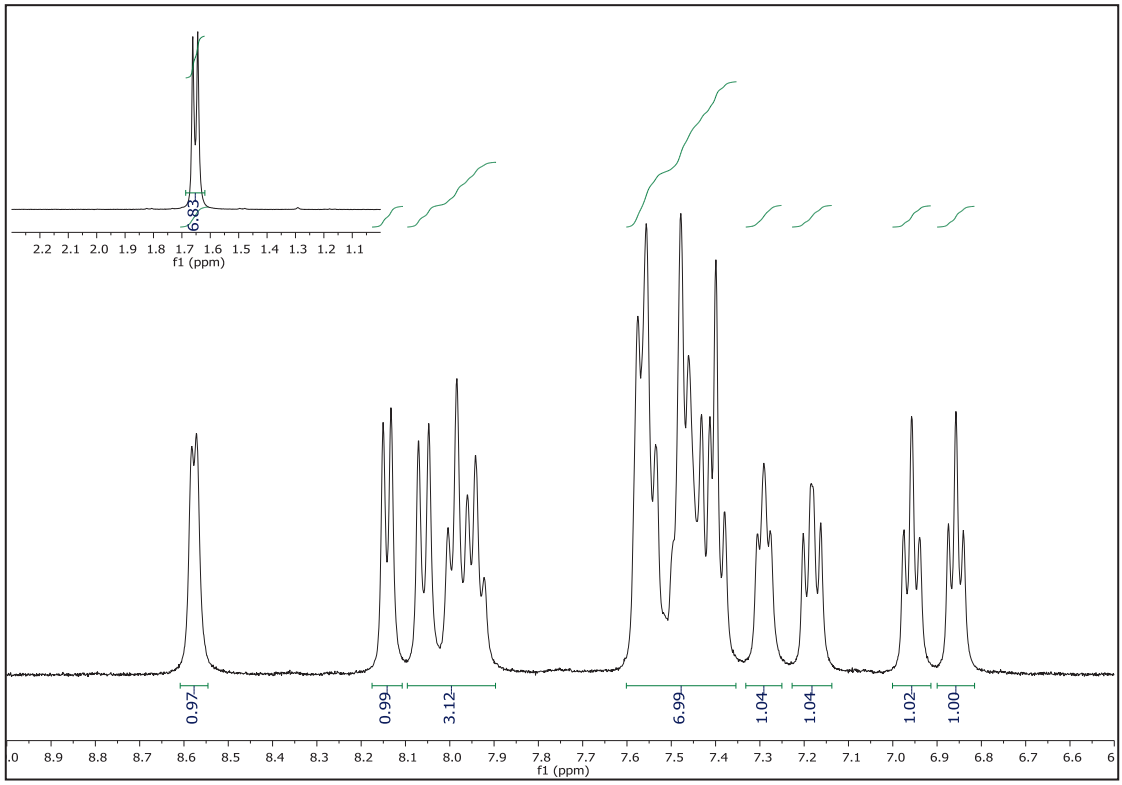

Figure 4.22 ^{1}H NMR (dichloromethane-d_2, 25°C) of $[Ag(PMe_2Ph)(L^{OH})](NO_3)$ (**18**).

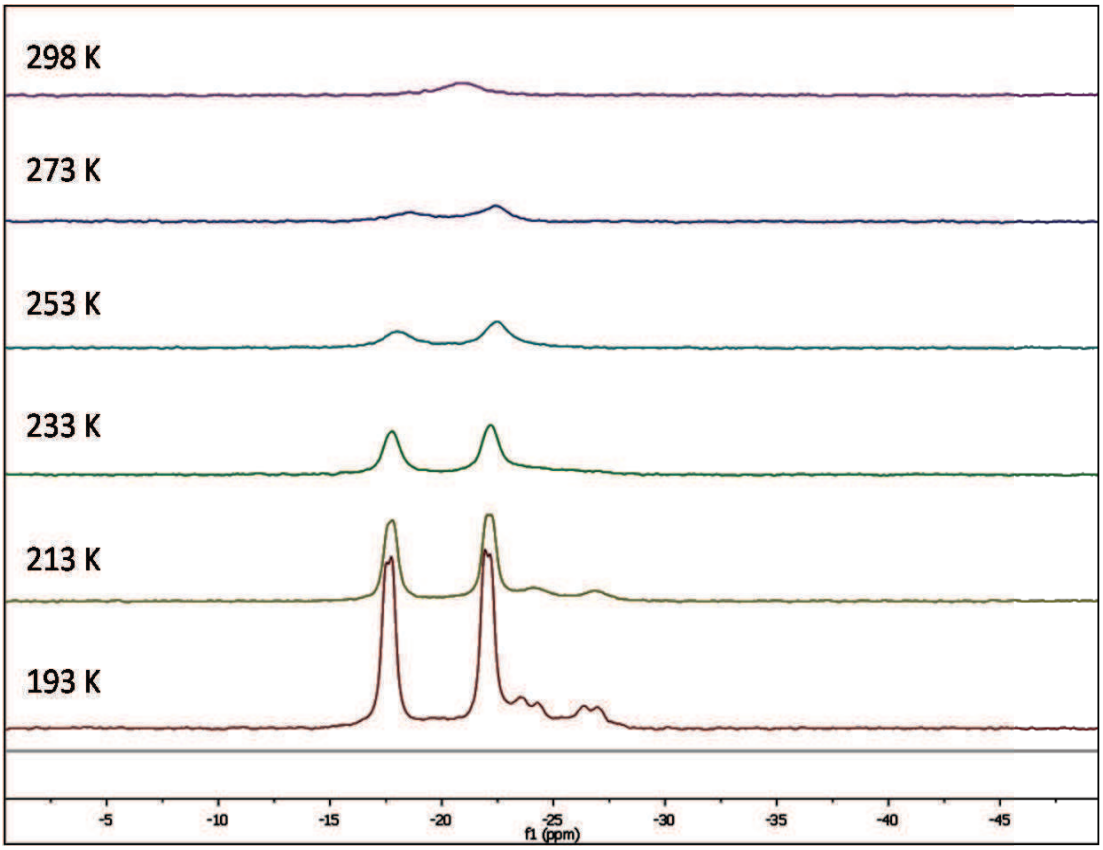

Figure 4.23 Variable temperature $^{31}P\{^{1}H\}$ NMR spectra (dichloromethane- d_2) of $[Ag(PPh_3)(L^{OH})](NO_3)$ (**18**).

Suitable crystals for X-ray analysis were grown by vapour diffusion of isopropyl ether into a dichloroethane solution of $[Ag(PMe_2Ph)(L^{OH})](NO_3)$ (**18**).

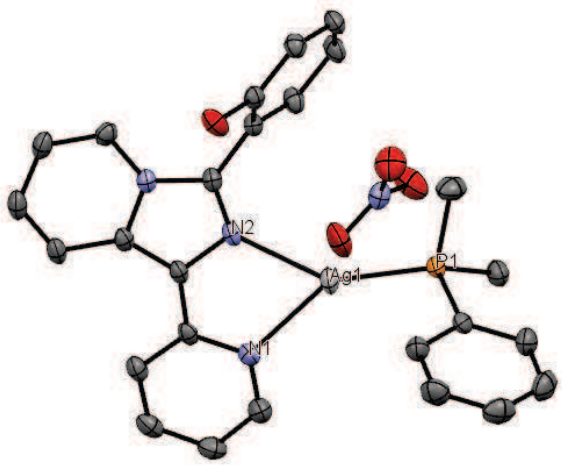

Figure 4.24 ORTEP representation of $[Ag(PMe_2Ph)(L^{OH})](NO_3)$ at 50% probability level. Hydrogen atoms are omitted for clarity.

Analysis of bond lengths and angles reveal that ligands surround the silver cation with a trigonal geometry: bond lengths difference between Ag-P and Ag-N(L^{OH}) are minimal (Ag-P1 = 2.356 Å; Ag-N1 = 2.359 Å; Ag-N2 = 2.288 Å), especially if compared with Ag-N(NO_3) bond (2.8 Å). N1-Ag-N2 angle (72.1°) is clearly smaller than N-Ag-P (N1-Ag-P1 = 146.2° and N2-Ag-P1 = 137.7°) because of the chelating features of L^{OH}. Selected bond lengths and angles are listed Table 4.1.

The [Ag($PMePh_2$)(L^{OH})](NO_3) (**19**) derivative has been obtained by the introduction of methyldiphenylphosphine.

Characterisation via infrared spectroscopy (Figure 4.25) revealed the presence of the nitrate anion at 1325 cm^{-1}. The stretching vibration of methyldiphenylphosphine give rise to bands at 3051 and 1097 cm^{-1} for the aromatic part of the molecule, while P-CH_3 stretching occur at 1434 cm^{-1}, together with the bands observed for the presence of L^{OH} at 1515 and 1597 cm^{-1}.

Again, the structural assignment of the complex and its behaviour in solution can be deduced from both its ^{1}H NMR (Figure 4.26) and low temperature $^{31}P\{^{1}H\}$ NMR (Figure 4.27). Thanks to signal integration in ^{1}H NMR, we can describe the coordination sphere with a 1:1 ratio between ligands. $^{31}P\{^{1}H\}$ NMR spectrum displays a “pseudo doublet” at room temperature centred at -2.54 ppm, which can be resolved carrying out low temperature experiments (Figure 4.27). It is noteworthy that in this case when the temperature is lowered, signals attributable to the presence of the tetrahedral complex do not appear.

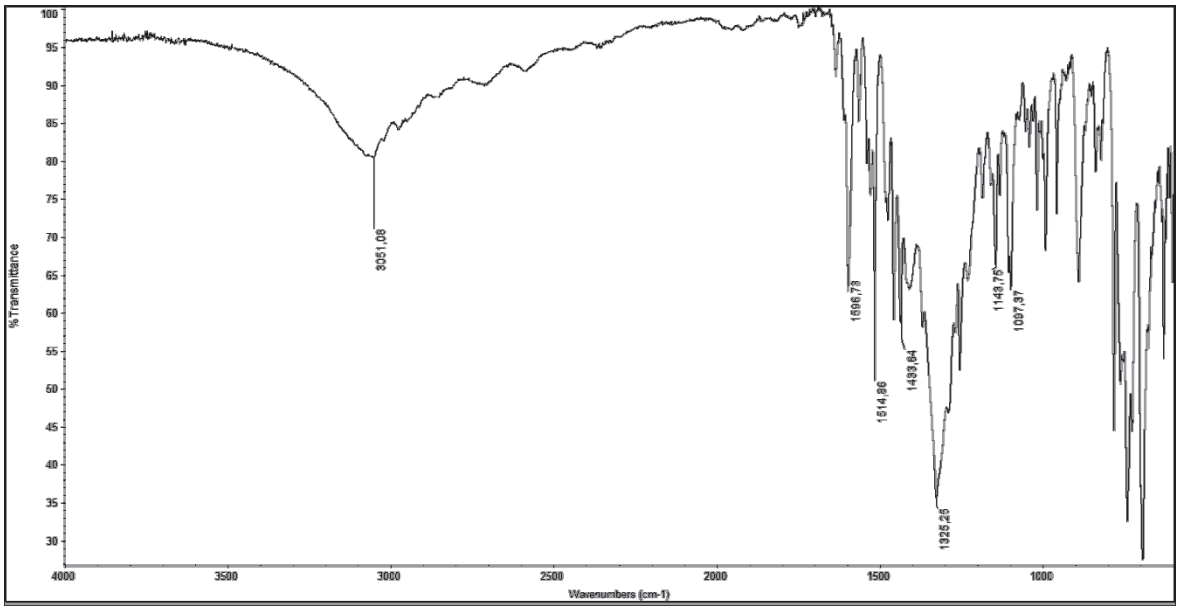

Figure 4.25 Infrared spectrum (ATR-IR technique) of [Ag(PMePh$_2$)(L^{OH})](NO$_3$) (**19**).

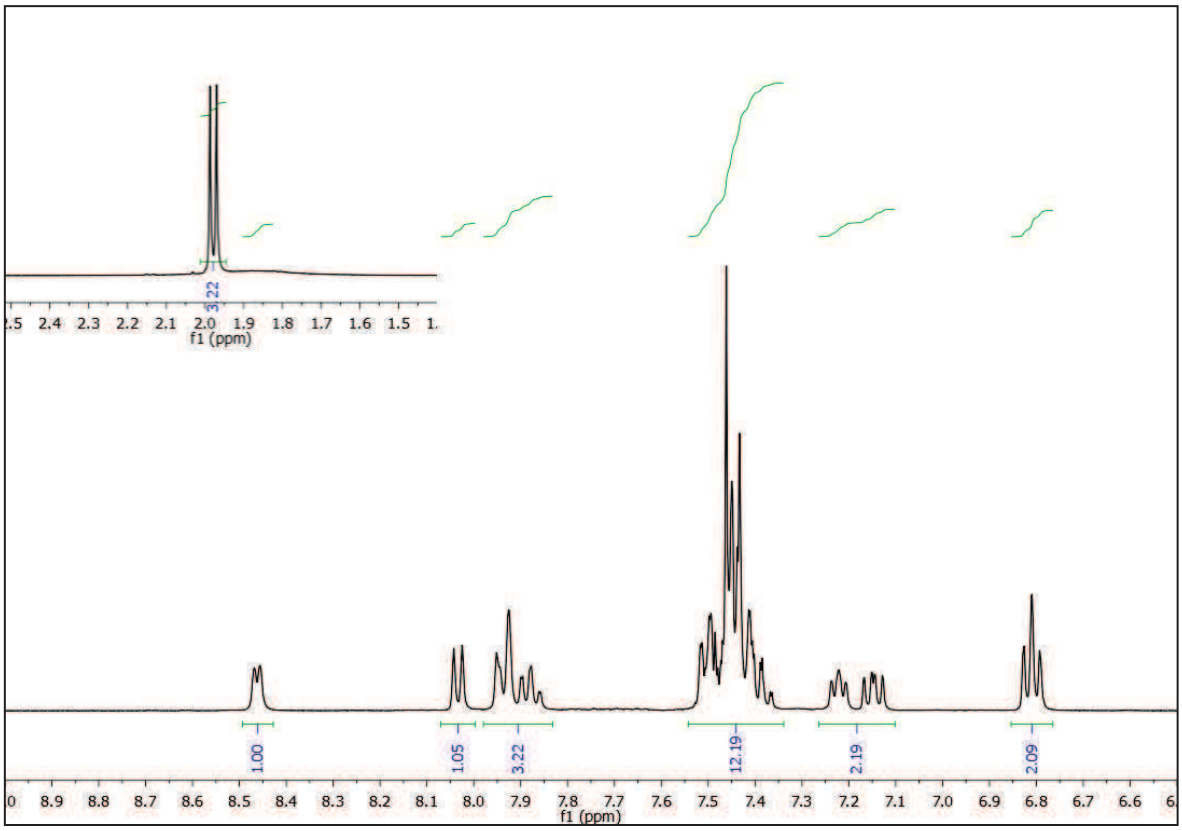

Figure 4.26 ^{1}H NMR (dichloromethane-d_2, 25°C) of [Ag(PMePh$_2$)(L^{OH})](NO$_3$) (**19**).

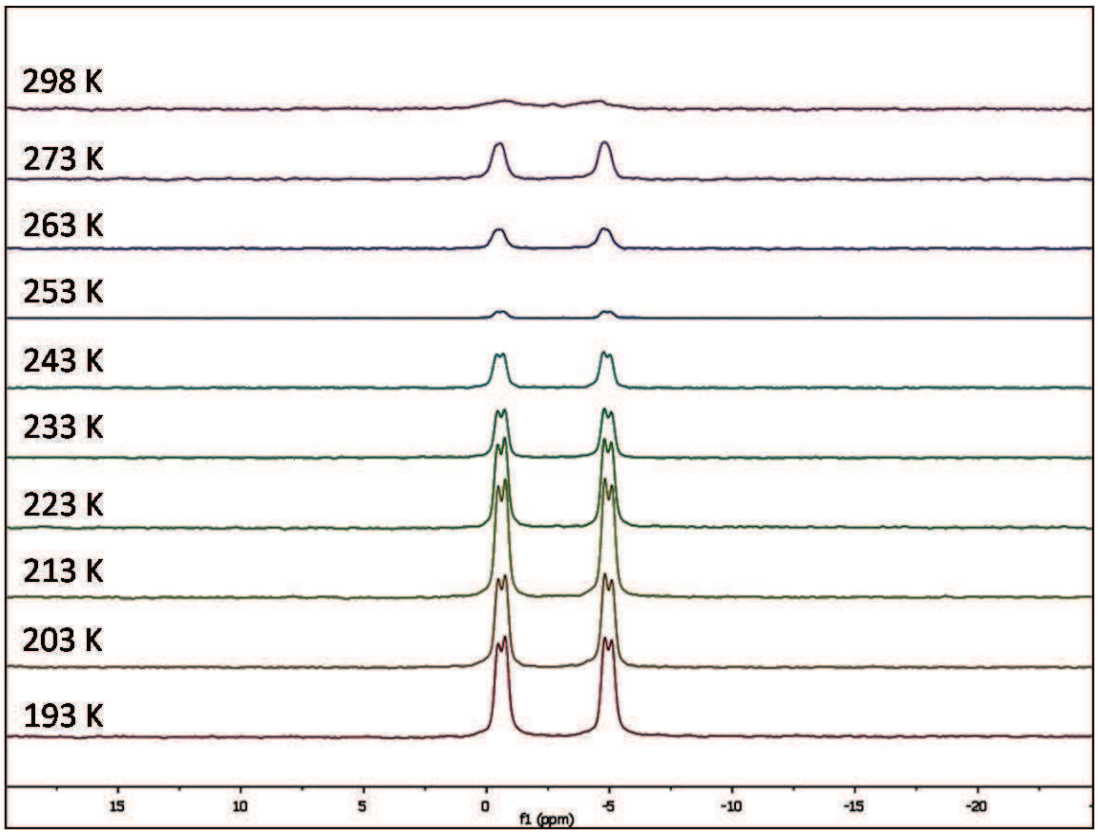

Figure 4.27 Variable temperature $^{31}P\{^{1}H\}$ NMR spectra (dichloromethane- d_2) of $[Ag(PMePh_2)(L^{OH})](NO_3)$ (**19**).

An aliphatic phosphines (PBu_3) then has been coordinated to the metal centre, affording complex $[Ag(PBu_3)(L^{OH})](NO_3)$ (**20**).

Infrared spectrum (Figure 4.28) show a broad stretching at 2927 cm^{-1}, which can be attributed to the C-H of the butyl substituent in PBu_3, in addition P-CH_2- stretching occurs as a sharp signal of medium intensity at 1434 cm^{-1}, in the same region where L^{OH} gives its typical signals.

^{1}H NMR spectrum (Figure 4.29) clearly shows both aliphatic and aromatic signals, and the integration analysis describe the system with a stoichiometric ratio 1:1 between L^{OH} and PBu_3. In Figure 4.30 is reported $^{31}P\{^{1}H\}$ NMR low temperature experiment which displays a doublet centred at 1.18 ppm which can be resolved in two doublets at 243 K without evidence of formation of tetrahedral complex.

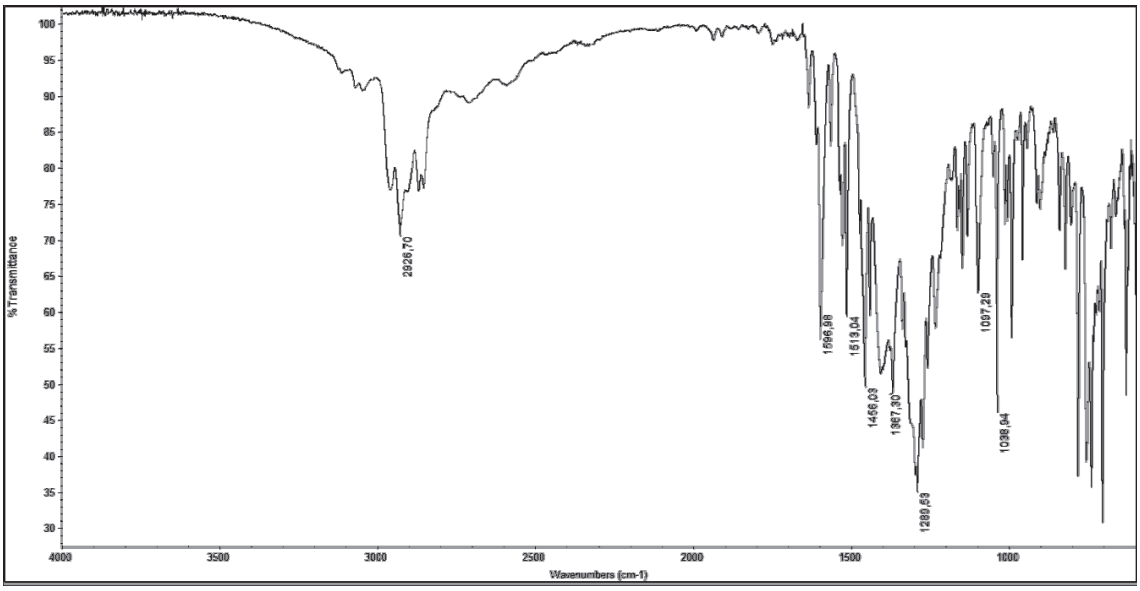

Figure 4.28 Infrared spectrum (ATR-IR technique) of [Ag(PBu_3)(L^{OH})](NO_3) (**20**).

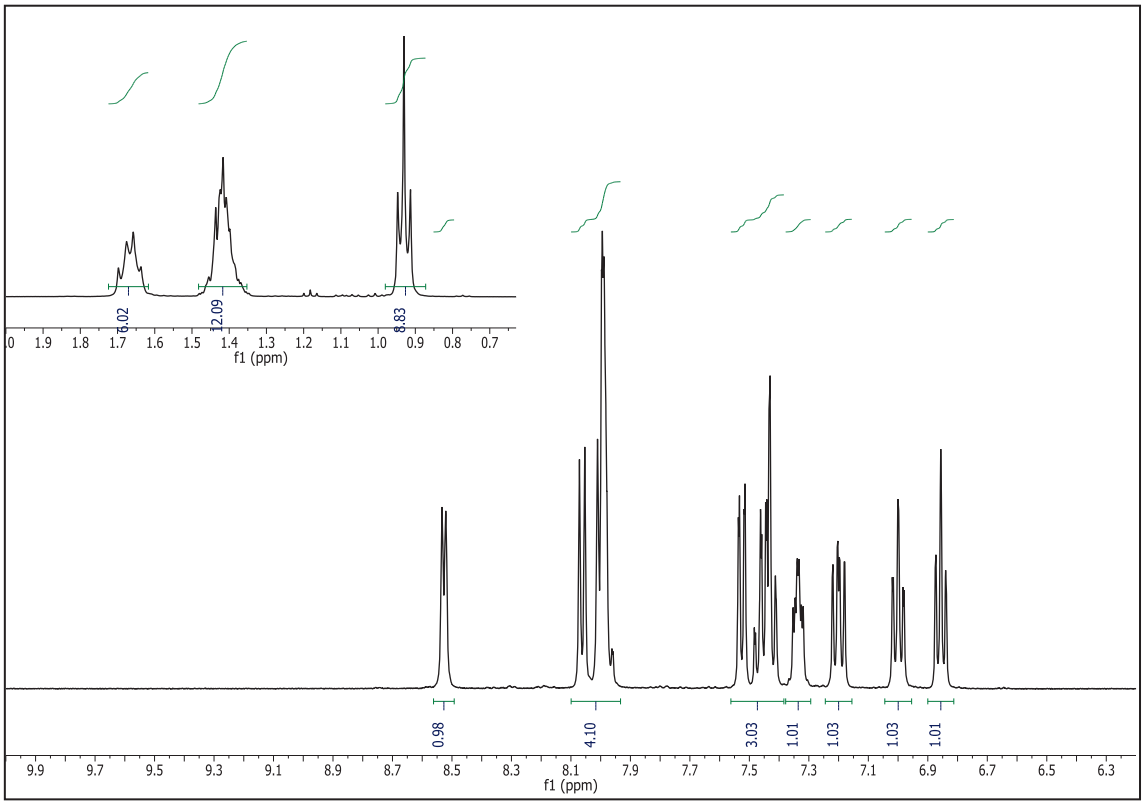

Figure 4.29 ^{1}H NMR (dichloromethane-d_2, 25°C) of [Ag(PBu_3)(L^{OH})](NO_3) (**20**).

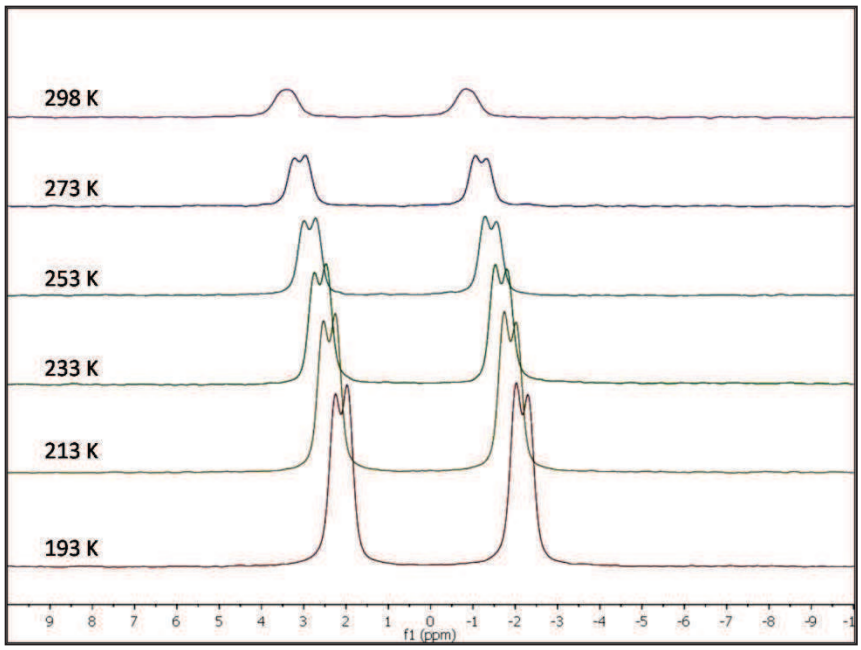

Figure 4.30 $^{31}P\{^{1}H\}$ NMR (dichloromethane-d_2, 25°C) of $[Ag(PBu_3)(L^{OH})](NO_3)$ (**20**).

For $[Ag(PBu_3)(L^{OH})](NO_3)$ (**20**), crystals suitable for X-ray crystal structure analysis were obtained by vapour diffusion of Et_2O into a CH_2Cl_2 solution of the silver(I) complex. The molecule is shown in Figure 4.31 and selected bond lengths and angles are listed in Table 4.1.

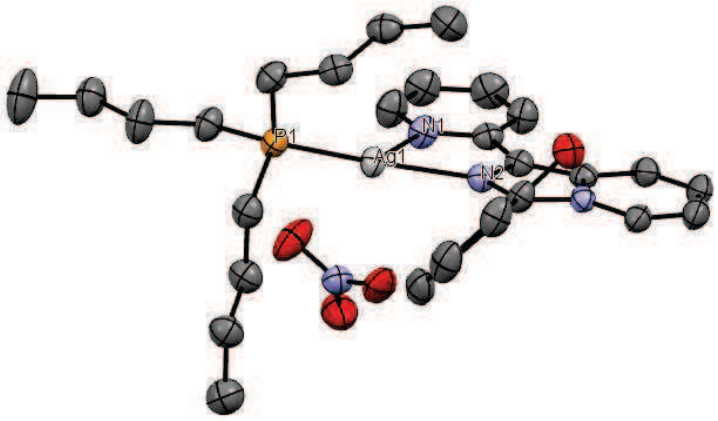

Figure 4.31 ORTEP representation of $[Ag(PBu_3)(L^{OH})](NO_3)$ at 50% probability level. Hydrogen atoms are omitted for clarity.

The structure of $[Ag(PBu_3)(L^{OH})](NO_3)$ (**20**) is very similar to the one reported for the other Ag(I) derivatives. The silver atom is tricoordinated in a slightly distorted trigonal geometry; L^{OH} behaves as a chelating ligand and the value of the bite angle is 71.8° while P1-Ag-N1 angle is 137.4° and P1-AgN2 angle is 147.0°. Bond lengths (Ag-P1 = 2.3Å; Ag-N1

= 2.4 Å; Ag-N2 = 2.3 Å) show analogies between them and distances measured for the other complex reported in this work, while the nitrate O atom is at a nonbonding distance from the Ag(I) centre (Ag-O(NO_3) = 2.8 Å). Selected bond lengths and angles are listed in Table 4.1.

Another derivative belonging to this class has been obtained by reaction with *p*-tolylphosphine: [Ag(P(*p*-tolyl)$_3$)(L^{OH})](NO_3) (**21**).

The interpretation of infrared spectrum (Figure 4.32) reveal the presence of the broad nitrate band at 1318 cm^{-1} and of both aromatic and aliphatic C-H stretching around 3000 cm^{-1} due to the presence of *p*-tolylphosphine. Sharp bands at 1512 and 1598 cm^{-1} belong to L^{OH} ligand.

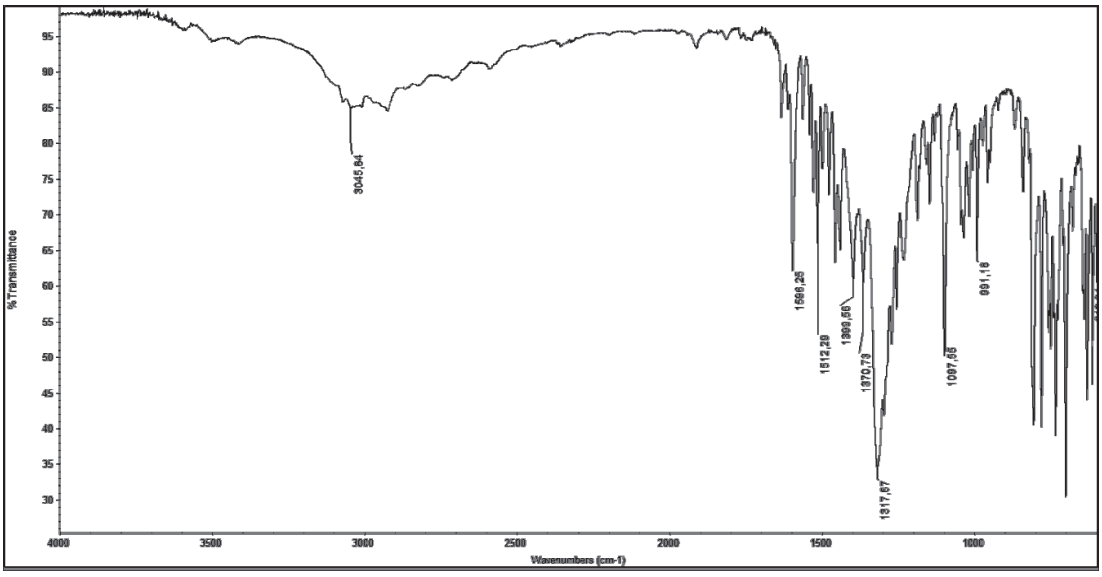

Figure 4.32 Infrared spectrum (ATR-IR technique) of [Ag(P(*p*-tolyl)$_3$)(L^{OH})](NO_3) (**21**).

The ^{1}H NMR spectrum is reported in Figure 4.33; it shows the expected pattern of the ligand, with some slight shifts due to N,N-coordination to the metal centre. On the other hand, integration of signal consents to determinate the ratio 1:1 between the L^{OH} and the phosphine.

$^{31}P\{^1H\}$ NMR spectra registered by lowering the temperature (Figure 4.34) illustrate the typical behaviour observed for this class of complexes: the broad signal that appear at room temperature is split into the two doublets at 243 K, moreover, even in this case there is no evidence of formation of tetrahedral complex.

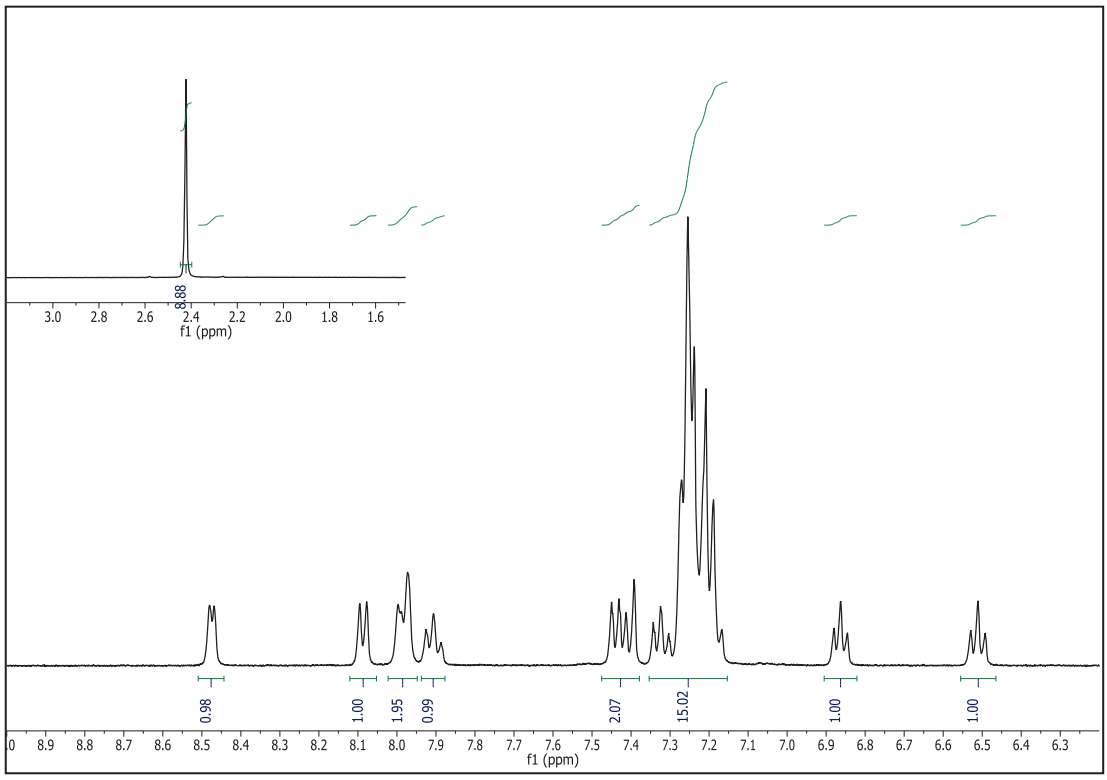

Figure 4.33 ^{1}H NMR (dichloromethane-d_2, 25°C) of [Ag(P(*p*-tolyl)$_3$)(L^{OH})](NO$_3$) (**21**).

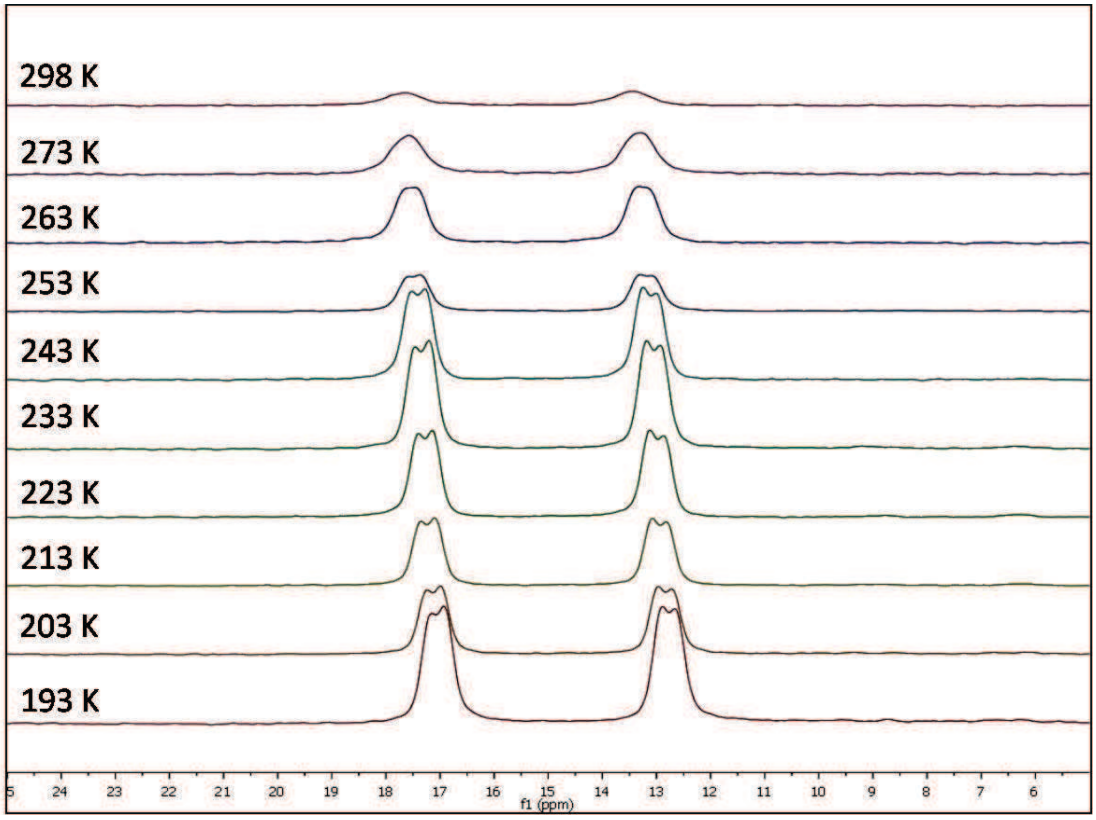

Figure 4.34 Variable temperature ^{31}P{^{1}H} NMR spectra (dichloromethane- d_2) of [Ag(P(*p*-tolyl)$_3$)(L^{OH})](NO$_3$) (**21**).

Finally, in order to more significantly modify the electronic properties, two derivatives with highly π-acceptor phosphorous ligands, namely $P(OPh)_3$ and $P(OEt)_3$, have been prepared and characterised as follow.

IR spectroscopy (Figures 4.35 and 4.36) reveal for both complexes the presence of nitrate band around 1300 cm^{-1}, together with stretchings due to the presence of aza-bidentate ligand between 1500 and 1600 cm^{-1}. The most significant bands attributable to P-O-C groups occurs at 920 cm^{-1} and at 1015 cm^{-1} for $[Ag(P(OPh)_3)(L^{OH})](NO_3)$ (**22**) and for $[Ag(P(OEt)_3)(L^{OH})](NO_3)$ (**23**), respectively.

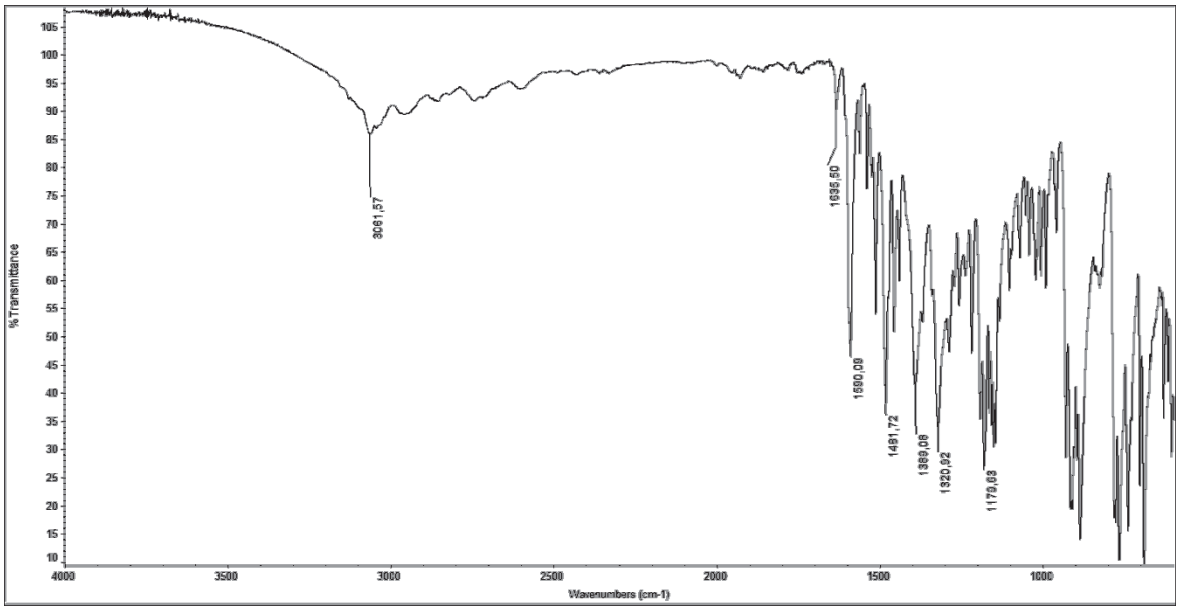

Figure 4.35 Infrared spectrum (ATR-IR technique) of $[Ag(P(OPh)_3)(L^{OH})](NO_3)$ (**22**).

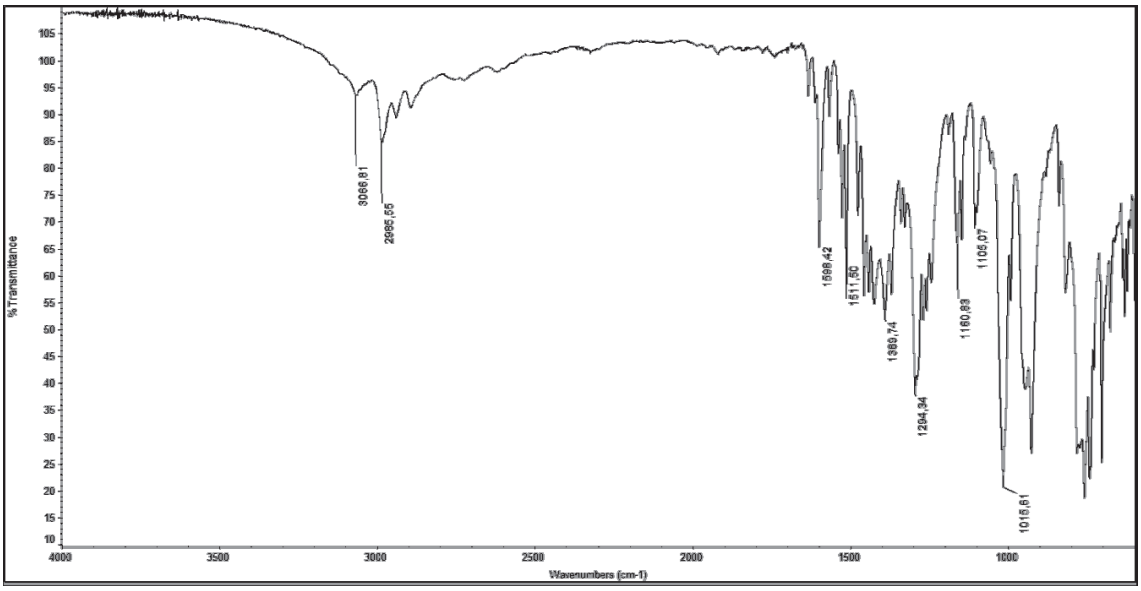

Figure 4.36 Infrared spectrum (ATR-IR technique) of $[Ag(P(OEt)_3)(L^{OH})](NO_3)$ (**23**).

Again their ^{1}H NMR behaviour was examined in dichloromethane-d_2 at room temperature (Figure 4.37 and Figure 4.38); it revealed that both L^{OH} and phosphite are coordinated in the two complexes and in both cases they are present in a 1:1 ratio.

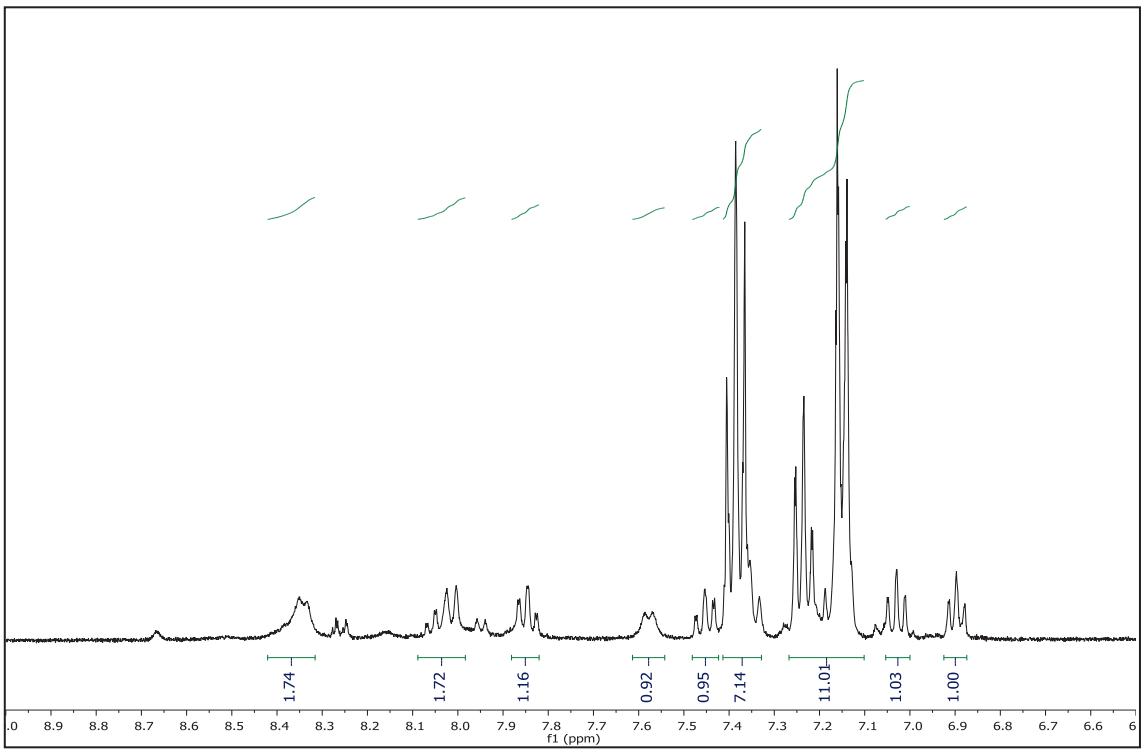

Figure 4.37 ^{1}H NMR (dichloromethane-d_2, 25°C) of $[Ag(P(OPh)_3)(L^{OH})](NO_3)$ (**22**).

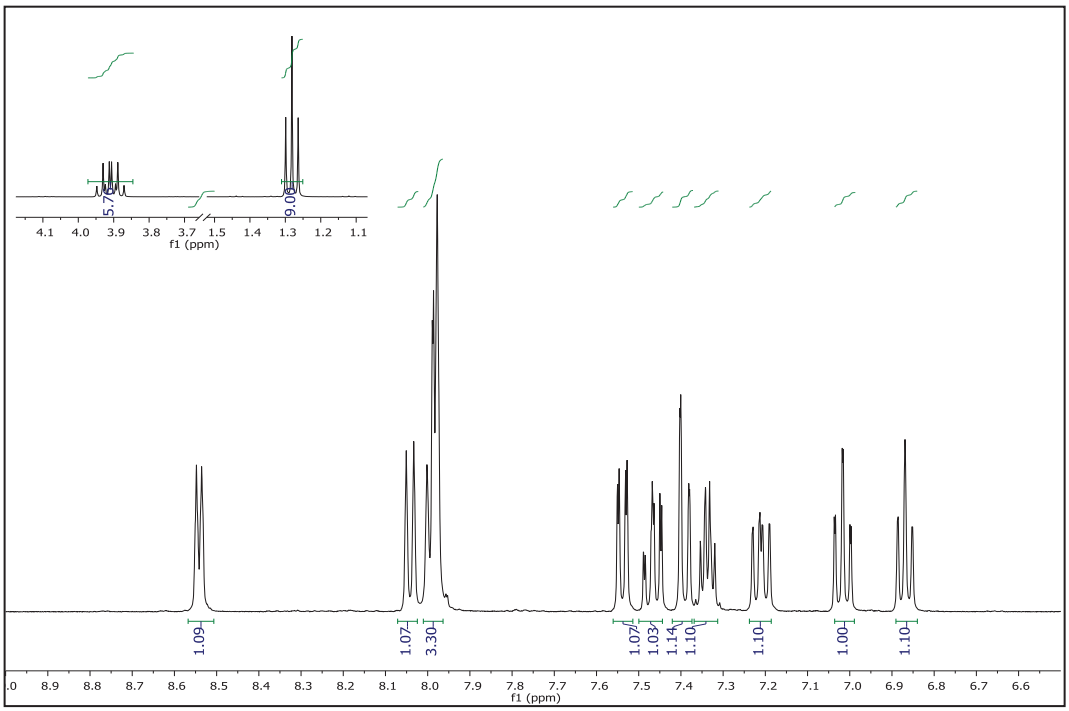

Figure 4.38 ^{1}H NMR (dichloromethane-d_2, 25°C) of [Ag(P(OEt)$_3$)(L^{OH})](NO$_3$) (**23**). Inset: alkyl signal from alkoxy group.

^{31}P{^{1}H} NMR spectrum of [Ag(P(OPh)$_3$)(L^{OH})](NO$_3$) (**22**) registered at room temperature (Figure 4.39) shows a single signal at 125.2 ppm.

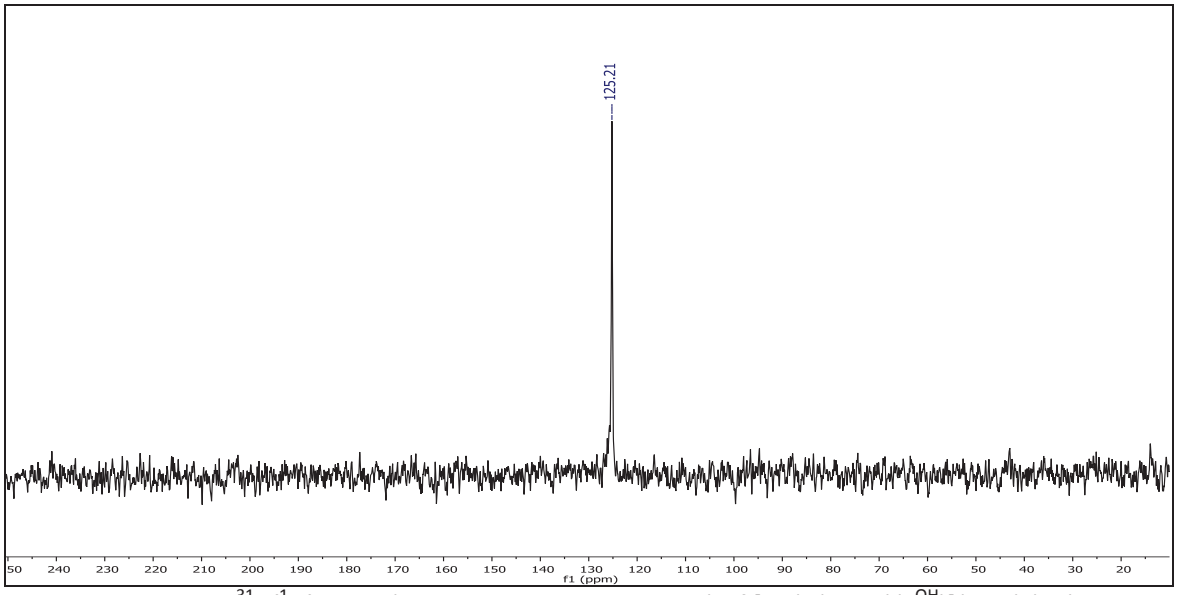

Figure 4.39 ^{31}P{^{1}H} NMR (dichloromethane-d_2, 25°C) of [Ag(P(OPh$_3$)(L^{OH})](NO$_3$) (**22**).

In $^{31}P\{^{1}H\}$ NMR spectra registered at low temperature (Figure 4.40) the "pseudo doublet" appearing at room temperature for $[Ag(P(OEt)_3)(L^{OH})](NO_3)$ is split into the two doublets at 253 K, again there is no evidence of formation of tetrahedral complex.

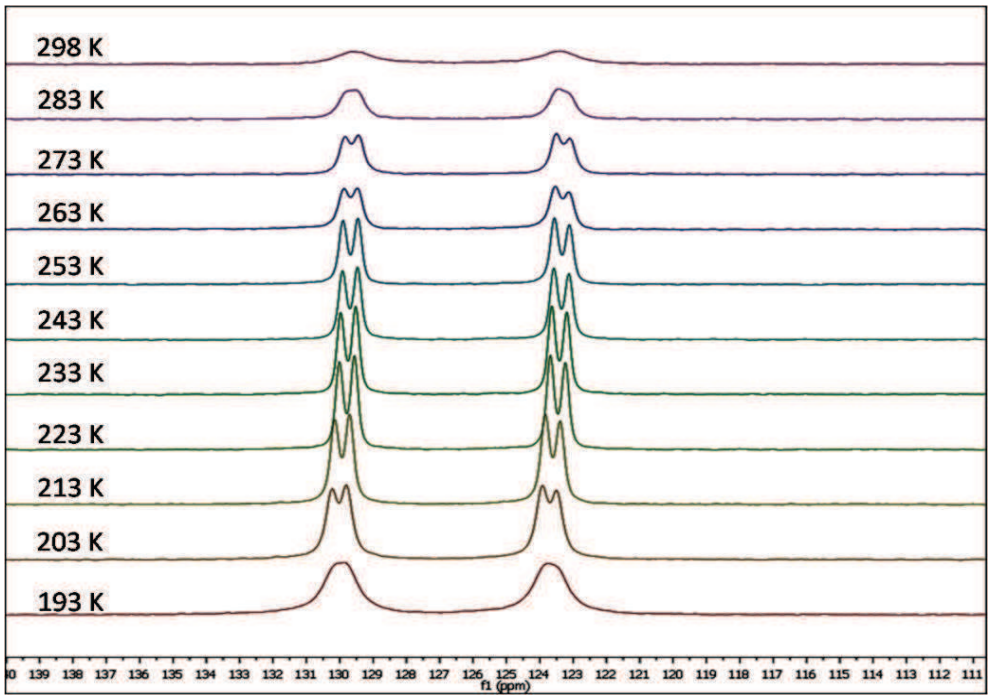

Figure 4.40 Variable temperature $^{31}P\{^{1}H\}$ NMR spectra (dichloromethane- d_2) of $[Ag(P(OEt)_3)(L^{OH})](NO_3)$ (**23**) registered by lowering temperature.

Finally, for $[Ag(P(OPh)_3)(L^{OH})](NO_3)$ X-ray structural analysis has been performed (Figure 4.41), again confirming the trigonal geometry around the silver centre. Selected bond lengths and angles are listed Table 4.1.

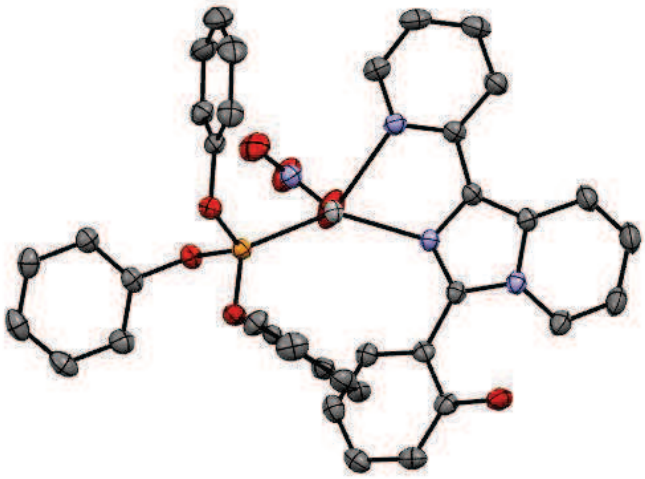

Figure 4.41 ORTEP representation of $[Ag(P(OPh)_3)(L^{OH})](NO_3)$ at 50% probability level. Hydrogen atoms are omitted for clarity.

$Ag(PPh_3)(L^{OH})](NO_3)$ (17)			
Bond	Lenght (Å)	Angle	Degrees (°)
Ag2 – P4	2.348	N3-Ag2-N4	72.25
Ag2 – N4	2.327	N3-Ag2-P4	130.39
Ag2 – N3	2.293	N4-Ag2-P4	144.21
Ag2 – N (NO_3)	2.742	(N-Ag-N)plane - (Ag-P)bond	25.31
$[Ag(PMe_2Ph)(L^{OH})](NO_3)$ (18)			
Bond	Lenght (Å)	Angle	Degrees (°)
Ag1 – P1	2.356	N1-Ag1-N2	72.07
Ag1 – N1	2.359	N1-Ag1-P1	146.16
Ag1 – N2	2.288	N2-Ag1-P1	137.65
Ag1 – N (NO_3)	2.839	(N-Ag-N)plane - (Ag-P)bond	13.75
$[Ag(PBu_3)(L^{OH})](NO_3)$ (20)			
Bond	Lenght (Å)	Angle	Degrees (°)
Ag1 – P1	2.340	N1-Ag1-N2	71.75
Ag1 – N1	2.368	N1-Ag1-P1	137.39
Ag1 – N2	2.261	N2-Ag1-P1	146.96
Ag1 – N (NO_3)	2.780	(N-Ag-N)plane - (Ag-P)bond	11.12
$[Ag(P(OPh)_3)(L^{OH})](NO_3)$ (22)			
Bond	Lenght (Å)	Angle	Degrees (°)
Ag1 – P1	2.311	N1-Ag1-N2	72.20
Ag1 – N1	2.352	N1-Ag1-P1	140.46
Ag1 – N2	2.253	N2-Ag1-P1	142.03
Ag1 – N (NO_3)	2.532	(N-Ag-N)plane - (Ag-P)bond	15.28

Table 4.1 Bond lengths and angles of complex obtained by X-ray diffraction.

LUMINESCENT PROPERTIES

As mentioned above, the introduction of different phosphorous ligands leads to a variation of photophysical properties, i.e. tuning of luminescence emission and different values of photophysical quantum yield. This can be attributed to electronic effects of the ligands, which can change the electronic features of the complexes and possibly modify frontier orbitals energies; consequently the emission properties can be influenced by changing electronic characteristic of P-ligands.

Figure 4.42 reports normalised UV-Vis spectra of [Ag(P)(L^{OH})](NO_3) derivatives recorded as $1 \cdot 10^{-5}$ M solution in dichloromethane.

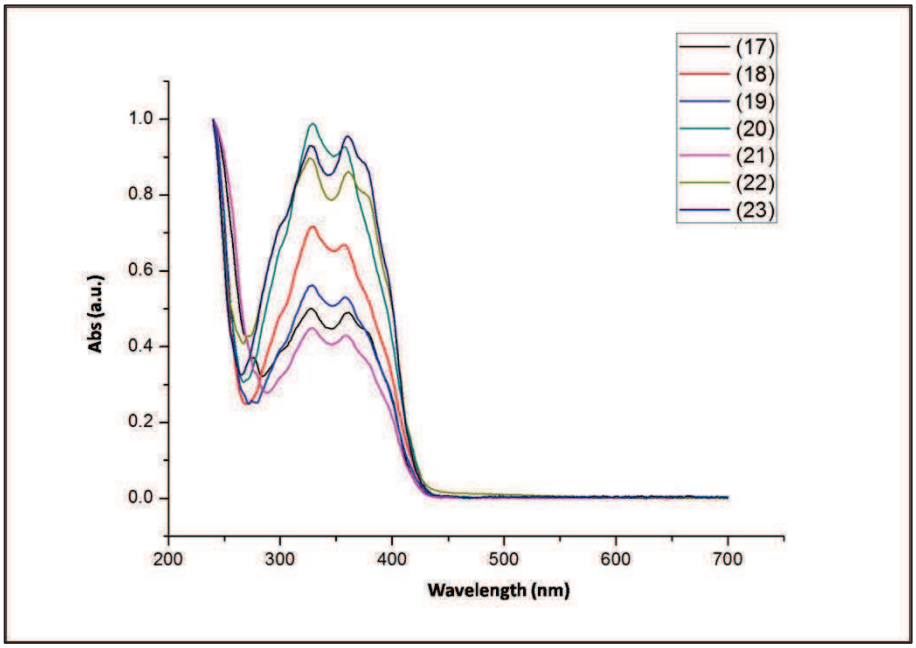

Figure 4.42 Normalised UV-Vis spectra of the studied derivatives [Ag(P)(L^{OH})](NO_3) in dichloromethane solution $1 \cdot 10^{-5}$M.

The spectra show essentially an absorption band with two shoulders appearing at about 330 and 360 nm respectively. All the complexes exhibit the same behaviour in solution and it is clearly possible to affirm that there is no evidence of bands related to the presence of free ligand or other species in solution. TD-DFT calculations revealed that the absorption band at lower energy is assigned to a ligand (L^{OH}) centred HOMO-LUMO transition. As an example frontier orbitals calculated for [Ag(PMe_2Ph)(L^{OH})] are shown in Figure 4.43.

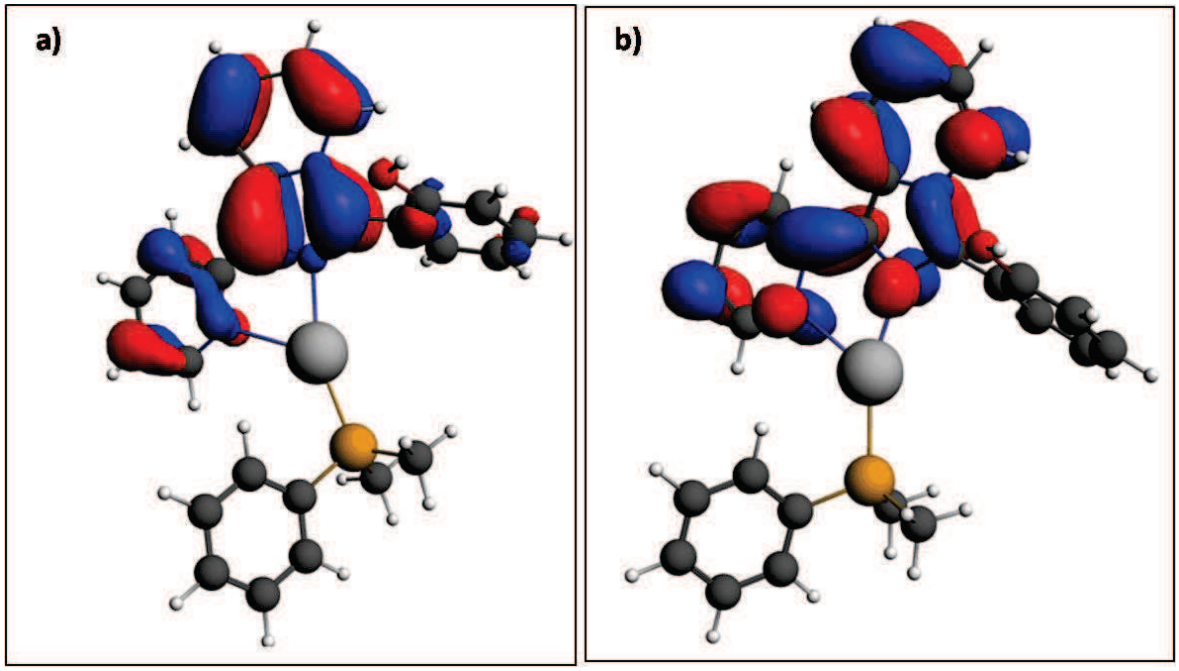

Figure 4.43 Frontier molecular orbitals for complex [Ag(PMe_2Ph_3)(L^{OH})](**18**):
a) HOMO (**18**); b) LUMO (**18**).

Luminescent measurement of the samples in dichloromethane solution at a concentration of $1 \cdot 10^{-5}$M at room temperature were taken for each complex. The excitation and emission spectra of the different compounds, reported in figure 4.44, show similar bands.

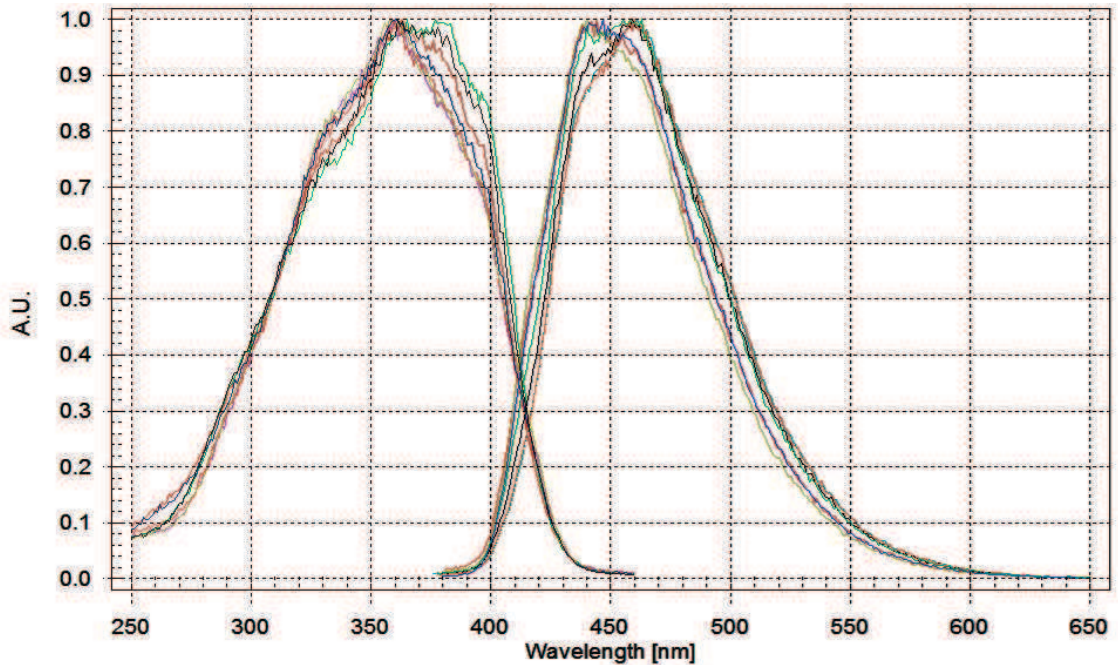

Figure 4.44 Excitation and emission spectra of the studied derivatives [Ag(P)(L^{OH})](NO_3) in dichloromethane solution $1 \cdot 10^{-5}$M.

The excitation spectra reflect the pattern registered for UV-Vis analysis, where the maximum excitation wavelength for all derivatives is about 460 nm, absorption band related to the HOMO-LUMO transition centred on the ligand. The emission spectra are relatively broad and unstructured, moreover this class of complexes exhibit a weak ipsochromic shift of the maximum emission wavelength going from complexes bearing pure *σ*-donor phosphines (PBu_3) to those containing *π*-acid phosphites. Photophysical data, i.e. maximum excitation wavelengths, maximum emission wavelength and Φ_{PL} for each complex are collected in Table 4.2:

	λ_{exc} (nm)	λ_{em} (nm)	Φ_{PL}
$[Ag(PBu_3)(L^{OH})](NO_3)$	358	465	0.36
$[Ag(PMe_2Ph)(L^{OH})](NO_3)$	356	461	0.38
$[Ag(P(p\text{-tolyl})_3)(L^{OH})](NO_3)$	358	461	0.38
$[Ag(PMePh_2)(L^{OH})](NO_3)$	358	460	0.37
$[Ag(PPh_3)(L^{OH})](NO_3)$	361	460	0.52
$[Ag(P(OEt)_3)(L^{OH})](NO_3)$	360	457	0.36
$[Ag(P(OPh)_3)(L^{OH})](NO_3)$	361	453	0.30

Table 4.2 Photoluminescence properties in solution of the complexes studied in this work.

In order to explain the effect of the introduction of *σ*-donor or *π*-acid phosphorous ligands, we examined relations between the emission properties and the electronic features of the phosphorous ligand and consequently of the complex. In 1976 Tolman[77] reported an empirical equation to estimate the value of CO stretching for monosubstitued nichel carbonyls complexes $Ni(CO)_3L$ (L = phosphorous ligand):

$$\text{For } PX_IX_{II}X_{III} \qquad \nu = 2056.1 + \sum_{i=1}^{3} \chi_i$$

where χ is the substituent contribution which is additive and tabulated.

Here subsequently, the maximum emission expressed in wavenumber for each [Ag(P)(L^{OH})](NO_3) complex has been plotted *vs.* the substituent contribution χ as reported in Figure 4.45:

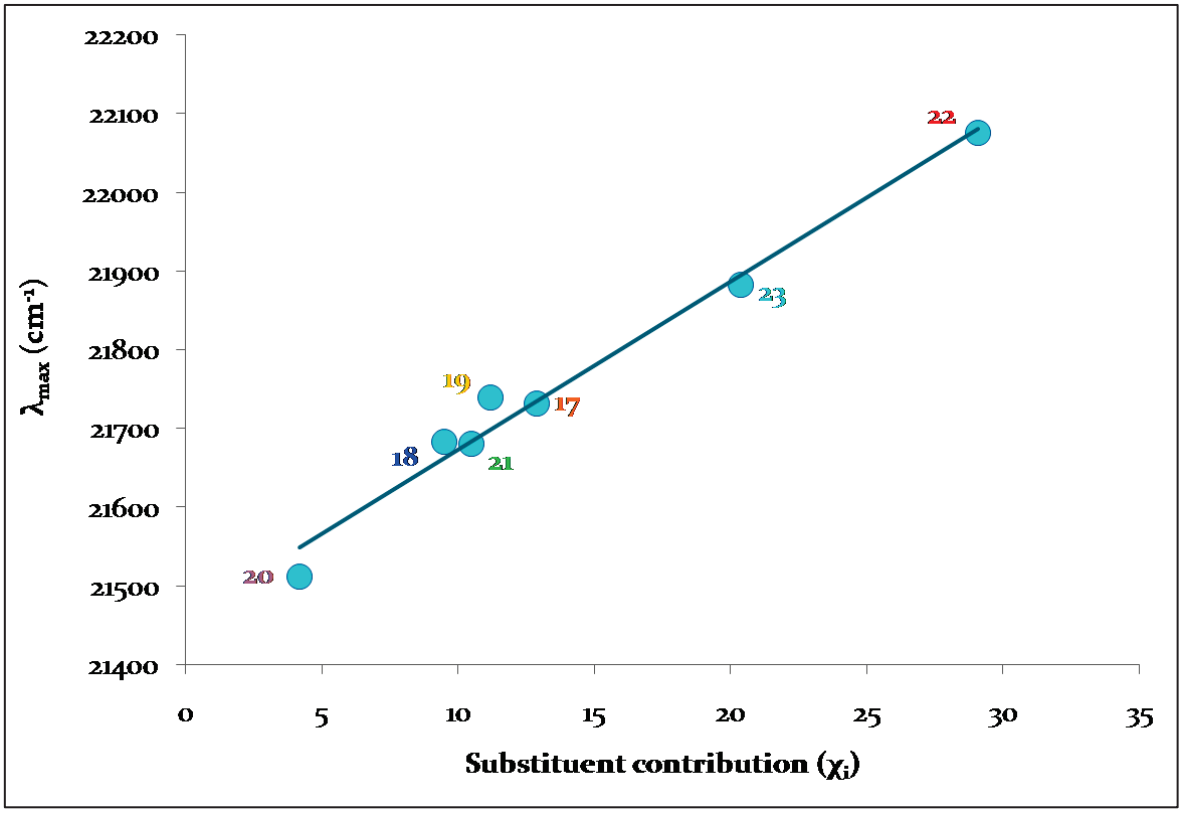

Figure 4.45 Maximum emission *vs.* substituent contribution of studied complexes.

It is noteworthy that all the data follow a linear trend with a good R^2 value of 0.980, as shown in the graph; moreover the sequence of the complexes on the line reflect the variation of basic characteristic of the phosphorous ligands.

In Table 4.2 are also reported the photoluminescence quantum yield values. These complexes exhibit good PLQY in solution, comprised between 0.30 and 0.40, the only exception being the PPh_3 derivative with a remarkable higher Φ_{PL} = 0.52.

Photophysical properties has been investigated also in the solid state. The emission spectra of all the Ag(I) compounds studied are shown in Figure 4.46.

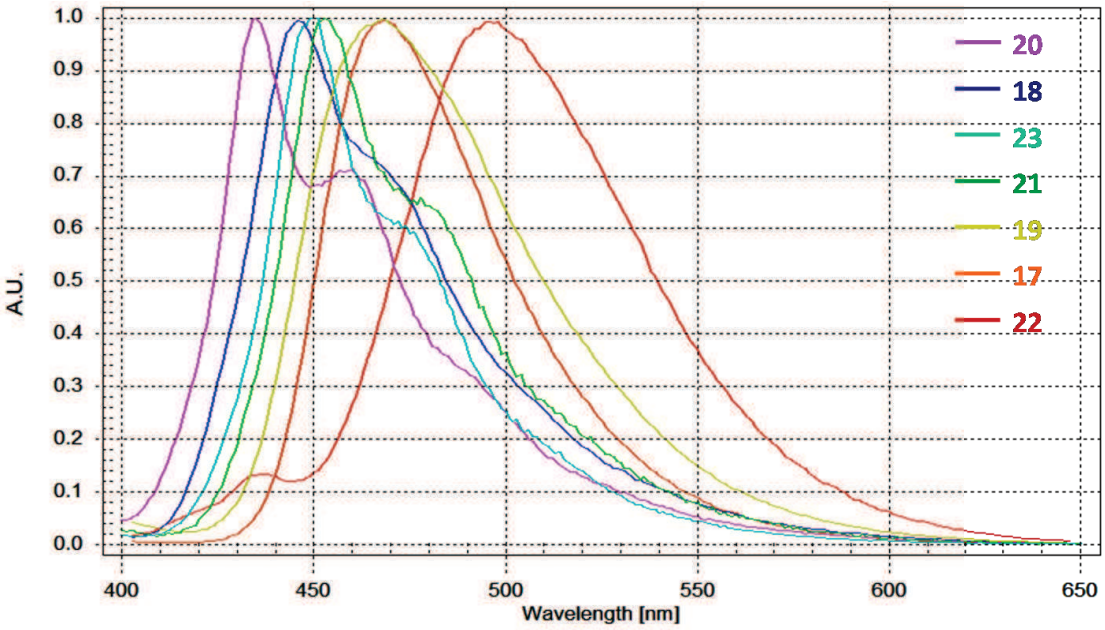

Figure 4.46 Emission spectra of the studied derivatives [Ag(P)(L^{OH})](NO_3) in the solid state.

Again, emission pattern are relatively broad and unstructured and the variation of the maximum emission wavelength is in agreement with the data collected in solution and, clearly, with the electronic features of phosphorous ligands. Indeed complex [Ag(PBu_3)(L^{OH})](NO_3) (**20**) containing a pure σ-donor and strong basic phosphine, exhibits emission at 435 nm, while λ_{max} complexes bearing PMe_2Ph (**18**) and P(*p*-tolyl)$_3$ (**21**) are weakly red-shifted. The introduction of more π-acidic phosphines, such as PPh_2Me (**19**) and PPh_3 (**17**), results in a further batochromic shift of the emission; finally it is possible to shift the emission more to red for the complex [Ag($P(OPh)_3$)(L^{OH})](NO_3) (22), which contains triphenylphosphite, a strong π-acid ligand.

Photophysical data for complexes studied at the solid state are reported in Table 4.3:

	λ_{exc} (nm)	λ_{em} (nm)	Φ_{PL}
$[Ag(PBu_3)(L^{OH})](NO_3)$	412	435	0.14
$[Ag(PMe_2Ph)(L^{OH})](NO_3)$	420	446	0.18
$[Ag(P(OEt)_3)(L^{OH})](NO_3)$	419	450	0.19
$[Ag(P(p\text{-tolyl})_3)(L^{OH})](NO_3)$	430	453	0.20
$[Ag(PMePh_2)(L^{OH})](NO_3)$	435	468	0.18
$[Ag(PPh_3)(L^{OH})](NO_3)$	440	469	0.68
$[Ag(P(OPh)_3)(L^{OH})](NO_3)$	400	496	0.16

Table 4.3 Photoluminescence characteristics at the solid state of the complexes studied in this work.

The PLQY values are all lower than those reported for the derivatives studied in solution except for the green-emitting complex $[Ag(PPh_3)(L^{OH})](NO_3)$, which reached a value of Φ_{PL} = 0.68. Further studies are in progress to explain this behaviour.

Chapter 5

Self-Complexation in Polymeric Matrix of Luminescent Eu(III) Complexes for Downshifting

Part of the PhD Thesis (February 2013 – August 2013) has been carried out in the laboratories of School of Chemistry at University of Edinburgh under the supervision of Dr. Neil Robertson. The project developed during this period has concerned the synthesis and the optical characterisation of luminescent materials for downshifting.

Photovoltaic (PV) devices exhibit a poor spectral response to light in the UV and blue wavelengths of the solar spectrum and have a low quantum efficiency in that region.[78] The high-energy content of short-λ photons is difficult to harness efficiently because of interactions with the front layers of a PV device: absorption and reflection by the front glass or the encapsulating materials are some of the possible loss mechanism of energy observed for photovoltaic devices.

An important challenge in the field of solar technologies is the improvement of properties of solar cells which do not require modifications to the well established manufacturing process of PV modules.

Luminescent down-shifting (LDS) was first proposed as means to improve the poor short-λ response of solar cells in 1979 by Hovel et al.[79] who hypothesised the use of an independent layer on top of a pre-existing PV device. The addition of this extra layer enabled reduction of problems and costs in manufacturing, because there were no need to disrupt the already existing and efficient photovoltaic device, nevertheless its applications were limited by the availability of luminescent materials.

In fact, LDS technology relies on layering a transparent polymer host matrix in which a luminescent dye is incorporated. The luminescent layer can absorb light in the UV and blue region of the incident sunlight and emit photons at longer wavelength which better match the spectral response of a particular solar cell.

It has been proved that for solar cells based on CdTe, usually displaying a huge loss of absorption at wavelengths shorter than 500 nm, a LDS layer, which can absorb below 500 nm and re-emit above this wavelength, allows the solar cell to achieve better performances at its maximum efficiency.[80] Also, there are studies reporting the investigation and the optimisation of short wavelengths response and conversion efficiency of a production-ready alternative that requires no modification to the well-established manufacturing process of wafer-based silicon modules.[81]

As we might expect, some inevitably losses occur during LDS process, but, broadly speaking, it is possible to define the characteristic of an ideal LDS material as follows:

- strong absorption over the entire UV–blue region of the spectrum;
- emission at longer wavelength that matches the peak of the solar cell's response;
- large Stokes shift to avoid re-absorption events;
- nearly 1 (i.e., ≈100%) value of photoluminescence quantum yield (PLQY);
- adequate photostability under long-term exposure to sunlight.

To optimise the luminescent material, the transparent polymeric material used is crucial in the development and in the efficiency of LDS; the most commonly used are polymethylmethacrylate (PMMA) and polycarbonate (PC), usually chosen because of low cost, simple preparation, with excellent optical quality. Furthermore, it is necessary to select a suitable luminescent dye to incorporate in the polymeric matrix. In recent years good results have been achieved using lanthanides complexes due to their intense, narrow emission bands and their long lived excited states.[82] Though the rare-earth ions typically exhibit weak absorption, it has been demonstrated that by introducing an appropriate "antenna" chromophore it is possible to increase the absorbance of the complex in the visible and UV regions. The antenna effect is an energy conversion process which involves a ligand able to collect the light and transfer the energy to a metal ion.[83]
Eu(III) and Tb(III) are the most common lanthanides studied because they emit in the visible region, while for NIR emission, Nd(III) and Yb(III) have been widely investigated.

Recently, a number of papers reported the use of Eu(III) based complexes because of the main emission peak at 614 nm, where microcrystalline silicon (mc-Si) and CdTe solar cell has a high quantum efficiency.[84] Moreover this complexes exhibit a large Stokes shift: the absence of overlap between absorption and emission bands reduces the possibility of re-absorption events.
Robertson *et al*. described the synthesis and investigation of an Eu(III) complex which shows very high photoluminescence quantum yields (80%), but, unfortunately, this compound does not absorb light beyond 350 nm.

In the light of above, the following step, has been trying a different approach that allows to achieve the luminescent complex avoiding the need to synthesise and isolate it. The idea was to mix directly in solution the Eu(III) precursor and a UV-absorbing ligand with a polymer and spin-coat the mixture into a polymer film onto a glass support. Results obtained by Robertson *et al.*[85] starting from $[Eu(hfac)_3(H_2O)_2]$ (hfac = hexafluoroacetylacetonate), a coronene salt as antenna ligand and polyvinyl alcohol as polymeric matrix, encouraged to follow this way, testing this self-assembling method with different ligands showing good absorption in the UV and blue region of electromagnetic spectrum.

5.1 RESULTS AND DISCUSSION

Initially ligand 4-((4-(diphenylamino)phenyl)ethynyl)benzoic acid (L^I) (Figure 5.1), which has been previously synthesised in Dr. Robertson's research group, was tested adjusting the procedure reported in literature for self-assembling of $[Eu(hfac)_3(H_2O)_2]$ with coronene salt in PVA matrix, while the transparent material used as waveguide was poly(methyl methacrilate) (PMMA) and the Eu(III) precursor was $[Eu(hfac)_3(H_2O)_2]$, prepared as reported in literature.[86]

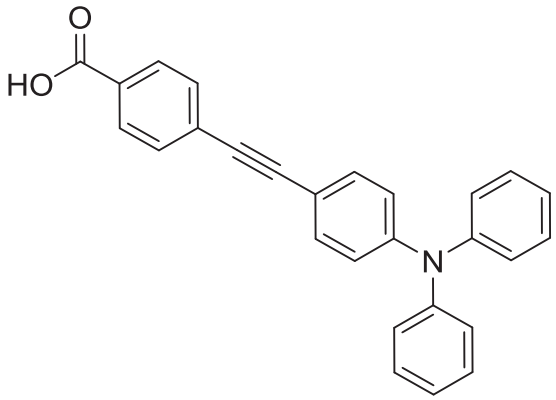

Figure 5.1 Structure of ligand (L^I) used to adjust the procedure.

The procedure is developed in different steps. Firstly the optical properties of the ligand have to be investigated after incorporation in the polymeric matrix. Thin films were obtained by mixing different quantities of L^{I} in concentrated chlorobenzene:acetonitrile = 1:1 solutions of PMMA, followed by spin-coating.

The optimal concentration of the ligand was determined through UV-vis analysis, as reported in Figure 5.2. For this ligand it was found to be 3mM, giving a maximum of absorbance near 0.1 at the main absorption peak (375 nm).

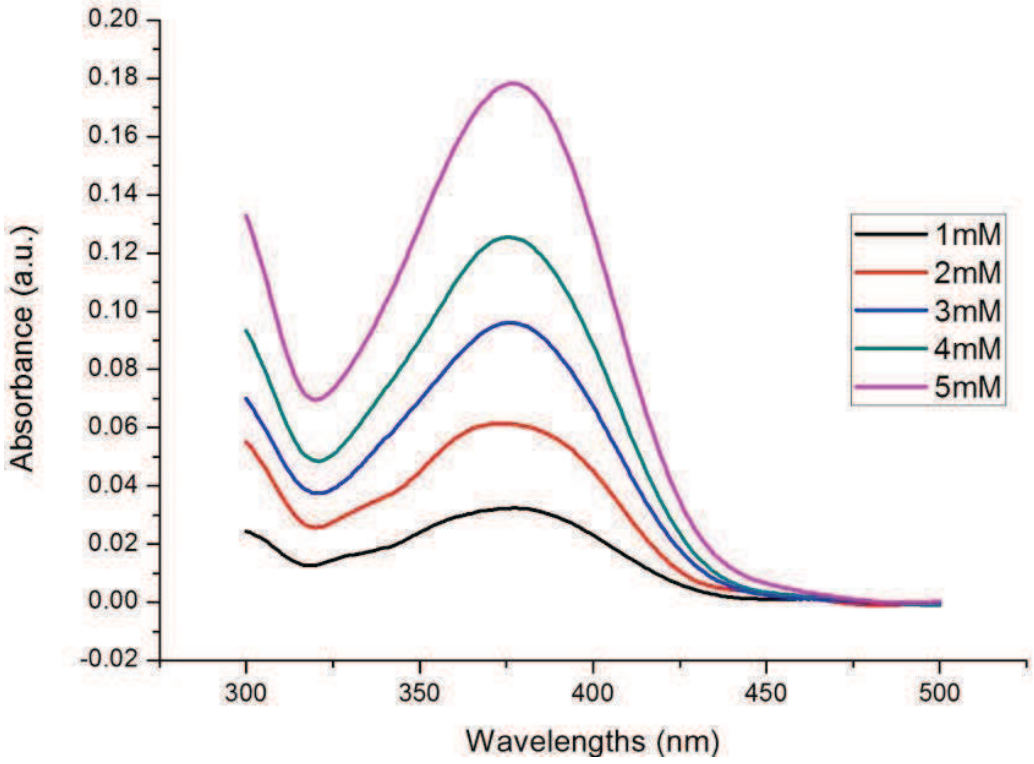

Figure 5.2 UV-vis spectra (PMMA thin film) of L^{I}.

The second step of this procedure aims to investigate the optical properties of different blends of the ligand and Eu(III) precursor. Films were obtained by mixing L^{I} and $[Eu(hfac)_3(H_2O)_2]$ in different ratios (1:0.5; 1:1; 1:2), the obtained PMMA solution were then spin-coated (see experimental section).

The optical properties of the thin layers were investigated with UV-vis analysis and, as reported in Figure 5.3, the absorption band related to the presence of $[Eu(hfac)_3(H_2O)_2]$ appears with a maximum at 300 nm which increases at higher concentrations of the Eu(III) complex, while the absorption band attributable to L^I (375 nm) does not display significant differences compared to the spectrum of pristine ligand.

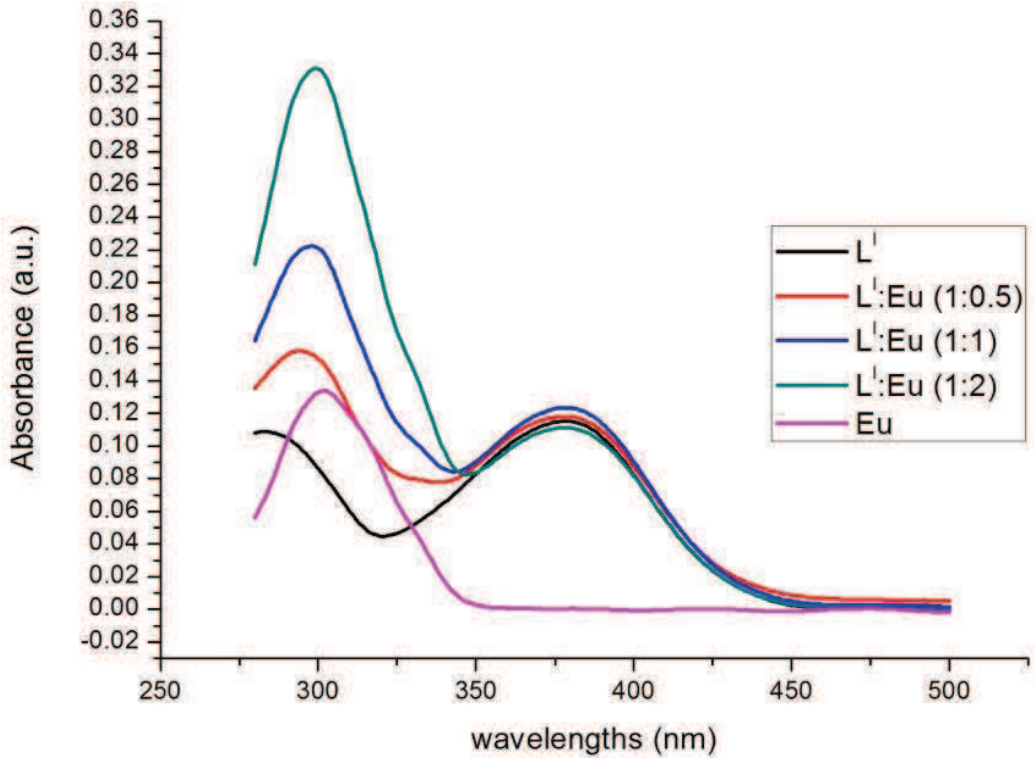

Figure 5.3 UV-vis spectra (PMMA thin film) of L^I:Eu blends.

The following step was then to study photoluminescent properties by exciting the different PMMA thin films at the main absorption band of the ligand, *i.e.* 375 nm. The emission spectra reported in Figure 5.4 reveal that the intensity of the emission of the ligand (485 nm) does not decrease significantly changing the Eu:L ratio. In parallel, the emission band attributable to Eu(III), which is centred at 614 nm as reported in figure 5.5, does not increase as we would expect if there was energy transfer between the antenna ligand and the europium ion.[85] The emission observed at 614 nm in fact could be due to a weak direct excitation at 375 of the "free" complex.

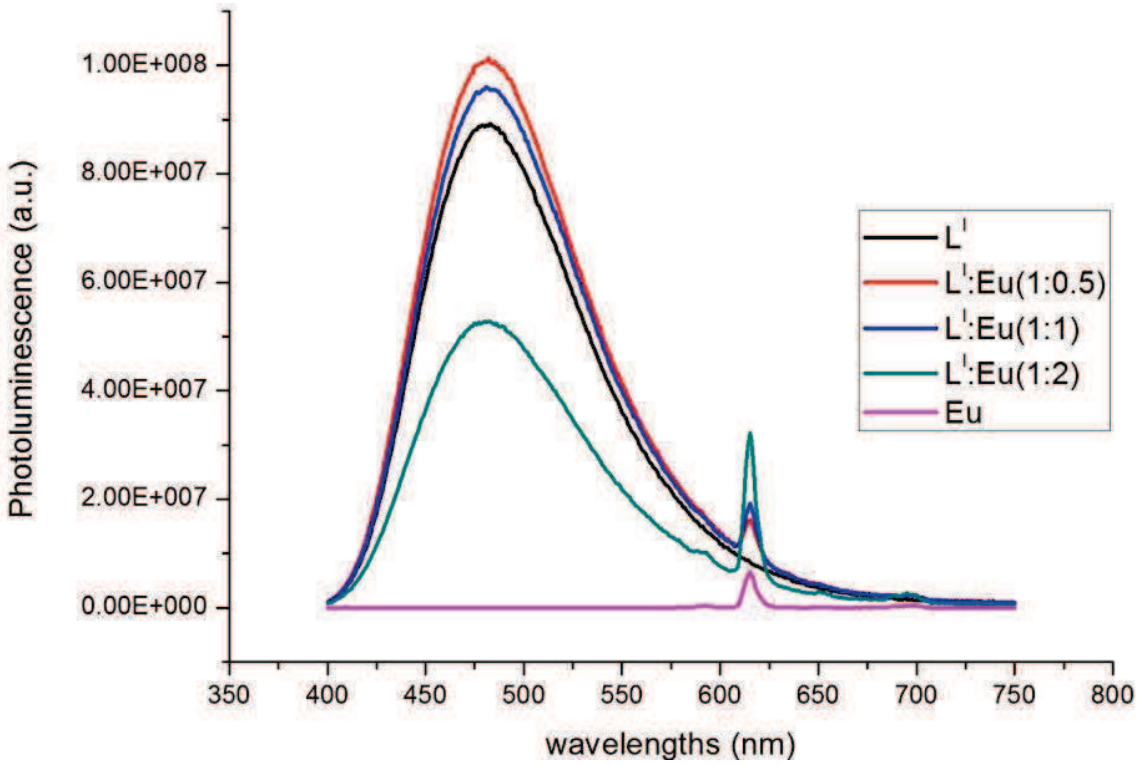

Figure 5.4 Emission spectra (PMMA thin film; excitation wavelength 375 nm) of L':Eu blends.

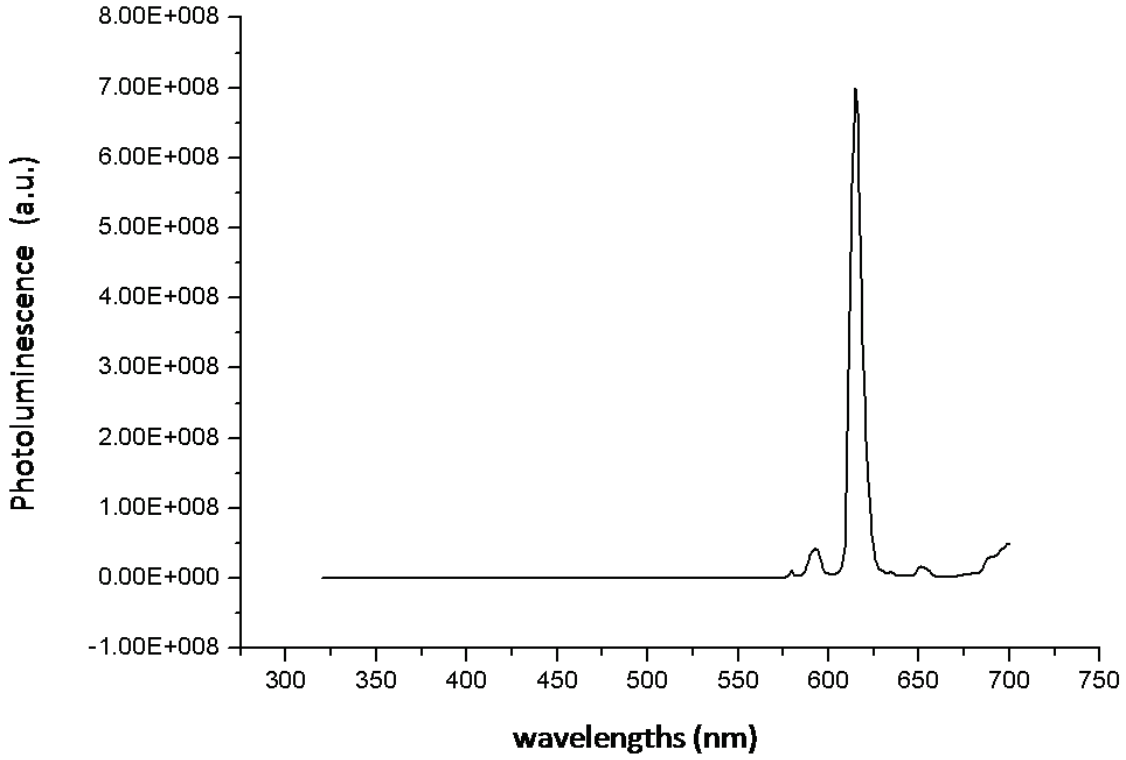

Figure 5.5 Emission spectra (PMMA thin film; excitation wavelength 300 nm) of $[Eu(hfac)_3(H_2O)_2]$.

An additional proof that could demonstrate the role of L^{I} as sensitiser is given by acquiring excitation spectra of the thin films fixing the emission wavelength at 614 nm where $[Eu(hfac)_3(H_2O)_2]$ shows its maximum emission (Figure 5.6).

As reported in Figure 5.6 the excitation spectra are characteristic of Eu(III), in fact the highest values of excitation reflect the absorption pattern of wavelengths attributable to the Eu precursor; the minimal excitation component due to the presence of the ligand allows to confirm that energy transfer between L^{I} and $[Eu(hfac)_3(H_2O)_2]$ has not occurred.

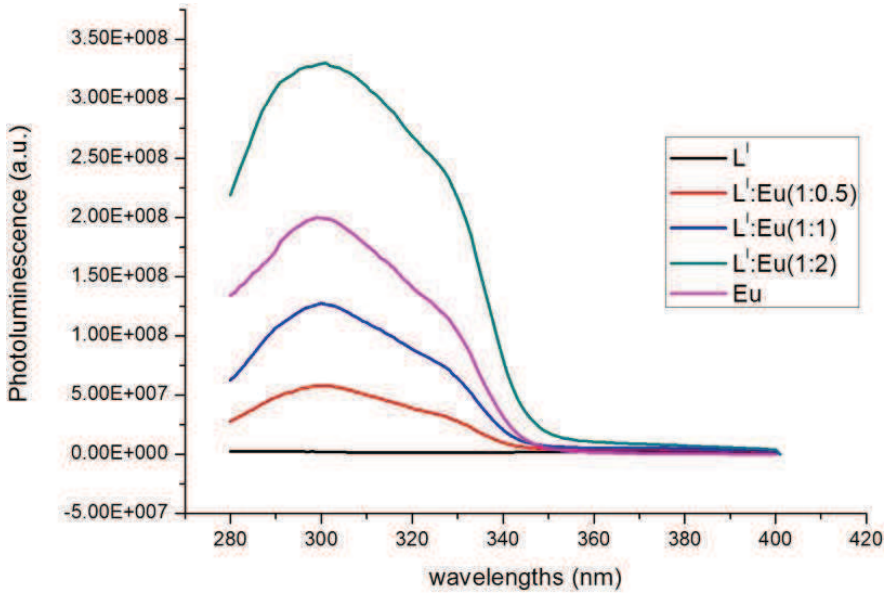

Figure 5.6 Excitation spectra (PMMA thin film; emission wavelength 390 nm) of L^{I}:Eu blends.

Other commercially available chelating ligands (Figure 5.7) have been investigated following the procedure above illustrated; in addition, has been analysed a ligand belonging to the class of 3-aryl substituted 1-(pyridin-2-yl)imidazo[1,5-*a*]pyridine, obtained as reported in the literature[51] and illustrated in Figure 5.8.

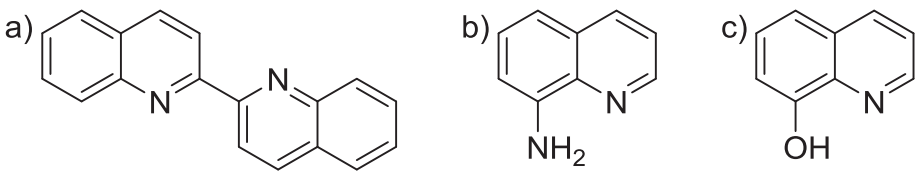

Figure 5.7 Ligand tested for self-assembling in PMMA matrix: a) 2,2^{I}-biquinoline; b) 8-aminoquinoline; c) 8-hydroxyquinoline.

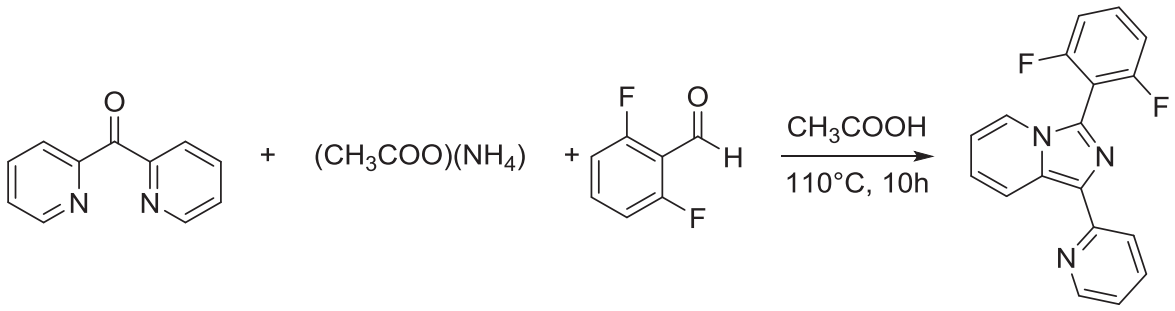

Figure 5.8 Reaction scheme for the synthesis of the ligand 1-(pyridin-2-yl)-3-(2,6-difluorophenyl)imidazo[1,5-*a*]pyridine ($L^{F,F}$).

The purity of the ligand 1-(pyridin-2-yl)-3-(2,6-difluorophenyl)imidazo[1,5-*a*]pyridine ($L^{F,F}$) was assessed by ^{1}H, ^{19}F NMR (chloroform-*d*, 25°C) and elemental analysis (see experimental section) and its structure was confirmed by X-ray single crystal analysis (Figure 5.9).

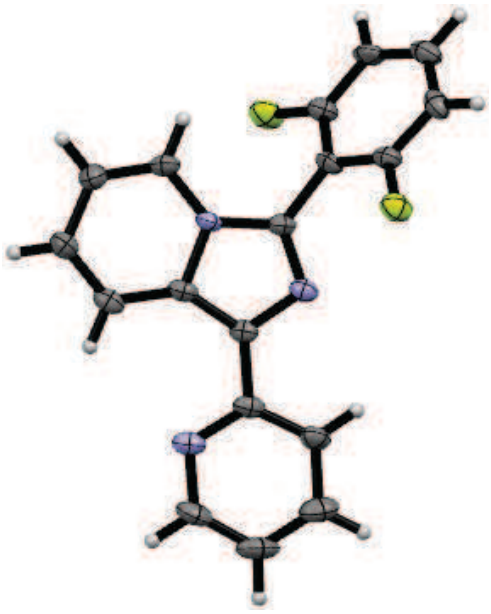

Figure 5.9 Crystal structure of $L^{F,F}$.[†]

Among the ligands tested, only results achieved with $L^{F,F}$ have shown interactions between the ligand and the Eu precursor, and, though weak, are reported hereunder.

[†] We thank The University of Edinburgh for funding the diffractometer purchase of this structure.

Uv-vis analysis of thin films has revealed that the optimal concentration of $L^{F,F}$ in PMMA chlorobenzene:acetonitrile = 1:1 solutions giving a value of absorption near 0.1 is 5 mM.

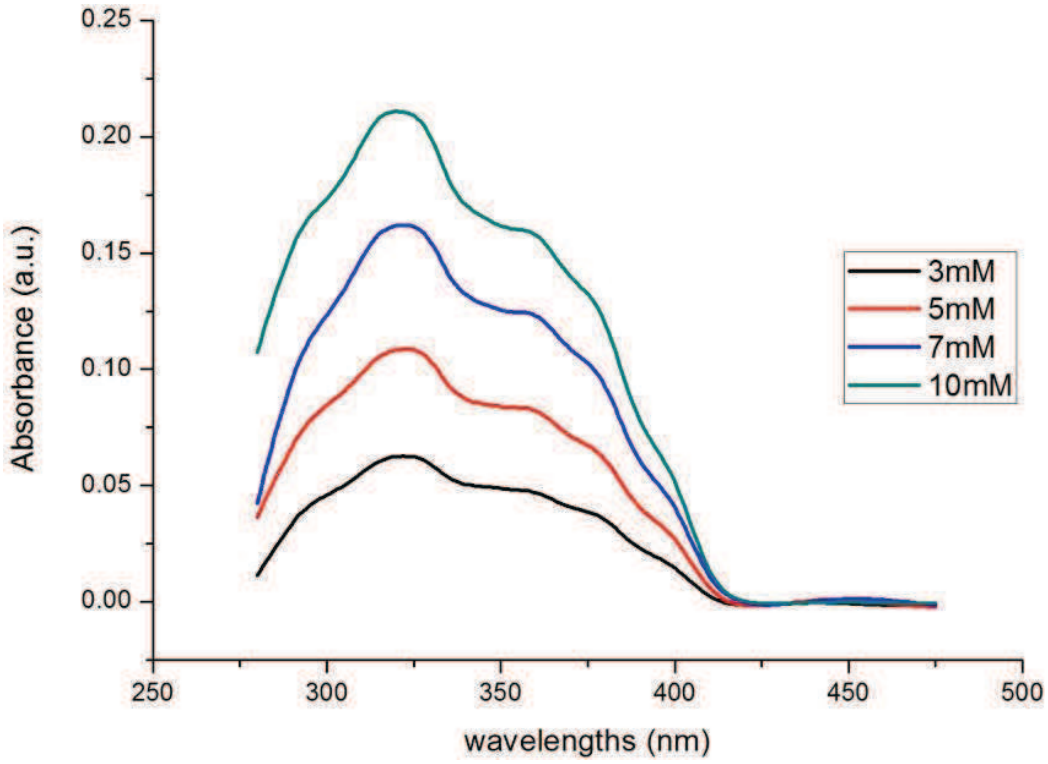

Figure 5.10 UV-vis spectra (PMMA thin film) of $L^{F,F}$.

Films obtained upon addition of $[Eu(hfac)_3(H_2O)_2]$, exhibit the absorption band of the ligand essentially unvaried, whereas the band at 300 nm increases with higher concentration of the Eu precursor (Figure 5.11).

The photoluminescent properties of the thin layers have been investigated firstly exciting them at a longer wavelength than the maximum absorption of the ligand, in order to reduce direct excitation of the free complex. As reported in Figure 5.12, even though there is a slight increase of the emission band centred at 614 nm, on the other hand there is not a parallel decrease of the emission band attributable to the ligand.

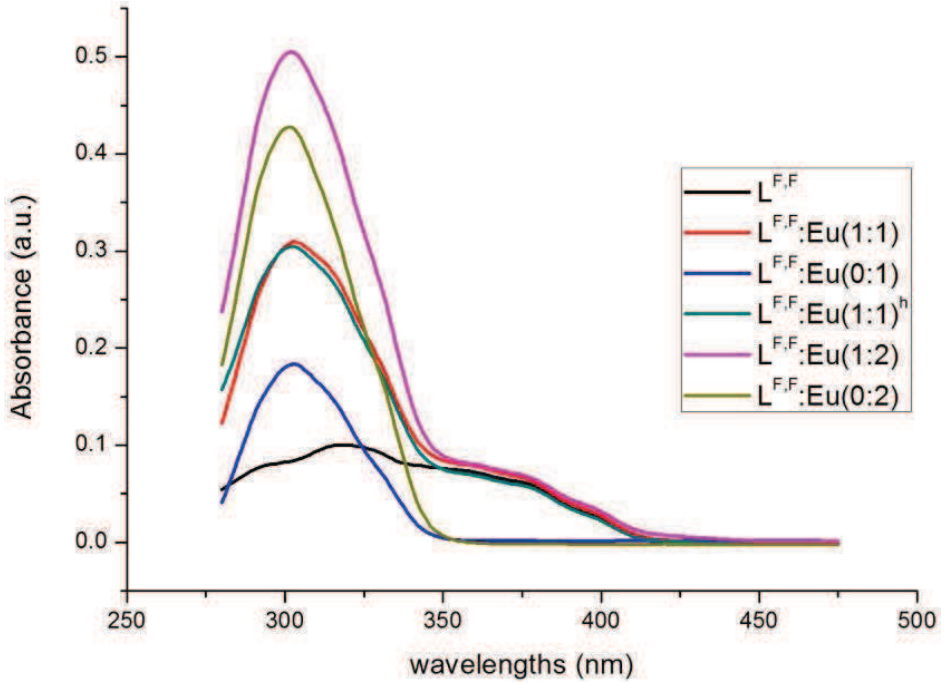

Figure 5.11 UV-vis spectra (PMMA thin film) of L^{I}:Eu blends. Sample tagged with (^{h}) has been obtained by heating the blend for 1 hour before spin-coating.

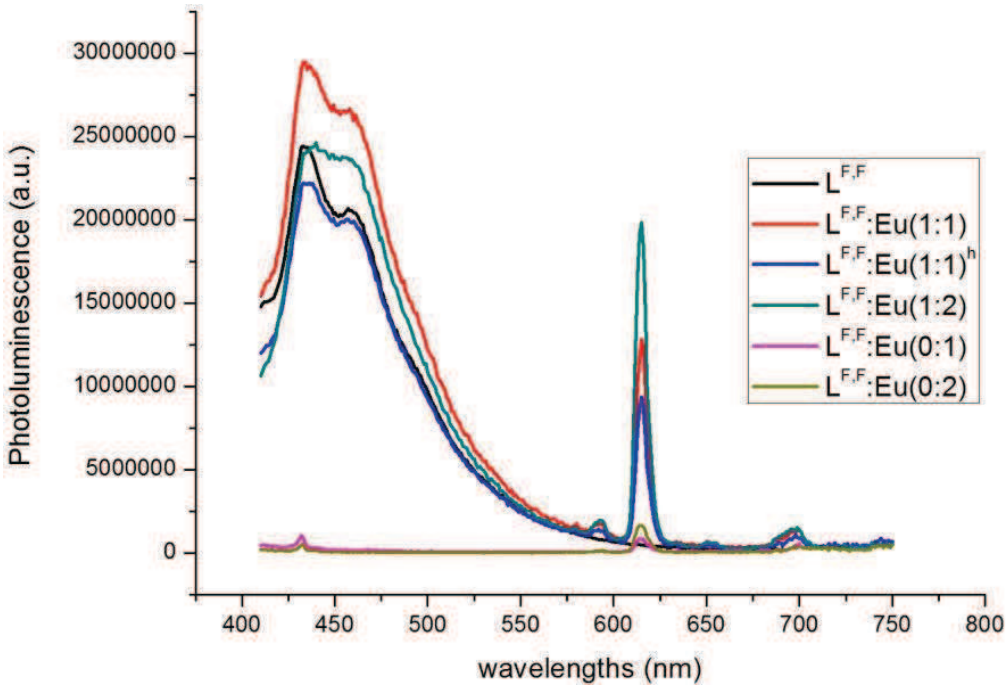

Figure 5.12 Emission spectra (PMMA thin film; excitation wavelength 390 nm) of $L^{F,F}$:Eu blends. Sample tagged with (^{h}) has been obtained by heating the blend for 1 hour before spin-coating.

Again, the excitation spectra of PMMA films acquired fixing the emission wavelength at 614 nm (Figure 5.13), has revealed to be a decisive proof which indicates the efficiency of energy transfer process between $L^{F,F}$ and the Eu(III) centre. Recording the emission at the

main Eu emission peak, nearly only the europium precursor is observed, with a weak "tail" attributable to $L^{F,F}$ observed at higher wavelengths (360-400 nm).

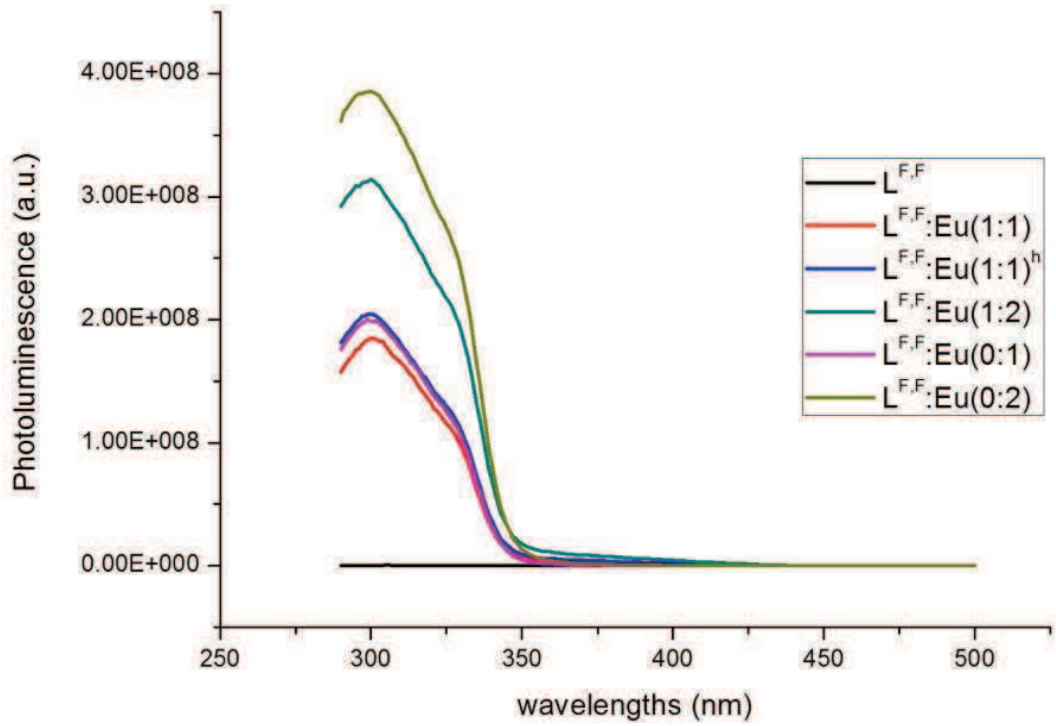

Figure 5.13 Excitation spectra (PMMA thin film; emission wavelength 614 nm) of L^{l}:Eu blends. Sample tagged with (^{h}) has been obtained by heating the blend for 1 hour before spin-coating.

There could be different reasons that do not permit the energy transfer from ligand to Eu centre in "in situ" generated PMMA films. Since one of that could be the absence of coordination of the ligand to Eu, we have tried to isolate the complex reacting $[Eu(hfac)_3(H_2O)_2]$ with $L^{F,F}$. Despite different reaction conditions have been tried, it has not been possible to achieve the product in which $L^{F,F}$ coordinates to Eu(III); probably, the N,N-azabidentate ligand does not exhibit enough affinity towards the Eu centre.

Though the reported method to fabricate "in situ" luminescent polymers films for downshifting has revealed not to be efficient for the ligands checked, it could be considered as a simple and quick process which could be used as a preventive check to try out different combinations of metal, ligand and polymer for potential applications as LDS materials.

Chapter 6

Conclusions

In this Thesis work, three new classes of d^{10}-metals luminescent compounds with N-donor and P-donor ligands have been synthesised. The complexes have been fully characterised and their behaviour in solution and in the solid state has been elucidated. Moreover, an investigation on their photophysical features was performed in order to have a better understanding of their structure-properties correlation and their possible further application in material science.

In Chapter 2 have been reported results achieved studying a Cu(I) class of complexes bearing lactate as anion. The presence of lactate made possible to establish diverse H-bonding interactions, which led to a class of complexes showing interesting luminescent properties. Starting from $[Cu(PPh_3)_2(lact)]$ as precursor, the introduction of different P- and N-donor ligands, allowed the tuning of emission properties of the corresponding derivatives $[Cu_2(\mu\text{-dppm})_2(\mu\text{-}\eta^2\text{-lact})(\eta^1\text{-lact})]$ (**1**), $[Cu(phen)(PPh_3)_2(lact)]$ (**2**) and $[Cu(PPh_3)_2(L^{OH})](lact)$ (**3**), L^{OH} = 2-(1-(pyridin-2-yl)imidazo[1,5-*a*]pyridin-3-yl)phenol). Within the current approach photoluminescence quantum yields are not significant, but further studies and measurements (i.e., lifetime decay) could explain deeply their features and hopefully give a starting point for future improvements.

Chapter 3 have focused on two classes of Zn(II) derivatives bearing 3-aryl substituited 1-pyridylimidazo[1,5-a]pyridine ligands.

The first class has been obtained by coordinating L^{Me} (1-(pyridin-2-yl)-3-*o*-tolylimidazo[1,5-*a*]pyridine) and the above mentioned L^{OH} to zinc(II) halides giving a series of blue emitting compounds having a $Zn(N\cap N)X_2$ core. Their optical properties have been analysed in the solid state, demonstrating blue emission with absolute quantum yields values close to similar $Zn(N\cap N)X_2$ complexes reported in literature. The two ligands showed different behaviour when coordinated to ZnX_2 fragments: in the case of L^{Me}, a decrease of PLQY was noticed when coordinated to ZnX_2 fragments, while L^{OH} has a poor quantum yield which increased after coordination to zinc. This is related to the presence of intermolecular H-bonds in the solid structure of L^{OH}, which favour thermal non-radiative relaxation processes hence being responsible of the reduced fluorescence emission. In the $[Zn(L^{OH})X_2]$ complexes, the absence of H-bonds network (as corroborated by spectroscopic and crystallographic data), enhances the emission quantum yield of the

system when compared to the free ligand. The blue emitting complexes discussed in this Chapter can be considered an interesting example in which emission properties are structure-dependent, again, related to intermolecular hydrogen bonds.

The second class of Zn(II) derivatives has been obtained focusing the attention on L^{OH}, which has been coordinated to zinc(II) salts with a polyatomic anion, $ZnY_2 \cdot nH_2O$ (Y = ClO_4^-; NO_3^-, BF_4^-; PF_6^-) in a 2:1 molar ratio, obtaining a series of blue-green emitting complexes formulated as $[Zn(L^{OH})_2](Y)_2 \cdot nH_2O$. A full spectroscopic characterisation of these species has determined the water content in each compound, also confirmed by the single crystal X-ray structure analysis of two derivatives. In the solid state, these species showed blue-green emission (491- 494 nm) with a general red shift of about 40-48 nm with respect to the free ligand. A slightly different behaviour was noticed for compound $[Zn(L^{OH})_2](NO_3)_2 \cdot H_2O$ (**11**), displaying a remarkably minor bathochromic shift (16 nm) compared to L^{OH}. These complexes displayed absolute photoluminescence quantum yields (Φ_{PL}) comprised between 0.09 and 0.16, slightly inferior compared to the above reported $[Zn(L^{OH})X_2]$ (X = Cl, Br, I) species.

In Chapter 4 we have mainly addressed our attention on the photophysical properties of a class of heteroleptic Ag(I) complexes, formulated as $[Ag(L^{OH})(P)](NO_3)$ (P = PPh_3 (**17**), PPh_2Me (**18**), $PPhMe_2$ (**19**), PBu_3 (**20**), P(*p*-tolil)$_3$ (**21**), $P(OPh)_3$ (**22**), $P(OEt)_3$ (**23**). These species have been fully characterised in solution and in the solid state, and a similar behaviour has been noted for all the reported derivatives: they all show a N_2P, trigonal environment around the silver ion, the NO_3 anion being not coordinated to the metal.
As far as concerns luminescence, a strict correlation between the emission properties and the electronic features of the phosphorous ligand, and consequently of the complex, has been successfully confirmed. Indeed, keeping the $[Ag(L^{OH})]^+$ fragment fixed, by simply changing the electronic properties of ancillary phosphine it was possible to modulate the λ_{max} of emission of the resulting compounds from 435 nm (P = PBu_3) to 496 nm (P = $P(OPh)_3$).
The effect of the P-donor ligand can be nicely showed by plotting the maximum emission of the complexes expressed in wavenumber *vs.* Tolman's substituent contribution χ.

Furthermore this correlation has been confirmed also analysing luminescence in the solid state, where the increasing π-acidity of phosphorous ligands results in a batochromic shift of the emission.
All the derivatives analysed displayed good absolute photoluminescence quantum yields (Φ_{PL}) values in solution, comprised between 0.30 and 0.52; Φ_{PL} recorded in the solid state were a little bit lower, except for $[Ag(L^{OH})(PPh_3)](NO_3)$ which showed a remarkably higher value (0.68, to be compared with 0.52 obtained in solution).

In Chapter 5 are reported results achieved during the period spent at University of Edinburgh under the supervision of Dr. Neil Robertson. Though the investigation on luminescent material for downshifting has not given successful results with the ligands tested, has been highlighted a useful methodology for a preventive check of different combinations of metal, ligand and polymer for potential applications as LDS materials

In conclusion, despite additional studies are needed to fully exploit the behaviour of the abovementioned compounds, this work highlighted the possibility to employ d^{10}-metals to synthesise coordination compounds with interesting luminescent features, strictly depending on the electronic (and steric) environment around the metal centre imposed by ancillary ligands.

Chapter 7

Experimental Section

7.1 General Remarks

Caution! *Although we have experienced no difficulties, perchlorate salts of metal complexes with organic ligands are potentially explosive and should be handled with care even in small quantities.*

All reactions were carried out under inert atmosphere using standard Schlenk techniques. Solvents were deoxygenated with nitrogen prior to use. NMR spectra were recorded with an AVANCE 400 Bruker spectrometer at 400 MHz for ^{1}H NMR, 100 MHz for ^{13}C{^{1}H} NMR and 162 MHz for ^{31}P{^{1}H} NMR. Chemical shifts are given as δ values in ppm relative to residual solvent peaks as the internal reference (for ^{1}H and ^{13}C NMR) and to external H_3PO_4 (85%) (for ^{31}P NMR). *J* values are given in Hz. ^{13}C NMR spectra are ^{1}H-decoupled and the determination of the multiplicities was achieved by the APT pulse sequence. Elemental analyses were performed with a Perkin-Elmer CHN Analyzer 2400 Series II. Infrared Spectra were acquired on a Shimadzu Prestige 21 instrument with a 1-cm^{-1} resolution. ATR-IR Spectra were acquired on a Nicolet iS10 FT-IR instrument equipped with Smart iTR ATR accessory with a 1-cm^{-1} resolution. Thermogravimetric analyses (TGA) were performed in a N_2 stream on a Netzsch STA 409 PC Luxx (heating rate 10°C/min). Uv-vis Spectra were acquired on a Thermo Scientific Evolution 220 UV-vis Spectrophotometer. Excitation and emission spectra were recorded on a Photon Technologies International QuantaMaster QM-40 spectrometer (equipped with Xe arc lamp, 70 W) and were corrected for the wavelength response of the instrument. Absolute fluorescence quantum yields were determined using a PhotoMed GmbH K-Sphere Integrating Sphere (3.2 inch. diameter).

University of Edinburgh Absorption spectra were recorded with a UV/Vis/NIR spectrophotometer Jasco V-670. Emission spectra at room temperature in PMMA matrix were measured by FluoroMax-3. Excitation light was delivered with a 150 W Ozone-free xenon arc lamp and the emission was detected by R928P photo counting PMT (185-850 nm).

All reagents used in the syntheses (SigmaAldrich) were of commercial grade and used as received. Ligands 1-(pyridin-2-yl)-3-*o*-tolylimidazo[1,5-*a*]pyridine (L^{Me}) and 2-(1-(pyridin-2-yl)imidazo[1,5-*a*]pyridin-3-yl)phenol (L^{OH}) were prepared following a published procedure.[51] Starting materials $[Cu(PPh_3)_2(lact)]$[37], $ZnBF_4$ hydrate and $ZnPF_6$ hydrate[57] were prepared as reported elsewhere.

University of Edinburgh All reagents used in the synthesis (Sigma Aldrich) were of commercial grade and used as received. The polymer matrix consisted of PMMA with $M_W \approx 15000$. Tris(hexafluoroacetylacetonate)europium(III) dihydrate was synthesised according to a published procedure[86].

Thin films were prepared on 1 mm thick 25x25 mm glass slides. Glass slides were cleaned by sequential sonication in Deacon 90 detergent(x2), distilled water (x2) and isopropanol (x2). PMMA solution (100 mg/mL) was prepared dissolving 500mg of PMMA in 5 mL of solution chlorobenzene:actonitrile=9:1. Ligands and $[Eu(hfac)_3(H_2O)_2]$ were mixed in PMMA solutions at different ratios keeping the right concentration to achieve convenient spectroscopic intensities without saturation. Then, 100 µL of the PMMA mixture was drop onto a glass slide and spin-coated for 60 seconds at 1000 rpm, followed by 15 second at 4000 rpm.
Spin-coating was performed with a Spin-Coater by Laurell Technologies (Model WS-65OS-6NPP/LITE).

7.2 Synthesis of $[Cu(dppm)(lact)]_2$ (1)

Complex $[Cu(PPh_3)_2(lact)]$ (250 mg, 0.369 mmol) was added to a solution of 1,1-bis(diphenylphosphino)methane (dppm, 142 mg, 0.369 mmol) in diethylether (15 mL); the resulting mixture was allowed to stir at room temperature for 24 hours. The white solid was filtered, washed with diethylether and then dried under vacuum. Yield: 95 mg (48%). IR (nujol, ν/cm^{-1}): 3434br (OH), 1583s (CO), 1610s (CO). ^1H NMR (400 MHz, $CD_3C(O)CD_3$, 25°C): δ 1.30 (d, 3H, C*H*$_3$), 3.53 (s, 2H, *CH*$_2$), 3.99 (q, 1H, C*H*), 7.06-7.56 (m, 20H, PPh_2) ppm. $^{31}P\{^1H\}$ NMR (162 MHz, $CD_3C(O)CD_3$, 25°C): δ -13.57 ppm. Elemental analysis calcd. for $C_{56}H_{56}Cu_2O_6P_4$ (1074.03): C 62.51, H 5.25; found C 62.58, H 5.49 %.

7.3 Synthesis of $[Cu(phen)(PPh_3)_2(lact)]$ (2)

To a solution of 1,10-phenanthroline (phen, 70 mg, 0.389 mmol) in diethylether (15 mL), $[Cu(PPh_3)_2(lact)]$ (250 mg, 0.369 mmol) was added. Suddenly a dark green suspension formed which was stirred at room temperature for 24 hours; during this time the formation of a yellow suspension occurred. Then the solid was filtered, washed with diethylether and dried under vacuum. Yield: 215 mg (68%). IR (nujol, ν/cm^{-1}): 3324br (OH), 1614s (CO). ^1H NMR (400 MHz, $CD_3C(O)CD_3$, 25°C): δ 1.44 (s, br, 3H, C*H*$_3$), 4.10 (s, br, 1H, C*H*), 7-28-7.32 (m, 30H, PPh_3) 7.75 (s, br, phen), 8.01 (s, br, phen), 8.48 (s, br, phen), 8.86 (s, br, phen). $^{31}P\{^1H\}$ NMR (162 MHz, $CD_3C(O)CD_3$, 25°C): δ -2.16 ppm. Elemental analysis calcd. for $C_{51}H_{42}CuN_2O_3P_2$ (857.41): C 71.44, H 5.06, N 3.27; found C 71.58, H 5.39, N 3.25 %.

7.4 Synthesis of $[Cu(PPh_3)_2(L^{OH})](lact)$ (3)

Complex $[Cu(PPh_3)_2(lact)]$ (250 mg, 0.369 mmol) was added to a suspension of L^{OH} (111 mg, 0.388 mmol) in diethylether (15 mL) And the resulting yellow suspension was allowed to stir for 24 hours at room temperature. Then the solvent was evaporated to half the volume, methanol (10 mL) was added and the suspension stirred for 1 hour at 50°C, affording a yellow solution. The solvent was removed under reduced pressure and the crude product was suspended in diethylether (10 mL); the yellow solid was filtered off,

washed with diethylether and dried under vacuum. Yield: 309 mg (87 %). IR (nujol, ν/cm^{-1}): 3396br (OH), 1600w (CO), 1544w, 1516w. ^{1}H NMR (400 MHz, $CD_3C(O)CD_3$, 25°C): δ 1.23 (d, $J_{H,H}$ = 6.4 Hz, 3H, C*H*$_3$), 3.84 (s, br, 1H, C*H*), 6.36 (s, br, L^{OH}), 6.86 (s, br, L^{OH}), 6.85 (s, br, L^{OH}), 7.03-7.07 (m, PPh_3), 7.14-7.18 (m, PPh_3), 7.21-7.25 (m, L^{OH}), 7.32-7.36 (m, PPh_3), 7.44 (s, br, L^{OH}), 7.81-7.85 (m, L^{OH}), 7.94-8.01 (m, L^{OH}). $^{31}P\{^{1}H\}$ NMR (162 MHz, $CD_3C(O)CD_3$, 25°C): δ 0.62 ppm. Elemental analysis calcd. for $C_{57}H_{48}CuN_3O_4P_2$ (964.52): C 70.98, H 5.02, N 4.36; found C 71.09, H 5.27, N 4.43 %.

7.5 Synthesis of [Zn(L^{Me})X$_2$] complexes (X = Cl, Br, I)

To a suspension of L^{Me} (100 mg, 0.350 mmol) in methanol (15 mL), anhydrous ZnX_2 (0.400 mmol) was added and a yellow suspension immediately formed. It was stirred at room temperature for 2 hours, then it was filtered and the yellow solid was washed with methanol, diethylether and then dried under vacuum.

[Zn(L^{Me})Cl$_2$] (4): Yield 110 mg (74%). ^{1}H NMR (400 MHz, CD_2Cl_2, 25 °C): δ = 2.24 (s, 3H, C*H*$_3$), 6.97 (td, $J_{H,H}$ = 6.9 Hz, $J_{H,H}$ 1.0 Hz, 1H, Ar-H), 7.35 (ddd, $J_{H,H}$ = 9.0 Hz, $J_{H,H}$ = 6.7 Hz, $J_{H,H}$ 1.0 Hz, 1H, Ar-H), 7.46-7.54 (m, 3H, Ar-H), 7.63 (td, $J_{H,H}$ = 7.5 Hz, $J_{H,H}$ 1.4 Hz, 1H, Ar-H), 7.71 (m, 2H, Ar-H), 8.05 (ddt, $J_{H,H}$ = 8.2 Hz, $J_{H,H}$ = 6.9 Hz, $J_{H,H}$ = 1.2 Hz, 2H, Ar-H), 8.09-8.16 (m, 1H, Ar-H), 8.65 (dt, $J_{H,H}$ = 5.2 Hz, $J_{H,H}$ = 1.3 Hz, 1H, Ar-H). $^{13}C\{^{1}H\}$ NMR (100 MHz, CD_2Cl_2, 25 °C): δ = 19.41 (*C*H$_3$), 115.93, 118.13, 120.07, 123.32, 123.43, 124.54, 124.92, 125.50, 126.83, 128.70, 131.07, 131.27, 131.74, 138.64, 139.64, 140.58, 148.09, 148.64 ppm. Elemental analysis calcd. for $C_{19}H_{15}Cl_2N_3Zn$ (421.66): C 54.12, H 3.59, N 9.97; found C 54.35, H 3.33, N 9.86 %.

Single crystals suitable for X-ray analysis were grown by slow diffusion of hexane into a solution of compound **4** in CH_2Cl_2.

$[Zn(L^{Me})Br_2]$ (5): Yield: 125 mg (70%). ^{1}H NMR (400 MHz, CD_2Cl_2, 25 °C): δ = 2.23 (s, 3H, C*H*$_3$), 6.98 (td, $J_{H,H}$ = 6.9 Hz, $J_{H,H}$ = 1.1 Hz, 1H, Ar-H), 7.36 (ddd, $J_{H,H}$ = 9.4 Hz, *J*H,H = 6.7 Hz, $J_{H,H}$= 1.0 Hz, 1H, Ar-H), 7.49-7.53 (m, 3H, Ar-H), 7.63 (td, $J_{H,H}$= 7.7 Hz, $J_{H,H}$= 1.4 Hz, 1H, Ar-H), 7.72 (m, 2H, Ar-H), 8.02-8.07 (m, 2H, Ar-H), 8.12 (td, $J_{H,H}$= 7.9 Hz, $J_{H,H}$ = 1.7 Hz, 1H, Ar-H), 8.66 (dt, $J_{H,H}$ = 5.3 Hz, $J_{H,H}$ = 1.3 Hz, 1H, Ar-H). ^{13}C{^{1}H} NMR (100 MHz, CD_2Cl_2, 25 °C): δ = 19.47 (*C*H$_3$), 115.93, 118.08, 120.03, 123.35, 123.39, 124.38, 124.82, 125.52, 126.77, 128.72, 130.98, 131.39, 131.78, 138.67, 139.69, 140.55, 147.90, 148.57 ppm. Elemental analysis calcd. for $C_{19}H_{15}Br_2N_3Zn$ (510.56): C 44.70, H 2.96, N 8.23; found C 44.38, H 3.05, N 8.41 %.

$[Zn(L^{Me})I_2]$ (6): Yield: 140 mg (66%). ^{1}H NMR (400 MHz, CD_2Cl_2, 25 °C): δ = 2.21 (s, 3H, C*H*$_3$), 6.98 (td, $J_{H,H}$ = 6.8 Hz, $J_{H,H}$ = 1.0 Hz, 1H, Ar-H), 7.36 (ddd, $J_{H,H}$= 9.4 Hz, $J_{H,H}$= 6.7 Hz, $J_{H,H}$ = 1.0 Hz, 1H, Ar-H), 7.46-7.54 (m, 3H, Ar-H), 7.63 (td, $J_{H,H}$ = 7.7 Hz, $J_{H,H}$ = 1.4 Hz, 1H, Ar-H), 7.69 (dt, $J_{H,H}$= 7.2 Hz, $J_{H,H}$= 1.1 Hz, 1H, Ar-H), 7.72-7.79 (m, 1H, Ar-H), 8.05 (ddt, $J_{H,H}$= 10.1 Hz, $J_{H,H}$= 8.3 Hz, $J_{H,H}$= 1.2 Hz, 2H, Ar-H), 8.11 (td, $J_{H,H}$= 7.9 Hz, $J_{H,H}$= 1.7 Hz, 1H, Ar-H), 8.67 (dt, $J_{H,H}$= 5.3 Hz, $J_{H,H}$= 1.3 Hz, 1H, Ar-H). ^{13}C{^{1}H} NMR (100 MHz, CD_2Cl_2, 25 °C): δ = 19.68 (*C*H$_3$), 115.96, 118.05, 120.03, 123.29, 123.33, 124.15, 124.71, 125.57, 126.69, 128.77, 130.89, 131.60, 131.81, 138.67, 139.73, 140.51, 147.60, 148.38 ppm. Elemental analysis calcd. for $C_{19}H_{15}I_2N_3Zn$ (604.56): C 37.75, H 2.50, N 6.95; found C 37.43, H 2.59, N 6.86 %. Single crystals suitable for X-ray analysis were grown by slow diffusion of hexane into a solution of compound **6** in CH_2Cl_2.

7.6 Synthesis of $[Zn(L^{OH})X_2]$ complexes

To a suspension of L^{OH} (100 mg, 0.348 mmol) in methanol (15 mL), anhydrous ZnX_2 (0.400 mmol) was added and a yellow suspension immediately formed. It was stirred at room temperature for 2 hours, then it was filtered and the yellow solid was washed with methanol, diethylether and dried under vacuum.

$[Zn(L^{OH})Cl_2]$ (7): Yield: 118 mg (80%). IR (hexachlorobutadiene): ν/cm^{-1} 3277 (s, OH). Elemental analysis calcd. for $C_{18}H_{13}Cl_2N_3OZn$ (426.63): C 51.03, H 3.09, N 9.92; found C 50.86, H 2.99, N 9.61 %.

Single crystals suitable for X-ray analysis were grown by slow diffusion of diethylether into a solution of compound **7** in DMF.

Elemental analysis of grinded crystals calcd. for $C_{21}H_{20}Cl_2N_4O_2Zn$ (496.73): C 50.78, H 4.06, N 11.28; found C 50.83, H 3.98, N 11.32 %.

$[Zn(L^{OH})Br_2]$ (8): Yield: 139 mg (78%). IR (hexachlorobutadiene): ν/cm^{-1} 3276 (s, OH). Elemental analysis calcd. for $C_{18}H_{13}Br_2N_3OZn$ (512.53): C 42.18, H 2.56, N 8.20; found C 42.05, H 2.68, N 8.07 %.

$[Zn(L^{OH})I_2]$ (9): Yield: 158 mg (75%). IR (hexachlorobutadiene): ν/cm^{-1} 3282 (s, OH). Elemental analysis calcd. for $C_{18}H_{13}I_2N_3OZn$ (606.53): C 35.64, H 2.16, N 6.93; found C 35.48, H 2.29, N 6.68 %.

7.7 Synthesis of $[Zn(L^{OH})_2](ClO_4)_2 \cdot H_2O$ (10)

To a suspension of L^{OH} (200 mg, 0.696 mmol) in methanol (15 mL), $Zn(ClO_4)_2 \cdot 6H_2O$ (130 mg, 0.349 mmol) was added and the resulting suspension was stirred at room temperature for 1 hour. During this time a clear yellow solution formed, which was further stirred for other 3 hours. Then the solvent was removed under reduced pressure, the residue was suspended in diethylether (10 mL) and the yellow solid was filtered off, washed with diethylether and dried under vacuum. Yield: 215 mg (71%). IR (nujol, ν/cm^{-1}): 3352br (OH), 1639m, 1613s, 1567m, 1550m, 1517m, 1132-1099br (ClO_4). ^{1}H NMR (400 MHz, $CD_3C(O)CD_3$, 25°C): δ 6.62 (td, $J_{H,H}$ = 7.6 Hz, $J_{H,H}$ = 1.1 Hz, 1H, Ar-H), 6.85 (dd, $J_{H,H}$ = 8.4 Hz, $J_{H,H}$ = 1.1 Hz, 1H, Ar-H), 7.15-7.11 (m, 2H, Ar-H), 7.23-7.18 (m, 1H, Ar-H), 7.34 (ddd, $J_{H,H}$ = 7.6 Hz, $J_{H,H}$ = 5.3 Hz, $J_{H,H}$ = 1.1 Hz, 1H, Ar-H), 7.49 (ddd, $J_{H,H}$ = 9.6 Hz, $J_{H,H}$ = 6.6 Hz, $J_{H,H}$ = 1.0 Hz, 1H, Ar-H), 8.06 (d, $J_{H,H}$ = 7.3 Hz, 1H, Ar-H), 8.14 (td, $J_{H,H}$ = 7.9 Hz, $J_{H,H}$ = 1.7 Hz, 1H, Ar-H), 8.30 (d, $J_{H,H}$ = 8.1 Hz, 1H, Ar-H), 8.40 (d, $J_{H,H}$ = 9.4 Hz, 1H, Ar-H), 8.51 (d, $J_{H,H}$ = 4.7 Hz, 1H, Ar-H), 9.15 (s, 1H, OH). Elemental analysis calcd. for $C_{36}H_{28}Cl_2N_6O_{11}Zn$: C, 50.46; H, 3.29; N, 9.81; found: C, 50.51; H, 3.23; N, 9.86%.

Single crystals suitable for X-ray analysis were obtained by slow diffusion of pentane in a saturated solution of **10** in methyl ethyl ketone.

7.8 Synthesis of $[Zn(L^{OH})_2](NO_3)_2 \cdot H_2O$ (11)

To a suspension of L^{OH} (200 mg, 0.696 mmol) in methanol (15 mL), $Zn(NO_3)_2 \cdot 6H_2O$ (104 mg, 0.349 mmol) was added and the resulting suspension was stirred at room temperature for 4 hours. Then it was filtered and the yellow solid was washed with methanol, diethylether and dried under vacuum.

Yield: 156 mg (57%).

IR (nujol, ν/cm^{-1}): 3480br (OH), 1642m, 1613s, 1566m, 1548m, 1516m, 1341m (NO_3), 1290s (NO_3).

Elemental analysis calcd. for $C_{36}H_{28}N_8O_9Zn$: C, 55.29; H, 3.61; N, 14.33; found: C, 55.88; H, 3.48; N, 14.25%.

7.9 Synthesis of $[Zn(L^{OH})_2](BF_4)_2 \cdot 4H_2O$ (12)

To a suspension of L^{OH} (200 mg, 0.696 mmol) in methanol (15 mL), $Zn(BF_4)_2 \cdot xH_2O$ (83 mg, 0.348 mmol, anhydrous basis) was added and the resulting suspension was stirred at room temperature for 1 hour. During this time a clear yellow solution formed, which was further stirred for other 3 hours. Then the solvent was removed under reduced pressure, the residue was suspended in diethylether (10 mL) and the yellow solid was filtered off, washed with diethylether and dried under vacuum. Yield: 248 mg (81%). IR (nujol, ν/cm^{-1}): 3480br (OH), 1639m, 1612s, 1568m, 1549m, 1516m, 1053br (BF_4). ^{1}H NMR (400 MHz, $CD_3C(O)CD_3$, 25°C): δ 6.60 (td, $J_{H,H}$ = 7.8 Hz, $J_{H,H}$ = 1.1 Hz, 1H, Ar-H), 6.85 (dd, $J_{H,H}$ = 8.3 Hz, $J_{H,H}$ = 1.1 Hz, 1H, Ar-H), 7.13-7.10 (m, 2H, Ar-H), 7.22-7.18 (m, 1H, Ar-H), 7.34 (td, $J_{H,H}$ = 6.4 Hz, $J_{H,H}$ = 1.2 Hz, 1H, Ar-H), 7.48 (ddd, $J_{H,H}$ = 9.5 Hz, $J_{H,H}$ = 6.5 Hz, $J_{H,H}$ = 1.0 Hz, 1H, Ar-H), 8.03 (d, $J_{H,H}$ = 7.2 Hz, 1H, Ar-H), 8.13 (td, $J_{H,H}$ = 7.8 Hz, $J_{H,H}$ = 1.7 Hz, 1H, Ar-H), 8.29 (d, $J_{H,H}$ = 8.4 Hz, 1H, Ar-H), 8.39 (d, $J_{H,H}$ = 9.5 Hz, 1H, Ar-H), 8.50 (d, $J_{H,H}$ = 5.3 Hz, 1H, Ar-H), 9.09 (s, 1H, OH). Elemental analysis calcd. for $C_{36}H_{34}B_2F_8N_6O_6Zn$: C, 48.82; H, 3.87; N, 9.49; found: C, 48.91; H, 3.68; N, 9.99%.

7.10 Synthesis of $[Zn(L^{OH})_2](PF_6)_2 \cdot H_2O$ (13)

Step A. To a solution of $AgNO_3$ (1 g, 5.882 mmol) in CH_3CN was added an equimolar amount of KPF_6 (1.083 g, 5.883 mmol) and the resulting suspension was stirred at room temperature for 1 hour. Then insoluble KNO_3 was filtered off, and the solvent was removed under reduced pressure from the filtrate. The white residue was suspended in diethylether and the solid was filtered, dried in vacuum and stored in a dry, dark atmosphere.

Step B. To a solution of L^{OH} (400 mg, 1.392 mmol) and $[Zn(L^{OH})Cl_2]$ [prepared as reported in procedure 5.6] (590 mg, 1.392 mmol) in CH_2Cl_2 (10 mL), $AgPF_6$ from step A (739 mg, 2.924 mmol) was added and suddenly a yellowish suspension formed, which was stirred for 1 h. The mixture was separated by filtration affording a white solid (AgCl) which was discarded, and a yellow solution. The solvent was removed under rotary evaporation, then the crude product was suspended in diethylether (10 mL) and the yellow solid was filtered off, washed with diethylether, dried and stored in a dry atmosphere. Yield: 1.216 g (94%). IR (nujol, v/cm^{-1}): 3641br (OH), 3507br (OH), 1607s, 1533m, 1337m, 1295s, 825s (PF_6). ^{1}H NMR (400 MHz, $CD_3C(O)CD_3$, 25°C): δ 6.58 (t, $J_{H,H}$ = 7.7 Hz, 1H, Ar-H), 6.83 (d, $J_{H,H}$ = 8.3Hz, 1H, Ar-H), 7.11-7.06 (m, 2H, Ar-H), 7.20 (t, $J_{H,H}$ = 7.6 Hz, 1H, Ar-H), 7.31 (t, $J_{H,H}$ = 6.5 Hz, 1H, Ar-H), 7.46 (t, $J_{H,H}$ = 8.3 Hz, 1H, Ar-H), 7.99 (d, $J_{H,H}$ = 7.1 Hz, 1H, Ar-H), 8.13-8.07 (m, 1H, Ar-H), 8.24 (d, $J_{H,H}$ = 8.3 Hz), 8.36 (d, $J_{H,H}$ = 9.5 Hz, 1H, Ar-H), 8.47 (d, $J_{H,H}$ = 5.4 Hz, 1H, Ar-H), 9.16 (s, 1H, OH). $^{31}P\{^1H\}$ NMR (162 MHz, $CD_3C(O)CD_3$, 25°C): δ -144.22 (hept, $J_{P,F}$ = 708.0 Hz). Elemental analysis calcd. for $C_{36}H_{28}F_{12}N_6O_3P_2Zn$: C, 45.61; H, 2.98; N, 8.87; found: C, 45.50; H, 2.82; N, 9.03.

7.11 Synthesis of $[Zn(L^{OH})_2(PO_2F_2)](PF_6)$ (14)

To a suspension of L^{OH} (200 mg, 0.696 mmol) in methanol (15 mL), $Zn(PF_6)_2 \cdot xH_2O$ (124 mg, 0.348 mmol, on anhydrous basis) was added and the resulting suspension was stirred at room temperature for 1 h. During this time a clear yellow solution formed, which was stirred for other 3 hours. Then the solvent was removed under reduced pressure, the residue was suspended in diethylether (10 mL) and the yellow solid was filtered, washed

with diethylether and dried under vacuum. Yield: 214 mg (69%). IR (nujol, ν/cm^{-1}): 3630br (OH), 3490br (OH), 1607s, 1532m, 1332m, 1288m, 849s (PF_6). ^{1}H NMR (400 MHz, $CD_3C(O)CD_3$, 25°C): δ 6.68-6.54 (m, 1H, Ar-H), 6.81-6.63 (m, 1H, Ar-H), 7.15-6.93 (m, 2H, Ar-H), 7.39-7.26 (m, 2H, Ar-H), 7.48 (t, $J_{H,H}$ = 7.5 Hz, 1H, Ar-H), 7.85-7.74 (m, 2H, Ar-H), 7.95-7.88 (m, 1H, Ar-H), 8.03 (t, $J_{H,H}$ = 10.1 Hz, 1H, Ar-H), 8.11 (d, $J_{H,H}$ = 10.4 Hz, 1H, Ar-H), 9.38 (s, 1H, OH). ^{31}P{^{1}H} NMR (162 MHz, $CD_3C(O)CD_3$, 25°C): δ -144.26 (hept, $J_{P,F}$ = 706.4 Hz), -16.52 (t, $J_{P,F}$ = 949.8 Hz). Elemental analysis calcd. for $C_{36}H_{28}F_8N_6O_5P_2Zn$: C, 47.83; H, 3.12; N, 9.30; found: C, 47.78; H, 3.17; N, 9.12%.

7.12 Synthesis of $[Zn(L^{OH})_2](ClO_4)_2$ (10b)

Complex $[Zn(L^{OH})_2](ClO_4)_2 \cdot H_2O$ (**10**) (100 mg, 0.117 mmol) was cautiously heated overnight at 120°C, in a dry atmosphere. The resulting yellow powder was formulated as $[Zn(L^{OH})_2](ClO_4)_2$ (**15**). Yield: 96 mg (98%). IR (nujol, ν/cm^{-1}): 3351br (OH), 1640m, 1615s, 1568m, 1550m, 1519m, 1130-1095br (ClO_4). Elemental analysis calcd. for $C_{36}H_{26}Cl_2N_6O_{10}Zn$: C, 51.54; H, 3.12; N, 10.02; found: C, 51.35; H, 3.08; N, 9.97%.

7.13 Synthesis of $[Ag(L^{OH})(L^{O})]$ (15)

To a solution of $AgNO_3$ (148 mg, 0.870 mmol) in acetonitrile (10 mL), L^{OH} (500 mg, 1.740 mmol) was added. The suspension was stirred in presence of Et_3N (120.9 µL, 0.870 mmol) for 2 hours at room temperature. The lime green precipitate was filtered off, washed with acetonitrile, dried under vacuum and stored away from light. Yield: 584 mg (98 %). IR (nujol, ν/cm^{-1}): 1634s, 1593s, 1512s, 1438s, 1332s. Elemental analysis calcd. for $C_{36}H_{25}N_6AgO_2$: C, 63.45 ; H, 3.70; N, 12.33; found: C, 63.27; H, 3.68; N, 12.11 %.

7.14 Synthesis of $[Cu(L^{OH})_2(BF_4)]$ (16)

To a solution of L^{OH} (500 mg, 1,740 mmol) in dichloromethane (10 mL), $[Cu(CH_3CN)_4]BF_4$ (274 mg, 0.870 mmol) was added. The suspension was allowed to stir for 2 hours at room temperature. The rust solid was filtered off, washed with dichloromethane, dried and stored under vacuum. Yield: 557 mg (88 %). IR (nujol, v/cm^{-1}): 1636s, 1595s, 1513s, 1436s, 1337s, 1049br (BF_4). Elemental analysis calcd. for $C_{36}H_{26}N_6BCuF_4O_2$: C, 59.64 ; H, 3.61; N, 11.59; found: C, 59.73; H, 3.51; N, 11.27 %.

7.15 Synthesis of $[Ag(P)(L^{OH})](NO_3)$ complexes

A solution of $AgNO_3$ (250 mg, 1.472 mmol) in CH_2Cl_2:MeOH 5:1 (12 mL) was stirred for one hour at room temperature in the presence of one equivalent of $PR_1R_2R_3$, affording a colourless solution. Then one equivalent of L^{OH} was added and a yellow suspension formed. After one hour the solvent was evaporated and the crude product suspended in diethylether (10 mL); the yellow solid was filtered off, washed with diethylether, dried under vacuum and stored away from light.

$[Ag(PPh_3)(L^{OH})](NO_3)$ (17): Yield 987 mg (93 %). ^{1}H NMR (400 MHz, CD_2Cl_2, 25 °C): δ = 6.48 (td, $J_{H,H}$= 7.5 Hz, $J_{H,H}$= 1.2 Hz, 1H, Ar-H), 6.92 (t, $J_{H,H}$= 6.8 Hz 1H, Ar-H), 7.23-7.41 (m, 11H, Ar-H), 7.47 (td, $J_{H,H}$= 7.5 Hz, $J_{H,H}$= 1.6 Hz, 7H, Ar-H), 7.52-7.58 (m, 3H, Ar-H), 7.93-8.06 (m, 3H, Ar-H), 8.10 (d, $J_{H,H}$= 7.2 Hz, 1H, Ar-H), 8.50 (d, $J_{H,H}$= 5.1 Hz, 1H, Ar-H), 11.21 (s, 1H, OH). ^{31}P{^{1}H} NMR (162 MHz, CD_2Cl_2, 25 °C): δ 17.68 ppm (d $J_{P\text{-}Ag}$ = 702.3 Hz). Elemental analysis calcd. for $C_{37}H_{29}N_3AgO_4P$ (718.50): C 61.85, H 4.07, N 5.85; found C 61.53, H 4.16, N 5.79 %.

Single crystals suitable for X-ray analysis were grown by vapour diffusion of diethylether into a solution of compound **18** in CH_2Cl_2.

[Ag(PMe$_2$Ph)(L^{OH})](NO$_3$) (18): Yield 765 mg (87 %). ^{1}H NMR (400 MHz, CD_2Cl_2, 25 °C): δ = 1.64 (s, 3H, CH_3), 1.66 (s, 3H, CH_3), 6.86 (t, $J_{H,H}$= 6.9 Hz 1H, Ar-H), 6.96 (t, $J_{H,H}$= 7.3 Hz 1H, Ar-H), 7.18 (dd, $J_{H,H}$= 9.4 Hz, $J_{H,H}$= 6.5 Hz, 1H, Ar-H), 7.29 (t, $J_{H,H}$= 6.3 Hz 1H, Ar-H), 7.38-7.58 (m, 7H, Ar-H), 7.92-8.07 (m, 3H, Ar-H), 8.14 (d, $J_{H,H}$= 7.2 Hz, 1H, Ar-H), 8.58 (d, $J_{H,H}$= 5.1 Hz, 1H, Ar-H). ^{31}P{^{1}H} NMR (162 MHz, CD_2Cl_2, 25 °C): δ -20.84 ppm. Elemental analysis calcd. for $C_{27}H_{25}N_3AgO_4P$ (594.36): C 54.56, H 4.24, N 7.07; found C 54.53, H 4.13, N 7.09 %.

X-ray quality crystals were grown by vapour diffusion of isopropyl ether into a solution of **19** in dichloroethane.

[Ag(PMePh$_2$)(L^{OH})](NO$_3$) (19): Yield 732 mg (76%). ^{1}H NMR (400 MHz, CD_2Cl_2, 25 °C): δ = 1.98 (d, $J_{H,H}$= 6.7 Hz, 3H, CH_3), 6.79-6.83 (m, 2H, Ar-H), 7.15 (ddd, $J_{H,H}$= 9.4 Hz, JH,H = 6.6 Hz, $J_{H,H}$= 1.0 Hz, 1H, Ar-H), 7.22 (ddd, $J_{H,H}$= 7.0 Hz, $J_{H,H}$= 5.1 Hz, $J_{H,H}$= 1.3 Hz, 1H, Ar-H), 7.36-7.52 (m, 12H, Ar-H), 7.86-7.95 (m, 3H, Ar-H), 8.03 (dd, $J_{H,H}$= 7.2 Hz, $J_{H,H}$= 1.2 Hz, 1H, Ar-H), 8.46 (d, $J_{H,H}$= 4.7 Hz, 1H, Ar-H), 11.20 (s, 1H, OH). ^{31}P{^{1}H} NMR (162 MHz, CD_2Cl_2, 25 °C): δ -2.54 ppm (d, $J_{P\text{-}Ag}$ = 585.0 Hz). Elemental analysis calcd. for $C_{32}H_{27}N_3AgO_4P$ (656.43): C 58.55, H 4.15, N 6.40; found C 58.43, H 4.10, N 6.09 %.

[Ag(PBu$_3$)(L^{OH})](NO$_3$) (20): Yield 934 mg (91 %). ^{1}H NMR (400 MHz, CD_2Cl_2, 25 °C): δ = 0.93 (t, $J_{H,H}$= 6.8 Hz, 9H, CH_3), 1.35-1.48 (m, 12H, CH_2), 1.67 (q, $J_{H,H}$= 8.3 Hz, $J_{H,H}$= 7.9 Hz, 6H, P-CH_2), 6.84-6.88 (m, 1H, Ar-H), 7.00 (td, $J_{H,H}$= 7.3 Hz, $J_{H,H}$= 1.6 Hz, 1H, Ar-H), 7.20 (td, $J_{H,H}$= 9.3 Hz, $J_{H,H}$= 6.4 Hz, 1H, Ar-H), 7.34 (td, $J_{H,H}$= 5.5 Hz, $J_{H,H}$= 2.6 Hz, 1H, Ar-H), 7.41-7.54 (m, 3H, Ar-H), 7.96-8.07 (m, 4H, Ar-H), 8.53 (dd, $J_{H,H}$= 4.9 Hz, $J_{H,H}$= 1.5 Hz, 1H, Ar-H), 11.23 (s, 1H, OH). ^{31}P{^{1}H} NMR (162 MHz, CD_2Cl_2, 25 °C): δ 1.17 ppm (d $J_{P\text{-}Ag}$ = 687.7 Hz). Elemental analysis calcd. for $C_{31}H_{41}N_3AgO_4P$ (658.53): C 56.54, H 6.28, N 6.38; found C 56.33, H 6.12, N 6.57 %.

Single crystals suitable for X-ray analysis were grown by vapour diffusion of diethylether into a solution of compound **21** in CH_2Cl_2.

[Ag(P(p-tolyl)$_3$)(L^{OH})](NO$_3$) (21): Yield 995 mg (89 %). ^{1}H NMR (400 MHz, CD_2Cl_2, 25 °C): δ = 2.42 (s, 9H, CH_3), 6.51 (td, $J_{H,H}$ = 7.6 Hz, $J_{H,H}$ = 1.3 Hz, 1H, Ar-H), 6.86 (t, $J_{H,H}$ = 6.9 Hz, 1H, Ar-H), 7.17-7.30 (m, 14H, Ar-H), 7.32 (dd, $J_{H,H}$ = 8.6 Hz, $J_{H,H}$ = 6.9 Hz, 1H, Ar-H), 7.39-7.45 (m, 2H, Ar-H), 7.91 (t, $J_{H,H}$ = 8.00 Hz, 1H, Ar-H), 7.97-8.00 (m, 2H, Ar-H), 8.09 (d, $J_{H,H}$ = 7.2 Hz, 1H, Ar-H), 8.47 (d, $J_{H,H}$ = 5.00 Hz, 1H, Ar-H). $^{31}P\{^1H\}$ NMR (162 MHz, CD_2Cl_2, 25 °C): δ 15.55 ppm (d $J_{P\text{-}Ag}$ = 682.8 Hz). Elemental analysis calcd. for $C_{40}H_{35}N_3AgO_4P$ (658.53): C 63.17, H 4.64, N 5.52; found C 62.98, H 4.78, N 5.59 %.

[Ag(P(OPh)$_3$)(L^{OH})](NO$_3$) (22): Yield 973 mg (86%). ^{1}H NMR (400 MHz, CD_2Cl_2, 25 °C): δ = 6.88-6.92 (m, 1H, Ar-H), 7.01-7.06 (m, 1H, Ar-H), 7.13-7.28 (m, 12H, Ar-H), 7.33-7.41 (m, 8H, Ar-H), 7.45 (ddd, $J_{H,H}$= 8.5 Hz, $J_{H,H}$= 7.3 Hz, $J_{H,H}$= 1.7 Hz, 1H, Ar-H),7.58 (d, $J_{H,H}$= 7.5 Hz, 1H, Ar-H), 7.85 (td, $J_{H,H}$= 7.7 Hz, $J_{H,H}$= 1.8 Hz, 1H, Ar-H), 8.00-8.07 (m, 2H, Ar-H), 8.35 (s, 2H, Ar-H), 8.67 (s, 1H, OH). $^{31}P\{^1H\}$ NMR (162 MHz, CD_2Cl_2, 25 °C): δ 125.21 ppm. Elemental analysis calcd. for $C_{37}H_{29}N_3AgO_7P$ (658.53): C 57.98, H 3.81, N 5.48; found C 58.26, H 4.12, N 5.50 %.

Single crystals suitable for X-ray analysis were grown by vapour diffusion of diethylether into a solution of compound **23** in CH_2Cl_2.

[Ag(P(OEt)$_3$)(L^{OH})](NO$_3$) (23): Yield 768 mg (84 %). ^{1}H NMR (400 MHz, CD_2Cl_2, 25 °C): δ = 1.28 (t, $J_{H,H}$= 7.10 Hz, 9H, CH_3), 3.91 (dq, $J_{H,H}$= 7.10 Hz, 6H, CH_2), 6.87 (td, $J_{H,H}$= 6.9 Hz, $J_{H,H}$= 1.0 Hz, 1H, Ar-H), 7.02 (td, $J_{H,H}$= 7.4 Hz, $J_{H,H}$= 1.2 Hz, 1H, Ar-H), 7.21 (ddd, $J_{H,H}$= 9.2 Hz, $J_{H,H}$= 6.5 Hz, $J_{H,H}$1.0 Hz, 1H, Ar-H), 7.34 (td, $J_{H,H}$= 4.9 Hz, $J_{H,H}$= 3.7 Hz, 1H, Ar-H), 7.39 (dd, $J_{H,H}$= 8.4 Hz, $J_{H,H}$= 1.2 Hz, 1H, Ar-H), 7.47 (ddd, $J_{H,H}$= 8.9 Hz, $J_{H,H}$= 7.2 Hz, $J_{H,H}$ = 1.7 Hz, 1H, Ar-H), 7.54 (dd, $J_{H,H}$= 7.6 Hz, $J_{H,H}$= 1.7 Hz, 1H, Ar-H), 7.97-8.00 (m, 3H, Ar-H), 8.04 (td, $J_{H,H}$= 7.2 Hz, $J_{H,H}$= 1.1 Hz, 1H, Ar-H), 8.54 (td, $J_{H,H}$= 5.0 Hz, $J_{H,H}$= 1.4 Hz, 1H, Ar-H), 11.15 (s, 1H, OH). $^{31}P\{^1H\}$ NMR (162 MHz, CD_2Cl_2, 25 °C): δ 126.49 ppm (d $J_{P\text{-}Ag}$ = 991.9 Hz). Elemental analysis calcd. for $C_{25}H_{29}N_3AgO_7P$ (658.53): C 48.25, H 4.70, N 6.75; found C 48.36, H 4.42, N 6.68 %.

7.16 Synthesis of 1-(pyridin-2-yl)-3-(2,6-difluorophenyl) imidazo[1,5-*a*]pyridine ($L^{F,F}$)

In 30 mL of deossigenated acetic acid were dissolved di(2-pyridyl) ketone (500 mg, 2.715 mmol), 2,6-difluorobenzaldehyde (585.8 µL, 5.43 mmol) and ammonium acetate (1.046 g, 13.573 mmol). The solution was stirred at 110 °C for 10 hours. After cooling to room temperature, the solution was added to H_2O (150 mL) and extracted with CH_2Cl_2 (100 mL x 2). The organic portion was washed with a solution of $H_2O/NaHCO_3$ and then dried over anhydrous Na_2SO_4. The solvent was removed under reduced pressure obtaining a yellow solid. The crude product was allowed to stir in hexane overnight in order to remove the excess aldehyde and the solid was isolated by filtration and dried in vacuum. Yield: 769 mg (92%). ^{1}H NMR (400 MHz, chloroform-*d*, 25°C) : δ = 6.74 (ddd, $J_{H,H}$ = 7.1 Hz, $J_{H,H}$ = 6.5 Hz, $J_{H,H}$ 1.2 Hz, 1H, Ar-H), 7.03 (ddd, $J_{H,H}$ = 9.2 Hz, $J_{H,H}$ = 6.4 Hz, $J_{H,H}$ 1.0 Hz, 1H, Ar-H), 7.11-7.17 (m, 3H, Ar-H), 7.52 (tt, $J_{H,H}$ = 8.4 Hz, $J_{H,H}$ 6.3 Hz, 1H, Ar-H), 7.69-7.76 (m, 2H, Ar-H), 8.26 (dt $J_{H,H}$ = 8.1 Hz, $J_{H,H}$ 1.1 Hz, 1H, Ar-H), 8.67 (ddd, $J_{H,H}$ = 4.9 Hz, $J_{H,H}$ = 1.9 Hz, $J_{H,H}$ 0.9 Hz, 1H, Ar-H), 8.79 (dt $J_{H,H}$ = 9.3 Hz, $J_{H,H}$ 1.2 Hz, 1H, Ar-H). ^{19}F{^{1}H} NMR (376 MHz, chloroform-*d*, 25°C): δ = 66.04 ppm. Elemental analysis calcd. for $C_{18}H_{11}N_3F_2$ (594.36): C 70.35, H 3.61, N 13.67; found C 70.25, H 3.53, N 13.64 %.

X-ray quality crystals were grown by slow cooling a hot saturated methanol solution of the ligand.

7.17 Absolute Quantum Yields Measurements

A PTFE-coated integrating sphere (PhotoMed GmbH) with 3.2 inches diameter was mounted into a Photon Technologies International QuantaMaster QM-40. The top part of the sphere was lifted, and the holder for powder samples was accommodated into the sphere, with the quartz window facing the excitation light beam. The measured luminescence spectra were background corrected by subtracting the spectrum obtained using a blank substrate (Al_2O_3) and subsequently corrected for the wavelength sensitivity of the fluorimeter and the spectral response of the sphere. This correction was applied to all subsequently recorded spectra in the measurement of PLQY of samples. The integrated luminescence area were obtained by the software Felix32 Analysis (© 2001) and used to determine the absolute PLQY (Φ_{PL}) (with uncertainties of 5%) according to the equation below:[87]

$$\Phi_{PL} = \frac{E_i(\lambda) - (1 - A) \cdot E_0(\lambda)}{L_e(\lambda) \cdot A}$$

where

$$A = \frac{L_0(\lambda) - L_i(\lambda)}{L_0(\lambda)}$$

$E_i(\lambda)$ = integrated emission under direct excitation of the sample;

$E_0(\lambda)$ = integrated emission under secondary excitation of the sample;

$L_i(\lambda)$ = integrated excitation under direct excitation of the sample;

$L_0(\lambda)$ = integrated excitation under secondary excitation of the sample;

$L_e(\lambda)$ = integrated excitation profile for the empty sphere.

7.18 Computational Details

All calculations were carried out at the density functional level of theory with the ADF2012.2 program package.[88] The hybrid functional PBE0[89] was employed for geometry optimization, vibrational frequency analysis and electronic excitation energy evaluation. The PBE0 exchange correlation functional is based on the generalized gradient corrected exchange correlation functional by Perdew-Burke-Ernzerhof (PBE) with a fixed amount of 25% of Hartree-Fock exchange energy. This functional has been chosen in response to a benchmark comparison with the classical B3LYP[90] and the meta-GGA M06L[91] functionals which showed results slightly less in agreement with the experimental data. Restricted formalism was applied for all closed shell systems (free ligands and complexes). Atomic coordinates of complexes **4**, **6** and **7**, derived by X-ray structure determination, were used as starting point in the geometry optimizations of complexes changing the halogen atoms coordinated to zinc. Frequency calculations were carried out for all optimized structures in order to establish the nature of the stationary points. TD-DFT implemented in the ADF package was used to determine the excitation energies. The 20 lowest singlet-singlet excitation were calculated using the optimized geometries. For geometry optimization C, H, N, O and Cl atoms were described through TZP basis sets (triple-ζ STO plus one polarization function); the QZ4P set of basis (quadruple-ζ STO plus four polarization function) was used for Br, I and Zn atoms. The corresponding augmented set of basis was employed in TD-DFT calculations.[92] All basis are given in the program database. The no-frozen-core approximation (all-electron) was used in all calculations.

For the simulation of solvent effects on the ground-state geometries and excitation energies, the conductor-like continuum solvent model (COSMO)[93] as implemented in ADF has been used.

7.19 Single Crystal X-ray Structure Analysis

X-ray structural analysis were performed by Dr. Bruno Therrien (Institute of Chemistry, Université de Neuchâtel, Switzerland).

Crystals of L^{Me}, L^{OH}, **4**, **6** and **7** · DMF were mounted on a Stoe Mark II-Image Plate Diffraction System, using Mo-Kαgraphite monochromated radiation, image plate distance 135 mm, 2ϑ range from 2.4-51.3°, D_{max}-D_{min} = 16.029-0.836 Å. The structures were solved by direct methods using the program SHELXS-97.[94] Refinement and all further calculations were carried out using SHELXL-97.[85] The H-atoms were included in calculated positions and treated as riding atoms using the SHELXL default parameters. The non-H atoms were refined anisotropically, using weighted full-matrix least-square on F^2. In complexes **4** and **6**, the tolyl group was disordered over two positions (50:50 occupation factors). Crystallographic details for ligands L^{Me} and L^{OH} and complexes **4**, **6** and **7** · DMF are summarized in Table 6.1 - 6.15. Figures 6.1, 6.2, 6.3, 6.4 and 6.5 were drawn with ORTEP.[95]

Crystals of complexes $[Zn(L^{OH})_2](ClO_4)_2{\cdot}H_2O$ (**10**) and $[Zn(L^{OH})_2(CH_3CN)_2](BF_4)_2$ (**12b**) were mounted on a Stoe Image Plate Diffraction system equipped with a ϕ circle goniometer, using Mo-Kα graphite monochromated radiation (λ = 0.71073 Å) with ϕ range 0-200º. The structures were solved by direct methods using the program SHELXS-97, while the refinement and all further calculations were carried out using SHELXL-97[85]. The H-atoms were found on Fourier difference map or included in calculated positions and treated as riding atoms using the SHELXL default parameters. The non-H atoms were refined anisotropically, using weighted full-matrix least-square on F^2. Crystallographic details are summarized in Table 6.16 – 6.21 Figures 6.6 and 6.7 were drawn with ORTEP.[86]

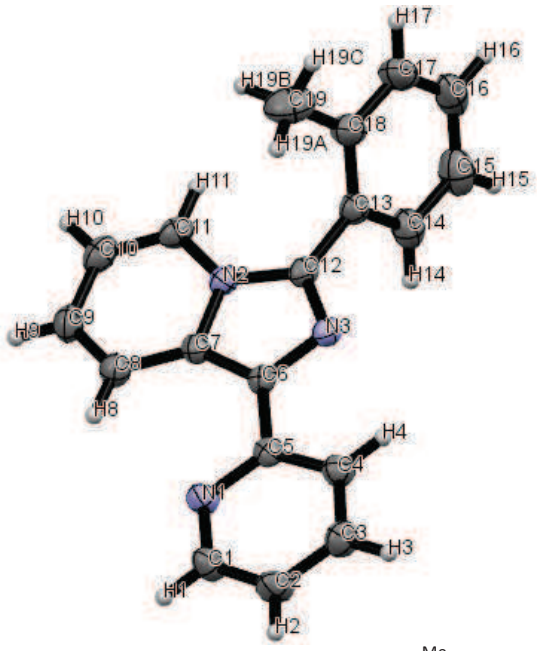

Figure 7.1 Cristal structure of L^{Me}.

L^{Me}	
Formula	$C_{19}H_{15}N_3$
Space Group	P $2_12_12_1$
Cell Lengths	*a* = 9.777(2) *b* = 10.560(2) *c* = 14.680(3)
Cell Angles	α = β = γ = 90°
Cell Volume	1515.64
Z,Z'	Z = 4, Z' = 0
R-Factor (%)	6.75

Table 7.1 Crystallographic parameters obtained by X-ray diffraction for L^{Me}.

Atom1	Atom2	Length (Å)	Atom1	Atom2	Length (Å)
C1	H1	0.931	C10	C11	1.344(4)
C1	C2	1.374(4)	C11	H11	0.930
C1	N1	1.343(4)	C11	N2	1.389(4)
C2	H2	0.931	C12	C13	1.477(4)
C2	C3	1.382(4)	C12	N2	1.382(3)
C3	H3	0.930	C12	N3	1.328(3)
C3	C4	1.383(4)	C13	C14	1.401(4)
C4	H4	0.931	C13	C18	1.397(4)
C4	C5	1.392(4)	C14	H14	0.930
C5	C6	1.463(3)	C14	C15	1.372(5)
C5	N1	1.350(3)	C15	H15	0.930
C6	C7	1.395(4)	C15	C16	1.373(6)
C6	N3	1.378(3)	C16	H16	0.930
C7	C8	1.419(3)	C16	C17	1.361(5)
C7	N2	1.398(3)	C17	H17	0.930
C8	H8	0.930	C17	C18	1.400(4)
C8	C9	1.361(4)	C18	C19	1.490(5)
C9	H9	0.930	C19	H19A	0.960
C9	C10	1.420(4)	C19	H19B	0.960
C10	H10	0.930	C19	H19C	0.960

Table 7.2 Bond lengths obtained by X-ray diffraction for L^{Me}.

Atom1	Atom2	Atom3	Angle (°)	Atom1	Atom2	Atom3	Angle (°)
H1	C1	C2	117.6	C13	C12	N2	123.0(2)
H1	C1	N1	117.6	C13	C12	N3	126.9(2)
C2	C1	N1	124.8(3)	N2	C12	N3	110.0(2)
C1	C2	H2	121.1	C12	C13	C14	118.4(2)
C1	C2	C3	117.8(3)	C12	C13	C18	121.6(3)
H2	C2	C3	121.1	C14	C13	C18	120.0(3)
C2	C3	H3	120.3	C13	C14	H14	119.5
C2	C3	C4	119.2(3)	C13	C14	C15	120.9(3)
H3	C3	C4	120.5	H14	C14	C15	119.6
C3	C4	H4	120.5	C14	C15	H15	120.5
C3	C4	C5	119.1(3)	C14	C15	C16	119.0(3)
H4	C4	C5	120.4	H15	C15	C16	120.4
C4	C5	C6	120.6(2)	C15	C16	H16	119.5
C4	C5	N1	122.4(2)	C15	C16	C17	121.0(3)
C6	C5	N1	116.9(2)	H16	C16	C17	119.5
C5	C6	C7	129.1(2)	C16	C17	H17	119.2
C5	C6	N3	121.0(2)	C16	C17	C18	121.6(3)
C7	C6	N3	109.9(2)	H17	C17	C18	119.2
C6	C7	C8	137.7(2)	C13	C18	C17	117.4(3)
C6	C7	N2	104.7(2)	C13	C18	C19	122.5(3)
C8	C7	N2	117.5(2)	C17	C18	C19	120.0(3)
C7	C8	H8	120.2	C18	C19	H19A	109.5
C7	C8	C9	119.5(3)	C18	C19	H19B	109.5
H8	C8	C9	120.3	C18	C19	H19C	109.5
C8	C9	H9	119.6	H19A	C19	H19B	109.5
C8	C9	C10	120.8(3)	H19A	C19	H19C	109.4
H9	C9	C10	119.6	H19B	C19	H19C	109.5
C9	C10	H10	119.6	C1	N1	C5	116.6(2)
C9	C10	C11	120.9(3)	C7	N2	C11	122.8(2)
H10	C10	C11	119.6	C7	N2	C12	108.0(2)
C10	C11	H11	120.8	C11	N2	C12	129.1(2)
C10	C11	N2	118.5(3)	C6	N3	C12	107.3(2)
H11	C11	N2	120.7				

Table 7.3 Angles obtained by X-ray diffraction for L^{Me}.

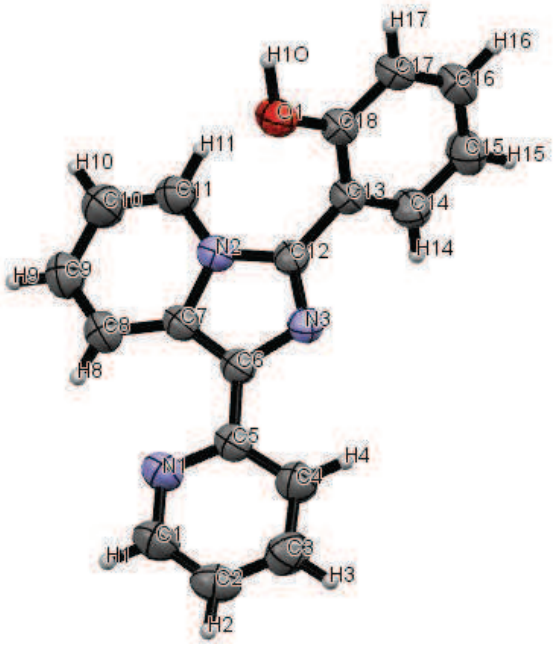

Figure 7.2 Cristal structure of L^{OH}.

	$\mathbf{L^{OH}}$
Formula	$C_{18}H_{13}N_3O$
Space Group	Pbca
Cell Lengths	*a* = 12.415(2) *b* = 9.795(2) *c* = 24.103(5)
Cell Angles	α = β = γ = 90°
Cell Volume	2931.04
Z,Z'	Z = 8, Z' = 0
R-Factor (%)	3.76

Table 7.4 Crystallographic parameters obtained by X-ray diffraction for L^{OH}.

Atom1	Atom2	Length (Å)	Atom1	Atom2	Length (Å)
C1	C2	1.391(3)	C10	H10	0.930(2)
C1	C6	1.394(2)	C10	C11	1.343(3)
C1	O1	1.349(3)	C11	H11	0.931(2)
C2	H2	0.929(2)	C11	C12	1.415(3)
C2	C3	1.362(3)	C12	C13	1.375(3)
C3	H3	0.930(2)	C12	N1	1.405(2)
C3	C4	1.381(3)	C13	C14	1.457(3)
C4	H4	0.929(2)	C13	N2	1.386(2)
C4	C5	1.385(3)	C14	C15	1.376(3)
C5	H5	0.930(2)	C14	N3	1.349(3)
C5	C6	1.375(3)	C15	H15	0.929(2)
C6	C7	1.472(2)	C15	C16	1.376(3)
C7	N1	1.370(2)	C16	H16	0.930(2)
C7	N2	1.319(3)	C16	C17	1.368(3)
C8	H8	0.931(2)	C17	H17	0.931(3)
C8	C9	1.336(3)	C17	C18	1.354(4)
C8	N1	1.375(3)	C18	H18	0.930(2)
C9	H9	0.931(2)	C18	N3	1.335(3)
C9	C10	1.421(3)	O1	H1O	1.07(3)

Table 7.5 Bond lengths obtained by X-ray diffraction for L^{OH}.

Atom1	Atom2	Atom3	Angle (°)	Atom1	Atom2	Atom3	Angle (°)
C2	C1	C6	118.9(2)	C10	C11	H11	120.1(2)
C2	C1	O1	123.3(2)	C10	C11	C12	119.9(2)
C6	C1	O1	117.7(2)	H11	C11	C12	120.0(2)
C1	C2	H2	119.7(2)	C11	C12	C13	136.9(2)
C1	C2	C3	120.6(2)	C11	C12	N1	117.4(2)
H2	C2	C3	119.7(2)	C13	C12	N1	105.7(2)
C2	C3	H3	119.4(2)	C12	C13	C14	129.2(2)
C2	C3	C4	121.3(2)	C12	C13	N2	109.0(2)
H3	C3	C4	119.3(2)	C14	C13	N2	121.7(2)
C3	C4	H4	121.0(2)	C13	C14	C15	123.1(2)
C3	C4	C5	118.0(2)	C13	C14	N3	115.6(2)
H4	C4	C5	121.0(2)	C15	C14	N3	121.3(2)
C4	C5	H5	119.1(2)	C14	C15	H15	120.0(2)
C4	C5	C6	121.8(2)	C14	C15	C16	119.9(2)
H5	C5	C6	119.1(2)	H15	C15	C16	120.1(2)
C1	C6	C5	119.3(2)	C15	C16	H16	120.5(2)
C1	C6	C7	120.4(2)	C15	C16	C17	119.0(2)
C5	C6	C7	120.2(2)	H16	C16	C17	120.5(2)
C6	C7	N1	124.2(2)	C16	C17	H17	121.1(2)
C6	C7	N2	125.6(2)	C16	C17	C18	117.8(2)
N1	C7	N2	110.3(2)	H17	C17	C18	121.1(2)
H8	C8	C9	120.7(2)	C17	C18	H18	117.5(2)
H8	C8	N1	120.7(2)	C17	C18	N3	125.1(2)
C9	C8	N1	118.7(2)	H18	C18	N3	117.4(2)
C8	C9	H9	119.4(2)	C7	N1	C8	130.3(2)
C8	C9	C10	121.2(2)	C7	N1	C12	107.3(1)
H9	C9	C10	119.4(2)	C8	N1	C12	122.4(2)
C9	C10	H10	119.7(2)	C7	N2	C13	107.7(2)
C9	C10	C11	120.4(2)	C14	N3	C18	116.9(2)
H10	C10	C11	119.8(2)	C1	O1	H1O	111(2)

Table 7.6 Angles obtained by X-ray diffraction for L^{OH}.

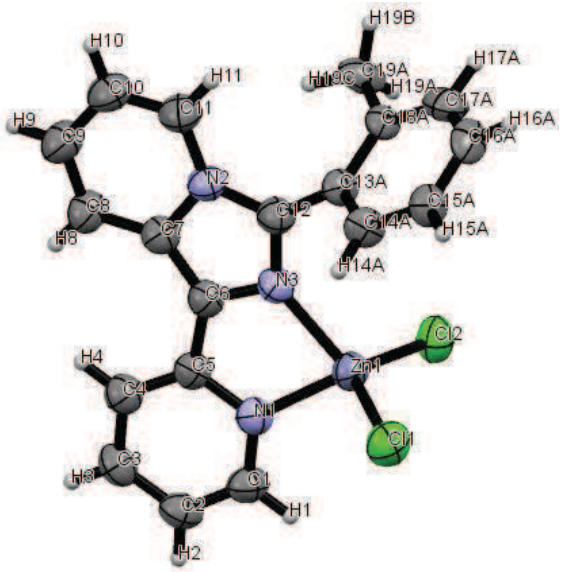

Figure 7.3 Cristal structure of complex (**4**).

$[Zn(L^{Me})Cl_2]$ (4)	
Formula	$C_{19}H_{15}Cl_2N_3Zn$
Space Group	P $2_1/c$
Cell Lengths	*a* = 9.6500(8) *b* = 18.2820(15) *c* = 13.1111(11)
Cell Angles	α = γ = 90° β = 127.887(5)
Cell Volume	1825.53
Z,Z'	Z = 4, Z' = 0
R-Factor (%)	6.24

Table 7.7 Crystallographic parameters obtained by X-ray diffraction for complex (**4**).

Atom1	Atom2	Length(Å)	Atom1	Atom2	Length(Å)
C1	H1	0.929	C11	N2	1.384(5)
C1	C2	1.379(7)	C12	C13A	1.52(1)
C1	N1	1.339(5)	C12	N2	1.368(5)
C2	H2	0.930	C12	N3	1.329(5)
C2	C3	1.380(6)	C13A	C14A	1.35(2)
C3	H3	0.930	C13A	C18A	1.42(2)
C3	C4	1.382(5)	C14A	H14A	0.93
C4	H4	0.930	C14A	C15A	1.42(2)
C4	C5	1.390(6)	C15A	H15A	0.930
C5	C6	1.451(5)	C15A	C16A	1.39(2)
C5	N1	1.361(5)	C16A	H16A	0.930
C6	C7	1.396(5)	C16A	C17A	1.34(2)
C6	N3	1.385(5)	C17A	H17A	0.93
C7	C8	1.414(6)	C17A	C18A	1.39(2)
C7	N2	1.403(5)	C18A	C19A	1.53(2)
C8	H8	0.930	C19A	H19A	0.96
C8	C9	1.363(5)	C19A	H19B	0.96
C9	H9	0.931	C19A	H19C	0.96
C9	C10	1.421(7)	Cl1	Zn1	2.206(1)
C10	H10	0.930	Cl2	Zn1	2.223(2)
C10	C11	1.346(6)	N1	Zn1	2.083(4)
C11	H11	0.930	N3	Zn1	2.044(3)

Table 7.8 Bond lengths obtained by X-ray diffraction for complex (**4**).

Atom1	Atom2	Atom3	Angle (°)	Atom1	Atom2	Atom3	Angle (°)
H1	C1	C2	118.5	C14A	C13A	C18A	118(1)
H1	C1	N1	118.5	C13A	C14A	H14A	119
C2	C1	N1	123.0(4)	C13A	C14A	C15A	123(1)
C1	C2	H2	120.8	H14A	C14A	C15A	119
C1	C2	C3	118.4(4)	C14A	C15A	H15A	120.4
H2	C2	C3	120.8	C14A	C15A	C16A	119(1)
C2	C3	H3	120.3	H15A	C15A	C16A	120.4
C2	C3	C4	119.5(4)	C15A	C16A	H16A	122
H3	C3	C4	120.3	C15A	C16A	C17A	117(1)
C3	C4	H4	120.2	H16A	C16A	C17A	122
C3	C4	C5	119.6(4)	C16A	C17A	H17A	117
H4	C4	C5	120.2	C16A	C17A	C18A	126(2)
C4	C5	C6	125.2(4)	H17A	C17A	C18A	117
C4	C5	N1	120.6(4)	C13A	C18A	C17A	118(1)
C6	C5	N1	114.2(3)	C13A	C18A	C19A	121(1)
C5	C6	C7	132.5(4)	C17A	C18A	C19A	121(1)
C5	C6	N3	118.9(3)	C18A	C19A	H19A	109
C7	C6	N3	108.6(3)	C18A	C19A	H19B	110
C6	C7	C8	136.9(4)	C18A	C19A	H19C	109
C6	C7	N2	105.0(3)	H19A	C19A	H19B	110
C8	C7	N2	118.1(4)	H19A	C19A	H19C	109
C7	C8	H8	120.3	H19B	C19A	H19C	109
C7	C8	C9	119.4(4)	C1	N1	C5	118.9(4)
H8	C8	C9	120.4	C1	N1	Zn1	127.0(3)
C8	C9	H9	119.7	C5	N1	Zn1	114.0(3)
C8	C9	C10	120.7(4)	C7	N2	C11	122.0(4)
H9	C9	C10	119.6	C7	N2	C12	108.7(4)
C9	C10	H10	119.7	C11	N2	C12	129.3(4)
C9	C10	C11	120.7(4)	C6	N3	C12	108.5(4)
H10	C10	C11	119.7	C6	N3	Zn1	111.7(3)
C10	C11	H11	120.5	C12	N3	Zn1	139.3(3)
C10	C11	N2	119.1(4)	Cl1	Zn1	Cl2	117.94(5)
H11	C11	N2	120.5	Cl1	Zn1	N1	110.7(1)
C13A	C12	N2	128.4(6)	Cl1	Zn1	N3	120.0(1)
C13A	C12	N3	121.4(6)	Cl2	Zn1	N1	109.9(1)
N2	C12	N3	109.3(4)	Cl2	Zn1	N3	111.1(1)
C12	C13A	C14A	121(1)	N1	Zn1	N3	81.0(1)
C12	C13A	C18A	121(1)				

Table 7.9 Angles obtained by X-ray diffraction for complex (**4**).

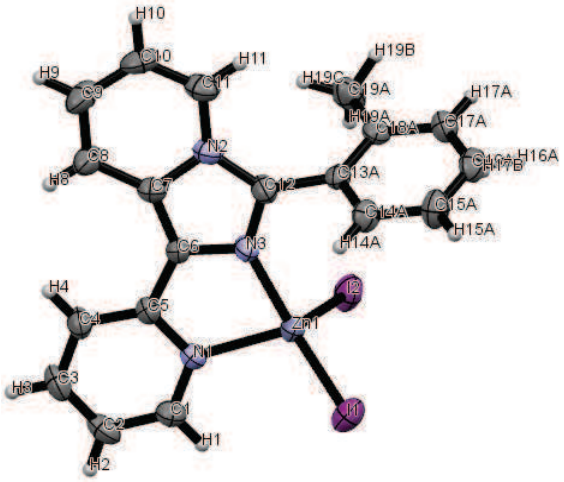

Figure 7.4 Cristal structure of complex (**6**).

[Zn(L^{Me})I$_2$] (6)	
Formula	$C_{19}H_{15}I_2N_3Zn$
Space Group	P 2_1/n
Cell Lengths	*a* = 10.1682(6) *b* = 18.4026(13) *c* = 10.8856(6)
Cell Angles	α = γ = 90° β = 97.251(5)
Cell Volume	2020.64
Z,Z^I	Z = 4, Z^I = 0
R-Factor (%)	3.82

Table 7.10 Crystallographic parameters obtained by X-ray diffraction for complex (**6**).

Atom1	Atom2	Length(Å)	Atom1	Atom2	Length(Å)
C1	H1	0.930	C11	N2	1.382(5)
C1	C2	1.382(6)	C12	C13A	1.56(1)
C1	N1	1.331(5)	C12	N2	1.368(5)
C2	H2	0.931	C12	N3	1.314(5)
C2	C3	1.379(6)	C13A	C14A	1.38(2)
C3	H3	0.930	C13A	C18A	1.39(1)
C3	C4	1.387(7)	C14A	H14A	0.93
C4	H4	0.930	C14A	C15A	1.44(2)
C4	C5	1.393(5)	C15A	H15A	0.929
C5	C6	1.454(5)	C15A	C16A	1.36(1)
C5	N1	1.360(5)	C16A	H16A	0.93
C6	C7	1.388(5)	C16A	C17A	1.38(2)
C6	N3	1.378(5)	C17A	H17A	0.93
C7	C8	1.419(6)	C17A	C18A	1.40(2)
C7	N2	1.402(5)	C18A	C19A	1.49(2)
C8	H8	0.931	C19A	H19A	0.96
C8	C9	1.361(5)	C19A	H19B	0.96
C9	H9	0.929	C19A	H19C	0.96
C9	C10	1.418(7)	I1	Zn1	2.5316(5)
C10	H10	0.929	I2	Zn1	2.5382(5)
C10	C11	1.345(6)	N1	Zn1	2.078(3)
C11	H11	0.931	N3	Zn1	2.038(3)

Table 7.11 Bond lengths obtained by X-ray diffraction for complex (**6**).

Atom1	Atom2	Atom3	Angle (°)	Atom1	Atom2	Atom3	Angle (°)
H1	C1	C2	118.4	C14A	C13A	C18A	121(1)
H1	C1	N1	118.4	C13A	C14A	H14A	120
C2	C1	N1	123.2(4)	C13A	C14A	C15A	120(1)
C1	C2	H2	121.0	H14A	C14A	C15A	120
C1	C2	C3	118.1(4)	C14A	C15A	H15A	120
H2	C2	C3	120.9	C14A	C15A	C16A	119(1)
C2	C3	H3	120.1	H15A	C15A	C16A	121
C2	C3	C4	119.8(4)	C15A	C16A	H16A	120
H3	C3	C4	120.1	C15A	C16A	C17A	121(1)
C3	C4	H4	120.5	H16A	C16A	C17A	120
C3	C4	C5	119.1(4)	C16A	C17A	H17A	119
H4	C4	C5	120.4	C16A	C17A	C18A	121(1)
C4	C5	C6	125.1(3)	H17A	C17A	C18A	119
C4	C5	N1	120.8(3)	C13A	C18A	C17A	118.1(8)
C6	C5	N1	114.1(3)	C13A	C18A	C19A	122(1)
C5	C6	C7	133.1(3)	C17A	C18A	C19A	120(1)
C5	C6	N3	118.3(3)	C18A	C19A	H19A	109
C7	C6	N3	108.5(3)	C18A	C19A	H19B	109
C6	C7	C8	137.2(3)	C18A	C19A	H19C	110
C6	C7	N2	104.8(3)	H19A	C19A	H19B	109
C8	C7	N2	118.0(3)	H19A	C19A	H19C	109
C7	C8	H8	120.1	H19B	C19A	H19C	110
C7	C8	C9	119.8(4)	C1	N1	C5	119.0(3)
H8	C8	C9	120.1	C1	N1	Zn1	126.9(3)
C8	C9	H9	120.1	C5	N1	Zn1	114.1(2)
C8	C9	C10	119.8(4)	C7	N2	C11	121.9(3)
H9	C9	C10	120.1	C7	N2	C12	108.7(3)
C9	C10	H10	119.2	C11	N2	C12	129.4(3)
C9	C10	C11	121.7(4)	C6	N3	C12	109.1(3)
H10	C10	C11	119.2	C6	N3	Zn1	112.4(2)
C10	C11	H11	120.6	C12	N3	Zn1	137.4(3)
C10	C11	N2	118.8(4)	I1	Zn1	I2	119.81(2)
H11	C11	N2	120.6	I1	Zn1	N1	107.88(9)
C13A	C12	N2	130.4(4)	I1	Zn1	N3	121.06(9)
C13A	C12	N3	119.3(4)	I2	Zn1	N1	112.52(9)
N2	C12	N3	109.0(3)	I2	Zn1	N3	108.09(9)
C12	C13A	C14A	120.2(9)	N1	Zn1	N3	80.8(1)
C12	C13A	C18A	118.0(7)				

Table 7.12 Angles obtained by X-ray diffraction for complex (**6**).

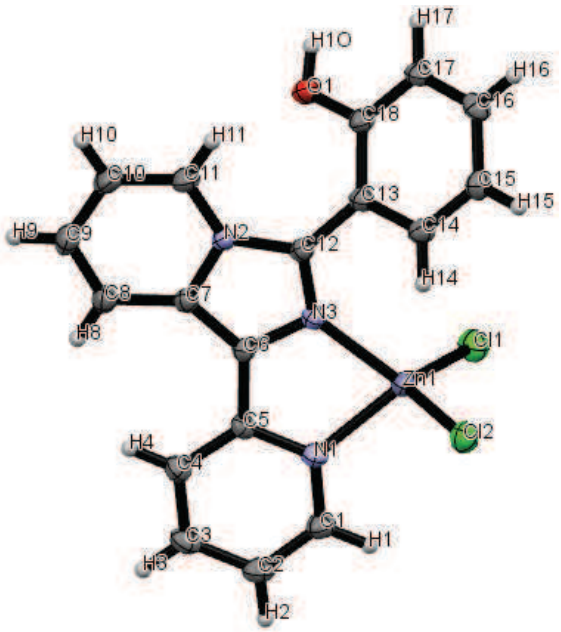

Figure 7.5 Cristal structure of complex (**7**).

$[Zn(L^{OH})Cl_2](7)\cdot DMF$	
Formula	$C_{21}H_{20}Cl_2N_4O_2Zn$
Space Group	P -1
Cell Lengths	*a* = 7.8713(5) *b* = 10.5041(7) *c* = 13.2157(8)
Cell Angles	α = 98.323(5) β = 95.308(5) γ = 95.448(5)
Cell Volume	1070.01
Z,Z'	Z = 2, Z' = 0
R-Factor (%)	4.62

Table 7.13 Crystallographic parameters obtained by X-ray diffraction for complex (**7**)·DMF.

Atom1	Atom2	Length(Å)	Atom1	Atom2	Length(Å)	Atom1	Atom2	Length(Å)
C1	H1	0.930	C9	C10	1.424(5)	C18	O1	1.357(4)
C1	C2	1.377(4)	C10	H10	0.930	Cl1	Zn1	2.217(1)
C1	N1	1.340(3)	C10	C11	1.354(5)	Cl2	Zn1	2.2147(9)
C2	H2	0.930	C11	H11	0.930	N1	Zn1	2.070(2)
C2	C3	1.395(4)	C11	N2	1.388(4)	N3	Zn1	2.039(2)
C3	H3	0.930	C12	C13	1.468(4)	O1	H1O	0.81(5)
C3	C4	1.385(4)	C12	N2	1.380(4)	C19	H19	0.930
C4	H4	0.931	C12	N3	1.328(3)	C19	N4	1.328(4)
C4	C5	1.397(4)	C13	C14	1.406(4)	C19	O2	1.237(3)
C5	C6	1.464(4)	C13	C18	1.407(4)	C20	H20A	0.960
C5	N1	1.366(4)	C14	H14	0.930	C20	H20B	0.960
C6	C7	1.394(4)	C14	C15	1.385(4)	C20	H20C	0.959
C6	N3	1.377(4)	C15	H15	0.930	C20	N4	1.447(5)
C7	C8	1.425(4)	C15	C16	1.391(4)	C21	H21A	0.961
C7	N2	1.403(3)	C16	H16	0.931	C21	H21B	0.960
C8	H8	0.930	C16	C17	1.382(4)	C21	H21C	0.960
C8	C9	1.359(4)	C17	H17	0.930	C21	N4	1.456(4)
C9	H9	0.931	C17	C18	1.398(4)			

Table 7.14 Bond lengths obtained by X-ray diffraction for complex (**7**)·DMF.

Atom1	Atom2	Atom3	Angle (°)	Atom1	Atom2	Atom3	Angle (°)
H1	C1	C2	118.3	H15	C15	C16	120.2
H1	C1	N1	118.3	C15	C16	H16	119.8
C2	C1	N1	123.3(3)	C15	C16	C17	120.4(3)
C1	C2	H2	121.0	H16	C16	C17	119.8
C1	C2	C3	118.0(3)	C16	C17	H17	119.8
H2	C2	C3	121.0	C16	C17	C18	120.4(3)
C2	C3	H3	120.1	H17	C17	C18	119.9
C2	C3	C4	119.9(3)	C13	C18	C17	119.8(3)
H3	C3	C4	120.1	C13	C18	O1	117.8(3)
C3	C4	H4	120.5	C17	C18	O1	122.5(3)
C3	C4	C5	118.9(3)	C1	N1	C5	118.9(2)
H4	C4	C5	120.6	C1	N1	Zn1	126.7(2)
C4	C5	C6	125.1(3)	C5	N1	Zn1	114.4(2)
C4	C5	N1	121.0(3)	C7	N2	C11	121.9(2)
C6	C5	N1	113.8(2)	C7	N2	C12	108.9(2)
C5	C6	C7	132.9(3)	C11	N2	C12	129.0(2)
C5	C6	N3	118.2(2)	C6	N3	C12	109.1(2)
C7	C6	N3	108.9(2)	C6	N3	Zn1	112.6(2)
C6	C7	C8	137.3(3)	C12	N3	Zn1	138.3(2)
C6	C7	N2	104.6(2)	C18	O1	H1O	108(4)
C8	C7	N2	118.0(2)	Cl1	Zn1	Cl2	117.15(3)
C7	C8	H8	120.3	Cl1	Zn1	N1	112.75(7)
C7	C8	C9	119.3(3)	Cl1	Zn1	N3	117.89(7)
H8	C8	C9	120.4	Cl2	Zn1	N1	108.71(7)
C8	C9	H9	119.6	Cl2	Zn1	N3	113.46(7)
C8	C9	C10	120.9(3)	N1	Zn1	N3	80.94(9)
H9	C9	C10	119.6	H19	C19	N4	118.2
C9	C10	H10	119.7	H19	C19	O2	118.2
C9	C10	C11	120.6(3)	N4	C19	O2	123.6(3)
H10	C10	C11	119.7	H20A	C20	H20B	109.5
C10	C11	H11	120.6	H20A	C20	H20C	109.5
C10	C11	N2	118.9(3)	H20A	C20	N4	109.4
H11	C11	N2	120.5	H20B	C20	H20C	109.5
C13	C12	N2	125.7(2)	H20B	C20	N4	109.5
C13	C12	N3	125.8(3)	H20C	C20	N4	109.5
N2	C12	N3	108.4(2)	H21A	C21	H21B	109.4
C12	C13	C14	119.2(3)	H21A	C21	H21C	109.5
C12	C13	C18	122.1(3)	H21A	C21	N4	109.5
C14	C13	C18	118.7(3)	H21B	C21	H21C	109.5
C13	C14	H14	119.5	H21B	C21	N4	109.5
C13	C14	C15	120.8(3)	H21C	C21	N4	109.5
H14	C14	C15	119.7	C19	N4	C20	120.9(3)
C14	C15	H15	120.0	C19	N4	C21	121.2(3)
C14	C15	C16	119.8(3)	C20	N4	C21	117.9(3)

Table 7.15 Angles obtained by X-ray diffraction for complex (**7**)·DMF.

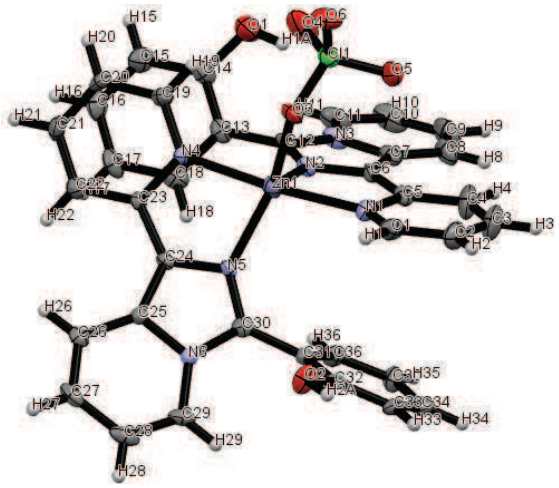

Figure 7.6 Cristal structure of complex (**10**).

$[Zn(L^{OH})_2](ClO_4)_2\ H_2O$ (10)	
Formula	$C_{36}H_{28}Cl_2N_6O_{11}Zn$
Space Group	C 2/c
Cell Lengths	*a* = 34.213(2) *b* = 10.3413(3) *c* = 25.7849(19)
Cell Angles	α = γ = 90° β = 129.302(5)
Cell Volume	7059.45
Z,Z'	Z = 8, Z' = 0
R-Factor (%)	10.1

Table 7.16 Crystallographic parameters obtained by X-ray diffraction for complex (**10**).

Atom1	Atom2	Length(Å)	Atom1	Atom2	Length(Å)	Atom1	Atom2	Length(Å)
C1	H1	0.931	C15	C16	1.37(1)	C30	N5	1.33(1)
C1	C2	1.384(9)	C16	H16	0.929	C30	N6	1.375(7)
C1	N1	1.341(8)	C16	C17	1.39(2)	C31	C32	1.403(9)
C2	H2	0.930	C17	H17	0.929	C31	C36	1.397(7)
C2	C3	1.371(9)	C17	C18	1.38(1)	C32	C33	1.387(8)
C3	H3	0.931	C18	H18	0.93	C32	O2	1.352(6)
C3	C4	1.38(1)	C19	H19	0.932	C33	H33	0.930
C4	H4	0.930	C19	C20	1.381(8)	C33	C34	1.375(7)
C4	C5	1.394(9)	C19	N4	1.34(1)	C34	H34	0.928
C5	C6	1.463(9)	C20	H20	0.931	C34	C35	1.400(9)
C5	N1	1.354(6)	C20	C21	1.38(1)	C35	H35	0.930
C6	C7	1.380(8)	C21	H21	0.930	C35	C36	1.378(8)
C6	N2	1.391(7)	C21	C22	1.37(1)	C36	H36	0.930
C7	C8	1.419(6)	C22	H22	0.931	Cl1	O3	1.467(6)
C7	N3	1.402(8)	C22	C23	1.380(7)	Cl1	O4	1.423(6)
C8	H8	0.929	C23	C24	1.45(1)	Cl1	O5	1.435(5)
C8	C9	1.35(1)	C23	N4	1.366(9)	Cl1	O6	1.424(7)
C9	H9	0.931	C24	C25	1.40(1)	N1	Zn1	2.097(5)
C9	C10	1.42(1)	C24	N5	1.374(6)	N2	Zn1	2.025(4)
C10	H10	0.929	C25	C26	1.415(7)	N4	Zn1	2.070(5)
C10	C11	1.359(8)	C25	N6	1.403(9)	N5	Zn1	2.049(6)
C11	H11	0.930	C26	H26	0.931	O1	H1A	0.820
C11	N3	1.396(8)	C26	C27	1.36(1)	O2	H2A	0.820

Atom1	Atom2	Length(Å)	Atom1	Atom2	Length(Å)	Atom1	Atom2	Length(Å)
C12	C13	1.466(8)	C27	H27	0.929	O3	Zn1	2.229(6)
C12	C13	1.466(8)	C27	H27	0.929	O3	Zn1	2.229(6)
C12	N2	1.327(8)	C27	C28	1.43(1)	Cl2	O7	1.412(6)
C12	N3	1.385(6)	C28	H28	0.93	Cl2	O8	1.420(8)
C13	C14	1.39(1)	C28	C29	1.351(7)	Cl2	O9	1.448(6)
C13	C18	1.42(1)	C29	H29	0.931	Cl2	O10	1.422(9)
C14	C15	1.384(9)	C29	N6	1.39(1)	O11	H11A	0.853
C14	O1	1.357(9)	C30	C31	1.460(8)	O11	H11B	0.92
C15	H15	0.93						

Table 7.17 Bond lengths obtained by X-ray diffraction for complex (**10)**.

Atom1	Atom2	Atom3	Angle (°)	Atom1	Atom2	Atom3	Angle (°)
H1	C1	C2	119.0	C25	C26	C27	119.3(6)
H1	C1	N1	119.0	H26	C26	C27	120.3
C2	C1	N1	122.0(7)	C26	C27	H27	119.9
C1	C2	H2	120.7	C26	C27	C28	120.5(7)
C1	C2	C3	118.4(8)	H27	C27	C28	119.6
H2	C2	C3	120.9	C27	C28	H28	119.3
C2	C3	H3	119.8	C27	C28	C29	121.4(7)
C2	C3	C4	120.5(9)	H28	C28	C29	119.3
H3	C3	C4	119.7	C28	C29	H29	121.0
C3	C4	H4	120.6	C28	C29	N6	118.1(6)
C3	C4	C5	118.8(8)	H29	C29	N6	121.0
H4	C4	C5	120.6	C31	C30	N5	126.0(6)
C4	C5	C6	124.9(7)	C31	C30	N6	125.1(6)
C4	C5	N1	120.6(7)	N5	C30	N6	108.7(5)
C6	C5	N1	114.5(6)	C30	C31	C32	122.8(6)
C5	C6	C7	132.9(6)	C30	C31	C36	118.7(6)
C5	C6	N2	117.7(6)	C32	C31	C36	118.4(6)
C7	C6	N2	109.4(6)	C31	C32	C33	119.6(6)
C6	C7	C8	137.9(7)	C31	C32	O2	117.0(6)
C6	C7	N3	104.9(6)	C33	C32	O2	123.5(6)
C8	C7	N3	117.2(6)	C32	C33	H33	119.5
C7	C8	H8	120.0	C32	C33	C34	120.8(6)
C7	C8	C9	120.0(7)	H33	C33	C34	119.7
H8	C8	C9	120.1	C33	C34	H34	119.6
C8	C9	H9	119.3	C33	C34	C35	120.8(6)
C8	C9	C10	121.3(8)	H34	C34	C35	119.6
H9	C9	C10	119.4	C34	C35	H35	120.9
C9	C10	H10	119.6	C34	C35	C36	118.0(6)
C9	C10	C11	120.8(8)	H35	C35	C36	121.1
H10	C10	C11	119.6	C31	C36	C35	122.4(6)
C10	C11	H11	121.1	C31	C36	H36	118.8
C10	C11	N3	117.7(7)	C35	C36	H36	118.8
H11	C11	N3	121.2	O3	Cl1	O4	108.9(3)

Atom1	Atom2	Atom3	Angle (°)	Atom1	Atom2	Atom3	Angle (°)
C13	C12	N2	126.4(6)	O3	Cl1	O5	109.7(3)
C13	C12	N3	124.9(6)	O3	Cl1	O6	108.6(3)
N2	C12	N3	108.6(6)	O4	Cl1	O5	110.5(3)
C12	C13	C14	121.2(6)	O4	Cl1	O6	110.7(3)
C12	C13	C18	119.3(6)	O5	Cl1	O6	108.4(3)
C14	C13	C18	119.3(7)	C1	N1	C5	119.7(6)
C13	C14	C15	119.5(7)	C1	N1	Zn1	126.0(5)
C13	C14	O1	118.6(7)	C5	N1	Zn1	113.7(4)
C15	C14	O1	121.9(7)	C6	N2	C12	108.3(6)
C14	C15	H15	119.5	C6	N2	Zn1	113.0(4)
C14	C15	C16	120.9(8)	C12	N2	Zn1	138.6(5)
H15	C15	C16	119.6	C7	N3	C11	123.0(6)
C15	C16	H16	119.7	C7	N3	C12	108.8(6)
C15	C16	C17	120.6(8)	C11	N3	C12	128.2(6)
H16	C16	C17	119.7	C19	N4	C23	118.9(5)
C16	C17	H17	120.1	C19	N4	Zn1	126.5(4)
C16	C17	C18	119.6(8)	C23	N4	Zn1	114.2(4)
H17	C17	C18	120.3	C24	N5	C30	108.8(5)
C13	C18	C17	120.0(7)	C24	N5	Zn1	111.4(4)
C13	C18	H18	120.0	C30	N5	Zn1	138.9(4)
C17	C18	H18	120.0	C25	N6	C29	122.1(5)
H19	C19	C20	118.8	C25	N6	C30	109.2(5)
H19	C19	N4	119.0	C29	N6	C30	128.7(5)
C20	C19	N4	122.2(6)	C14	O1	H1A	109.6
C19	C20	H20	120.7	C32	O2	H2A	109.5
C19	C20	C21	118.7(6)	Cl1	O3	Zn1	124.1(3)
H20	C20	C21	120.6	N1	Zn1	N2	80.8(2)
C20	C21	H21	120.3	N1	Zn1	N4	168.3(2)
C20	C21	C22	119.5(6)	N1	Zn1	N5	102.1(2)
H21	C21	C22	120.2	N1	Zn1	O3	83.5(2)
C21	C22	H22	119.9	N2	Zn1	N4	107.4(2)
C21	C22	C23	120.2(6)	N2	Zn1	N5	122.1(2)
H22	C22	C23	119.9	N2	Zn1	O3	113.2(2)
C22	C23	C24	126.4(6)	N4	Zn1	N5	80.9(2)
C22	C23	N4	120.4(6)	N4	Zn1	O3	85.4(2)
C24	C23	N4	113.2(6)	N5	Zn1	O3	124.7(2)
C23	C24	C25	131.3(6)	O7	Cl2	O8	109.8(4)
C23	C24	N5	119.4(6)	O7	Cl2	O9	111.6(4)
C25	C24	N5	109.1(6)	O7	Cl2	O10	109.8(5)
C24	C25	C26	137.1(6)	O8	Cl2	O9	110.0(4)
C24	C25	N6	104.3(5)	O8	Cl2	O10	108.0(5)
C26	C25	N6	118.6(6)	O9	Cl2	O10	107.6(5)
C25	C26	H26	120.4	H11A	O11	H11B	142

Table 7.18 Angles obtained by X-ray diffraction for complex (**10)**.

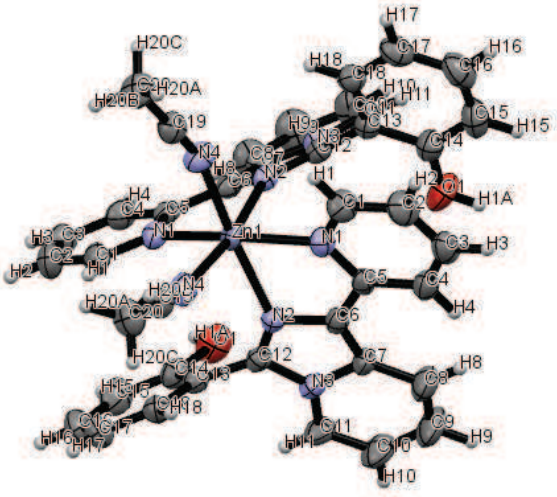

Figure 7.7 Cristal structure of complex (**12b**).

$[Zn(L^{OH})_2(CH_3CN)](BF_4)_2$ **(12b)**	
Formula	$C_{40}H_{32}B_2F_8N_8O_2Zn$
Space Group	C 2/c
Cell Lengths	*a* = 17.8778(18) *b* = 20.5170(15) *c* = 13.6658(14)
Cell Angles	α = γ = 90° β = 119.331(7)
Cell Volume	4370.01
Z,Z'	Z = 4, Z' = 0
R-Factor (%)	6.34

Table 7.19 Crystallographic parameters obtained by X-ray diffraction for complex (**12b**).

Atom1	Atom2	Length(Å)	Atom1	Atom2	Length(Å)	Atom1	Atom2	Length(Å)
C1	H1	0.929	C16	H16	0.931	C8	H8	0.930
C1	C2	1.372(8)	C16	C17	1.386(7)	C8	C9	1.348(8)
C1	N1	1.348(7)	C17	H17	0.930	C9	H9	0.930
C2	H2	0.931	C17	C18	1.377(9)	C9	C10	1.43(1)
C2	C3	1.371(6)	C18	H18	0.930	C10	H10	0.929
C3	H3	0.931	C19	C20	1.453(6)	C10	C11	1.340(7)
C3	C4	1.378(8)	C19	N4	1.134(5)	C11	H11	0.931
C4	H4	0.930	C20	H20A	0.959	C11	N3	1.396(6)
C4	C5	1.393(7)	C20	H20B	0.960	C12	C13	1.461(6)
C5	C6	1.461(6)	C20	H20C	0.959	C12	N2	1.323(6)
C5	N1	1.351(4)	N1	Zn1	2.129	C12	N3	1.372(4)
C6	C7	1.390(5)	N2	Zn1	2.169	C13	C14	1.394(6)
C6	N2	1.373(5)	N4	Zn1	2.185	C13	C18	1.398(5)
C7	C8	1.410(6)	O1	H1A	0.820	C14	C15	1.385(9)
C7	N3	1.401(6)	Zn1	N1	2.129	C14	O1	1.359(6)
C8	H8	0.930	Zn1	N2	2.169	C15	H15	0.931
C8	C9	1.348(8)	Zn1	N4	2.185	C15	C16	1.381(8)
C9	H9	0.930	C1	H1	0.929	C16	H16	0.931
C9	C10	1.43(1)	C1	C2	1.372(8)	C16	C17	1.386(7)
C10	H10	0.929	C1	N1	1.348(7)	C17	H17	0.930
C10	C11	1.340(7)	C2	H2	0.931	C17	C18	1.377(9)
C11	H11	0.931	C2	C3	1.371(6)	C18	H18	0.930
C11	N3	1.396(6)	C3	H3	0.931	C19	C20	1.453(6)

Atom1	Atom2	Length(Å)	Atom1	Atom2	Length(Å)	Atom1	Atom2	Length(Å)
C12	C13	1.461(6)	C3	C4	1.378(8)	C19	N4	1.134(5)
C12	N2	1.323(6)	C4	H4	0.930	C20	H20A	0.959
C12	N3	1.372(4)	C4	C5	1.393(7)	C20	H20B	0.960
C13	C14	1.394(6)	C5	C6	1.461(6)	C20	H20C	0.959
C13	C18	1.398(5)	C5	N1	1.351(4)	O1	H1A	0.820
C14	C15	1.385(9)	C6	C7	1.390(5)	B1	F1	1.319(7)
C14	O1	1.359(6)	C6	N2	1.373(5)	B1	F2	1.227(6)
C15	H15	0.931	C7	C8	1.410(6)	B1	F3	1.347(8)
C15	C16	1.381(8)	C7	N3	1.401(6)	B1	F4	1.31(2)

Table 7.20 Bond lengths obtained by X-ray diffraction for complex (**12b)**.

Atom1	Atom2	Atom3	Angle (°)	Atom1	Atom2	Atom3	Angle (°)
H1	C1	C2	118.6	N4	Zn1	N4	81.6
H1	C1	N1	118.8	N1	Zn1	N2	76.8
C2	C1	N1	122.6(4)	N1	Zn1	N4	95.4
C1	C2	H2	120.3	N2	Zn1	N4	94.2
C1	C2	C3	119.3(5)	H1	C1	C2	118.6
H2	C2	C3	120.4	H1	C1	N1	118.8
C2	C3	H3	120.4	C2	C1	N1	122.6(4)
C2	C3	C4	119.2(5)	C1	C2	H2	120.3
H3	C3	C4	120.4	C1	C2	C3	119.3(5)
C3	C4	H4	120.3	H2	C2	C3	120.4
C3	C4	C5	119.3(4)	C2	C3	H3	120.4
H4	C4	C5	120.4	C2	C3	C4	119.2(5)
C4	C5	C6	124.2(4)	H3	C3	C4	120.4
C4	C5	N1	121.3(4)	C3	C4	H4	120.3
C6	C5	N1	114.5(3)	C3	C4	C5	119.3(4)
C5	C6	C7	132.4(3)	H4	C4	C5	120.4
C5	C6	N2	117.9(3)	C4	C5	C6	124.2(4)
C7	C6	N2	109.7(3)	C4	C5	N1	121.3(4)
C6	C7	C8	138.0(4)	C6	C5	N1	114.5(3)
C6	C7	N3	104.0(3)	C5	C6	C7	132.4(3)
C8	C7	N3	118.0(4)	C5	C6	N2	117.9(3)
C7	C8	H8	120.3	C7	C6	N2	109.7(3)
C7	C8	C9	119.4(5)	C6	C7	C8	138.0(4)
H8	C8	C9	120.3	C6	C7	N3	104.0(3)
C8	C9	H9	119.3	C8	C7	N3	118.0(4)
C8	C9	C10	121.4(5)	C7	C8	H8	120.3
H9	C9	C10	119.3	C7	C8	C9	119.4(5)
C9	C10	H10	119.9	H8	C8	C9	120.3
C9	C10	C11	120.2(5)	C8	C9	H9	119.3
H10	C10	C11	119.9	C8	C9	C10	121.4(5)
C10	C11	H11	120.7	H9	C9	C10	119.3
C10	C11	N3	118.7(4)	C9	C10	H10	119.9
H11	C11	N3	120.6	C9	C10	C11	120.2(5)

Atom1	Atom2	Atom3	Angle (°)	Atom1	Atom2	Atom3	Angle (°)
C13	C12	N2	127.4(3)	H10	C10	C11	119.9
C13	C12	N3	123.1(3)	C10	C11	H11	120.7
N2	C12	N3	108.9(3)	C10	C11	N3	118.7(4)
C12	C13	C14	121.4(4)	H11	C11	N3	120.6
C12	C13	C18	119.1(3)	C13	C12	N2	127.4(3)
C14	C13	C18	119.4(4)	C13	C12	N3	123.1(3)
C13	C14	C15	119.6(4)	N2	C12	N3	108.9(3)
C13	C14	O1	117.2(4)	C12	C13	C14	121.4(4)
C15	C14	O1	123.2(4)	C12	C13	C18	119.1(3)
C14	C15	H15	120.0	C14	C13	C18	119.4(4)
C14	C15	C16	120.0(5)	C13	C14	C15	119.6(4)
H15	C15	C16	119.9	C13	C14	O1	117.2(4)
C15	C16	H16	119.5	C15	C14	O1	123.2(4)
C15	C16	C17	121.1(5)	C14	C15	H15	120.0
H16	C16	C17	119.3	C14	C15	C16	120.0(5)
C16	C17	H17	120.5	H15	C15	C16	119.9
C16	C17	C18	118.9(5)	C15	C16	H16	119.5
H17	C17	C18	120.7	C15	C16	C17	121.1(5)
C13	C18	C17	120.9(4)	H16	C16	C17	119.3
C13	C18	H18	119.6	C16	C17	H17	120.5
C17	C18	H18	119.5	C16	C17	C18	118.9(5)
C20	C19	N4	179.1(5)	H17	C17	C18	120.7
C19	C20	H20A	109.5	C13	C18	C17	120.9(4)
C19	C20	H20B	109.4	C13	C18	H18	119.6
C19	C20	H20C	109.5	C17	C18	H18	119.5
H20A	C20	H20B	109.4	C20	C19	N4	179.1(5)
H20A	C20	H20C	109.5	C19	C20	H20A	109.5
H20B	C20	H20C	109.4	C19	C20	H20B	109.4
C1	N1	C5	118.3(4)	C19	C20	H20C	109.5
C1	N1	Zn1	125.5	H20A	C20	H20B	109.4
C5	N1	Zn1	115.9	H20A	C20	H20C	109.5
C6	N2	C12	108.3(3)	H20B	C20	H20C	109.4
C6	N2	Zn1	111.0	Zn1	N1	C1	125.5
C12	N2	Zn1	137.1	Zn1	N1	C5	115.9
C7	N3	C11	122.2(4)	C1	N1	C5	118.3(4)
C7	N3	C12	109.0(3)	Zn1	N2	C6	111.0
C11	N3	C12	128.7(4)	Zn1	N2	C12	137.1
C19	N4	Zn1	161.6	C6	N2	C12	108.3(3)
C14	O1	H1A	109.4	C7	N3	C11	122.2(4)
N1	Zn1	N2	76.8	C7	N3	C12	109.0(3)
N1	Zn1	N4	95.4	C11	N3	C12	128.7(4)
N1	Zn1	N1	166.1	Zn1	N4	C19	161.6
N1	Zn1	N2	93.4	C14	O1	H1A	109.4
N1	Zn1	N4	95.1	F1	B1	F2	116.8(6)
N2	Zn1	N4	94.2	F1	B1	F3	113.9(5)

Atom1	Atom2	Atom3	Angle (°)	Atom1	Atom2	Atom3	Angle (°)
N2	Zn1	N1	93.4	F1	B1	F4	109.3(7)
N2	Zn1	N2	91.2	F2	B1	F3	114.1(6)
N2	Zn1	N4	170.6	F2	B1	F4	99.3(7)
N4	Zn1	N1	95.1	F3	B1	F4	100.9(7)
N4	Zn1	N2	170.6				

Table 7.21 Angles obtained by X-ray diffraction for complex (**12b)**.

Chapter 8

References

REFERENCES

[1] K. Ye, J. S. Schultz, *Anal. Chem.* **2003**, *75* (14), 3451-3459.

[2] a) E. Saïdi, B. Samson, L. Aigouy, S. Volz, S. Löw, P. Bergaud, C. and Mortier M., *Nanotechnolgy* **2009**, 20; b) Patrick, T. K. Chin *et al, Nanotechnology* **2013***,* 24.

[3] H. F. Hess, E. Betzig, T. D. Harris, L. N. Pfeiffer, K. W. West , *Science* **1994**, *264* (5166), 1740-174.

[4] E. Klampaftis, M. Congiu, N. Robertson, B. S. Richards, *IEEE Journal of Photovoltaics* **2011**, *1*, 29-36.

[5] J. R. Lakowicz, *Principles of Fluorescence Spectroscopy (third edition)*, **2006.**

[6] a) X. Guo, L. Li, F. N. Castellano, H. Szmacinski, J. R. Lakowicz, *Anal. Biochem.* **1997**, *254*, 54; b) M. Gerstein, A. M. Lesk, C. Chothia, *Biochemistry* **1994**, *33*, 6739; c) L. Li, H. Szmacinski, J. R. Lakowicz, *Biospectroscopy* **1997**, *3*, 155; d) L. Li, H. Szmacinski, J. R. Lakowicz, *Anal. Biochem.* **1997**, *244*, 80.

[7] J. Kalinowski, V. Fattori, M. Cocchi, J. A. G. Williams, *Coord. Chem. Rev.* **2011**, *255*, 2401-2425.

[8] M. Tavasli, T. N. Moore, Y. Zheng, M. R. Bryce, M. A. Fox, G. C. Griffiths, V. Jankus, H. A. Al-Attar, A. P. *J.* Monkman, *Mater. Chem.* **2012**, *22*, 6419-6428.

[9] J.-F. Yin, M. Velayudham, D. Bhattacharya, H.-C. Lin, K.-L. Lu, *Coord. Chem. Rev*. **2012**, *256*, 3008-3035.

[10] X. Liu, H. Xia, W. Gao, Q. Wu, X. Fan, Y. Mu, C. Ma, *J. Mater. Chem*. **2012**, *22*, 3485-3492.

[11] C.-W. Hsu, C.-C. Lin, M.-W. Chung, Y. Chi, G.-H. Lee, P.-T. Chou, C.-H. Chang, P.-Y. Chen, *J. Am. Chem. Soc*. **2011**, *133*, 12085-12099.

[12] R. C. Evans, P. Douglas, C. J. Winscom, *Coord. Chem. Rev*. **2006**, *250*, 2093-2126.

[13] a) H. Y. Chao, W. Lu, Y. Li, M. C. Chan, C. M. Che, K. K. Cheung, N. Zhu, *J.Am. Chem. Soc.* **2002**, *124*, 14696 – 14706; b) Y. G. Ma, C. M. Che, H. Y. Chao, X. M. Zhou, W. H. Chan, J. C. Shen, *Adv. Mater.* **1999**, *11*, 852– 857; c) D. M. Zink, M. Bächle, T. Baumann, M. Nieger, M. Kuhn, C. Wang, W. Klopper, U. Monkowius, T. Hofbeck, H. Yersin, S. Bräse, *Inorg. Chem.* **2013**, *52*, 2292 –2305.

[14] C. W. Hsu, C. C. Lin, M. W. Chung, Y. Chi, G. H. Lee, P. T. Chou, C. H. Chang, P. Y. Chen, *J. Am. Chem. Soc.* **2011**, *133*, 12085 – 12099; b) A. Earnshaw, N. Greenwood, *Chemistry of the Elements* (*second edition*), **1997**; c) R. G. Pearson, *Inorg. Chim. Acta* **1995**, *240*, 93– 98; d) D. Saravanabharathi, M. Nethaji, A. G. Samuelson, *Polyhedron* **2002**, *21*, 2793 –2800; e) K. Tsuge, *Chem. Lett.* **2013**, *42*, 204 –208.

[15] a) Z. Li, A. Dellali, J. Malik, M. Motevalli, R. M. Nix, T. Olukoya, Y. Peng, H. Ye, W. P. Gillin, I. Hernández, P. B. Wyatt, *Inorg. Chem.* **2013**, *52*, 1379-1387; b) I. V. Sazanovich, C. Kirmaier, E. Hindin, L. Yu, D. F. Bocian, J. S. Lindsey, D. Holten, *J. Am. Chem. Soc.* **2004**, *126*, 2664-2665; c) T. Sano, Y. Nishio, H. Takahashi, T. Usuki, K. J. Shibata, *Mater. Chem.* **2000**, *10*, 157-161; d) Y.

Hamada, T. Sang, H. Fujii, Y. Nishio, H. Takanashi, K. Shibata, *Jpn. J. Appl. Phys. Part 2* **1996**, *35*, L1339-L1341.

[16] a) H. Kunkely, A. Vogler, *J. Chem. Soc. Chem. Commun.* **1990**, 1204-1205; b) R. Bertoncello, M. Bettinelli, M. Casarin, A. Gulino, E. Tondello, A. Vittadinilc, *Inorg. Chem.* **1992**, *31*, 1558-1565; c) C.-F. Lee, K.-F. Chin, S.-M. Peng, C.-M. Che, *J. Chem. Soc. Dalton Trans.* **1993**, 467-470; d) Y. Ma, H.-Y. Chao, Y. Wu, S. T. Lee, W.-Y. Yu, C.-M. Che, *Chem. Commun.* **1998**, 2491-2492; e) Y. Ma, T. Lai, Y. Wu, *Adv. Mater.* **2000**, *12*, 433-436.

[17] a) D. G. Cuttell, S.-M. Kuang, P. E. Fanwick, D. R. McMillin, R. A. Walton, *J. Am. Chem. Soc.* **2002**, *124*, 6−7; b) S. –M. Kuang, D. G. Cuttell, D. R. McMillin, P. E. Fanwick, R. A. Walton, *Inorg. Chem.* **2002**, *41*, 3313−3322.

[18] a) R. D. Costa, D. Tordera, E. Orti, H. Bolink, J. Schönle, S. Graber, C. E. Housecroft, E. C. Constable, J. A. Zampese, *J. Mater. Chem.* **2011**, *21*, 16108−16118; b) C. L. Linfoot, P. Richardson, T. E. Hewat, O. Moudam, M. M. Forde, A. Collins, F. White, N. Robertson, *Dalton Trans.* **2010**, *39*, 8945−8956; c) Q. Zhang, Q. Zhou, Y. Cheng, L. Wang, D. Ma, X. Jing, F. Wang, *Adv. Mater.* **2004**, *16*, 432−436; d) Q. Zhang, Q. Zhou, Y. Cheng, L. Wang, D. Ma, X. Jing, F. Wang, *Adv. Funct. Mater.* **2006**, *16*, 1203−1208; e) T. MacCormick, W. –L. Jia, S. Wang, *Inorg. Chem.* **2006**, *45*, 147−155; f) H. Ge, W. Wei, P. Shuai, G. Lei, S. Qing, *J. Lumin.* **2011**, *131*, 238−243; g) N. Armaroli, G. Accorsi, M. Holler, O. Moudam, J.-F. Nierengarten, Z. Zhou, R. T. Wegh, R. Welter, *Adv. Mater.* **2006**, *18*, 1313−1316; h) L. Yang, J. –K. Feng, A. –M. Ren, M. Zhang, Y. –G. Ma, X. –D. Liu, *Eur. J. Inorg. Chem.* **2005**, 1867−1879.

[19] A. Kaeser, B. Delavaux-Nicot, C. Duhyon, Y. Coppel, J. F. Nierengarten, *Inorg. Chem.* **2013**, *52*, 14343-14354.

[20] a) T. S. Andy Hor, *Inorg. Chim. Acta* **1988**, *149*, 157−158; b) M. C. Gimeno, P. G. Jones, A. Laguna, C. J. Sarroca, *Chem. Soc., Dalton Trans.* **1995**, 1473−1481; c) E. Bembenek, O. Crespo, M. C. Gimeno, P. G. Jones, A. Laguna, *Chem. Ber.* **1994**, *127*, 835−840; d) O. Crespo, M. C. Gimeno, P. G. Jones, A. Laguna, *J. Chem. Soc., Dalton Trans.* **1996**, *24*, 4583−4588; e) A. Cingolani, Effendi, F. Marchetti, C. Pettinari, R. Pettinari, B. W. Skelton, A. H. White, *Inorg. Chim. Acta* **2002**, *329*, 100−112; f) Effendi, J. V. Hanna, F. Marchetti, D. Martini, C. Pettinari, R. Pettinari, B.W. Skelton, A. H. White, *Inorg. Chim. Acta* **2004**, *357*, 1523−1537; g) Effendi; C. Di Nicola, M. Nitiatmodjo, C. Pettinari, B. W. Skelton, A. H. White, *Inorg. Chim. Acta* **2005**, *358*, 735−747; h) Effendi, C. Di Nicola, M. Fianchini, C. Pettinari, B. W. Skelton, N. Somers, A. H. White, *Inorg. Chim. Acta* **2005**, *358*, 763−795; i) A. Cingolani, Effendi; C. Pettinari, B. W. Skelton, A. H. White, *Inorg. Chim. Acta* **2006**, *359*, 2170−2177; l) Effendi; F. Marchetti, C. Pettinari, R. Pettinari, B. W. Skelton, A. H. White, *Inorg. Chim. Acta* **2007**, *360*, 1388−1413.

[21] (a) G. A. Ardizzoia, S. Brenna, S. Durini and B. Therrien, *Organometallics* **2012**, *31*, 5427-5437; (b) G. A. Ardizzoia, S. Brenna and B. Therrien, *Dalton Trans*. **2012**, *41*, 783-790; (c) G. A. Ardizzoia, S. Brenna and B. Therrien, *Eur. J. Inorg. Chem*. **2010**, 3365-3371; (d) G. A. Ardizzoia, S. Brenna, F. Castelli, S. Galli and N. Masciocchi, *Inorg. Chim. Acta* **2010**, *363*, 324-329.

[22] G. A. Ardizzoia, S. Brenna, S. Durini, I. Trentin and B. Therrien, *Dalton Trans*. **2013**, *42*, 12265-12273.

[23] (a) G. A. Ardizzoia, S. Brenna, F. Castelli, S. Galli, C. Marelli, A. Maspero, *J. Organomet. Chem*., **2008**, *693*, 1870-1876; (b) G. A. Ardizzoia, S. Brenna, S. Cenini, G. La Monica, N. Masciocchi, A. Maspero, *J. Mol. Catal. A: Chemical* **2003**, *204-205*, 333-340; (c) N. Masciocchi, G. A. Ardizzoia, G. LaMonica, A. Maspero, S. Galli, A. Sironi, *Inorg. Chem.* **2001**, *40*, 6983-6989.

[24] P. C. Ford, E. Cariati, J. Bourassa, *Chem. Rev.* 1999, **99**, 3625-3647.

[25] M. Hashimoto, S. Igawa, M. Yashima, I. Kawata, M. Hoshino, M. Osawa, *J. Am. Chem. Soc.* **2011**, *133*, 10348-10351.

[26] N. Armaroli, *Chem. Soc. Rev.* **2001**, *30*, 113-124.

[27] a) D. V. Scaltrito, D. W. Thompson, J. A. O'Callaghan, G. J. Meyer, *Coord. Chem. Rev.* **2000**, *208*, 243-266; b) M. Ruthkosky, C. A. Kelly, F. N. Castellano, G. J. Meyer, *Coord. Chem. Rev.* **1998**, *171*, 309-322.

[28] R. Ziolo, S. Lipton, Z. Dori, *Chem. Commun.* **1970**, 1124-1125.

[29] a) R. A. Rader, D. R. McMillin, M. T. Buckner, T. G. Matthews, D. J. Casadonte, R. K. Lengel, S. B. Whittaker, L. M. Darmon, F. E. Lytle, *J. Am. Chem. Soc.* **1981**, *103*, 5906-5912; b) P. A. Breddels, P. A. M. Berdowski, G. Blasse, D. R. McMillin, *J. Chem. Soc. Faradya Trans. 2*, **1982**, *78*, 595-601.

[30] D. G. Cuttell, S.-M. Kuang, P. E. Fanwick, D. R. McMillin, R. A. Walton, *J. Am. Chem. Soc.* **2002**, *124*, 6-7.

[31] Q. Zhang, Q. Zhou, Y. Cheng, L. Wang, D. Ma, X. Jing, F. Wang, *Adv. Mater.* **2004**, *16*, 432-436.

[32] N. Armaroli, G. Accorsi, M. Holler, O. Moudam, J.-F. Nierengarten, Z. Zhou, R. T. Wegh, R. Welter, *Adv. Mater.* **2006**, *18*, 1313-1316.

[33] H. Xia, L. He, M. Zhang, M. Zeng, X. Wang, D. Lu, Y. Ma, *Opt. Mater.* **2007**, *29*, 667-671.

[34] a) R. Czerwieniec, J. Yu, H. Yersin, *Inorg. Chem.* 2011, **50**, 8293-8301; b) M. G. Crestani, G. F. Manbeck, W. W. Brennessel, T. M. McCormick, R. Eisenberg, *Inorg. Chem.* **2011**, *50*, 7172-7188; c) L. Zhang, B. Li, Z. Su, *Langmuir* **2009**, *25*, 2068-2074.

[35] a) R. Hou, T.-H. Huang, X.-J. Wang, X.-F. Jiang, Q.-L. Ni, L.-C. Gui, Y.-J. Fan, Y.-L. Tan, *Dalton Trans.* **2011**, *40*, 7551-7558; b) L. Qin, Q. Zhang, W. Sun, J. Wang, C. Lu, Y. Cheng, L. Wang, *Dalton Trans.* **2009**, *38*, 9388-9381; c) F. Wei, L. Fang, Y. Huang, *Inorg. Chim. Acta* **2010**, *363*, 2600-2605.

[36] O. Moudam, A. Kaeser, B. Delavaux-Nicot, C. Duhayon, M. Holler, G. Accorsi, N. Armaroli, I. Séguy, J. Navarro, P. Destruel, J.-F. Nierengarten, *Chem. Commun.* **2007**, 3077-3079; b) A. Tsuboyama, K. Kuge, M. Furugori, S. Okada, M. Hoshino, K. Ueno, *Inorg. Chem.* **2007**, *46*, 1996-2001.

[37] S. Durini "Sintesi e caratterizzazione di complessi luminescenti di Cu(I) contententi l'anione lattato" Master Thesis, October 2011.

[38] R. Carballo, B. Covelo, N. Fernández-Hermida, E. García-Martínez, A. B. Lago, E. M. Vázquez-López, *J. Mol. Struct.* **2008**, *892*, 427-432 and references therein.

[39] X. Zhang, A. M. Wright, N. J. DeYonker, T. K. Hollis, N. I. Hammer, C. E. Webster, E. J. Valente, *Organometallics* **2012**, *31*, 1664-1672

[40] a) J. C. Deaton, S. C. Switalski, D. Y. Kondakov, R. H. Young, T. D. Pawlik, D. J. Giesen, S. B. Harkins, A. J. M. Miller, S. F. Mickenberg, J. C. Peters, *J. Am. Chem. Soc.* **2010**, *132*, 9499-9508; b) G.-F. Gao, M. Li, S.-Z. Zhan, Z. Lv, G.-H. Chen, D. Li, *Chem. Eur. J.* **2011**, *17*, 4113-4117.

[41] (a) D. Bose, S. H. Rahaman, G. Mostafa, R.D. Bailey-Walsh, M. J. Zaworotko, B. K. Ghosh, *Polyhedron* **2003**, *23*, 545; (b) N.Du, Q. Mei, M. Lu, *Synth. Met.* **2005**, *149*, 193; (c) J. Li, J. –H. Zhou, Y. –Z. Li, L. –H. Weng, X. –T. Chen, Z. Yu, Z. Xue, *Inorg. Chem. Commun.***2004**, *7*, 538; (d) S. –G. Liu, J. –L. Zuo, Y. Wang, Y. –Z. Li, X. –Z You, *J. Phys. Chem. Solids* **2005**, *66*, 735; (e) T. –R. Chen, *J. Mol. Struct.* **2005**, *737*, 35; (f) M. Qureshi, S. Manoharan, S. P. Singh, Y. N. Mahaptra, *Solid State Commun.* **2005**, *133*, 305; (g) A. Yeh, *Mater. Lett.* **2005**, *59*, 1811; (g) W. Guo, Z. Peng, D. Li, Y. Zhou, *Polyhedron* **2004**, *23*, 1701.

[42] N. Kundu, S. M. T. Abtab, S. Kundu, A. Endo, S. J. Teat and Muktimoy Chaudhury *Inorganic Chemistry* **2012**, *51* (4), 2652-2661.

[43] Q. –D. W. R. Liu, S. Wang, *J. Chem. Soc., Dalton Trans.* **2004**, 2073.

[44] S. V. Larionov, T. E. Kokina, V. F. Plyusnin, L. A. Glinskaya, A. V. Tkachev, Y. A. Bryleva, N. V. Kuratieva, M.I. Rakhmanova, E. S. Vasilyev, *Polyhedron* **2014**, *77*, 75.

[45] B. Bozic-Weber, E. C. Constable, N. Hostettler, C. E. Housecroft, R. Schmitt and E. Schönhofer, *Chem. Commun.* **2012**, *48*, 5727–5729.

[46] E. Yamaguchi, F. Shibahara and T. Murai, *J. Org. Chem*. **2011**, *76*, 6146-6158 and references therein.

[47] (a) M. Nakatsuka and T. Shimamura, *Jpn. Kokai Tokkyo Koho* JP 2001035664; *Chem. Abstr*. **2001**, *134*, 170632; (b) G. Tominaga, R. Kohama and A.Takano, *Jpn. Kokai Tokkyo Koho* JP 2001006877 *Chem. Abstr*. **2001**, *134*, 93136 (c) D. Kitazawa, G. Tominaga and A. Takano, *Jpn. Kokai Tokkyo Koho* JP 2001057292; *Chem. Abstr.* **2001**, *134*, 200276.

[48] H. Nakamura and H. Yamamoto, *PCT Int. Appl*. WO 2005043630; Chem. Abstr. **2005**, *142*, 440277.

[49] (a) L. Salassa, A. Albertino, C. Garino, G. Volpi, C. Nervi, R. Gobetto and K. I. Hardcastle, *Organometallics* **2008**, *27*, 1427-1435; (b) C. Garino, T. Ruiu, L. Salassa, A. Albertino, G. Volpi, C. Nervi, R. Gobetto and K. I. Hardcastle, *Eur. J. Inorg. Chem*. **2008**, 3587-3591.

[50] A. L. Guckian, M. Doering, M. Ciesielski, O. Walter, J. Hjelm, N. M. O'Boyle, W. Henry, W. R. Browne, J. J. McGarvey and J. G. Vos, *Dalton Trans*. **2004**, 3943-3949.

[51] J. Wang, L. Dyers Jr., Mason R. Jr., P. Amoyaw and X. R. Bu, *J. Org. Chem.* **2005**, 70, 2353-2356.

[52] G. A. Ardizzoia, S. Brenna, S. Durini, B. Therrien and M. Veronelli, *Eur. J. Inorg. Chem*. **2014**, 4310-4319.

[53] For a detailed discussion on L^{OH} structure and properties, M. Veronelli "Sintesi e studio delle proprietà luminescenti di leganti piridilimidazo-piridinici e dei loro derivati di metalli bivalenti" Master Thesis, Octobre 2011.

[54] (a) M. Gennari, M. Retegan, S. DeBeer, J. Pécaut, F. Neese, M.-N. Collomb, C. Duboc, *Inorg. Chem*. **2011**, *50*, 10047-10055; (b) A. D. Khalaji, G. Grivani, M. Seyyedi, K. Fejfarova, M. Dusek, *Polyhedron* **2013**, *49*, 19-23.

[55] (a) MOPAC2012, J. J. P. Stewart, Stewart Computational Chemistry, Colorado Springs, CO, USA, HTTP://OpenMOPAC.net; (b) J. J. P. Stewart, *J. Mol. Modeling* **2013**, *19*, 1-32

[56] G. A. Ardizzoia, S. Brenna, S. Durini, B. Therrien, submitted to *Polyhedron*, November **2014**.

[57] (a) D. Ballivet-Tkatchenko, C. Bremard, *J. Chem. Soc. Dalton Trans.* **1983,** 1143; (b) R. Fernández-Galán, B.R. Manzano, A. Otero, M. Lanfranchi, M.A. Pellinghelli, *Inorg. Chem.* **1994**, *33*, 2309; (c) N.V. Pavlenko, L.A. Babadzhanova, I.I. Gerus, Y.L. Yagupolskii, W. Tyrra, D. Naumann, *Eur. J. Inorg. Chem.* **2007**, 1501; (d) P. de Frémont, H. Clavier, V. Rosa, T. Avilés, P. Braunstein, *Organometallics* **2011**, *30*, 2241.

[58] The trigonality index, τ, is defined by the equation: $\tau = (\beta - \alpha)/60$, where α and β are the two major angles of a five coordinate system (with $\beta > \alpha$). Then, for ideally square pyramidal geometry $\tau = 0$ ($\alpha = \beta = 180°$), whereas for perfectly trigonal-bipyramidal geometry $\tau = 1$ ($\alpha = 120°$, $\beta = 180°$). For further explanation see: A.W. Addison, T.N. Rao, J. Reedijk, J. van Rijn, G.C. Verschoor, J. Chem. Soc., *Dalton Trans.* **1984**, 1349.

[59] S.-F. Liu, Q. Wu, H.L. Schmider, H. Aziz, N.-X. Hu, Z. Popović, S. Wang, *J. Am. Chem. Soc.* **2000**, *122*, 3671.

[60] Subtraction was performed using a dedicated software, Felix32 Analysis Module (© 2001)

[61] K. Kolmakov, V. N. Belov, J. Bierwagen, C. Ringemann, V. Müller, C. Eggeling, S. W. Hell, *Chem. Eur. J*. **2010**, *16*, 158-166.

[62] S. Milione, C. Capaccione, C. Cuomo, M. Strianese, V. Bertolasi and A. Grassi, *Inorg. Chem*. **2009**, *48*, 9510-9518

[63] a) E. Cariati, L. Bourassa, P. C. Ford, *Chem. Commun.* **1998**, 1623-1624; b) H. V. R. Dias, H. V. K. Diyabalanage, M. A. Rawashdeh-Omary, M. A. Franzman, M. A. Omary, *J. Am. Chem. Soc.* **2003**, *125*, 12072-12073; c) L. F. Shi, B. Li, *Eur. J. Inorg. Chem.* **2009**, 2294-2302.

[64] a) D. R. McMillin, K. M. McNett, *Chem. Rev.* **1998**, *98*, 1201–1219; b) E. A. Lewis, W. B. Tolman, *Chem. Rev.* **2004**, *104*, 1047–1076.

[65] a) Q. S. Zhang, Q. G. Zhou, Y. X. Cheng, L. X. Wang, D. G. Ma, X. B. Jing, F. S. Wang, *Adv. Mater.* **2004**, *16*, 432–436; b) W. L. Jia, T. McCormick, Y. Tao, J. P. Lu, S. N. Wang, *Inorg. Chem.* **2005**, *44*, 5706–5712; c) Q. S. Zhang, Q. G. Zhou, Y. X. Cheng, L. X. Wang, F. G. Ma, X. B. Jing, F. S. Wang, *Adv. Funct. Mater.* **2006**, *16*, 1203–1208; d) N. Armaroli, G. Accorsi, M. Holler, O. Moudam, J. F. Nierengarten, Z. Zhou, R. T. Wegh, R. Welter, *Adv. Mater.* **2006**, *18*, 1313–1316; e) Z. S. Su, G. B. Che, W. L. Li, W. M. Su, M. T. Li, B. Chu, B. Li, Z. Q. Zhang, Z. Z. Hu, *Appl. Phys. Lett.* **2006**, *88*, 213508 (1–3); f) Q. S. Zhang, J. Q. Ding, Y. X. Cheng, L. X. Wang, Z. Y. Xie, X. B. Jing, F. S. Wang, *Adv. Funct. Mater.* **2007**, *17*, 2983–2990; g) N. Robertson, *ChemSusChem* **2008**, *1*, 977–979.

[66] a) Y. –L. Tung, S. –W. Lee, Y. Chi, L. –S. Chen, C. –F. Shu, F. –I. Wu, A. J. Carty, P. –T. Chou, S. –M. Peng, G. –H. Lee, *Adv. Mater.* **2005**, *17*, 1059. b) Y. –L. Tung, S. –W. Lee, Y. Chi, Y. –T. Tao, C. –H. Chien, Y. –M. Cheng, P. –T. Chou, S. –M. Peng, C. –S. Liu, *J. Mater. Chem.* **2005**, *15*, 460. c) C. –H. Fang, Y. –L. Chen, C. –H. Yang, Y. Chi, T. –S. Yeh, E. Y. Li, T. –M. Cheng, C. –J. Hsu, P. –T. Chou, C. –T. Chen, *Chem. Eur. J.* **2007**, *13*, 2686.

[67] A. Barbieri, G. Accorsi, N. Armaroli, *Chem. Commun.* **2008**, 2185–2193.

[68] a) D. G. Cuttell, S. M. Kuang, P. E. Fanwick, D. R. McMillin, R. A. Walton, *J. Am. Chem. Soc.* **2002**, *124*, 6–7; b) S. M. Kuang, D. G. Cuttell, D. R. McMillin, P. E. Fanwick, R. A. Walton, *Inorg. Chem.* **2002**, *41*, 3313–3322.

[69] a) L. Yang, J. –K. Feng, A. -M Ren, M. Zhang, Y. –G. Ma, X. –D. Liu, *Eur. J. Inorg. Chem.* **2005**, 1867 –1879; b) C. L. Linfoot, P. Richardson, T. E. Hewat, O. Moudam, M. M. Forde, A. Collins, F. White, N. Robertson, *Dalton Trans.* **2010**, *39*, 8945 –8956; c) T. McCormick, W. –L. Jia, S. Wang, *Inorg. Chem.* **2006**, *45*, 147 –155; d) H. Ge, W. Wei, P. Shuai, G. Lei, S. Qing, *J. Lumin.* **2011**, *131*, 238 –243; f) R. D. Costa, D. Tordera, E. Orti, H. Bolink, J. Schçnle, S. Graber, C. E. Housecroft, E. C. Constable, J. A. Zampese, *J. Mater. Chem.* **2011**, *21*, 16108 –16118.

[70] a) J.P. Zhang, Y. Y. Lin, W. X. Zhang, X. M. Chen, *J. Am. Chem. Soc.* **2005**, *127*, 14162; b) J. G. Haasnoot, *Coord. Chem. Rev.* **2000**, 131, 200–202; c) G. Yang, R. G. Raptis, *Chem. Commun.* **2004**, 2058; d) Y. B. Dong, H. Y. Wang, J. P. Ma, R. Q. Huang, M. D. Smith, *Cryst. Growth Des.* **2005**, *5*,

789; d) Y. Wang, L. Yi, X. Yang, B. Ding, P. Cheng, D. Z. Liao, S. P. Yan, *Inorg. Chem.* **2007**, *46*, 5822; e) Y. Wang, B. Ding, P. Cheng, D. Z. Liao, S. P. Yan, *Inorg. Chem.* **2007**, *46*, 2002.

[71] R. A. Stein, C. Knobler, *Inorg. Chem.* **1977**, *16*, 242.

[72] a) M. R. Churchill, B. G. DeBoer, *Inorg. Chem.* **1975**, *14*, 2502; b) B. K. Teo, J. C. Calabrese, *J. Am. Chem. Soc.* **1972**, *97*, 1256; c) R. G. Goel, P. Pilon, *Inorg. Chem.* **1978**, *17*, 2876.

[73] A. T. S. Hor, *Inorg. Chim. Acta* **1988**, *149*, 157-158.

[74] A. Cingolani, Effendi; F. Marchetti, C. Pettinari, R. Pettinari, B. W. Skelton, A. H. White, *Inorg. Chim. Acta* **2002**, *329*, 100−112.

[75] A. Kaeser, B. Delavaux-Nicot, C. Duhayon, Y. Coppel and J. F. Nierengarten *Inorg. Chem.* **2013**, *52*, 14343-14354

[76] G. A. Ardizzoia, G. La Monica, A. Maspero, M. Moret and N. Masciocchi, *Inorg. Chem.* **1997**, *36*, 2321-2328

[77] C. A. Tolman, *Chem. Rev.* 1977, **77**, 313-348

[78] E. Klampaftis, D. Ross, K. R. McIntosh, and B. S. Richards, *Sol. Energ. Mat. Sol. C* **2009**, *93* (8), 1182–1194.

[79] H. J. Hovel, R. T. Hodgson, and J. M.Woodall, *Sol. Energ. Mat. Sol. C.* **1979**, *2* (1),19–29.

[80] L. Danos,T. Parel,T. Markvart,V. Barrioz, W. S. M. Brooks and S.J.C. Irvine, *Sol.Energy Mater.* **2012**, *98*, 486.

[81] E. Klampaftis, M. Congiu, N. Robertson, and B. S. Richards*,Photovoltaics, IEEE Journal of*, **2011**, *1*, 29-36.

[82] a) S. V. Eliseeva and J. C. G. Bünzli, *Chem. Soc. Rev.* **2010**, *39*, 189; b) L. Armelao, S. Quici, F. Barigelletti, G. Accorsi, G. Bottaro, M. Cavazzini, E. Tondello, *Coord. Chem. Rev.* **2009**, *254*, 487-505.

[83] G. A. Crosby, R. E. Whan, and R. M. Alire, *J. Chem. Phys.* **1964**, *34*, 743–748.

[84] a) A. Le Donne, M. Acciarri, D. Narducci, S. Marchionna, and S. Binetti, *Prog. Photovolt: Res. Appl*. **2009**, (*17*), 519–525; b) Z. Cheng, L. Pan, F. Su, M. Cao, and Z. Sun, *Surf. Rev.Lett.* **2009**, *16*, 669-673; c) T. Fukuda, S. Kato, E. Kin, K. Okaniwa, H. Morikawa, Z. Honda, and N. Kamata, *Opt. Mater.* **2009**, *32*, 22–25.

[85] M. Planells, E. Klampaftis, M. Congiu, R. Shivanna, K. V. Rao, O. Chepelin, A. C. Jones, B. S. Richards, S. J George, K. S. Narayan, N. Robertson, *Eur. J. Inorg. Chem.* **2014**, *19*, 3095–3100.

[86] O. Moudam, B. C. Rowan, M. Alamiry, P. Richardson, B. S. Richards, A. C. Jones, N. Robertson, *Chem. Commun.* **2009**, 6649–6651.

[87] L-O. Pålsson and A. P. Monkman, *Adv. Mater*. **2002**, *14*, 757-758.

[88] ADF2012, SCM, Theoretical Chemistry, Vrije Universiteit, Amsterdam, The Netherlands, http://www.scm.com.

[89] (a) J. P. Perdew, K. Burke and M. Ernzerhof, *Phys. Rev. Lett*. **1996**, *77*, 3865-3868; **1997**, *78*, 1396 (E); (b) J. P. Perdew, M. Ernzerhof and K. J. Burke, *Chem. Phys*. **1996**, *105*, 9982-9985; (c) C. Adamo and V. Barone, *J. Chem. Phys*. **1999**, *110*, 6158-6170.

[90] (a) A. D. Becke, *Phys. Rev. A* **1988**, *38*, 3098-3100; (b) C. Lee, W. Yang and R. G. Parr, *Phys. Rev. B* **1988**, *37*, 785-789; (c) A. D. Becke, *J. Chem. Phys*. **1993**, *98*, 5648-5652; (d) P. J. Stephens, F. J. Devlin, C. F. Chabalowski and M. J. Frisch, *J. Phys. Chem*. **1994**, *98*, 11623-11627.

[91] (a) Y. Zhao and D.G. Truhlar, *J. Chem. Phys*. **2006**, *110*, 13126-13130; (b) Y. Zhao and D. G. Truhlar, *Theor. Chem. Acc.* **2008**, *120*, 215-241.

[92] D. P. Chong, Mol. Phys. **2005**, *103*, 749-761.

[93] A. Klamt and G. J. Schürmann, *Chem. Soc., Perkin Trans*. **1993**, *2*, 799-805; (b) A. Klamt and V. Jonas, *J. Chem. Phys*. **1996**, *105*, 9972-9981; (c) C. C. Pye and T. Ziegler, *Theor. Chem. Acc*. **1999**, *101*, 396-408.

[94] G. M. Sheldrick, *Acta Cryst*. **2008**, *A64*, 112-122.

[95] L. J. Farrugia, *J. Appl. Cryst.* **1997,** *30*, 565.

ACKNOWLEDGEMENTS

I would like to sincerely thank my supervisor Dr. Stefano Brenna, without his help and support this work of thesis would have not been possible.

Thanks to Prof. G. Attilio Ardizzoia, who gave me the opportunity to work in his group and to grow as a chemist and as a person.

I would like to express my gratitude to Dr. Neil Robertson, who host me in his laboratory at University of Edinburgh, and to his group, who made me feel welcomed since the first day.

A special thanks to my lab mates and university colleagues, who made the period spent at Università dell'Insubria unforgettable.